COMPREHENSIVE APPROACH TO ELECTROCHEMICAL SENSING OF VOLATILE TOXIC ORGANIC COMPOUNDS

Abhilash Krishnamurthy

Doctoral Dissertation
Jožef Stefan International Postgraduate School
Ljubljana, Slovenia

Supervisor: Asst. Prof. Dr. Kristina Žagar Soderžnik, IPS and Jožef Stefan Institute, Ljubljana, Slovenia

Evaluation Board:
Prof. Dr. Kristina Žužek, Chair, IPS and Jožef Stefan Institute, Ljubljana, Slovenia
Asst. Prof. Dr. Gregor Marolt, Member, Faculty of Chemistry and Chemical Technology, University of Ljubljana, Slovenia
Prof. Dr. Cristian Fabrega Gallego, Member, University of Barcelona, Spain

MEDNARODNA PODIPLOMSKA ŠOLA JOŽEFA STEFANA
JOŽEF STEFAN INTERNATIONAL POSTGRADUATE SCHOOL



Abhilash Krishnamurthy

COMPREHENSIVE APPROACH TO ELECTROCHEMICAL SENSING OF VOLATILE TOXIC ORGANIC COMPOUNDS

Doctoral Dissertation

CELOVIT PRISTOP K ELEKTROKEMIJSKEMU ZAZNAVANJU HLAPNIH STRUPENIH ORGANSKIH SPOJIN

Doktorska disertacija

Supervisor: Asst. Prof. Dr. Kristina Žagar Soderžnik

Ljubljana, Slovenia, March 2026

To my parents and my family, whose steady belief, support, and encouragement carried me through every stage of this journey.
My friends, my surrogate family, who have proven that family is not only something you are born into but something you find, for standing beside me even when I felt completely isolated.
And all the unseen, hardworking students who doubt the value of their efforts and consider giving up: let this document serve as a reminder that your work matters, and so do you.

Acknowledgments

I would like to thank the Slovenian Research and Innovation Agency (ARIS) for funding this research through grants P2-0084 (Programme Nanostructured Materials), J2-1739 (High Performance Nanostructured Acrylamide Sensors), J2-3051 (SensePMC), and PR-09874 (Young Researcher Project). This funding made the work possible.

I would like to thank Asst. Prof. Kristina Žagar Soderžnik for providing great mentorship that went beyond the usual scope of academic supervision. She showed consistent confidence in my abilities. Her decision to accept me as a doctoral candidate at the outset of the project was both an honour and a pivotal moment in its development.

I would like to acknowledge the Electrochemical Sensors Group and the Department for Nanostructured Materials (K7) at the Jožef Stefan Institute for providing technical assistance and engaging in constructive discussions, both in the laboratory and informally. Their readiness to share expertise greatly advanced the research.

I would like to thank the Jožef Stefan International Postgraduate School (IPS) for fostering an environment that encourages curiosity and for providing the infrastructure, courses, and facilities essential for both experimental and theoretical work. The school's interdisciplinary atmosphere, opportunities for collaboration, and access to knowledge enriched my academic development and created the conditions for a productive and stimulating doctoral journey.

I would like to thank Primalab d.o.o. for supporting the research and generously loaning the Metrohm VIONIC potentiostat. This instrument proved indispensable in several key experiments, enabling precise electrochemical measurements and contributing directly to the quality and reliability of the results. I also appreciate their readiness to assist with technical questions, which helped keep experiments on schedule and ensured optimal use of the equipment.

I would like to thank Pika Štefančič for producing graphical artwork that improved the clarity and balance of the presentation of results. Her ability to rapidly create clear, visually coherent figures enhanced the accessibility of this work and ensured that the findings could be communicated effectively to both specialist and non-specialist audiences.

On a more personal note, I would like to express my deepest gratitude to my parents, Dr Bharathi Rangaswamy and Dr Krishnamurthy Balasundaram, and to the rest of my family for their unwavering support, encouragement, and understanding throughout this journey. Their belief in me has been a constant source of strength, especially during the most challenging periods of my doctoral work.

I am equally grateful to my closest friends, Anarghya Chander, Barbara Ljubec, Bharadwaj M. R., Giulia Della Pelle, Karthik K. C., Jurij Gracej, Mihaela Rebernik Gracej, Milan Vukšić, Nikhil Bhootpur, and Vinko Sršan whose companionship, humour, and steady presence helped me navigate moments of doubt. Their support extended far beyond academia and provided much-needed balance. I would also like to thank the Rebernik and Gracej families for their warmth and kindness, which made me feel at home from the very beginning.

I would also like to thank the University Karate Club, Ljubljana, and the Modern Sports Karate Association, especially Master Peter Brejc, for their guidance and discipline. I am equally grateful to Master Hamed Karim, his kickboxing club, and his students, whose commitment and energy created a space for focus, resilience, and personal growth. The training sessions offered not only physical conditioning but also mental clarity, both of which proved essential in sustaining motivation and wellbeing throughout this doctoral journey.

Finally, I would like to express my gratitude to the Republic of Slovenia for welcoming me and providing a place to call home throughout the duration of my studies. The country's high quality of life, along with the security and stability it offered, ensured that I could focus fully on my work. I have received nothing but warmth from the Slovenian people, and this generosity of spirit has left a lasting impression on me.

To all of you, I extend my sincere thanks. Your support, in its many forms, has shaped this work and the person behind it.

Abstract

This dissertation presents the design, fabrication, and evaluation of a portable electrochemical sensing platform for the detection of benzenediol isomers: catechol, hydroquinone and resorcinol, in acidic aqueous media. Using screen-printed carbon electrodes modified with carbon-supported platinum (Pt/C), the sensor demonstrated sensitive, selective, and reproducible electrochemical responses across a range of electrochemical techniques. The system was further validated on commercial products containing target analytes, confirming its applicability in complex, real-world matrices.

To ensure long-term reliability, the sensor was periodically characterised using electrochemical impedance spectroscopy and voltammetry-derived metrics such as polarisation resistance and effective double-layer capacitance. This enabled non-destructive monitoring of electrode degradation and fouling.

The study also examined the influence of potentiostat architecture on electrochemical processes, comparing analogue and digital scan modes and highlighting their impact on peak currents and capacitive artefacts.

A key innovation in this work was the application of frequency-domain analysis to electrochemical waveforms. Classical techniques such as cyclic voltammetry, linear sweep voltammetry, and differential pulse voltammetry were transformed into spectral representations using Fourier transforms. This provided new insight into the harmonic structure of applied electrochemical signals and the optimisation of waveform parameters. In addition, alternating current voltammetry was used to study the frequency response of the sensor, offering a deeper understanding of kinetic and capacitive processes.

All investigations contributed toward the development of a compact, Internet of Things-enabled electrochemical sensor platform. Both the hardware and software were designed from the ground up to meet specific user requirements, ensuring portability, real-time data acquisition, and wireless communication. This interdisciplinary effort merges concepts from analytical chemistry, materials science, electrical engineering, and embedded systems to advance the field of on-site electrochemical sensing.

Povzetek

Disertacija predstavlja zasnovo, izdelavo in ovrednotenje prenosne elektrokemijske senzorske platforme za detekcijo izomerov benzenediola: katehola, hidrokinona in rezorcinola v kislih vodnih medijih. Z uporabo sitotiskanih ogljikovih elektrod, modificiranih s platino na ogljikovem nosilcu (Pt/C), je bil razvit senzor, ki je izkazoval občutljive, selektivne in ponovljive elektrokemijske odzive pri uporabi različnih elektrokemijskih tehnik. Sistem je bil dodatno preverjen na realnih vzorcih, tj. komercialnih izdelkih, ki vsebujejo ciljne analite, s čimer je bila potrjena njegova uporabnost v kompleksnih, realnih matričnih okoljih.

Za zagotavljanje dolgoročne zanesljivosti je bil senzor periodično karakteriziran z uporabo elektrokemijske impedančne spektroskopije ter z metrikami, pridobljenimi iz voltametrije, kot sta polarizacijska upornost in efektivna kapacitivnost dvojne plasti. Ta pristop je omogočil nedestruktivno spremljanje degradacije elektrode in nalaganja površinskih nečistoč.

V študiji je bil analiziran tudi vpliv vrste potenciostata na elektrokemijske procese, s primerjavo analognih in digitalnih načinov skeniranja ter poudarkom na razlikah v vrhovih tokov in kapacitivnih motnjah.

Ključna inovacija v tem delu je bila uporaba frekvenčne domene za analizo elektrokemijskih valovnih oblik. Klasične tehnike, kot so ciklična voltametrija, linearna voltametrija in diferencialna pulzna voltametrija, so bile s Fourierjevo transformacijo pretvorjene v spektralne prikaze. S tem je bil pridobljen nov vpogled v harmonsko strukturo uporabljenih elektrokemijskih signalov in optimizacijo parametrov valovnih oblik. Poleg tega je bila uporabljena izmenična napetostna voltametrija za preučevanje frekvenčnega odziva senzorja, kar je omogočilo globlje razumevanje kinetičnih in kapacitivnih pojavov.

Vsa dognanja so prispevala k razvoju kompaktne, z internetom povezane elektrokemijske senzorske platforme. Tako strojna kot programska oprema sta bili zasnovani povsem na novo, prilagojeni specifičnim zahtevam uporabnikov, tako da omogočata prenosljivost, zajem podatkov v realnem času in brezžično komunikacijo. Tovrstini interdisciplinarni pristop združuje koncepte analizne kemije, znanosti o materialih, elektrotehnike in vgrajenih sistemov ter pomembno prispeva k razvoju terenskega elektrokemijskega zaznavanja.

Contents

List of Figures **xv**

Abbreviations **xvii**

Symbols **xix**

Glossary **xxi**

1 Introduction **1**
1.1 Need for Environmental Sensing ... 1
1.1.1 Environmental Protection and Monitoring ... 2
1.2 Fundamentals of Electrochemical Sensing ... 3
1.2.1 Examples of Established Electrochemical Sensors ... 4
1.2.1.1 Ion Selective Electrodes ... 5
1.2.1.2 Pellistors ... 5
1.3 Conventional Electrochemical Methods ... 5
1.3.1 Cyclic Voltammetry ... 6
1.3.2 Chronoamperometry ... 8
1.3.3 Differential Pulse Voltammetry ... 10
1.3.4 AC Voltammetry ... 12
1.3.5 Multi-Step Chronoamperometry ... 13
1.3.6 Electrochemical Impedance Spectroscopy ... 15
1.4 Frequency-Domain Analysis in Electrochemistry ... 18
1.4.1 Fourier Series and Fourier Transform ... 18
1.4.2 Laplace Transform as an Extension of Fourier Transform ... 19
1.4.3 Discrete Fourier Transform and Fast Fourier Transform ... 20
1.4.4 Short-Time Fourier Transform and the Heisenberg Uncertainty Principle ... 21
1.4.5 Gabor Transform and Optimal Time-Frequency Localisation ... 21
1.4.6 Wavelet Transform and Multi-scale (Multi-timescale) Electrochemical Analysis ... 22
1.4.7 Z Transform and Digital Electrochemistry ... 22
1.4.8 Emerging Directions: Multirate and Digital Electrochemistry ... 23
1.5 Fundamentals of Potentiostat Design ... 23
1.5.1 Analogue and Digital Signals ... 23
1.5.2 Overview of Potentiostat Architecture ... 25
1.5.3 IoT-Enabled Implementation for Field Use ... 27
1.6 Volatile Toxic Organic Compounds ... 29
1.6.1 Health Impact and Regulatory Context ... 30
1.6.2 Chemical Overview of Benzenediols ... 31
1.6.2.1 Catechol and Hydroquinone ... 31

1.6.2.2 Resorcinol 32
1.7 Catalytic Enhancement using Carbon-Supported Catalysts 33
1.7.1 Electron Transfer in Carbon-Based Materials 34
1.7.2 Platinum in Organic Redox Chemistry 35
1.7.3 Alternative Catalytic Materials 35
1.8 Synthesis 36

2 Aims and Hypotheses **37**

3 Experimental Methods and Materials **39**
3.1 Electrode Modification Techniques 39
3.2 Electrochemical Testing Protocols 41
3.3 Instrumentation and Custom Hardware Development 41
3.4 Signal Processing and Simulation Approaches 42
3.5 Sample Preparation and Real-World Testing Procedures 42
3.6 Material Characterisation 43

4 Results and Discussion **45**
4.1 Detection of Benzenediols Using Modified SPEs 45
4.2 Analysis of Real-World Samples 60
4.3 Sensor Characterisation via EIS 61
4.4 Frequency-Domain Characterisation via Fourier Analysis 73
4.5 Hardware Influence on Electrochemical Response (Analogue vs Digital) 87
4.6 Case Study: IoT Sensor for Formaldehyde Detection 103
4.7 Future Work 116

5 Conclusions **117**
5.1 Summary of Findings 118
5.2 Limitations and Recommendations 119

References **121**

Bibliography **125**

Biography **127**

List of Figures

Figure 1.1: Conceptual overview of on-site VTOC sensing across industrial, aquatic, and indoor environments. The illustration highlights the shift from offline, centralised measurements to real-time, location-specific detection using portable sensor platforms.....3
Figure 1.2: Transition from a conventional three-electrode electrochemical cell to a portable sensing system using screen-printed electrodes and a handheld potentiostat connected to a mobile device. 4
Figure 1.3: Triangular potential waveform used in cyclic voltammetry, showing a forward and reverse linear sweep between two vertex potentials over a fixed scan rate.....6
Figure 1.4: Cyclic voltammogram of 1 mM catechol in 1 M HCl on a Pt/C-modified SPE. 8
Figure 1.5: Cyclic voltammogram of 1 mM resorcinol in 1 M HCl on a Pt/C-modified SPE. 8
Figure 1.6: Step potential waveform used in chronoamperometry, showing a sudden change in potential held constant over time, with corresponding diffusion-limited current decay. 9
Figure 1.7: Chronoamperometric response of 10 mM hydroquinone in 1 M HCl at 0.52 V vs Ag. 10
Figure 1.8: Potential waveform used in differential pulse voltammetry, showing a staircase baseline with superimposed pulses, each producing a differential current measurement used to generate a peak-shaped voltammogram.....11
Figure 1.9: Potential waveform used in AC voltammetry, showing a sinusoidal modulation superimposed on a linear sweep, enabling frequency-dependent separation of electrochemical current components. 12
Figure 1.10: Potential waveform used in multi-step chronoamperometry, consisting of a sequence of constant potential levels applied over time to probe electrochemical responses across multiple conditions.....14
Figure 1.11: Potential waveform used in electrochemical impedance spectroscopy, consisting of a constant DC bias with a superimposed low-amplitude sine wave swept across a broad frequency range to probe impedance characteristics.....15
Figure 1.12: Block diagram of analogue signal acquisition and digitisation in an electrochemical sensor circuit.....24
Figure 1.13: General schematic of potentiostat architecture for electrochemical sensing, illustrating signal paths and control elements. 26
Figure 1.14: Schematic representation of an IoT-enabled electrochemical sensor platform with modular components and wireless communication. 28
Figure 1.15: Reversible redox behaviour of hydroquinone and catechol showing the formation of p-benzoquinone and o-benzoquinone, respectively. 32
Figure 1.16: Irreversible oxidation and electropolymerisation of resorcinol, resulting in the deposition of polymeric material on the electrode surface. 33
Figure 1.17: Schematic representation of platinum nanoparticles dispersed on a carbon support (Pt/C), highlighting active sites for organic electrooxidation.....35

Figure 3.1: Illustration of the catalyst ink drop casting process onto the carbon working electrode of a DS150 SPE, showing selective application and avoidance of the counter and reference electrodes. 40
Figure 4.1: Graphical abstract of the benzenediol sensing workflow. Adapted from Krishnamurthy *et al.*, *Electrochimica Acta* (2024), shared under CC BY-NC-ND 4.0 licensing. 46
Figure 4.2: Voltammograms showing detection of benzenediol isomers in real samples: a. CC in tea, b. RS in anti-dandruff solution, c. HQ in acne cream. 60
Figure 4.3: Graphical abstract of the EIS diagnostic workflow. Adapted from Krishnamurthy et al., Sensing and Bio-Sensing Research 50 (2025) 100871, shared under CC BY-NC-ND 4.0 licensing. 62
Figure 4.4: Graphical abstract of the frequency-domain analysis workflow. Adapted from Krishnamurthy et al., Measurement 259 volume B (2026) 119706, shared under CC BY-NC-ND 4.0 licensing 74
Figure 4.5: Comparison of analogue and digital waveforms, illustrating signal representation in potentiostat systems. Concept adapted from Krishnamurthy et al., Sensors 24 (2024) 4907 (https://doi.org/10.3390/s24154907). 88
Figure 4.6: Graphical abstract of the IoT formaldehyde sensing platform. Adapted from Trafela et al., Sensors 23 (2023) 4676, shared under CC BY 4.0 licensing 103

Abbreviations

AC ... Alternating Current
ACV ... Alternating Current Voltammetry
ADC ... Analogue-to-Digital Converter
Au/C ... Gold-on-Carbon Catalyst
BLE ... Bluetooth Low Energy
CA ... Chronoamperometry
CC ... Catechol (1,2-dihydroxybenzene)
CE ... Counter Electrode
CPE ... Constant Phase Element
CV ... Cyclic Voltammetry
DAC ... Digital-to-Analogue Converter
DC ... Direct Current
DPV ... Differential Pulse Voltammetry
DFT ... Discrete Fourier Transform
DWT ... Discrete Wavelet Transform
EIS ... Electrochemical Impedance Spectroscopy
EPA ... Environmental Protection Agency (USA)
ECHA ... European Chemicals Agency
FFT ... Fast Fourier Transform
FWT ... Fast Wavelet Transform
GT ... Gabor Transform
HQ ... Hydroquinone (1,4-dihydroxybenzene)
IoT ... Internet of Things
ISE ... Ion-Selective Electrode
LoD ... Limit of Detection
LoQ ... Limit of Quantification
LSV ... Linear Sweep Voltammetry
MSCA ... Multi-Step Chronoamperometry
PC ... Personal Computer (Windows)
PCA ... Principal Component Analysis
PCB ... Printed Circuit Board
PGM ... Platinum-Group Metal
Pt/C ... Platinum-on-Carbon Catalyst
RE ... Reference Electrode
REL ... Recommended Exposure Limit
RMS ... Root Mean Square
RS ... Resorcinol (1,3-dihydroxybenzene)
RTOS ... Real-Time Operating System
SBS ... Sick Building Syndrome
SNR ... Signal-to-Noise Ratio
SPE ... Screen-Printed Electrode

STFT ... Short-Time Fourier Transform
SWV ... Square Wave Voltammetry
TIA ... Transimpedance Amplifier
TCP/IP ... Transmission Control Protocol/Internet Protocol
TWA ... Time-Weighted Average (Exposure Limit)
UPLC ... Ultra-Performance Liquid Chromatography
USB ... Universal Serial Bus
VTOC ... Volatile Toxic Organic Compound
WHO ... World Health Organisation

Symbols

j	...	Unit imaginary number ($\sqrt{-1}$)
ω	...	Angular frequency (radian s^{-1})
f	...	Linear frequency (Hz)
n	...	Number of electrons transferred
F	...	Faraday constant (96485 C mol^{-1})
A	...	Electrode area (cm^2)
D	...	Diffusion coefficient (cm^2 s^{-1})
C	...	Analyte concentration (mol l^{-1})
C_0	...	Bulk analyte concentration (mol l^{-1})
R	...	Gas constant (8.314 J K^{-1} mol^{-1})
T	...	Absolute temperature (K)
I *or* i	...	Current (A)
E	...	Potential (V)
R_S	...	Solution resistance (Ω)
R_{ct}	...	Charge-transfer resistance (Ω)
R_P	...	Polarisation resistance (Ω)
C_{dl}	...	Double-layer capacitance (F)
C_{eff}	...	Effective capacitance (F)
Q_n	...	Net charge transferred (C)
Z	...	Impedance (Ω)
ϕ	...	Phase angle (° or radian)
σ	...	Warburg coefficient (Ω $s^{-0.5}$)
s	...	Complex Laplace variable (Hz)
z	...	Complex Z-transform variable
t	...	Time (s)
τ	...	Time constant (s)
Ψ	...	Wavelet function
α	...	CPE phase parameter
N	...	ADC/DAC bit resolution

Glossary

Term	Definition
Alternating Current Voltammetry	A voltammetric technique using a sinusoidal potential superimposed on a DC bias to study frequency-dependent electrochemical behaviour.
Benzenediol	Aromatic dihydroxy compounds: catechol, hydroquinone, and resorcinol, serving as model volatile toxic organic analytes.
Capacitive (Non-Faradaic) Process	Current response arising from charging or discharging of the electrical double layer rather than from redox reactions.
Catechol	1,2-dihydroxybenzene, a naturally occurring redox-active compound.
Chronoamperometry	Time-dependent electrochemical method measuring current response to a potential step.
Constant Phase Element	Equivalent circuit element describing non-ideal capacitive behaviour caused by surface roughness or heterogeneity.
Cottrell Equation	Expression describing diffusion-controlled current decay over time after a potential step in chronoamperometry.
Cyclic Voltammetry	Technique sweeping potential linearly between two limits in both directions to study redox mechanisms, reversibility and kinetics.
Differential Pulse Voltammetry	Pulse-based voltammetry improving resolution and sensitivity by subtracting consecutive current samples.
Diffusion Coefficient	Measure of how fast electroactive species move through solution.
Double-Layer Capacitance	Effective capacitance formed by charge separation at the electrode–electrolyte interface.
Electrochemical Impedance Spectroscopy	Frequency-domain method characterising interfacial charge transfer, diffusion, and capacitance.
Equivalent Circuit	Electrical model composed of resistive, capacitive, and diffusive elements representing an electrochemical interface.
Faradaic Current	Component of total current arising from redox reactions, distinct from capacitive currents.
Faradaic Process	Electron-transfer reaction producing measurable current in an electrochemical cell.

Fourier Transform	Mathematical operation converting a signal from the time to the frequency domain.
Frequency-Domain Analysis	Approach for resolving electrochemical signals according to their harmonic components.
Gabor Transform	Gaussian-windowed form of the STFT providing optimal time–frequency localisation.
Harmonics	Integral multiples of a base frequency appearing in nonlinear or modulated electrochemical signals.
Hydroquinone	1,4-dihydroxybenzene, an electroactive organic compound used as a model analyte.
Impedance	Complex measure of resistance and reactance describing how an electrochemical system responds to an AC perturbation.
IoT Potentiostat	Portable potentiostat incorporating wireless communication and embedded processing for field sensing.
Laplace Transform	Mathematical transform for analysing transient electrochemical phenomena.
Linearity	Degree to which signal response is directly proportional to analyte concentration.
Nyquist Plot	Complex-plane representation of impedance, showing real versus imaginary components across frequency.
Polarisation Resistance	Resistance to charge transfer at the electrode interface, derived from impedance data.
Principal Component Analysis	Multivariate statistical method reducing complex multidimensional datasets (e.g., EIS or voltammetric features) into orthogonal principal components.
Randles Circuit	Equivalent circuit representing an electrochemical interface by resistive, capacitive, and diffusive elements.
Resorcinol	1,3-dihydroxybenzene, an isomer exhibiting irreversible oxidation and electrode fouling.
Screen-Printed Electrode	Miniaturised, disposable electrode printed on a planar substrate.
Selectivity	Ability of a sensor or an analytical method to discriminate target analytes from interfering species in complex matrices.
Sensitivity	Ratio of change in measured signal (current or potential) to change in analyte concentration; defines sensor responsiveness.
Short-Time Fourier Transform	Time–frequency technique using windowed Fourier analysis to study non-stationary electrochemical signals.
Signal-to-Noise Ratio	Quantitative measure comparing useful signal amplitude to background noise level.
Solution Resistance	Ohmic resistance of the electrolyte between working and reference electrodes, contributing to potential drop.

Spectrum	Representation of signal amplitude or power as a function of frequency, derived from Fourier analysis.
Transimpedance Amplifier	Amplifier converting electrode current into voltage for data acquisition.
Voltammetry	Class of electroanalytical techniques measuring current as a function of applied potential.
Warburg Impedance	Frequency-dependent impedance associated with semi-infinite diffusion.
Wavelet Transform	Multi-scale signal decomposition revealing both temporal and spectral features of electrochemical responses.
Z-Transform	Discrete-time analogue of the Laplace transform used in digital electrochemical system modelling.

Chapter 1

Introduction

The increasing prevalence of volatile toxic organic compounds (VTOC) (Brown, 1994) in air and water has become a significant concern for both environmental and public health (Harvey, 1995). Organic compounds, both natural and synthetic, are found in everyday products including paints, adhesives, and cleaning agents, and are linked to a wide range of health issues, from headaches and respiratory irritation to long-term carcinogenic effects. Traditional detection methods such as gas chromatography with mass spectrometry (GC-MS) and ultra-performance liquid chromatography (UPLC), while accurate, are expensive, complex, and unsuitable for real-time or on-site deployment. This has created a growing demand for compact, cost-effective, and portable sensing platforms that can measure reliably and robustly in real time. Electrochemical sensors (Hayat, 2014) meet these criteria by converting chemical processes into electrical signals. They can be designed to be highly sensitive and selective for specific target analytes. Among them, screen-printed electrodes (SPE) offer a particularly attractive solution due to their low cost, ease of modification, and potential for single-use deployment. This dissertation explores a comprehensive framework for the electrochemical sensing of VTOCs (namely catechol, resorcinol and hydroquinone) using modified SPEs and custom hardware, with an emphasis on improving selectivity, operational stability, and real-world usability.

1.1 Need for Environmental Sensing

In recent years, there has been a burgeoning recognition of the health and environmental risks posed by VTOCs, which include both aliphatic (Nematollahi, 2018) and aromatic (Angerer, 1991) compounds. Increasing evidence links these compounds to a wide range of adverse effects, from acute symptoms like irritation and dizziness to chronic issues including endocrine disruption, organ toxicity, and cancer. This has prompted public health authorities and environmental agencies across the globe to introduce ever-increasing stringent regulations aimed at controlling exposure levels in both indoor and outdoor environments. Organisations such as the World Health Organization (WHO), the European Chemicals Agency (ECHA), and the United States Environmental Protection Agency (EPA) have issued updated guidelines and mandatory limits for VTOCs in air, water, and consumer products. These changes reflect not only a growing awareness of the chronic impact of low-level exposure, but also an increased emphasis on early detection and prevention. As the regulatory landscape evolves, there is a clear need for sensing technologies that can support compliance, risk assessment, and long-term monitoring. Real-time detection (Mall, 2009) of VTOCs has therefore become a critical tool in environmental protection strategies, helping to reduce both acute and cumulative harm to human health and ecosystems.

One of the more immediate and visible consequences of poor indoor air quality is "Sick Building Syndrome" (SBS) (Redlich, 1997), a condition in which occupants of a building experience a range of non-specific symptoms such as nausea, headaches, fatigue, eye and throat irritation, and respiratory discomfort. These symptoms often correlate with prolonged exposure to airborne contaminants, including volatile organic compounds released from paints, adhesives, synthetic flooring, and cleaning agents. While SBS is not attributed to any single disease or pathogen, it is increasingly linked to elevated levels of indoor VTOCs, especially in poorly ventilated or energy-sealed buildings (Zhang, 2003). The phenomenon has drawn regulatory attention in both occupational and residential contexts, driving demand for continuous air quality monitoring systems. As awareness of SBS continues to grow, electrochemical sensors capable of detecting low concentrations of airborne toxins in real-time are becoming essential for maintaining safe and healthy indoor environments (Desimoni, 2013).

1.1.1 Environmental Protection and Monitoring

Laboratory techniques such as gas chromatography-mass spectrometry (GC-MS) (Hübschmann, 2025) and ultra-performance liquid chromatography (UPLC) (Swartz, 2005) remain the gold standard for chemical detection due to their exceptional sensitivity, selectivity, and compound identification capabilities. However, their reliance on bulky instrumentation, high operational costs, and the need for trained personnel make them unsuitable for real-time or in-field environmental monitoring. These constraints have prompted the development of compact sensing technologies capable of providing rapid, decentralised detection of pollutants in both gaseous and liquid media.

Among the most common VTOC sensor categories are optical (Elosua, 2006), calorimetric, and electrochemical platforms (Szulczyński, 2017). Optical sensors offer fast response times and high selectivity but can often be prohibitively expensive and complex. At the other end of the spectrum, pellistors (calorimetric sensors based on catalytic bead combustion) are widely used due to their low cost and simplicity but suffer from poor selectivity, limited sensitivity, and vulnerability to poisoning by common contaminants such as sulphur-containing compounds and halogenated hydrocarbons.

Electrochemical sensors offer a practical balance, combining good sensitivity with low power consumption, low production costs, and miniaturisation potential. They are especially well suited for detecting redox-active species in air and water, and their signal output can be tuned or amplified through electrode material modification or circuit-level optimisation. In recent years, advances in SPEs, nanomaterial catalysts, surface functionalisation, the integration of bio-recognition materials and embedded electronics have significantly improved the selectivity and stability of electrochemical sensors, making them strong candidates for use in environmental protection frameworks. Whether monitoring indoor air quality, industrial effluents, or drinking water supplies, these sensors represent a scalable solution for continuous and location-specific pollutant tracking.

The goal of this work is to develop a sensing platform that enables reliable, real-time detection of volatile toxic organic compounds directly at the point of exposure. Whether in industrial zones, contaminated water sources, or indoor environments, such a system must balance sensitivity, affordability, and portability to meet both regulatory and practical demands. The schematic below (Figure 1.1) illustrates this transition from conventional centralised analysis to on-site sensing using compact, electrochemical devices.



Figure 1.1: Conceptual overview of on-site VTOC sensing across industrial, aquatic, and indoor environments. The illustration highlights the shift from offline, centralised measurements to real-time, location-specific detection using portable sensor platforms.

1.2 Fundamentals of Electrochemical Sensing

Electrochemical sensing (Bakker, 2002) operates by converting chemical information into an electrical signal through redox reactions that occur at the interface between the analyte and the electrode. A standard configuration involves three electrodes: a working electrode, typically made of glassy carbon, platinum, or gold, where the electrochemical reaction occurs. These materials are favoured for their high electrochemical activity, chemical stability, and compatibility with a wide range of analytes. The reference electrode, commonly silver/silver chloride (Ag/AgCl), reversible hydrogen (RHE) or saturated calomel (SCE), provides a stable and well-defined reference potential, with minimal drift over time. The measurements were performed using a quasi-reference electrode, which provides a stable but not absolute reference potential and may exhibit slight drift compared to standard reference electrodes. The counter electrode, often a carbon rod or platinum wire or mesh, completes the circuit by enabling charge flow. Carbon or platinum are commonly chosen due to their inertness, high conductivity, and ability to sustain redox reactions without participating in them, thus maintaining the integrity of the system. When a controlled potential is applied, electroactive species in the sample undergo oxidation or reduction, and the resulting current is recorded. This current is directly

proportional to the concentration of the analyte, providing a quantitative output. The method is valued for its sensitivity, fast response time, and compatibility with miniaturised, low-power platforms.

However, the technique is limited to analytes that are electrochemically active within the accessible potential window. The potential window is primarily restricted by the electrochemical stability of the solvent, where water molecules undergo electrolysis to produce oxygen at the anodic limit and hydrogen at the cathodic limit. Compounds that do not readily participate in redox reactions, or do so only under extreme conditions, cannot be detected using conventional electrochemical methods. Additionally, the analyte must be in direct contact with the working electrode surface to enable charge transfer. This requirement limits the use of electrochemical sensors in samples that are highly viscous, poorly conductive, or physically separated from the electrode by membranes or barriers. Despite these constraints, the approach remains one of the most practical solutions for field-based chemical sensing, especially when paired with selective electrode modifications and optimised measurement protocols. To better understand how chemical detection is carried out in this context, it is useful to consider the basic layout of a standard three-electrode electrochemical cell shown in Figure 1.2. The transition from a conventional benchtop setup to a portable system is also shown.

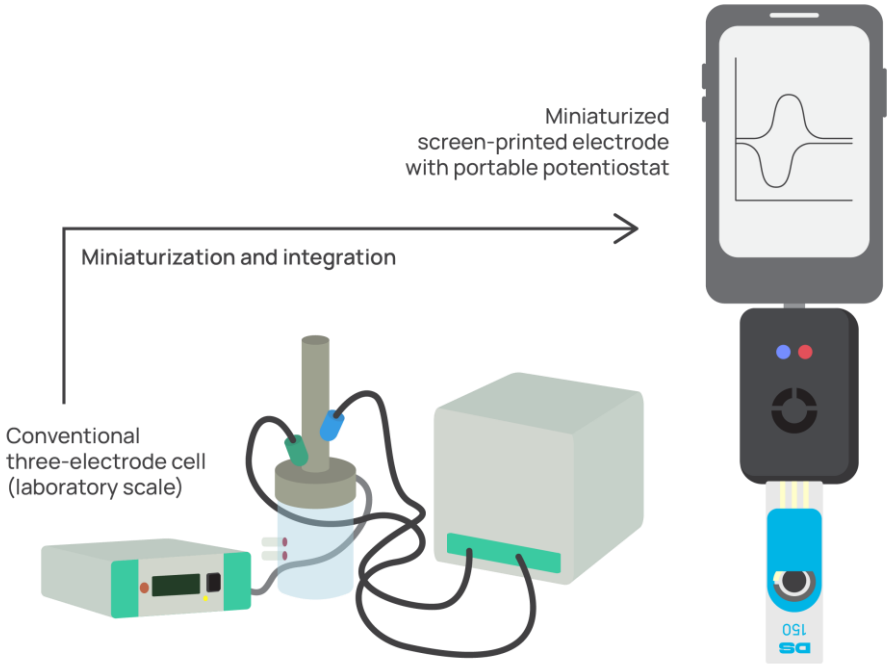


Figure 1.2: Transition from a conventional three-electrode electrochemical cell to a portable sensing system using screen-printed electrodes and a handheld potentiostat connected to a mobile device.

1.2.1 Examples of Established Electrochemical Sensors

Electrochemical sensors have been widely adopted in both environmental and biomedical applications due to their simplicity, responsiveness, and adaptability. A well-known example is the glucose sensor (Heller, 2008), which has revolutionised diabetes management by enabling rapid, disposable blood sugar testing through enzymatic oxidation on a

modified electrode. Discussed below are the two prominent electrochemical sensing technologies for VTOCs and heavy metals.

1.2.1.1 Ion Selective Electrodes

Ion-selective electrodes (ISEs) (Freiser, 2012) are a subclass of electrochemical sensors designed to respond selectively to specific ionic species in solution. Two well-established examples are the fluoride (Harwood, 1969) and potassium (Fiedler, 1973) ISEs, each relying on tailored membrane chemistries to achieve selective ion transport. Fluoride ISEs typically employ a single-crystal membrane composed of lanthanum fluoride (LaF_3) doped with europium fluoride (EuF_2), which introduces lattice vacancies that facilitate the movement of fluoride ions through the crystal structure. This configuration ensures high selectivity and low detection limits, making it suitable for applications in water quality testing and dental research. In contrast, potassium ISEs use a polymeric membrane embedded with valinomycin, a neutral carrier molecule that selectively complexes with potassium ions. The valinomycin–K^+ complex diffuses through the membrane, generating a potential that reflects the activity of potassium in the sample. While ISEs offer excellent selectivity, their operation is largely restricted to small, monovalent or divalent ionic species, as the ion transport mechanism depends on the presence of suitable vacancies or carrier interactions within the membrane. Larger or structurally complex analytes typically fall outside the functional scope of this class of sensors.

1.2.1.2 Pellistors

Pellistors, or catalytic bead sensors (Dücso, 2003), are widely used for detecting combustible gases in industrial and safety applications. They operate by oxidising the target gas on a heated catalytic surface, typically composed of a platinum coil embedded in a ceramic bead. This exothermic reaction increases the bead's temperature, changing its electrical resistance in proportion to the gas concentration. One of the main advantages of pellistors is their broad sensitivity, as they can detect virtually any flammable gas or vapour, including methane, propane, hydrogen, and alcohols. However, this generality comes at the cost of poor selectivity, since they cannot distinguish between different combustible species. In addition, they require elevated operating temperatures to maintain catalytic activity, which results in higher power consumption compared to ISEs or optical sensors. Their performance can also degrade over time due to catalyst poisoning or thermal stress, making them less suitable for long-term or battery-powered monitoring systems.

1.3 Conventional Electrochemical Methods

A range of time- and potential-dependent electrochemical techniques (Scozzari, 2008) are employed to investigate the redox behaviour of analytes, evaluate electrode performance, and quantify target compounds. Each method applies a specific electrical waveform to the electrochemical cell and records the resulting current or impedance response. These responses are governed by electron transfer kinetics, diffusion processes, and double-layer charging effects at the electrode interface. In the context of this work, multiple techniques have been applied to the detection and characterisation of benzenediol isomers, each offering distinct advantages in terms of sensitivity, selectivity, and temporal resolution (Bard, 2022). The following subsections briefly describe the waveform and electrochemical behaviour associated with each method used in this study.

1.3.1 Cyclic Voltammetry

Cyclic voltammetry (CV) (Kissinger, 1983) is one of the most commonly used techniques in electrochemical analysis due to its ability to probe redox behaviour and reaction reversibility. In this method, the applied potential is swept linearly between two set limits and then reversed, forming a triangular waveform over time. The resulting current is plotted against potential to produce a voltammogram, typically showing anodic and cathodic peaks that correspond to oxidation and reduction processes. For benzenediols, CV allows the characterisation of their reversible redox couples and the separation of closely spaced redox events. The shape and position of the peaks provide insight into electron transfer kinetics, diffusion rates, and adsorption phenomena, making CV a useful tool for preliminary evaluation of electrode modifications and reaction mechanisms. Electrochemical redox processes are typically classified as reversible, quasi-reversible, or irreversible based on kinetic and thermodynamic criteria. For a reversible one-electron transfer, the peak separation (ΔE_p) is approximately 59 mV at room temperature, and the anodic-to-cathodic peak current ratio (i_{pa}/i_{pc}) approaches unity. Quasi-reversible systems exhibit increased ΔE_p and deviations in peak symmetry due to finite electron transfer kinetics, while irreversible systems are characterised by the absence of a corresponding reverse peak or significantly broadened peak separation. The typical CV waveform consists of a linear ramp in potential that reverses after reaching a defined vertex, producing a symmetric triangle when plotted against time as shown in Figure 1.3.

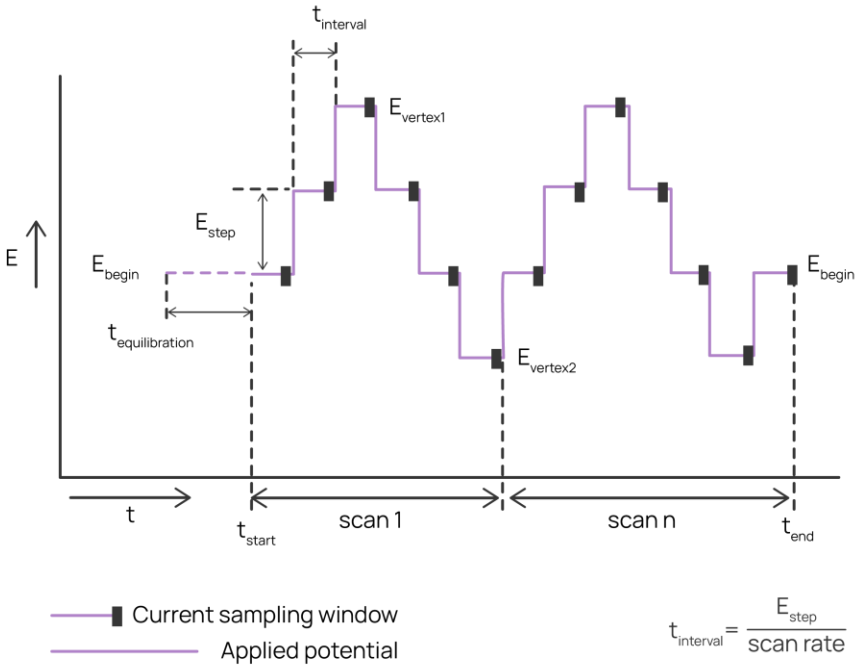


Figure 1.3: Triangular potential waveform used in cyclic voltammetry, showing a forward and reverse linear sweep between two vertex potentials over a fixed scan rate.

In reversible systems, the peak current response in CV is governed primarily by diffusion-controlled kinetics. The general temperature-dependent form is given by the Randles-Ševčík equation,

$$i_P = 0.4463nFAC\left(\frac{nF\upsilon D}{RT}\right)^{\frac{1}{2}} \tag{1.3.1}$$

where n is the number of electrons transferred, F is the Faraday constant, A is the electrode area (cm^2), C is the analyte concentration (mol cm^{-3}), υ is the scan rate (V s^{-1}), D is the diffusion coefficient (cm^2 s^{-1}), R is the gas constant, and T is the absolute temperature (K). At 298 K, with A in cm^2, D in cm^2 s^{-1}, C in mol cm^{-3}, and υ in V s^{-1}, this reduces to

$$i_P = (2.69 \times 10^5) n^{\frac{3}{2}} A C D^{\frac{1}{2}} \upsilon^{\frac{1}{2}} \tag{1.3.2}$$

which highlights the proportionality of peak current to $\upsilon^{\frac{1}{2}}$ under diffusion control. When departures from this behaviour are observed, adsorption effects or kinetic limitations are often implicated, allowing CV to serve as a diagnostic for distinguishing surface-controlled from diffusion-controlled mechanisms.

At slower scan rates, or when charge transfer is partially hindered, quasi-reversible behaviour may arise, characterised by broader peaks and an increased separation between anodic and cathodic maxima (ΔE_P). The magnitude of ΔE_P can be related to the standard heterogeneous rate constant k^0 which enables estimation of reaction rates directly from the voltammogram. These relationships provide the theoretical basis for quantitative and mechanistic interpretation of CV data.

In environmental sensing, CV functions as both a diagnostic and exploratory technique. It provides preliminary information on redox potentials, guiding the selection of bias windows for pulse or AC-based methods. It also reveals reversibility, electron transfer kinetics, and surface effects that inform electrode and protocol optimisation. Detection limits are typically in the micromolar range, so the method is generally more qualitative than quantitative when compared with pulse techniques. On portable digital instruments, staircase approximations that emulate linear sweeps can introduce minor capacitive artefacts, which should be considered during signal interpretation and waveform optimisation.

The CV in Figure 1.4 shows a near-reversible redox process with an anodic peak at approximately 0.58 V and a cathodic peak close to 0.52 V vs quasi-reference Ag. The peak separation (ΔE_P of roughly 60 mV and the comparable anodic and cathodic peak currents (27 µA and –23 µA, respectively) are indicative of a diffusion-controlled, near-reversible electron transfer process.

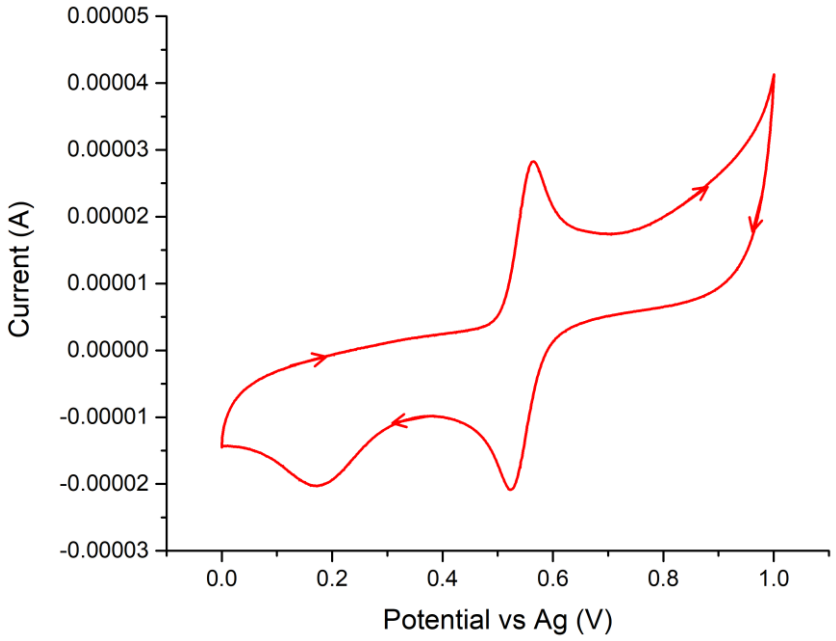


Figure 1.4: Cyclic voltammogram of 1 mM catechol in 1 M HCl on a Pt/C-modified SPE.

An irreversible electrochemical oxidation is shown in figure 1.5, with a single broad anodic peak at 0.95 V vs quasi reference Ag and no corresponding cathodic feature during the reverse scan. The lack of a reduction peak reflects the instability of the oxidised product and confirms the non-reversible electrochemical behaviour of RS under acidic conditions.

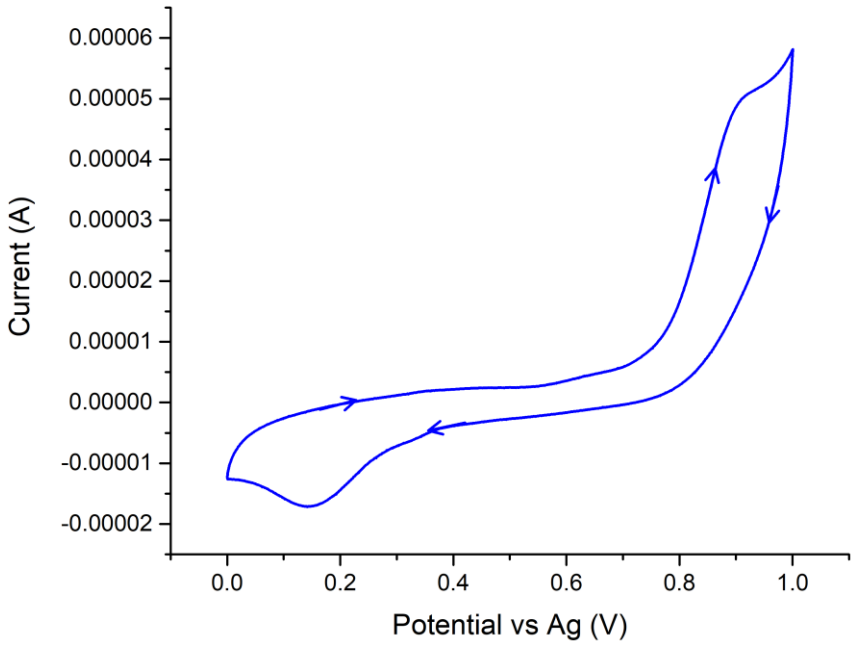


Figure 1.5: Cyclic voltammogram of 1 mM resorcinol in 1 M HCl on a Pt/C-modified SPE.

1.3.2 Chronoamperometry

Chronoamperometry (CA) (Inzelt, 2014) is a technique where a fixed potential step is applied to the working electrode and the resulting current is recorded as a function of time. The current response is governed primarily by the diffusion of electroactive species to the electrode surface. Upon application of the potential, there is an initial spike in current due to capacitive charging, If the applied potential exceeds the redox threshold, a faradaic current is observed, which subsequently decays due to the decreasing concentration gradient near the electrode. For benzenediol detection, CA is useful for quantifying the concentration of individual isomers at known redox potentials. It provides excellent temporal resolution and can be used for calibration curves in controlled environments. The current-time behaviour typically follows the Cottrell equation under diffusion-limited conditions. The applied potential waveform in CA is a single-step function, where the potential remains constant after the initial change as shown in Figure 1.6.

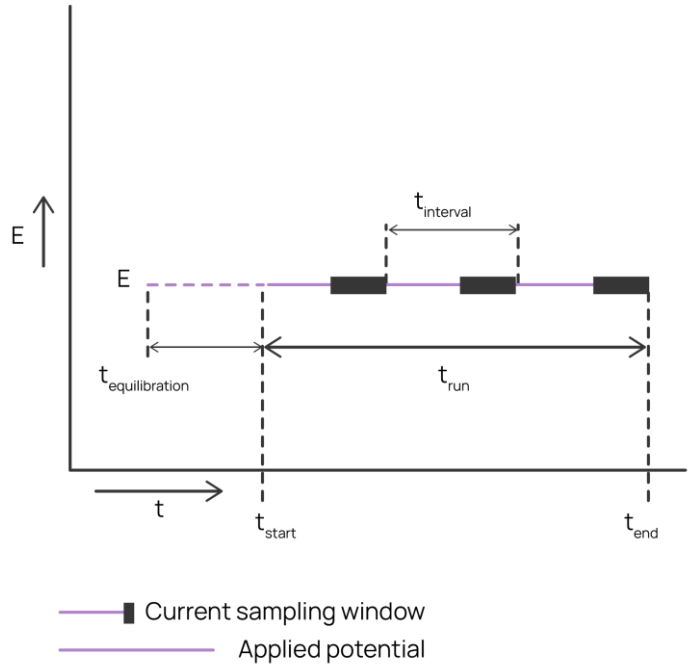


Figure 1.6: Step potential waveform used in chronoamperometry, showing a sudden change in potential held constant over time, with corresponding diffusion-limited current decay.

The quantitative interpretation of CA relies on the Cottrell equation, which describes the current–time relationship for a diffusion-controlled redox process following a potential step:

$$i(t) = \frac{nFACD^{\frac{1}{2}}}{\pi^{\frac{1}{2}} t^{\frac{1}{2}}} \tag{1.3.3}$$

where $i(t)$ is the instantaneous current, n is the number of electrons transferred, F is the Faraday constant, A is the electrode area (cm^2), D is the diffusion coefficient ($\mathrm{cm}^2\ \mathrm{s}^{-1}$), C is the bulk analyte concentration ($\mathrm{mol\ cm}^{-3}$), and t is time (s). The inverse square root dependence on time reflects the progressive expansion of the diffusion layer as the experiment proceeds. This relationship is valid for purely diffusion-limited systems where convection and migration effects are negligible, and it forms the theoretical basis for extracting diffusion coefficients and concentration values from chronoamperometric data.

Immediately after the potential step, a transient non-faradaic current appears due to charging of the electrical double layer at the electrode surface. This capacitive component decays rapidly (e^{-t}), typically within milliseconds, after which the faradaic current dominates ($t^{-\frac{1}{2}}$ decay). Distinguishing between these two contributions is essential when performing quantitative analyses, as residual capacitive current can obscure the early-time response. In practice, the capacitive portion is often suppressed through background subtraction or the use of differential techniques.

At sufficiently short timescales or in systems with high analyte reactivity, deviations from ideal Cottrell behaviour may arise. These include kinetic limitations at the electrode surface, coupled chemical reactions, or adsorption of intermediates. In such cases, the observed current decay deviates from the $t^{-\frac{1}{2}}$ dependence, providing valuable diagnostic information on reaction mechanisms and surface processes.

CA offers several advantages in electrochemical sensing, particularly for concentration quantification once the redox potential of the analyte has been established by preliminary techniques such as CV. It provides high temporal resolution and relatively simple data interpretation, making it suitable for calibration studies and signal validation under controlled conditions. However, because CA measurements integrate all faradaic processes occurring at the selected potential, selectivity depends strongly on the chosen bias and on the electrode's surface composition. In portable systems, minimising electrical noise and maintaining stable potential control are critical for ensuring reproducible current–time transients, especially when operating in low-conductivity media such as aqueous environmental samples.

Figure 1.7 shows a typical CA measurement. Upon applying a potential step, an initial spike in current is followed by a decay consistent with diffusion-limited charge transfer. The current reaches a steady value of around 40 µA after 60 s. The response follows the Cottrell behaviour expected for planar electrodes, validating the suitability of chronoamperometry for time-resolved concentration measurements.

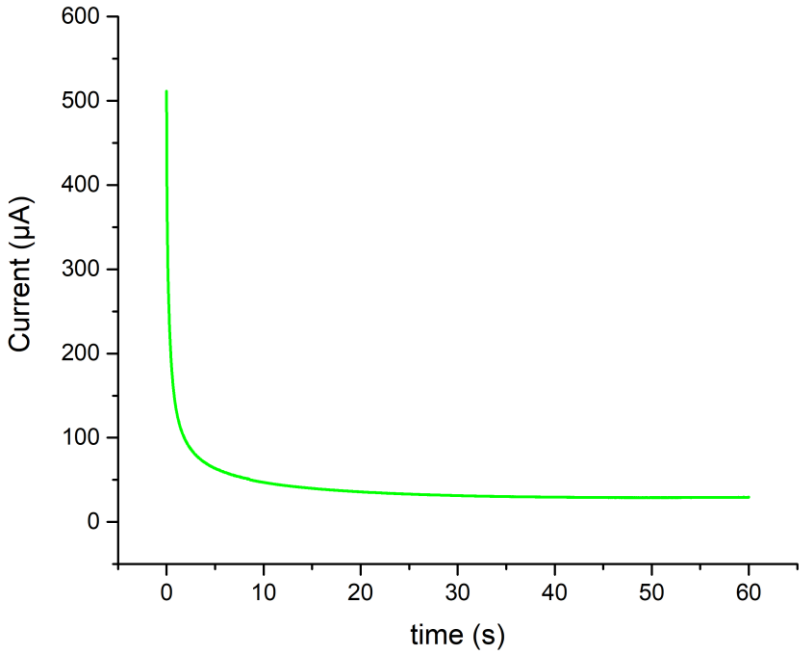


Figure 1.7: Chronoamperometric response of 10 mM hydroquinone in 1 M HCl at 0.52 V vs Ag.

1.3.3 Differential Pulse Voltammetry

Differential Pulse Voltammetry (DPV) (Lovrić, 1982) is a sensitive electroanalytical technique designed to improve resolution and signal-to-noise ratio by superimposing a series of periodic voltage pulses onto a baseline potential ramp. At each step, the current is measured twice: just before the pulse and at the end of the pulse. The difference between these two current values is plotted against the applied potential, producing a series of well-defined peaks corresponding to redox events. This double-sampling approach minimises capacitive current contributions, making DPV particularly suitable for detecting closely spaced redox processes, such as those observed in benzenediol isomers. The technique is especially valuable for trace-level analysis due to its enhanced selectivity and low detection limits. The applied waveform in DPV consists of a staircase potential overlaid with periodic short pulses, as shown in Figure 1.8.

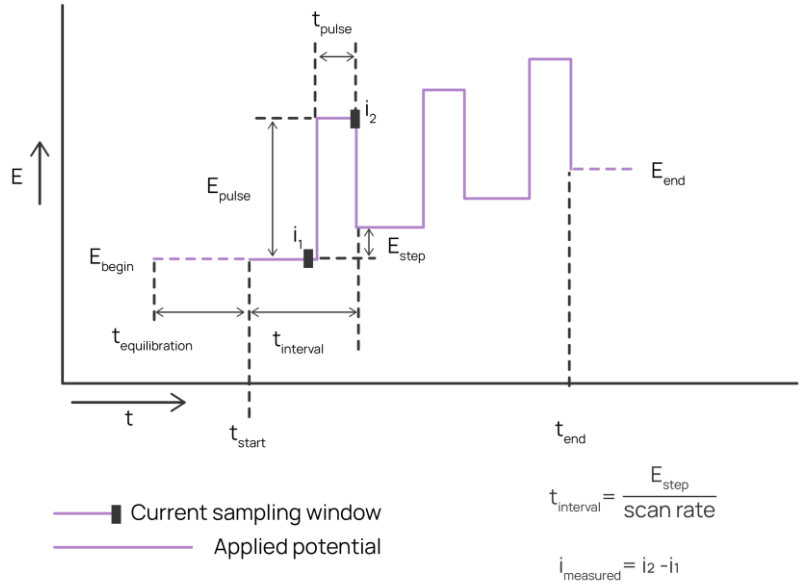


Figure 1.8: Potential waveform used in differential pulse voltammetry, showing a staircase baseline with superimposed pulses, each producing a differential current measurement used to generate a peak-shaped voltammogram.

DPV achieves enhanced sensitivity by minimising capacitive contributions to the total current. The technique operates by superimposing a sequence of potential pulses onto an incremental baseline ramp and measuring current twice during each pulse: once immediately before the pulse and again at the end of the pulse period. The differential current, obtained by subtracting these two values, effectively cancels most of the non-faradaic charging current while preserving the faradaic signal arising from redox processes. This approach yields sharp, peak-shaped responses that correspond to oxidation or reduction events, allowing for improved analytical resolution compared with continuous-scan methods.

The magnitude of the measured current difference, Δi, is directly related to the kinetics of electron transfer and the diffusion of electroactive species to the electrode surface. In ideal diffusion-controlled systems, Δi is proportional to the analyte concentration, making DPV suitable for quantitative analysis. The shape and width of the resulting peaks depend on parameters such as pulse amplitude and duration, which can be optimised to enhance selectivity or to resolve closely spaced redox processes.

An analytical advantage of DPV is its ability to separate overlapping peaks when two or more electroactive species have oxidation potentials that differ by only a few tens of mV. The combination of baseline correction and differential measurement improves signal-to-noise ratio, often by an order of magnitude relative to conventional CV. For this reason, DPV is commonly used in trace analysis, biosensing, and environmental monitoring, where target analytes may be present at low concentrations within complex matrices.

From an instrumental perspective, the accuracy of DPV depends strongly on pulse timing, potential resolution, and the precision of current sampling. On digital potentiostats, these parameters are determined by the sampling rate and the stability of the digital-to-analogue conversion process. In miniaturised systems, maintaining synchronisation between potential control and current acquisition is essential to avoid artificial broadening or attenuation of peaks. Despite these challenges, DPV remains one of the most reliable and

widely used techniques for quantitative electrochemical analysis and serves as an essential method in the validation of portable sensing systems designed for real-world applications.

1.3.4 AC Voltammetry

AC Voltammetry (ACV) (Mooring, 1977) enhances the analysis of electrochemical systems by introducing a small amplitude sinusoidal voltage onto a slowly varying linear sweep. This superimposed AC signal enables frequency-resolved measurements, making it possible to distinguish between faradaic and non-faradaic contributions to the total current as the frequency of the sinusoidal component can be tuned to probe specific electrochemical dynamics. In the case of benzenediols, ACV provides enhanced resolution of redox peaks by allowing capacitive and faradaic responses to be separated more effectively than in purely time-domain methods. The applied potential waveform in ACV consists of a sine wave overlaid on a linear ramp, as shown in Figure 1.9.

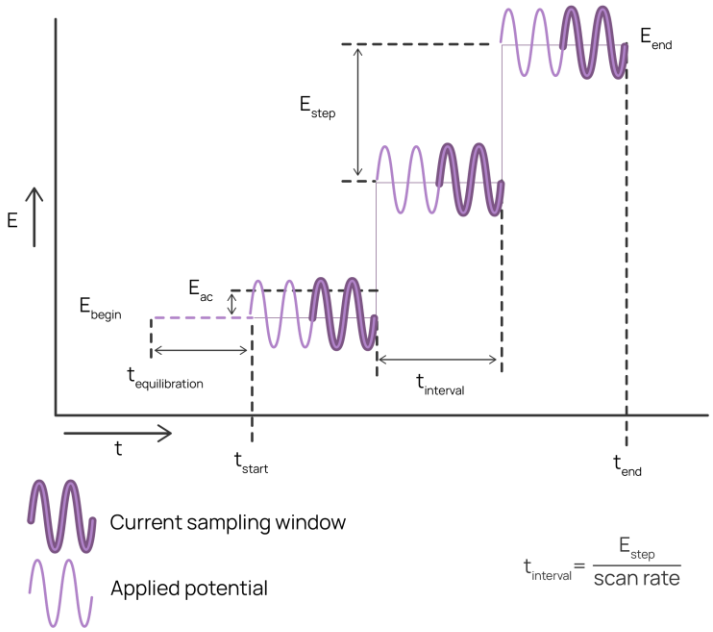


Figure 1.9: Potential waveform used in AC voltammetry, showing a sinusoidal modulation superimposed on a linear sweep, enabling frequency-dependent separation of electrochemical current components.

ACV extends the interpretative capability of potential sweep techniques by decomposing the electrochemical response into its frequency-dependent components. The applied potential can be expressed as

$$E(t) = E_s + \Delta E \sin(\omega t) \tag{1.3.4}$$

where E_s is the slowly varying base potential, ΔE is the small sinusoidal modulation amplitude, and ω is the angular frequency of the perturbation. The total current response comprises both faradaic and non-faradaic contributions, each exhibiting distinct phase relationships with the driving potential. By resolving the in-phase and out-of-phase components through Fourier analysis or lock-in amplification, it becomes possible to separate charge-transfer and capacitive processes with high precision.

At low frequencies, faradaic currents dominate because the system has sufficient time to respond to the perturbation, while at high frequencies the current is increasingly governed by capacitive charging. The resulting complex current can be represented as

$$i(t) = i_f \sin(\omega t + \phi_f) + i_c \sin(\omega t + \phi_c) \tag{1.3.5}$$

where i_f and i_c are the amplitudes of the faradaic and capacitive currents, and ϕ_f and ϕ_c are their respective phase angles relative to the applied potential. The difference in phase behaviour provides a means to quantify kinetic parameters such as charge-transfer resistance and double-layer capacitance, forming the conceptual link between ACV and impedance spectroscopy.

ACV is particularly useful for distinguishing electrochemical processes that occur on similar timescales or at overlapping potentials. By varying the frequency of the AC component, it is possible to probe different kinetic regimes, thereby revealing subtle mechanistic features that are often obscured in time-domain measurements. This capability makes ACV a powerful diagnostic tool for systems exhibiting both capacitive and faradaic behaviour, such as redox-active organic compounds and modified electrode surfaces.

In the context of environmental and sensor-oriented electrochemistry, ACV offers a pathway toward enhanced selectivity and reduced baseline noise without requiring complex post-processing. The technique also serves as a foundation for more advanced frequency-based approaches, including electrochemical impedance spectroscopy, which extends these principles over a broader range of frequencies. On compact or portable instrumentation, implementing ACV requires precise waveform generation and synchronised signal sampling to preserve phase fidelity and ensure reproducible amplitude measurements.

1.3.5 Multi-Step Chronoamperometry

Multi-step chronoamperometry (MSCA) (Patel, 2020) extends the basic chronoamperometric method by applying a sequence of discrete potential steps, each held for a fixed duration. This allows the investigation of multiple redox processes or the same redox event under varying conditions within a single experiment. It is useful for distinguishing between isomers based on their response profiles at different potentials. The applied waveform in MSCA consists of a series of square potential steps held at different levels, as shown in Figure 1.10.

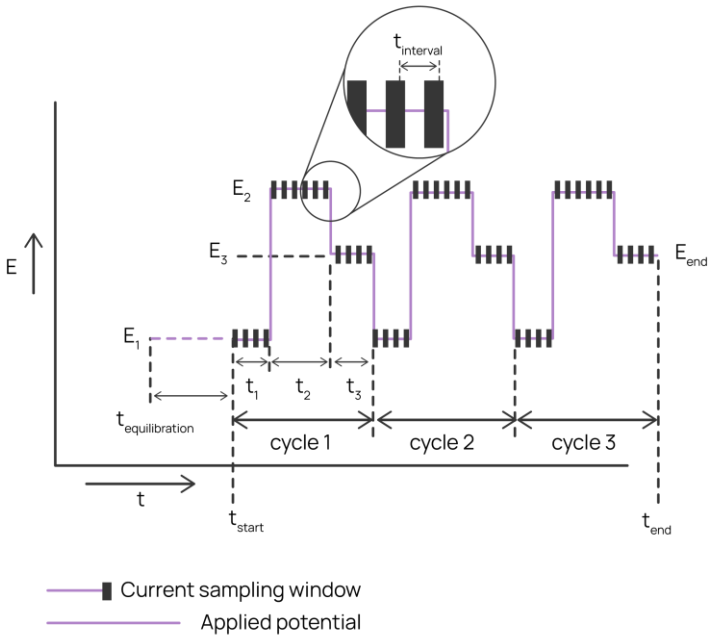


Figure 1.10: Potential waveform used in multi-step chronoamperometry, consisting of a sequence of constant potential levels applied over time to probe electrochemical responses across multiple conditions.

MSCA is an extension of single-step potential control methods and provides a structured way to probe redox dynamics across several discrete potential levels within a single experiment. Each potential step generates a transient current that follows diffusion-controlled kinetics similar to those described by the Cottrell equation, but with cumulative effects arising from the sequence of steps. By analysing the current–time behaviour at each level, it becomes possible to assess reaction reversibility, adsorption, and surface regeneration under varying electrochemical conditions.

In a typical MSCA experiment, the applied potential is incremented in fixed steps between successive holding periods, allowing multiple redox events to be captured. The response at each potential reflects the balance between faradaic and capacitive processes, and the comparison of consecutive transients can reveal subtle differences in reaction pathways. The temporal profile of the current can be represented as

$$i(t) = \sum_{n=1}^{N} \frac{nFAC_n D^{\frac{1}{2}}}{\pi^{\frac{1}{2}}(t - t_n)^{\frac{1}{2}}} \tag{1.3.6}$$

where t_n denotes the onset time of the n^{th} potential step and C_n represents the instantaneous concentration of the electroactive species available at that stage. This formulation demonstrates how the transient response at any given potential is influenced by the preceding step through residual concentration gradients near the electrode surface.

One of the principal advantages of MSCA is its capacity to monitor processes that evolve over time, such as electrode fouling, adsorption–desorption cycles, or degradation of catalytic layers. By using short step durations, it is possible to capture near-instantaneous charge-transfer events, whereas longer holds allow diffusion profiles to stabilise. The ability to vary both the potential and duration systematically provides a flexible framework for dissecting multi-electron or sequential reactions that may not be resolved in continuous-scan voltammetry.

In environmental sensing applications, MSCA is particularly useful for differentiating analytes that exhibit potential-dependent fouling behaviour or multi-stage oxidation mechanisms, such as phenols and benzenediols. By monitoring the change in current response over successive steps, one can infer whether the electrode surface undergoes passivation, regeneration, or catalytic enhancement. The technique is therefore valuable for assessing sensor durability and for optimising the operational potential range in portable devices where long-term stability is critical. On compact instrumentation, implementing MSCA requires accurate potential switching with minimal delay between steps to maintain waveform integrity and ensure consistent diffusion profiles across each interval.

1.3.6 Electrochemical Impedance Spectroscopy

Electrochemical Impedance Spectroscopy (EIS) (Chang, 2010) is a frequency-domain technique used to characterise interfacial processes by measuring the system's response to a small amplitude sinusoidal voltage over a wide range of frequencies. Rather than tracking current or voltage in the time domain, EIS evaluates the complex impedance of the electrochemical cell, which reflects contributions from charge transfer resistance, double-layer capacitance, diffusion, and solution resistance. The data are typically represented in Nyquist or Bode plots and can be modelled using equivalent circuits to extract parameters related to reaction kinetics and electrode behaviour. In this work, EIS plays a critical role in tracking sensor stability, surface degradation, and signal drift over time during benzenediol detection. The applied potential waveform in EIS is a fixed DC bias with a small sinusoidal perturbation applied across a range of frequencies, as shown in Figure 1.11.

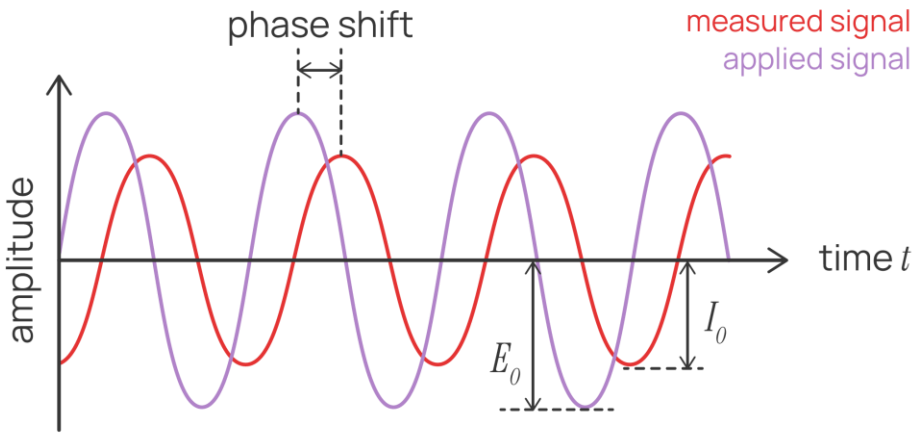


Figure 1.11: Potential waveform used in electrochemical impedance spectroscopy, consisting of a constant DC bias with a superimposed low-amplitude sine wave swept across a broad frequency range to probe impedance characteristics.

EIS characterises interfacial and transport processes by measuring the linear response of an electrochemical system to a small sinusoidal perturbation. The complex impedance is defined as

$$Z(\omega) = \frac{\tilde{E}(\omega)}{\tilde{I}(\omega)} = Z'(\omega) + Z''(\omega) \tag{1.3.7}$$

where $\tilde{E}$ and $\tilde{I}$ are the Fourier components of potential and current at angular frequency ω, and Z' and Z'' are the real and imaginary parts. Data are commonly presented as Nyquist plots, $-Z''$ versus Z', and as Bode plots, magnitude $|Z|$ and phase ϕ versus frequency. Interpretation relies on linearity, time invariance and causality, which can be assessed by consistency checks such as Kramers–Kronig relations. Violation of these conditions typically indicates excessive perturbation amplitude, drift, or non-stationary surface chemistry.

For ideal circuit elements, the impedance expressions are

$$Z_R = R \tag{1.3.8}$$

$$Z_C = \frac{1}{j\omega C} \tag{1.3.9}$$

$$Z_L = j\omega L \tag{1.3.10}$$

which represent pure resistance (R), capacitance (C) and inductance (L). Real electrode interfaces are seldom ideal capacitors, and are better described by a constant phase element (CPE)

$$Z_{CPE} = \frac{1}{Q(j\omega)^{\alpha}} \tag{1.3.11}$$

where $0 < \alpha \leq 1$ and Q is the magnitude parameter. $\alpha = 1$ reduces to an ideal capacitor with $Q = C$. Values of $\alpha < 1$ capture distributed relaxation arising from surface heterogeneity, porosity and roughness that are typical of carbon inks and catalyst layers on SPEs. Reporting a single effective capacitance from a CPE is model dependent, and conversions should be stated explicitly when used.

Mass transport introduces characteristic frequency dispersion. For semi-infinite diffusion the Warburg impedance is

$$Z_W = \frac{\sigma}{\sqrt{j\omega}} \tag{1.3.12}$$

Where σ is the Warburg coefficient, and Z_W produces a Nyquist line at -45°. Finite-length diffusion, for example through a film or in a bounded electrolyte layer, is represented by finite Warburg forms with reflective or transmissive boundaries, which bend the low-frequency tail toward the real axis. Reaction–diffusion coupling can be represented by a Gerischer element, which is useful when chemical steps follow electron transfer.

A compact but informative description of many liquid electrochemical systems is provided by the Randles circuit. In its simplest form this comprises a solution resistance R_S in series with a parallel network of charge-transfer resistance R_{ct} and double-layer capacitance C_{dl} or a CPE. With semi-infinite diffusion the parallel branch includes Z_W. The total impedance is

$$Z(\omega) = R_S + \left[\frac{1}{R_{ct}} + j\omega C_{dl} + \frac{1}{Z_W}\right]^{-1} \tag{1.3.13}$$

with the appropriate replacement of C_{dl} by a CPE when non-ideality is pronounced. The polarisation resistance R_P measured at very low frequencies is often used as a stability metric. For a single faradaic process, $R_P \approx R_{ct}$. Through the Butler–Volmer framework,

$$R_{ct} = \frac{RT}{nFi_0} \tag{1.3.14}$$

which links impedance parameters to the exchange current i_0, and therefore to intrinsic kinetics and catalytic activity at the modified electrode.

Experimental configuration strongly influences data quality. The AC amplitude should be small enough to maintain linearity, typically 5 to 10 mV rms (root mean square value) at the working bias, while still providing adequate signal-to-noise ratio. The DC bias determines which region of the faradaic landscape is probed, for example open circuit to characterise the double layer, or near a redox potential to capture charge transfer. Frequency range selection should cover several decades where practical, so that solution resistance, interfacial processes and diffusion can be separated. Uncompensated resistance and poor shielding introduce high-frequency artefacts, including inductive loops, which appear as positive Z'' at the highest frequencies. Cable inductance, reference electrode impedance, and lead geometry can all contribute to these features. On SPE platforms, spreading resistance in the thin electrolyte layer and the finite size of the working electrode modify R_S and the effective current distribution, which should be considered when comparing different layouts.

Data analysis typically uses non-linear least squares fitting to parameterised circuit models. Appropriate weighting is important, for example using the modulus or the real and imaginary parts with variance estimates, to avoid bias toward high-magnitude points. Parameter correlation can lead to non-unique fits, particularly when R_{ct}, C_{dl} or CPE parameters and diffusion terms capture similar portions of the spectrum. Reporting confidence intervals, residuals, and goodness-of-fit metrics, such as reduced chi-squared, helps to demonstrate identifiability. Alternative approaches include distribution of relaxation times analysis, which avoids a priori circuit selection by reconstructing a spectrum of time constants that can be interpreted post hoc.

In the present context, EIS serves two roles. First, it provides an in situ diagnostic for sensor drift by tracking R_P and interfacial capacitance during repeated measurements. Increases in R_P can indicate loss of catalytic activity, surface fouling or degradation of conductive pathways in the catalyst layer. Changes in CPE α or in the apparent capacitance can reflect altered surface roughness, adsorption, or polymer growth, which are particularly relevant for RS where electropolymerisation occurs. Second, EIS complements voltammetric data by separating resistive and capacitive contributions that are inseparable in the time domain, thereby supporting rational selection of bias conditions and waveform parameters for quantitative sensing.

On portable instrumentation, maintaining phase accuracy and low-noise current measurement is critical. Short, low-impedance connections, stable reference electrodes, and careful grounding improve the fidelity of high-frequency data. Automated checks for linearity and stationarity, such as repeating a few frequencies at the start and end of a sweep, can reveal drift during the experiment. When equivalent circuits are used for monitoring rather than full mechanistic assignment, adopting a minimal model that captures the dominant features, and using a consistent fitting protocol, yields robust comparative metrics across electrodes, catalysts and operating histories.

1.4 Frequency-Domain Analysis in Electrochemistry

While conventional electrochemical methods primarily operate in the time domain, frequency-domain analysis (Macdonald, 1998) provides a complementary perspective that can reveal deeper insights into system behaviour. By converting time-dependent signals into their frequency components, it becomes possible to separate overlapping processes such as faradaic reactions, capacitive charging, and mass transport. Frequency-domain tools, particularly Fourier (Grafakos, 2008) and Laplace (Spiegel, 1965) transforms, are therefore valuable in resolving dynamic electrochemical signals and designing optimised waveforms for enhanced sensing.

1.4.1 Fourier Series and Fourier Transform

The Fourier series is used to express periodic time-domain signals as a sum of simpler, sinusoidal components. It provides a powerful tool for analysing the frequency content of waveforms commonly used in electrochemistry. There are two standard forms: the trigonometric form and the complex exponential form.
The trigonometric form represents a real-valued periodic function $f(t)$ with period T as:

$$f(t) = a_o + \sum_{n=1}^{\infty} a_n \cos \omega_n t + \sum_{n=1}^{\infty} b_n \sin \omega_n t \tag{1.4.1}$$

a_o is the DC component (average value) of the signal; a_n and b_n are the coefficients representing the amplitude of the cosine and sine components, respectively, at the n$^{\text{th}}$ harmonic angular frequency ($\omega_n = 2\pi n f_0$). These coefficients can be calculated using the following integrals over one period T:

$$a_0 = \frac{1}{T}\int_0^T f(t)dt \tag{1.4.2}$$

$$a_n = \frac{2}{T}\int_0^T f(t)\, cos\, \omega_n t\, dt \tag{1.4.3}$$

$$b_n = \frac{2}{T}\int_0^T f(t)\, sin\, \omega_n t\, dt \tag{1.4.4}$$

Although intuitive, this form becomes cumbersome when dealing with phase shifts or impedance in electrochemical systems. The complex exponential form is preferred in such cases:

Using Euler's formula,

$$e^{j\omega_n t} = cos\, \omega_n t + j\, sin\, \omega_n t \tag{1.4.5}$$

The Fourier series can be expressed in the exponential form as,

$$f(t) = \sum_{n=-\infty}^{\infty} c_n e^{-j\omega_n t} \tag{1.4.6}$$

Where,

$$c_n = \frac{1}{T} \int_0^T f(t) e^{-j\omega_n t} dt \tag{1.4.7}$$

This version offers compactness and inherently encodes both amplitude and phase. It aligns directly with the Fourier Transform, which is used for non-periodic signals:

$$F(\omega) = \int_{-\infty}^{\infty} f(t)\, e^{-j\omega t} dt \tag{1.4.8}$$

where:

ω is the angular frequency (in rad s^{-1}), and $\omega = 2\pi f$ (where f is the linear frequency in hertz).

j is the unit imaginary ($\sqrt{-1}$).

$F(\omega)$ is a complex-valued function representing the frequency spectrum of the signal, with its magnitude $|F(\omega)|$ indicating the amplitude of each frequency component and its phase $\angle F(\omega)$ indicating the phase shift of each frequency component.

The original time-domain signal $f(t)$ can be recovered from its Fourier transform using the inverse Fourier transform:

$$f(t) = \frac{1}{2\pi} \int_{-\infty}^{\infty} F(\omega)\, e^{j\omega t} d\omega \tag{1.4.9}$$

This frequency-domain representation allows voltammetric signals to be decomposed into harmonics, helping to isolate redox behaviour, suppress background noise, and refine waveform design in electrochemical sensing.

1.4.2 Laplace Transform as an Extension of Fourier Transform

The Laplace transform is a generalisation of the Fourier transform that enables analysis of both steady-state and transient behaviours in dynamic systems. While the Fourier transform is well-suited to periodic or steady signals, the Laplace transform extends this capability to systems with exponential decay, growth, or initial conditions. This makes it especially valuable in electrochemical modelling, where transient behaviour such as double-layer charging, adsorption kinetics, or drift must be accounted for.

In electrochemical impedance analysis, Laplace-domain methods are used to represent equivalent circuit elements such as resistors, capacitors, and diffusion components using algebraic expressions. This simplifies the mathematical treatment of complex cell responses and enables frequency-dependent behaviour to be captured within a generalised framework.

The Laplace transform of a time-domain function $f(t)$, for $t \geq 0$, is defined as:

$$L\{f(t)\} = F(s) = \int_0^\infty f(t)\, e^{-st} dt \tag{1.4.10}$$

Where:

s is a complex variable, defined as $s = \sigma + j\omega$.

$F(s)$ is the Laplace transform of $f(t)$.

The inverse Laplace transform, which reconstructs the original time-domain function from its Laplace representation, is given by:

$$L^{-1}\{F(s)\} = f(t) = \frac{1}{2\pi j} \lim_{T\to\infty} \int_{\sigma-jT}^{\sigma+jT} F(s)\, e^{st} ds \tag{1.4.11}$$

Where:

The integral is evaluated along a vertical line in the complex plane (the Bromwich contour).

σ is chosen such that the contour lies within the region of convergence of $F(s)$.

Together with the Fourier transform, the Laplace transform provides a comprehensive mathematical foundation for analysing frequency-dependent behaviour in electrochemical systems, particularly when time-domain techniques fall short.

1.4.3 Discrete Fourier Transform and Fast Fourier Transform

In practical electrochemical systems, experimental data are always acquired in discrete form. Even when the underlying process is continuous, the potential, current, or impedance signals are sampled at uniform time intervals, making the discrete Fourier transform (DFT) (Sundararajan, 2001) the natural mathematical tool for frequency-domain interpretation. The DFT converts a finite sequence of sampled values $x[n]$ into a set of frequency-domain coefficients $X[k]$, representing the amplitude and phase of the discrete harmonics contained within the signal:

$$X[k] = \sum_{n=0}^{N-1} x[n] e^{-\frac{j2\pi kn}{N}} \tag{1.4.12}$$

where N is the number of samples in the sequence. The inverse transform reconstructs the time-domain signal from its frequency components. This formulation bridges continuous Fourier analysis and digital signal processing, enabling practical spectral evaluation of experimental electrochemical data. The development of the fast Fourier transform (FFT) (Cochran, 1967) algorithm made this computation efficient enough to be applied routinely, reducing computational complexity from $O(N^2)$ to $O(NlogN)$. The FFT is now integrated into most modern potentiostat systems and supports real-time spectral processing of voltammetric or impedance signals during acquisition.

Applying discrete transforms to electrochemical signals introduces sampling-related constraints. The sampling frequency must be at least twice the highest significant frequency present in the signal to satisfy the Nyquist criterion and prevent aliasing. Finite-length acquisition windows introduce spectral leakage, which can be mitigated using window functions such as Hanning or Blackman profiles. These considerations, standard in digital signal processing, have become increasingly relevant in electrochemistry as signals are

generated, sampled, and interpreted digitally. The FFT therefore represents not only a computational tool but also a conceptual transition point, defining the shift from analogue to digital electrochemical measurement.

1.4.4 Short-Time Fourier Transform and the Heisenberg Uncertainty Principle

While the Fourier transform provides complete frequency decomposition, it assumes that the signal is stationary and its spectral content does not vary over time. Electrochemical processes often violate this assumption, as current responses evolve dynamically during potential sweeps or modulated experiments. The short-time Fourier transform (STFT) (Griffin, 1984)) addresses this limitation by analysing small segments of the signal within a finite window, allowing the localised spectral content to be observed as a function of time:

$$X(t,\omega) = \int_{-\infty}^{\infty} x(\tau)w(\tau - t)e^{-j\omega\tau}d\tau \tag{1.4.13}$$

where $w(t)$ is a window function that defines the time–frequency resolution. The STFT produces a two-dimensional representation of amplitude versus time and frequency, commonly visualised as a spectrogram. The window length determines the trade-off between temporal and frequency resolution: narrow windows provide good time localisation but poor frequency resolution, while wider windows achieve the opposite.

This trade-off between time and frequency resolution reflects the Heisenberg uncertainty principle, which states that the product of the variances of a signal's time and frequency representations has a finite lower bound. In its simplest form,

$$\Delta t \Delta\omega \geq 0.5 \tag{1.4.14}$$

where Δt and $\Delta\omega$ denote the standard deviations of time and angular frequency, respectively. In practice, this means that improving time localisation inevitably reduces frequency precision and vice versa. The Gaussian window used in the Gabor transform achieves equality in this relation, providing the optimal compromise permitted by the uncertainty limit. In electrochemical analysis, this constraint defines how precisely transient processes can be resolved spectrally and illustrates the practical balance between temporal and frequency-domain characterisation.

1.4.5 Gabor Transform and Optimal Time-Frequency Localisation

A special case of the STFT is the Gabor transform (GT) (Yao, 1993), which applies a Gaussian window function $g(t)$ to achieve optimal time–frequency localisation. It is expressed as

$$G(t,\omega) = \int_{-\infty}^{\infty} x(\tau)g(\tau - t)e^{-j\omega\tau}d\tau \tag{1.4.15}$$

where $g(t)$ is a Gaussian of adjustable width. This formulation satisfies the lower bound of the time–frequency uncertainty principle and provides a smooth, continuous mapping of spectral evolution over time. In electrochemical applications, the GT can highlight gradual potential-dependent transitions such as capacitive charging or intermediate species formation that are often obscured in conventional voltammetry.

1.4.6 Wavelet Transform and Multi-scale (Multi-timescale) Electrochemical Analysis

Although the STFT and GT extend the Fourier framework into the time–frequency domain, both rely on fixed window widths and therefore cannot simultaneously achieve high resolution across all frequencies. To overcome this limitation, multi-scale methods such as the Wavelet Transform (Mallat, 1999) are used. The Continuous Wavelet Transform (CWT) decomposes a signal into a family of basis functions obtained by scaling and shifting a prototype waveform, or mother wavelet $\Psi(t)$

$$W(a,b) = \frac{1}{\sqrt{|a|}} \int_{-\infty}^{\infty} x(t)\Psi^* \left(\frac{t-b}{a}\right) dt \tag{1.4.16}$$

where a is the scale parameter controlling frequency localisation, b is the translation parameter defining temporal position, and the asterisk $(*)$ denotes complex conjugation. Small values of a correspond to high-frequency components with fine temporal detail, while large a values capture slower, low-frequency variations. This adaptability makes wavelets particularly useful for resolving rapid transient events alongside slower diffusion-controlled processes within the same electrochemical signal.

In digital analysis, the continuous formulation can be discretised to produce the Discrete Wavelet Transform (DWT), which uses dyadic sampling of scale and translation parameters:

$$W_{j,k} = \sum_{n=0}^{N-1} x[n]\,\Psi_{j,k}^*[n] = \sum_{n=0}^{N-1} x[n]\Psi(2^{-j}n - k) \tag{1.4.17}$$

where j and k represent scale and position indices, respectively. The DWT decomposes a signal into approximation and detail coefficients, enabling efficient multi-level analysis. The computational efficiency of this process was greatly improved by the Fast Wavelet Transform (FWT), which recursively applies low-pass and high-pass filtering followed by down-sampling to achieve $O(N)$ complexity. This efficiency, comparable to that of the FFT, has made wavelet-based methods increasingly accessible for real-time electrochemical data analysis, particularly in portable or embedded systems.

1.4.7 Z Transform and Digital Electrochemistry

The use of discrete transforms also opens the path toward digital electrochemistry, where systems are modelled directly in the discrete-time domain. In this context, the Z-transform (Vretblad, 2003) provides a fundamental mathematical framework for analysing sampled signals and discrete systems. It is defined as

$$X(z) = \sum_{n=0}^{\infty} x[n] z^{-n} \tag{1.4.18}$$

where z is a complex variable representing both magnitude and phase information of the discrete frequency response. The Z-domain formulation generalises the Fourier transform and enables the study of system stability, feedback behaviour, and digital filtering, which are integral to potentiostat control and signal processing. By combining the Z-transform with discrete-time circuit models, it becomes possible to treat the electrode–electrolyte interface and its driving electronics as a unified digital system, allowing both chemical and electrical dynamics to be described within the same analytical framework.

1.4.8 Emerging Directions: Multirate and Digital Electrochemistry

Time–frequency and multirate analysis frameworks, encompassing the STFT, Gabor, and wavelet transforms, provide a mathematical foundation for examining electrochemical signals across multiple temporal and spectral domains. These methods extend the classical Fourier approach by offering variable resolution in time and frequency, enabling the characterisation of transient and diffusion-limited processes within the same analytical framework. Their development represents the theoretical pathway through which electrochemistry continues to expand into the frequency domain, refining how dynamic behaviour is described and understood.

In parallel, the increasing reliance on digital instrumentation has opened a second and equally significant direction. Modern potentiostats and control systems operate in discrete time, where sampled signals and feedback loops are better represented through the Z-transform rather than continuous-domain mathematics. This perspective forms the basis of digital electrochemistry, in which experimental control, signal generation, and data interpretation are governed by computational algorithms rather than purely analogue circuitry. Together, these two directions outline complementary but distinct trajectories for the field: one advancing its theoretical description of electrochemical phenomena, and the other redefining the practical means through which those phenomena are observed.

1.5 Fundamentals of Potentiostat Design

Modern electrochemical sensors rely on compact and efficient potentiostat (Colburn, 2021) systems to interface with electrodes and collect meaningful data from redox-active species. This section provides a brief overview of signal handling, core architecture, and recent advances that enable portable, IoT-enabled sensing platforms (Alaba, 2017) for real-world environmental applications.

1.5.1 Analogue and Digital Signals

Electrochemical sensors operate at the interface between analogue chemistry and digital electronics. The potentiostat outputs carefully controlled voltage waveforms, such as steps, ramps, or sinusoidal signals (Oppenheim, 1997), and measures the resulting currents at the working electrode. These analogue signals are typically low in amplitude and susceptible to noise, which makes signal conditioning through amplification and filtering essential.

Once conditioned, the analogue current signals are digitised using analogue-to-digital converters (ADC) for further processing, visualisation, or transmission. In the reverse direction, digital-to-analogue converters (DAC) are used to generate voltage waveforms under software control. The choice of filter design, gain settings, and sampling

frequency all have a significant impact on data fidelity (Tietze, 2015). A simplified diagram of this signal flow is shown in Figure 1.12.

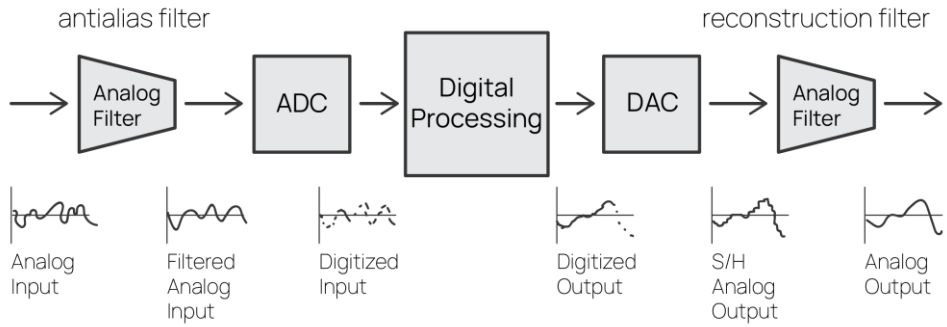


Figure 1.12: Block diagram of analogue signal acquisition and digitisation in an electrochemical sensor circuit.

In potentiostatic control, the quality of the measured electrochemical signal is determined by how accurately the analogue waveform is generated, transmitted, and digitised. The analogue domain is inherently continuous, whereas the digital representation used for data acquisition is discrete in both time and amplitude. The transition between these domains introduces quantisation and sampling effects that must be carefully managed to preserve signal fidelity.

Signal conditioning forms the first stage of this interface. The current output from the working electrode is typically low in amplitude and susceptible to environmental interference. Transimpedance amplifiers are used to convert this current into a measurable voltage, which is then filtered to suppress noise and avoid aliasing before being digitised. The design of these analogue filters, particularly their cut-off frequency and order, must balance noise suppression with temporal resolution, ensuring that the essential features of transient or modulated signals are retained.

Digitisation is performed by an ADC, which samples the conditioned signal at a defined frequency and maps each voltage value to a discrete numerical level determined by the converter's resolution. The sampling frequency must satisfy the Nyquist criterion, typically at least twice the highest signal frequency, to prevent spectral overlap and distortion. In practice, oversampling is often employed to improve effective resolution through averaging, which is particularly beneficial for low-level electrochemical currents in the nanoampere range. The bit depth of the ADC directly limits the smallest distinguishable current increment, meaning that high-resolution converters (16 to 24 bit) are preferred in quantitative analysis.

DACs perform the complementary task of generating potential waveforms under software control. Their update rate, linearity, and output stability determine how accurately potential steps, ramps, or sinusoidal modulations are applied to the electrochemical cell. Any deviation between the intended and delivered potential can manifest as peak broadening, baseline drift, or phase error, especially in dynamic techniques such as DPV or ACV. The fidelity of the DAC output is often expressed in terms of total harmonic distortion (THD), which quantifies the amplitude of unwanted harmonics relative to the fundamental signal. Lower THD corresponds to a purer waveform, which is critical for frequency-dependent experiments. The theoretical signal-to-noise ratio (SNR) of an ideal N-bit DAC follows the relation SNR = 6.02N+1.76 dB, illustrating how bit depth directly influences the dynamic range and noise performance of the applied potential.

To minimise artefacts, feedback loops within the potentiostat continuously compare the commanded potential with the measured cell potential and correct any offset in real time. Electromagnetic interference, ground loops, and common-mode voltage coupling can significantly affect signal integrity, particularly in miniaturised systems where traces and connectors are closely spaced. Shielded cables, proper circuit grounding, and the use of differential measurement configurations help mitigate these effects. In field-deployable potentiostats, additional considerations include temperature stability, component tolerance, and the influence of power-supply noise, which may vary with battery discharge or wireless communication cycles. These factors collectively determine the effective signal-to-noise ratio and, consequently, the accuracy and reliability of the electrochemical measurement.

The interplay between analogue precision and digital control defines the overall performance of modern electrochemical instrumentation. Achieving high temporal and amplitude resolution while maintaining low power consumption remains a core challenge in the design of portable and IoT-enabled systems. The ability to reproduce and interpret complex waveforms depends not only on the quality of the electrochemical interface but also on the robustness of the electronic signal path that supports it.

1.5.2 Overview of Potentiostat Architecture

A potentiostat controls the voltage between the working and reference electrodes while measuring the current between the working and counter electrodes. Traditional benchtop systems offer high performance but are bulky and power-intensive. In contrast, miniaturised versions preserve the same functionality while reducing circuit complexity by incorporating key components such as op-amps (Roberge, 1975), DACs, ADCs, and microcontrollers (Hintz) onto a single printed circuit board.

The main functional blocks include a voltage control loop to stabilise the potential at the working electrode, a transimpedance amplifier (TIA) to convert current into voltage, and a microcontroller to handle signal generation and data acquisition. Figure 1.13 illustrates a general potentiostat architecture that highlights these signal paths and control elements.

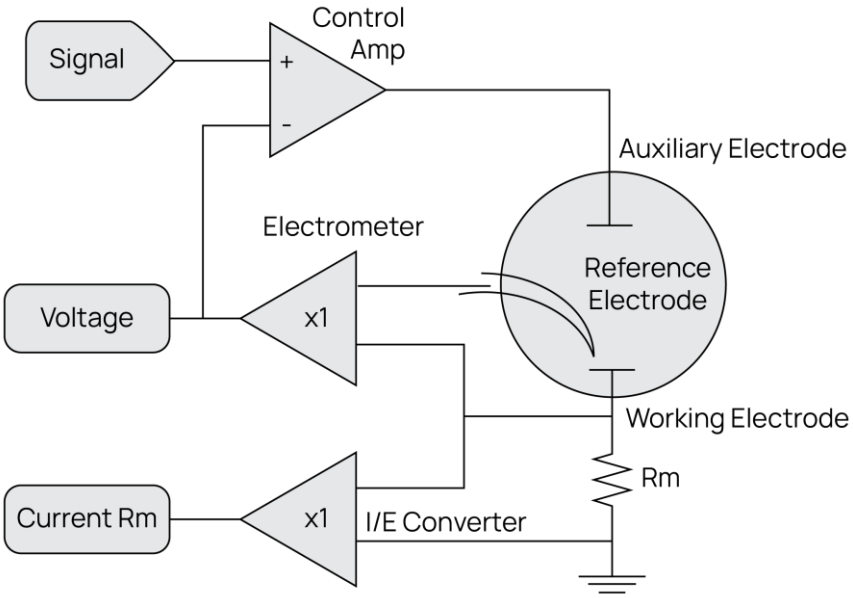


Figure 1.13: General schematic of potentiostat architecture for electrochemical sensing, illustrating signal paths and control elements.

A potentiostat functions as a closed-loop control system designed to maintain a specified potential difference between the working and reference electrodes while measuring the resulting current at the working electrode. The stability and accuracy of this control depend on the design of the feedback loop and the dynamic performance of the operational amplifiers used in each stage. The classical configuration consists of three main blocks: the control amplifier, the I/E converter or transimpedance amplifier, and the data acquisition interface. Each contributes independently to the overall linearity, bandwidth, and noise characteristics of the system.

The control amplifier regulates the potential applied between the working and reference electrodes by continuously adjusting the output voltage at the counter electrode. The loop gain of this amplifier determines how effectively the potentiostat compensates for variations in electrode impedance or solution resistance. Insufficient loop gain or bandwidth can lead to oscillations or sluggish response, while excessive gain without adequate phase margin can cause instability. Careful frequency compensation and proper selection of feedback resistors and capacitors are therefore essential to ensure stable control across the operational frequency range.

The TIA converts the current flowing at the working electrode into a proportional voltage signal. The feedback resistor, typically in the range of kΩ to GΩ depending on the expected current level, defines the current-to-voltage conversion factor. The selection of this resistor must consider both thermal noise and bandwidth requirements, as higher resistance improves sensitivity but reduces the achievable frequency response. Low input bias current and low input capacitance operational amplifiers are preferred to minimise measurement error and phase distortion, particularly for techniques such as EIS or ACV where precise phase information is critical.

Modern potentiostats incorporate programmable gain amplifiers or switched feedback networks to automatically adjust sensitivity across several current ranges. This dynamic scaling extends the measurable current span from nanoamperes to milliamperes without compromising resolution. Current range switching is typically handled through relays or low-leakage analogue switches, and switching transients must be minimised

through appropriate timing control to prevent artefacts in recorded data. In addition, offset voltages introduced by amplifier drift are often compensated through digital calibration routines executed prior to each measurement.

Power supply design also plays a critical role in potentiostat performance. Dual supply rails allow the amplifier outputs to swing symmetrically around ground, supporting both anodic and cathodic potential control. In portable or USB-powered systems, charge pumps or DC–DC converters generate the required dual rails, but these circuits can introduce switching noise that must be filtered to prevent interference with low-level signals. Decoupling capacitors placed close to amplifier power pins and star-ground topologies help maintain stable operation across varying load conditions.

Commercial potentiostats often employ precision analogue components and extensive shielding to achieve low noise and wide frequency response, but these advantages come at increased cost and reduced portability. In contrast, compact systems such as Sensit demonstrate how comparable analytical performance can be achieved through efficient circuit design and software-driven compensation. These designs rely on microcontrollers or system-on-chip architectures that integrate DACs, ADCs, and communication interfaces within a small footprint, enabling direct control of waveform generation and data acquisition. While their noise performance and stability may be more limited than that of benchtop instruments, they offer sufficient accuracy for most applied sensing scenarios, particularly when supported by appropriate digital filtering and calibration routines.

The architecture of a potentiostat thus represents a balance between precision, bandwidth, and power efficiency. The ability to maintain potential control with minimal phase error while accurately measuring currents spanning several orders of magnitude is a key determinant of analytical performance. Continuous improvements in mixed-signal electronics and embedded computing are gradually reducing the performance gap between portable and laboratory-scale instruments, making it increasingly feasible to deploy high-quality electrochemical measurement systems in non-laboratory environments.

1.5.3 IoT-Enabled Implementation for Field Use

Recent developments in embedded electronics have enabled the integration of potentiostats with wireless communication modules, creating compact systems suitable for field deployment. These platforms typically include a microcontroller, low-power potentiostat circuitry, and a wireless interface such as Wi-Fi or Bluetooth. The entire system can be powered through USB or battery and enclosed for operation in harsh environments.

In environmental sensing, this configuration allows real-time data collection, wireless transmission to cloud servers or local terminals, and flexible reprogramming. Combined with screen-printed electrodes, these systems support portable and disposable sensing formats that are ideal for *in situ* monitoring of pollutants. Their small size, low cost, and programmability make them practical for large-scale deployment in smart sensing networks (Lewis, 2004). A schematic representation of such a field-ready system is shown in Figure 1.14.

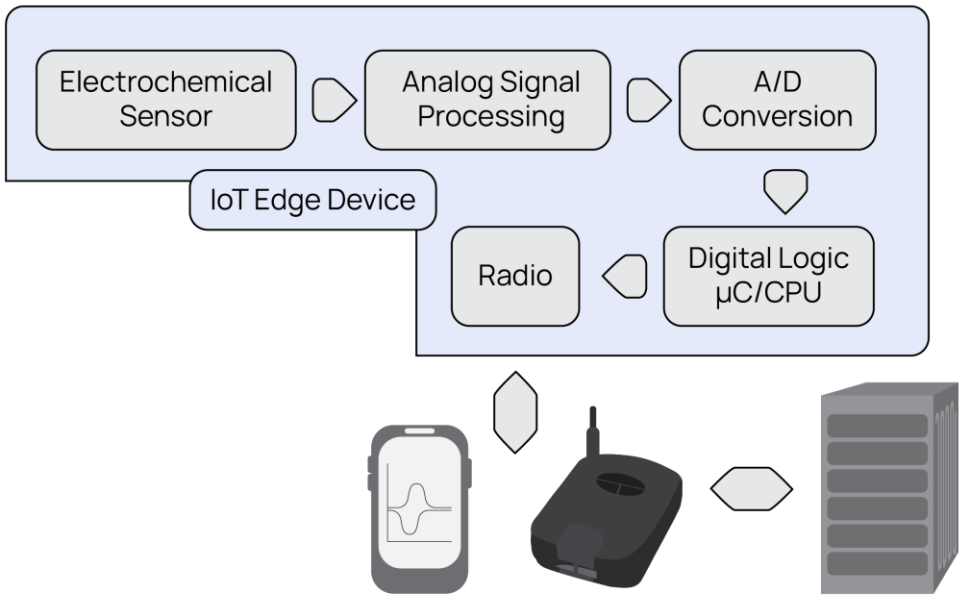


Figure 1.14: Schematic representation of an IoT-enabled electrochemical sensor platform with modular components and wireless communication.

The integration of potentiostat circuitry with Internet-enabled microcontrollers transforms electrochemical systems from laboratory instruments into distributed analytical platforms capable of autonomous operation and remote monitoring. In such architectures, the potentiostat hardware functions as the analogue front end, while the embedded processor performs waveform generation, data acquisition, and communication. The interface between these domains must maintain electrical isolation and temporal synchronisation to prevent measurement drift or data corruption during wireless transmission.

Wireless modules such as Wireless Fidelity (Wi-Fi), Bluetooth Low Energy (BLE), and Low-Power Wide Area Network (LoRaWAN) are commonly employed to transmit measurement data to local gateways or cloud servers. Each communication protocol presents specific trade-offs between bandwidth, range, latency, and power consumption. Wi-Fi supports higher data throughput and direct cloud connectivity but consumes more power, making it suitable for mains-powered installations or intermittent transmission. BLE offers lower energy demand and is preferred for battery-operated sensors that transmit compact data packets at defined intervals. LoRaWAN extends the operational range to several kilometres and is therefore attractive for large-scale environmental monitoring networks, though its low data rate constrains real-time waveform streaming.

Power management is a central challenge in IoT-enabled systems. Battery-operated potentiostats must balance energy efficiency with measurement fidelity. Techniques such as duty-cycling, adaptive sampling, and dynamic power scaling of analogue components are routinely employed to minimise consumption during idle periods. The microcontroller can enter low-power sleep states between measurement cycles, waking periodically to perform electrochemical scans and transmit summarised data. The choice of power source, whether lithium-ion, alkaline, or energy-harvesting modules, determines operational lifetime and environmental suitability.

Firmware design governs the reliability and versatility of these platforms. Real-time operating systems (RTOS) or lightweight scheduling loops ensure deterministic

execution of waveform generation, data acquisition, and transmission tasks. Synchronisation between DAC updates and ADC sampling must be handled with microsecond precision to preserve waveform integrity, particularly in frequency-modulated or pulsed techniques. Data integrity is further maintained through checksum verification and buffering strategies that prevent packet loss when network coverage fluctuates. Firmware also implements calibration routines and error detection. In some cases, it includes adaptive control logic that adjusts measurement parameters based on sensor response.

At the system level, IoT integration enables distributed sensing, where multiple potentiostat units operate in parallel and relay data to a central processing node. Cloud-based analysis pipelines can perform signal averaging, drift correction, and anomaly detection, extending the analytical power of individual low-cost sensors. However, the transition to networked measurement also introduces concerns regarding cybersecurity and data authenticity. Encryption of transmitted data and secure authentication protocols are increasingly being adopted to ensure that collected information remains trustworthy and tamper-proof, particularly in regulatory or industrial monitoring contexts.

The combination of embedded potentiostat hardware, wireless communication, and software-defined control has redefined the operational scope of electrochemical sensing. By enabling real-time data access, remote configuration, and long-term autonomous operation, IoT-enabled platforms support applications that were previously limited to centralised laboratories. For environmental monitoring, this convergence allows pollutant detection networks to be deployed across geographically dispersed sites, providing continuous, high-resolution datasets that can inform regulatory compliance, risk assessment, and early-warning systems.

1.6 Volatile Toxic Organic Compounds

VTOCs are a broad class of environmental pollutants that pose significant risks to both human health and ecological systems. Among them, benzenediols are of particular concern due to their dual role as both naturally occurring antioxidants and synthetic additives in pharmaceutical and cosmetic formulations. Understanding their electrochemical behaviour is essential for developing sensors that enable precise, on-site detection (Chen, 2017). This section provides a focused discussion on the health impact and chemistry of benzenediols, with an emphasis on their relevance to electrochemical sensing.

VTOCs represent a broad category of organic pollutants that readily evaporate at ambient conditions and persist across air, water, and soil systems. Their environmental distribution depends on vapour pressure, solubility, and reactivity toward oxidising agents present in air and natural waters. In urban environments, their primary sources include fuel combustion, industrial discharge, and solvent-based manufacturing processes, while secondary sources arise from the degradation of organic materials and consumer products. Many of these compounds are semi-volatile, partitioning between the gaseous and aqueous phases, and are therefore encountered simultaneously in indoor air and surface water.

Among VTOCs, compounds such as benzenediols are of particular interest due to their dual occurrence in natural and synthetic systems. Catechol, for example, is a naturally occurring antioxidant that forms through the oxidation of plant-derived catechins, and its redox activity plays a role in biological protection against oxidative stress (Lin, Sensitive and rapid determination of catechol in tea samples using mesoporous Al-doped silica modified electrode., 2009). Hydroquinone and resorcinol, in contrast, are primarily synthetic and appear in a wide range of pharmaceutical and cosmetic formulations, including topical creams, antiseptics, and hair treatments. These compounds enter the

environment through direct discharge, wastewater effluent, or leaching from discarded consumer products.

Although their concentrations in environmental samples are often low, their continual release leads to long-term persistence and accumulation (Flickinger, 1976). Similar to other lipophilic compounds such as DDT and polychlorinated biphenyls, benzenediols can adsorb onto organic matter and sediments, gradually entering the food chain. While heavy metals and organometallic compounds exhibit stronger bioaccumulation tendencies, the repeated introduction of aromatic organics into aquatic ecosystems raises comparable concerns. Their partial oxidation in natural waters produces reactive intermediates that can bind to biological macromolecules or act as secondary pollutants influencing aquatic oxygen demand and toxicity (Subramanyam, 2013).

From a toxicological perspective, these compounds are classified as irritants and potential sensitising agents, with hydroquinone additionally associated with depigmentation and possible carcinogenicity at high exposure levels. Chronic exposure is primarily an occupational concern in industries involving dyes, photography, and polymer manufacture, but the widespread use of personal care products containing benzenediols extends the risk to the general population. Environmental surveillance has therefore shifted toward low-concentration, long-term detection to assess cumulative exposure and support regulatory control.

Electrochemical sensing provides an effective means of detecting these compounds in both industrial and environmental samples because of their intrinsic redox activity. Their oxidation to quinonoid forms produces distinct electrochemical signatures that enable selective detection even in complex matrices. Monitoring benzenediols serves a dual purpose: it provides insight into anthropogenic contamination pathways and supports the development of analytical strategies for related aromatic pollutants. Their role as both functional ingredients and environmental contaminants makes them ideal model analytes for demonstrating the capabilities of portable electrochemical sensors.

Benzenediol isomers are widely encountered in environmental systems due to their origin in industrial processes, biomass degradation, and atmospheric oxidation of aromatic compounds. These species are commonly detected in wastewater, surface waters, and atmospheric particulate matter, with reported concentrations typically ranging in the low micromolar levels range in contaminated environments. Due to their toxicity, persistence, and potential for bioaccumulation, they are considered pollutants, necessitating reliable and sensitive analytical detection methods for environmental monitoring (Karuppiah, 2023).

1.6.1 Health Impact and Regulatory Context

Prolonged exposure to benzenediols has been linked to a variety of health effects, which differ depending on the isomer and route of exposure. While Catechol (CC) is a naturally occurring antioxidant found in plant matter, it can act as a respiratory and skin irritant when inhaled or absorbed in concentrated forms. Hydroquinone (HQ) and Resorcinol (RS), on the other hand, are synthetic compounds commonly used in skincare, hair dyes, and pharmaceutical products. These are associated with a higher toxicological burden, including skin sensitisation, endocrine disruption, and in the case of HQ, possible carcinogenicity.

Due to these risks, several national and international agencies have established occupational exposure limits to protect workers and consumers. A summary of key recommended limits is provided below:

Catechol: National Institute for Occupational Safety and Health (NIOSH) recommended Exposure Limit (REL) is 5 ppm (20 mg/m^3), with similar guidance from The American Conference of Governmental Industrial Hygienists (ACGIH). While not listed under a

specific Occupational Safety and Health Administration (OSHA) Permissible Exposure Limit (PEL), it is treated as a controlled irritant in occupational settings (Hudson, 2019).
Hydroquinone: Both OSHA and NIOSH recommend a limit of 2 mg/m^3 Time-Weighted Average (TWA). ACGIH also maintains a threshold of 2 mg/m^3, based on evidence of skin depigmentation, systemic toxicity, and potential carcinogenicity with long-term exposure (Control, 1990).
Resorcinol: NIOSH and ACGIH recommend a limit of 10 ppm (45 mg/m^3), with a short-term exposure limit (STEL) of 15 ppm. RS is noted for its potential to cause methemoglobinemia and disrupt thyroid function (Hahn, 2006).

These regulatory thresholds reinforce the need for low-level, continuous monitoring in both workplace and domestic environments. As awareness of chronic low-dose exposure risks grows, sensor platforms capable of real-time detection are becoming critical components of environmental safety strategies.

1.6.2 Chemical Overview of Benzenediols

Benzenediols consist of a benzene ring with two hydroxyl groups as three isomeric forms: CC (1,2-dihydroxybenzene), RS (1,3-dihydroxybenzene), and HQ (1,4-dihydroxybenzene). These isomers display varying electrochemical behaviours due to the relative positioning of their hydroxyl groups, which affects their resonance stability and redox mechanisms.

The electrochemical redox activity of benzenediols is due to the reversible oxidation of the hydroxyl groups to quinonoid forms. This makes them ideal candidates for detection via voltammetry and amperometry, where onset potentials and the potentials at which peak currents are recorded serve as qualitative and quantitative indicators. However, not all benzenediols behave the same electrochemically, and isomer-specific redox processes aid in distinguishing them.

1.6.2.1 Catechol and Hydroquinone

CC and HQ both undergo reversible two-electron, two-proton oxidation to form o-benzoquinone and p-benzoquinone, respectively (Ghanem, 2007). Their redox behaviour is well characterised and typically exhibits distinct anodic and cathodic peaks in cyclic voltammetry. This reversibility allows for stable cycling and reproducible signal output, making both compounds ideal targets for sensor calibration and kinetic analysis.

Both isomers display standard diffusion-controlled current responses under varying scan rates, and their redox potentials are sufficiently separated to allow simultaneous detection under optimised conditions. The reversible redox mechanisms of CC and HQ are illustrated in Figure 1.15.

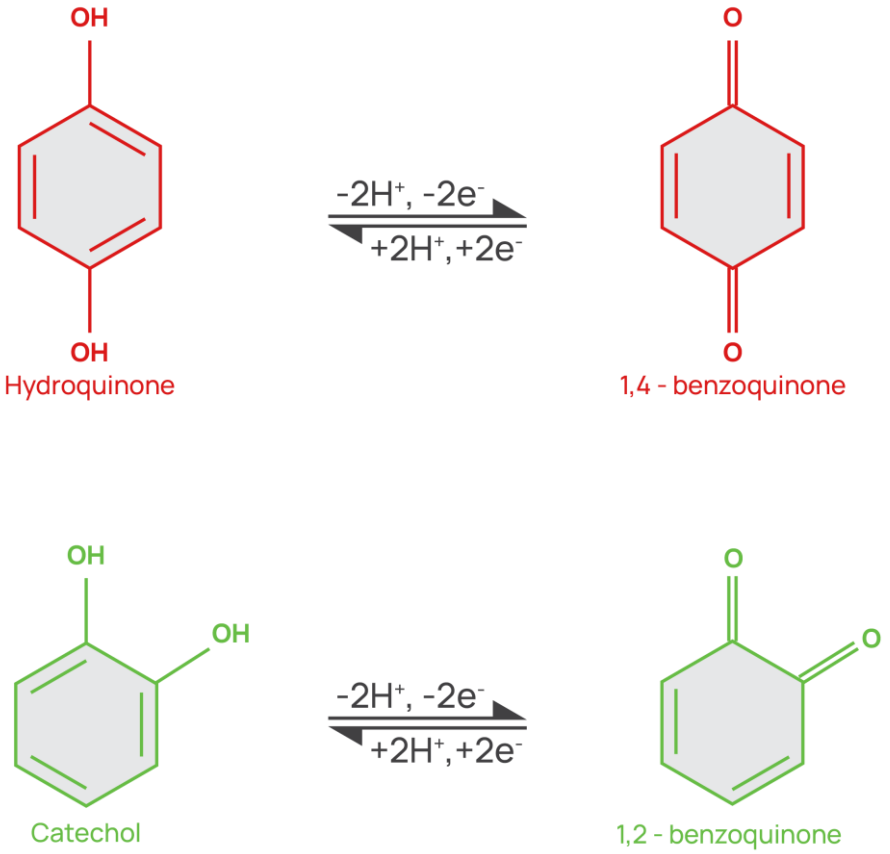


Figure 1.15: Reversible redox behaviour of hydroquinone and catechol showing the formation of p-benzoquinone and o-benzoquinone, respectively.

1.6.2.2 Resorcinol

Unlike CC and HQ, RS undergoes irreversible electrochemical oxidation, which is often followed by electropolymerisation on the electrode surface (Ngamchuea, 2020). Its 1,3-dihydroxy configuration lacks the resonance stabilisation needed for the oxidised intermediate to remain soluble, resulting in the formation of intermediary species that quickly couple and deposit as a polymeric film. This film significantly alters the electrode surface, decreasing sensitivity and increasing variability in long-term measurements.

The fouling behaviour of RS presents a major challenge in electrochemical sensing, requiring strategies such as surface regeneration, use of anti-fouling modifiers, or short-duration measurement cycles. Despite these limitations, RS remains an important target for environmental monitoring due to its frequent presence in pharmaceutical and industrial effluents. The irreversible oxidation and polymerisation pathway of RS is illustrated in Figure 1.16 (Mikolajczyk, 2018).

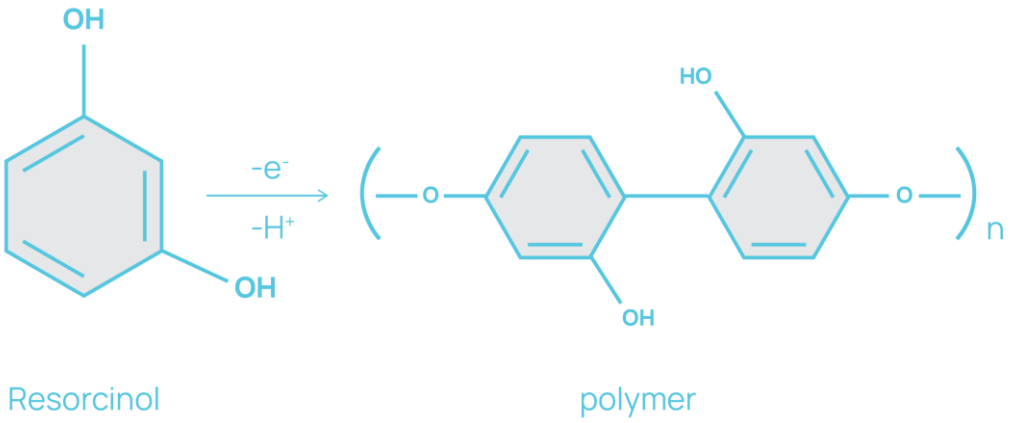


Figure 1.16: Irreversible oxidation and electropolymerisation of resorcinol, resulting in the deposition of polymeric material on the electrode surface.

1.7 Catalytic Enhancement using Carbon-Supported Catalysts

Electrochemical detection of organic analytes such as benzenediols relies heavily on the efficiency of the electron transfer process at the electrode surface. This efficiency is governed by both the electrode material and the catalytic properties of any surface modifiers. One widely used approach is the incorporation of noble metal nanoparticles, such as platinum, supported on high-surface-area carbon substrates (Auer, 1998). These materials enhance sensitivity, reduce overpotentials, and improve selectivity for target redox-active compounds. This section outlines the mechanisms behind such catalytic behaviour and highlights alternative catalyst options relevant to sensor development.

Catalytic modification of electrode surfaces remains one of the most effective strategies for improving both sensitivity and selectivity in electrochemical sensors. For carbon-based electrodes, catalytic enhancement typically aims to reduce overpotentials, increase electron-transfer rates, and suppress fouling reactions that otherwise hinder reproducibility. Among the most widely used modifiers are noble metal nanoparticles supported on high-surface-area carbon substrates, which combine the electrical conductivity of carbon with the catalytic activity of metals such as platinum, gold, or palladium.

In Pt/C systems, platinum nanoparticles act as active sites for the adsorption and oxidation of organic molecules. Their catalytic effect arises from the ability of Pt to facilitate electron exchange between adsorbed intermediates and the electrode, lowering activation barriers for redox reactions. The high density of surface atoms on nanoscale Pt clusters enhances this behaviour, while the carbon support provides electronic coupling and mechanical stability. For benzenediols, the use of Pt/C has been shown to lower oxidation potentials and improve current response stability by accelerating the conversion between hydroxy and quinonoid forms as discussed later in Sections 4.1 and 4.3. The resulting peak sharpening and increased reversibility contribute directly to improved analytical precision.

The performance of the catalyst is strongly influenced by the morphology and dispersion of the metallic nanoparticles. Uniformly distributed, finely divided Pt on conductive carbon produces high active surface areas and consistent electron-transfer characteristics, whereas particle agglomeration reduces available catalytic sites and

increases charge-transfer resistance. Achieving this balance is primarily a function of the synthesis route, drying rate, and binder composition used during electrode modification. The choice of carbon support, whether Vulcan XC-72R, carbon black, or graphene, also determines the electronic structure and the extent of π–π interaction with aromatic analytes, which in turn affects adsorption dynamics (Tang, 2018) (Wang W. Z., 2014).

While Pt/C remains the benchmark material, its high cost and susceptibility to poisoning by adsorbed intermediates have driven extensive research into alternative catalysts. Palladium (Pd/C) exhibits similar catalytic activity for the oxidation of small organic molecules, particularly in alkaline media, and offers improved tolerance to surface poisoning in some systems. Nickel- and cobalt-based oxides and hydroxides provide further cost-effective options and have been successfully employed for organic oxidation. These materials rely on redox transitions between multiple oxidation states to mediate electron transfer, and although their catalytic activity is generally lower than that of noble metals, they remain attractive for disposable or short-duration sensors.

Recent developments have focused on hybrid materials that integrate the high conductivity of carbon nanostructures with the tunable catalytic properties of transition metal oxides. Graphene and carbon nanotubes serve as effective scaffolds for dispersing metallic or mixed-metal oxide nanoparticles, creating a synergistic interface that enhances both electron mobility and surface reactivity. The resulting composites exhibit improved charge-transfer kinetics, reduced fouling, and greater mechanical stability under repeated cycling. For environmental sensing applications, such materials present a practical compromise between performance, cost, and environmental sustainability.

An emerging area of interest is the use of high-entropy alloys and oxides, which combine multiple elements in near-equimolar ratios to produce complex surface chemistries. These materials offer adjustable electronic structures and defect distributions that can be tailored for specific electrochemical reactions. Their compositional flexibility and resistance to poisoning make them promising candidates for next-generation sensing platforms where long-term operational stability is required.

In the context of this work, catalytic enhancement is viewed not only as a means of improving detection performance but also as a critical factor in defining sensor longevity and reproducibility. The use of Pt/C-modified electrodes demonstrates how targeted surface engineering can optimise the interplay between electron transfer, adsorption, and material stability. Future progress in this area will likely depend on the ability to combine catalytic efficiency with environmental compatibility, ensuring that the advantages of high-performance materials are achieved without compromising scalability or sustainability.

Other recent advances in electrochemical sensors for VTOCs have focused on enhancing performance through electrode modification strategies, including the use of nanostructured materials such as reduced graphene oxide (rGO) (Ye, 2022), carbon nanotubes, nanoribbons, and MXenes, as well as molecularly imprinted polymers (MIPs) (Wang, 2023) and biorecognition elements such as aptamers and antibodies (Xie, 2025). These approaches improve sensitivity, selectivity, and resistance to fouling while having specific drawbacks, thereby expanding the applicability of electrochemical sensing platforms in complex matrices.

1.7.1 Electron Transfer in Carbon-Based Materials

Carbon-based materials, such as graphite, glassy carbon, carbon black, and screen-printed carbon electrodes, provide a conductive and chemically stable matrix for electrochemical reactions (Gattia, 2009). Their surface properties, including defect sites, edge-plane exposure, and sp^2/sp^3 hybridisation ratios, influence their inherent electrocatalytic behaviour. However, pure carbon materials can sometimes suffer from sluggish kinetics for

certain redox processes, particularly involving organic compounds with multiple hydroxyl groups or unstable intermediates.

To address this limitation, carbon surfaces are often functionalised or modified with catalytic nanoparticles. These modifications increase the density of active sites and promote faster charge transfer, especially for analytes like CC and HQ, which undergo two-electron oxidation reactions that benefit from efficient surface mediation.

1.7.2 Platinum in Organic Redox Chemistry

Platinum nanoparticles supported on carbon (Pt/C) (Yu, 2007) are among the most widely used catalysts in both sensing and energy applications. In organic electrooxidation, Pt exhibits excellent activity for small organic, making it indispensable in the anode design of fuel cells. This catalytic efficiency arises from its ability to adsorb and activate hydroxyl-containing compounds while resisting poisoning from intermediates.
In the context of benzenediol detection, Pt/C electrodes lower the oxidation potential of CC and HQ and increase peak current responses by providing a high density of active sites and facilitating rapid electron transfer. The catalyst also contributes to better signal reproducibility, especially in repeated or long-term measurements. A representative structure of a Pt/C catalyst (platinum nanoparticles on Vulcan XC-72R) is shown in Figure 1.17.

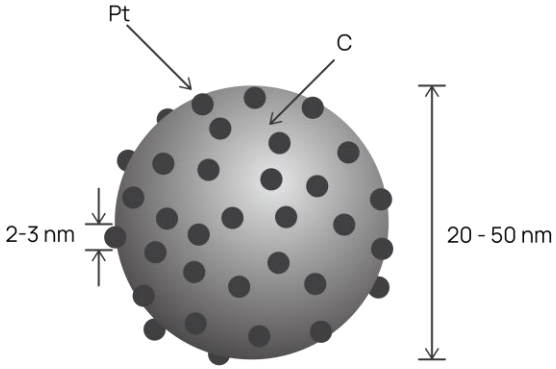


Figure 1.17: Schematic representation of platinum nanoparticles dispersed on a carbon support (Pt/C), highlighting active sites for organic electrooxidation.

1.7.3 Alternative Catalytic Materials

While Pt remains a benchmark catalyst, its high cost and vulnerability to surface poisoning have prompted the search for alternative catalytic materials with comparable performance. Among the platinum-group metals (PGMs) (Hughes, 2021), palladium (Pd) and ruthenium (Ru) have shown promising activity in the oxidation of organic molecules.

Beyond PGMs, several transition metal-based materials (Kung, 1989) are gaining attention as more affordable alternatives. Manganese dioxide (MnO_2) is widely studied for

its high surface area, redox activity, and low toxicity. It has been shown to enhance electrochemical responses for a variety of phenolic and oxygenated organic compounds. Similarly, nickel oxyhydroxide (NiOOH) has demonstrated good catalytic behaviour in alkaline conditions (Trafela, 2019), particularly for alcohol and diol oxidation. Ni-based catalysts also benefit from ease of electrodeposition, making them compatible with disposable sensor formats.

More recently, High Entropy Alloys (HEA) (Božiček, 2024) and their oxidised counterparts, High Entropy Oxides (HEO), have emerged as modular platforms for tuning electrocatalytic properties. These materials combine five or more elements in near-equimolar ratios, generating unique surface compositions and defect structures that can stabilise redox-active intermediates. Early studies suggest that HEOs may offer improved performance, tunability, and fouling resistance when used in electrochemical sensors targeting complex organics such as benzenediols.

Together, these alternative materials expand the design space for catalytic electrode surfaces and offer cost-effective pathways toward scalable, high-performance sensors.

1.8 Synthesis

The topics presented in this chapter outline the conceptual and technical framework underpinning the development of portable electrochemical sensors for environmental monitoring. The discussion began with the broader need for real-time detection of volatile organic pollutants and progressed through the theoretical basis of electrochemical sensing, the comparative assessment of conventional techniques, and the mathematical tools used to interpret their responses. The description of potentiostat architecture and signal handling principles established the link between electrochemistry and embedded electronics, while the analysis of benzenediols and catalytic surface modifications provided the chemical and material context relevant to this work. Together, these sections define the interdisciplinary foundation upon which the subsequent experimental methods and design objectives are constructed. Taken as a whole, this dissertation approaches electrochemical sensing not as a transparent analytical window onto chemical processes, but as a layered measurement system whose excitation, instrumentation, and evolving interface fundamentally constrain what can be inferred. At the foundational level, material choice and surface chemistry define the intrinsic electrochemical behaviour of the sensing interface. Built upon this, signal generation and analysis determine how redox processes are excited, observed, and distinguished from background contributions. Instrumentation, in the form of potentiostat architecture and signal handling, mediates how faithfully these electrochemical signals are produced and measured. Finally, system integration and deployment constraints govern whether laboratory performance can be translated into practical, field-ready sensing platforms. This conclusion is drawn from a comparative synthesis of multiple experimental studies conducted in this dissertation and in the associated literature, examining how waveform design, instrumentation architecture, and interface evolution jointly shape electrochemical sensor performance. The chapters that follow examine each of these layers in turn, with particular emphasis on how their interactions ultimately define sensitivity, selectivity, stability, and real-world usability.

Chapter 2

Aims and Hypotheses

The primary aim of the present research is to design, fabricate, and evaluate a portable electrochemical sensing system for the selective detection of benzenediol isomers: CC, HQ, RS in aqueous environments. The system is based on carbon-based SPEs modified with catalytic nanomaterials and coupled to a custom-built, IoT-enabled potentiostat platform. The goal is to create a cost-effective, real-time analytical tool that can be deployed outside laboratory settings, without compromising precision, stability, or interpretability.

To achieve this, the research is guided by the following technical goals:

- To develop and characterise surface-modified SPEs incorporating carbon-supported platinum and gold nanoparticles, and evaluate their catalytic activity toward benzenediol oxidation.
- To implement multiple electrochemical techniques, including CV, CA, DPV, ACV, and EIS, for the qualitative and quantitative analysis of redox-active benzenediols.
- To design and validate a modular potentiostat capable of executing waveform-driven techniques with fine-tuned signal resolution and frequency control.
- To investigate the role of frequency-domain decomposition in resolving overlapping redox signals, isolating capacitive currents, and evaluating sensor drift over time.
- To deploy the integrated sensing platform under field-simulated conditions, assessing sensor performance, reproducibility and longevity.

These goals are supported by a set of testable hypotheses that:

- Catalytic modification of SPE surfaces using Pt/C and Au/C nanoparticles will lower oxidation overpotentials and increase current responses for CC, RS and HQ.

Pt and Au as catalytic nanoparticles are known to facilitate electron transfer by lowering the activation energy required for redox reactions. When dispersed on a high-surface-area carbon support and applied to the SPE working electrode, these catalysts provide abundant active sites for the electrochemical oxidation of benzenediol isomers. As a result, peak potentials shift to lower values and current responses increase due to improved reaction kinetics.

- High-frequency voltammetric techniques (e.g., DPV, ACV) will enable better separation of isomer-specific redox peaks compared to conventional CV, thereby improving peak resolution and selectivity through suppression of capacitive (non-faradaic) current contributions.

Pulse and AC-based voltammetric methods suppress background capacitive currents more effectively than continuous scan techniques like CV. By differentially sampling the current or applying modulated perturbations, these methods increase the resolution of overlapping

redox events, a major advantage when analysing structurally similar compounds such as CC, HQ, and RS. The improved peak definition enables more accurate isomer discrimination in mixed or complex matrices, enhancing the selectivity of the sensing platform under real-world conditions.

- Frequency-resolved signal processing will allow isolation of faradaic components from background charging currents, improving detection limits and response clarity.

Fourier-based analysis of voltammetric signals enables decomposition into harmonic components, where faradaic and non-faradaic processes often exhibit distinct spectral characteristics. By evaluating the frequency content of the measured current, it becomes possible to filter or quantify specific signal contributions more precisely than in the time domain alone. This separation reduces noise, enhances sensitivity, and enables lower limits of detection, especially important in environmental applications where analyte concentrations may be trace-level.

- EIS, used intermittently or concurrently, will provide meaningful diagnostic information on sensor surface degradation and loss of electrochemical activity.

EIS captures interfacial properties such as charge-transfer resistance and double-layer capacitance, which evolve as the electrode surface ages or fouls. By periodically applying EIS during sensor operation, it is possible to track these parameters non-destructively and in real time, providing a diagnostic tool for sensor health. This information can inform and interpret signal drift, and distinguish between analyte-related effects and hardware degradation, ultimately improving measurement reliability and operational robustness.

- A miniaturised, programmable potentiostat with integrated wireless communication can execute complex analytical protocols with sufficient robustness, reliability and accuracy for field use.

Traditional potentiostats are bulky and laboratory-bound, but recent advances in embedded electronics allow for the integration of DACs, ADCs, and wireless modules on compact PCBs. A well-designed portable system can replicate key electrochemical techniques such as CV, CA and EIS while maintaining stable voltage control and precise current acquisition. Coupled with Bluetooth or Wi-Fi communication, such devices enable real-time data transmission and remote operation, making them highly suited for on-site chemical sensing in industrial, environmental, or clinical settings.

Collectively, this framework supports the creation of a robust, data-rich sensing platform that combines low-cost fabrication with high analytical performance, aimed at addressing the real-world need for portable environmental VTOC monitoring.

Chapter 3

Experimental Methods and Materials

The experimental workflow employed in this study integrates modified electrode fabrication, signal-driven electrochemical measurements, hardware development, and real-world sample testing, aimed at evaluating the response behaviour of benzenediol isomers (CC, HQ, RS) under analytically relevant conditions.

A range of electrochemical techniques, including CV, CA, DPV, ACV and EIS, were used to probe the redox behaviour of the analytes. These were applied across a suite of SPEs, both in their unmodified form and after surface enhancement with catalytic nanomaterials such as Pt/C and Au/C.

The electrodes were interfaced with a multiple potentiostat platforms, featuring both digital (staircase) and analogue (linear ramp) capabilities. The system allowed the testing of waveform effects, electrode degradation, and current–voltage relationships under varying scan rates and time-dependent inputs. Where appropriate, simulations of circuit responses were performed using MATLAB to validate experimental trends using electrochemical models such as the Randles circuit.

All electrochemical measurements were conducted in a temperature-controlled laboratory environment. Test analytes were prepared in standard aqueous matrices with pH and ionic strength adjusted to maintain favourable conditions for both detection and stability of the analytes. Acidic environments were found to minimise spontaneous oxidation of the benzenediols, and therefore all analyses were carried out in 1 M HCl. Where relevant, simulated matrices involving real samples were also used to evaluate sensor behaviour outside of well-controlled lab conditions, testing the sensor's applicability to situations where measured analytical concentrations could no longer be relied upon.

3.1 Electrode Modification Techniques

Screen-printed electrodes (SPEs) are modular, low-cost sensing platforms widely used in electrochemical detection due to their ease of use, disposability, and flexibility for surface modification. In this study, Metrohm DropSens DS150 SPEs were employed as the base sensor substrate. These consist of a 4 mm diameter carbon working electrode (WE), a platinum counter electrode (CE), and a silver quasi-reference electrode (qRE), all screen-printed onto a sintered alumina ceramic base. Each electrode is connected via silver conductive tracks that terminate in contact pads for potentiostat interfacing.

The DS150 layout supports reproducible three-electrode measurements on a compact, planar format, with well-defined geometries that facilitate quantitative comparisons. The working electrode surface is exposed for drop casting or modification, while the remainder of the substrate is coated with an insulating polymer layer that protects conduction paths and prevents cross-talk or shorting during measurement.

Although typically designed for single-use deployment, these SPEs can be reused under controlled conditions, and their chemically inert substrate allows for use in both aqueous and organic media. Their compatibility with drop cast catalyst inks and other nanomaterial coatings makes them an ideal platform for developing portable electrochemical sensors.

Prior to modification, the WE surface was cleaned with deionised water followed by absolute ethanol, and gently dried on a hot plate maintained at 55 °C to remove any surface contaminants. The catalyst ink was prepared by dispersing commercially sourced 20 wt.% platinum on carbon (Pt/C, 2–3 nm Pt on Vulcan XC-72R, 20–50 nm) or 20 wt.% gold on carbon (Au/C, 4–6 nm Au on Vulcan XC-72, 40–60 nm) in 0.995 mL of absolute ethanol, chosen to minimise solvent polarity-based surface effects observed with deionised water and isopropanol. To this, 5 µL of a 5% Nafion solution in ethanol was added to serve as a binder and stabilising agent. The resulting suspension was stirred using a 500 W ultrasonic probe at 25% amplitude for 2 minutes to ensure uniform dispersion of the catalyst particles.

A 10 µL aliquot of the freshly prepared ink was pipetted directly onto the carbon WE surface while the electrode remained on the hot plate to promote rapid and uniform drying. Care was taken to avoid contact between the ink and the CE or RE tracks to prevent cross-contamination. Each 10 µL deposition contained 10 µg of catalyst material, of which 2 µg was platinum, resulting in an estimated Pt or Au surface loading of approximately 160 ng mm^{-2} over the 4 mm diameter working electrode.

After modification, the sensor elements were stored in a dry, sealed container to prevent environmental exposure and to minimise tarnishing of the silver RE. The drop casting process used for electrode modification is illustrated in Figure 4.1.

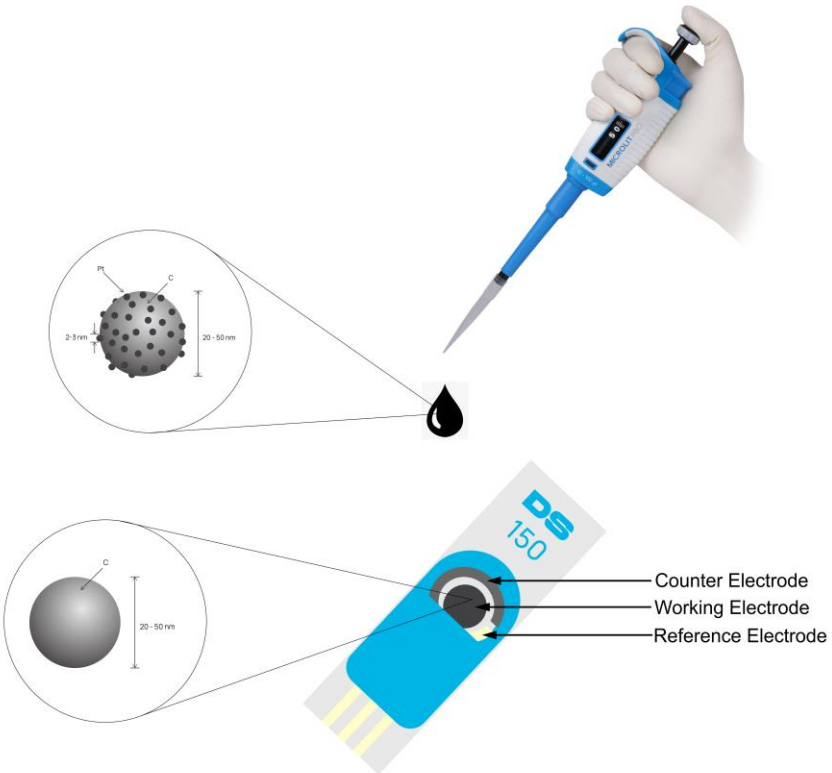


Figure 3.1: Illustration of the catalyst ink drop casting process onto the carbon working electrode of a DS150 SPE, showing selective application and avoidance of the counter and reference electrodes.

3.2 Electrochemical Testing Protocols

All electrochemical measurements were conducted under standard temperature and pressure (STP) conditions in a climate-controlled laboratory. A range of techniques was used to evaluate the redox behaviour of CC, HQ, RS, including CV, CA, DPV, ACV, and EIS. Measurements were carried out using a combination of commercial potentiostats: the PalmSens series (PalmSens4, EmStat3 Blue, Sensit BT and Sensit Smart), and Metrohm VIONIC.

CV was performed on both PalmSens series and Metrohm VIONIC instruments. For the PalmSens4, the scan range was 0 V to 1 V vs Ag qRE at a scan rate of 10 mV s^{-1} with differing number of cycles and ~1 mV step resolution. On the VIONIC, scans were performed over the same potential window at scan rates of 10, 25, 50, and 100 mV s^{-1} with three cycles each, using digital steps of ~1 mV. Analogue scans were also performed on the VIONIC to see if the hardware affected the electrochemical measurements qualitatively and quantitatively.

ACV was conducted using the PalmSens series with the following parameters: base scan rate of 10 mV s^{-1}, AC amplitude of 10 mV (rms), frequency range from 3 Hz to 2000 Hz, and step increment of 10 mV between 0 V and 1 V vs Ag qRE.

CA and DPV were performed using the PalmSens series. For CA, holding potentials were set at +0.52 V (HQ), +0.62 V (CC), and +0.94 V (RS), each with a run time of 60 s and a sampling interval of 10 ms. For DPV, the scan window ranged from 0 V to 1 V, with a step size of 10 mV, a pulse magnitude of 30 mV, and a pulse duration of 50 ms.

EIS was also carried out using the PalmSens series. A 10 mV (rms) AC perturbation was applied at a DC bias of 0 V over a frequency range of 0.5 Hz to 100 kHz using 54 points logarithmically spaced (10 per decade). The resulting impedance spectra were analysed using non-linear least squares fitting to an equivalent circuit. For representative datasets, reduced chi-squared values as low as 0.0020 were achieved, indicating excellent agreement between the experimental and simulated responses.

3.3 Instrumentation and Custom Hardware Development

Two versions of a custom potentiostat system were developed to enable portable electrochemical measurements outside traditional laboratory settings. The first prototype was assembled on a standard breadboard using discrete components, offering flexibility for initial testing and configuration of signal pathways. While fully functional, this version was physically bulky and lacked environmental protection, making it unsuitable for field deployment.

The finalised second prototype was designed on a compact custom PCB measuring 60 mm × 30 mm, integrating a digital potentiostat circuit with a Photon Wi-Fi Development Board. This version offered significantly reduced footprint, improved signal stability, and a USB-powered input consuming approximately 2.5 W. The system supported chronoamperometric measurements and was capable of generating stable DC potentials in the 0–1.5 V range. Signal acquisition and wireless transmission were handled via TCP/IP protocols, enabling remote monitoring and control by interfacing with a PC. The system could be programmed on the fly, wirelessly as long as a stable wireless connection was established.

Both prototypes interfaced directly with three-electrode screen-printed sensors through a simple screw terminal connector. The PCB version was enclosed in a water-resistant case, offering practical protection for environmental testing. Performance benchmarking against a benchtop potentiostat confirmed the system's reliability, with

comparable signal fidelity and response times, validating its use for *in situ* electrochemical sensing applications.

3.4 Signal Processing and Simulation Approaches

Signal processing in this work was implemented at both the hardware and analytical levels to support high-fidelity electrochemical data acquisition and interpretation. The custom-built potentiostat incorporated onboard filtering circuitry to reduce high-frequency interference and baseline drift.

A major focus of the analysis was the application of Fourier-based spectral decomposition to interpret voltammetric responses. Electrochemical techniques such as LSV, CV, DPV and SWV were each analysed in the frequency domain to evaluate the harmonic composition of their voltages as a function of time. This approach enabled separation of faradaic signal components from background or capacitive contributions, particularly for techniques involving pulsed or modulated waveforms.

The spectral analysis was performed using Fourier analysis applied to the time-resolved potential profiles. This allowed identification of frequency responses associated with redox processes and assessment of how waveform shape influenced the distribution of electrochemical energy. These insights informed the selection and optimisation of measurement techniques for different analytes, contributing to improved signal discrimination and sensitivity.

3.5 Sample Preparation and Real-World Testing Procedures

All analyte solutions were prepared using analytical-grade catechol, hydroquinone, and resorcinol, purchased from Sigma Aldrich with a stated purity above 99%. Initial stock (saturated) solutions were prepared by dissolving the respective benzenediols in 1 M hydrochloric acid (prepared by dilution of 37 % HCl) under ultrasonic stirring. The resulting concentrations were 3.9 M for CC, 0.54 M for HQ, and 5 M for RS. Working solutions of lower concentrations were obtained by serial dilution of these stocks with 1 M HCl.

For all electrochemical measurements, a fixed volume of 75 µl of the prepared analyte solution was applied directly to the SPE surface. This volume was sufficient to ensure full coverage of the working, reference, and counter electrodes without overflow or evaporation during the test period. All measurements were performed using fresh solution droplets to maintain consistent concentration, surface wetting, and electrode contact conditions.

Although no raw environmental samples were analysed in this study, several commercial chemical formulations containing the target analytes were tested to assess sensor performance in complex, real-world matrices. These included pharmaceutical and cosmetic products known to contain CC, HQ, or RS, which were diluted in 1 M HCl and processed using the same protocol as analytical-grade standards. This approach allowed evaluation of the sensor's capability to detect target compounds in the presence of stabilizers, solvents, and other additives, effectively simulating challenges encountered in real-world applications such as wastewater monitoring or product authentication.

3.6 Material Characterisation

To confirm the morphology, dispersion, and elemental composition of the catalyst layers applied to the SPE working electrodes, a combination of scanning electron microscopy (SEM) (JEOL 7600F), transmission electron microscopy (TEM) (JEOL 2100), and energy-dispersive X-ray spectroscopy (EDXS) was employed. These techniques provided complementary insights into the structural and compositional details of the modified electrodes.

SEM was used to examine the surface topography of Pt/C-modified electrodes at various magnifications and conditions. The analysis verified the deposition of the catalyst ink, with disparate regions corresponding to carbon support particles decorated with nanoscale metallic features. Surface features such as voids and agglomeration sites were also visible, providing indirect evidence of superficial homogeneity following the drop casting process.

TEM enabled high-resolution imaging of the individual platinum and gold nanoparticles dispersed on the carbon support. The observed particle sizes were consistent with the supplier specifications (2–3 nm for Pt, 4–6 nm for Au), and the lattice fringes of crystalline Pt and Au were resolved in several fields of view. This confirmed that the synthesis preserved nanoparticle size integrity and avoided significant agglomeration, leading to confidence during electrode modification.

EDXS, conducted in parallel with SEM, was used to confirm the elemental composition and spatial distribution of key constituents. The spectra showed clear peaks corresponding to Pt, Au, and C, with no significant impurities detected. Elemental mapping further confirmed the uniformity of noble metal dispersion across the working electrode area, supporting the assumption of consistent catalytic coverage for electrochemical measurements.

Chapter 4

Results and Discussion

This chapter presents the experimental findings and analytical interpretations from the electrochemical investigation of benzenediol isomers using SPEs. The results are organised by thematic focus, beginning with baseline detection in controlled matrices and progressing toward complex sample evaluation, sensor diagnostics, and waveform-specific behaviour. Each section draws from specific experimental datasets to demonstrate the performance, selectivity, and robustness of the developed sensing platform. Where applicable, insights from equivalent circuit modelling, frequency-domain analysis, and hardware variation studies are used to contextualise the sensor's electrochemical behaviour and operational limits.

The results are presented as a sequence of linked layers within the sensing workflow. The discussion progresses from materials and electrochemical behaviour (Section 4.1), through electrode-level stability and drift (Section 4.3), to signal structure and spectral characterisation (Section 4.4), and then to hardware implementation of waveform generation and measurement (Section 4.5). A brief real-sample demonstration (Section 4.2) is included as an extension of the materials/electrochemistry results. The chapter concludes with an integrated deployment-oriented case study (Section 4.6), tying these elements together in a practical sensing context.

4.1 Detection of Benzenediols Using Modified SPEs

This section addresses the materials and electrochemical layer of the sensing workflow. It establishes how catalytic modification of screen-printed electrodes shapes the redox behaviour and analytical response of the target benzenediols.

This work presents a comprehensive electrochemical detection strategy for the three benzenediol isomers: CC, HQ, and RS, using SPEs modified with Pt/C and Au/C catalysts. The objective was to develop a robust, low-cost sensing platform capable of selectively and sensitively detecting each isomer, both individually and in complex mixtures.

Single-isomer detection was carried out using CV, which produced distinct oxidation and (for CC and HQ) reduction peaks corresponding to their reversible redox transitions to the respective benzoquinones. RS, in contrast, showed irreversible oxidation due to surface polymerisation, which helped distinguish its electrochemical signature from the other two isomers.

Simultaneous detection was achieved using DPV. This technique discriminated against capacitive noise and enabled the resolution of all three analytes within mixed solutions. Well-separated oxidation potentials allowed each isomer to be identified even when present together, especially at lower concentrations.

Quantification was performed by CA at analyte-specific oxidation potentials: +0.62 V for CC, +0.52 V for HQ, and +0.94 V for RS (all vs Ag). Calibration curves spanned a broad concentration range, from saturation levels down to 1 µM for CC and HQ, and 100 nM for RS. Although the full response range was non-linear, a usable pseudo-linear region from 100 µM to 1 mM was established.

Compared to similar sensors reported in the literature, the Pt/C-modified SPEs demonstrated competitive sensitivity, selectivity, and reproducibility while maintaining simplicity and low cost. Detection limits reached 0.33 µM for CC and HQ, and 33 nM for RS. Au/C-modified electrodes were able to detect the analytes qualitatively, though they exhibited instability at higher potentials, which particularly affected RS detection.

This work confirms the potential of catalyst-modified SPEs for real-time detection of volatile toxic organic compounds in both controlled and mixed sample conditions. Figure 4.1 shows the graphical abstract of the benzenediol detection workflow, illustrating the sensing process from analyte input through electrochemical signal acquisition.

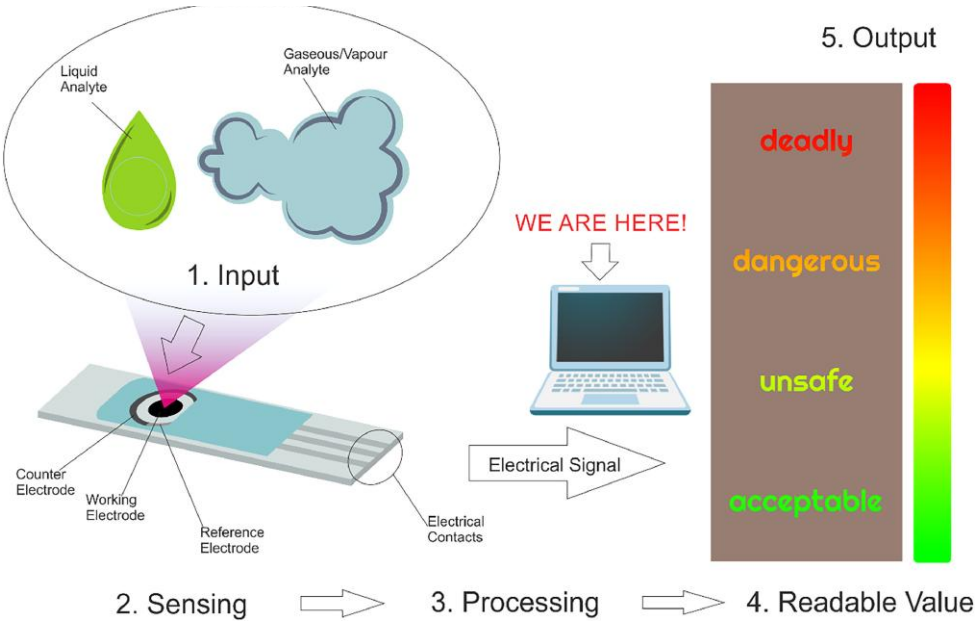


Figure 4.1: Graphical abstract of the benzenediol sensing workflow. Adapted from Krishnamurthy *et al.*, *Electrochimica Acta* (2024), shared under CC BY-NC-ND 4.0 licensing.

Full methodology and data are published in: Krishnamurthy et al., *Electrochimica Acta*, 493 (2024) 144389 https://doi.org/10.1016/j.electacta.2024.144389. The print version is shared in the following pages under the CC BY-NC-ND 4.0 license agreement.

Electrochimica Acta 493 (2024) 144389

Contents lists available at ScienceDirect

Electrochimica Acta

journal homepage: www.journals.elsevier.com/electrochimica-acta

Electrochemical detection of benzenediols using carbon-supported catalysts

Abhilash Krishnamurthy [a,b,*], Zoran Samardžija [a], Špela Trafela [a], Anja Korent [a,b], Sašo Šturm [a,b], Kristina Žagar Soderžnik [a,b]

[a] Department for Nanostructured Materials, Jožef Stefan Institute, Jamova 39, Ljubljana, SI 1000, Europe
[b] Jožef Stefan International Postgraduate School, Jamova 39, Ljubljana, SI 1000, Europe

ARTICLE INFO

Keywords:
Screen printed electrodes
Electrochemical sensor
Benzenediol
Catechol
Hydroquinone
Resorcinol

ABSTRACT

A novel implementation of an electrochemical sensors making use of Screen-Printed Electrodes (SPE) has been discussed. SPE's modified with Carbon-supported Platinum (Pt/C) and Gold (Au/C) were used to detect the three benzenediol isomers, Catechol (CC), Hydroquinone (HQ) and Resorcinol (RS) in acidic media using traditional electrochemical analytical methods such as Cyclic Voltammetry (CV), Chronoamperometry (CA) and Differential Pulse Voltammetry (DPV). Detection of each benzenediol in isolation was possible by CV measurements, and peak oxidation potentials for each isomer were noted. Simultaneous detection of more than one, or all analytes in the same solution was also observed through DPV, once again noting the peak oxidation potentials. Quantification limits were observed using CA's across concentration values ranging from close to saturation down to 1 mM for CC and HQ, and 100 nM for RS, until the recorded current values were nearly indistinguishable to a blank 1 M HCl solution containing no analyte(s), and also evaluating the maximum possible linear range of sensing. The analytes were introduced to the sensor elements in controlled amounts and the electrochemical responses of the sensor elements were recorded and processed. Measurements were repeated across two potentiostats to ensure reproducibility. With these results, successful detection of benzenediols in acidic environment was possible using modified SPE's, proving a potential viable mechanism for quick, simple and inexpensive Volatile Toxic Organic Compounds (VTOC) detection and monitoring.

1. Introduction

Recently, a more holistic approach to the well-being of people has come into focus due to advances in healthcare and general diagnostic techniques [1]. Noise [2], water [3] and air [4] pollution constitute different causes of health issues, and each have their own significance. Water and air pollution have been gaining notoriety due to the introduction of deleterious matter into the environment by both natural and anthropological sources. While outdoor air pollution [5], such as the harmful matter being introduced into the atmosphere by activities such as operation of industries and combustion engines has been well entrenched in popular discussions as an established problem, for a long-time indoor air pollution [6] has stayed rather obscure. Exposure to common household items containing a class of toxins known as Volatile Toxic Organic Compounds [7] has been linked to several detriments ranging from symptoms as mild as headaches and disorientation, to extreme ones such as elevated risk of lung diseases and cancers, a set of issues collectively called "Sick Building Syndrome" [8]. VTOC's may be found in everyday items [9], such as household cleaners, paints, cosmetics etc. Volatile Aromatic Compounds, i.e., organic compounds with benzene rings, in particular have been considered particularly problematic [10]. The EPA has set the following limits for the isomers our study focuses on, the three benzenediol isomers, 1,2-dihydroxybenzene (5 ppm), known as Catechol (CC), 1,3-dihydroxybenzene (10 ppm), known as Resorcinol (RS), and 1,4-dihydroxybenzene (0.5 ppm), known as Hydroquinone (HQ) [11]. Catechol is a common biproduct of several biological processes, occurring naturally in some fruits and vegetables along with its oxidative enzyme Catecholase [12], the combination of catechol and catecholase in the presence of oxygen produces the characteristic browning of certain fruits and vegetables such as apples, pears, potatoes and horseradish due to the conversion of catechol to 1,2-benzoquinone. Hydroquinone is widely used in pharmaceutical grade skin lightening creams [13] and Resorcinol is used as a remedy for acne [14]. While there are measures being considered to remove VTOC's [15] from both outdoor and indoor environments as a way to prevent potential problems, monitoring and measuring their presence [16] serves as a

* Corresponding author.
E-mail address: abhilash.krishnamurthy@ijs.si (A. Krishnamurthy).

https://doi.org/10.1016/j.electacta.2024.144389
Received 2 November 2023; Received in revised form 18 April 2024; Accepted 3 May 2024
Available online 10 May 2024
0013-4686/© 2024 The Authors. Published by Elsevier Ltd. This is an open access article under the CC BY-NC-ND license (http://creativecommons.org/licenses/by-nc-nd/4.0/).

good intermediary step. On the lab scale, there are plenty of well-known and viable processes and corresponding methods such as spectroscopy [17] and liquid/gas chromatography [18] to detect and measure VTOC's accurately and robustly, these processes are generally too expensive, convoluted and impractical for everyday applications. They also require highly-skilled operators to get the best possible results. Small-scale gas sensors sacrifice some of the accuracy and robustness in order to provide much more practical solutions. These sensors operate on a variety of principles, such as pellistors [19] (chemical, calorimetric) and optical fibres [20] (optical). Pellistors are inexpensive and simple, but they lack selectivity, i.e., the ability to distinguish between different causes of the sensor signal. Since they are triggered by any combustible gas/vapour, two different VTOC's might cause an output signal. Optical sensors on the other hand have excellent sensitivity, selectivity and quick response, but they are usually quite complex, require electrical circuits to process the signals and can therefore become prohibitively expensive. A good compromise between the two orthodox solutions is to utilize custom-solution electrochemical sensors, which can alleviate most of the problems. Screen-Printed Electrochemical sensors [21] can be cost-effective and simple, and can be designed to be sensitive, selective and quick, with non-linearity a small compromise. These are generally single-use, disposable sensors, so their shorter life spans compared with the existing solutions also need to be considered. A general description of a SPE is shown in Fig. 1, where the critical elements are shown and explained. The aim is to have an SPE as a simple sensor element, free from front- and back-end signal processing which can be plugged into an existing device such as a smartphone, computer or an IoT device through an appropriate and possibly universal interface. The sensor element provides the raw signal, which can then be captured and processed either locally, or through cloud computing to analyse the presence of Benzenediols. In this work, modified SPE's, where the main working surface is coated with an electrocatalyst to improve the necessary electrochemical and sensing parameters have been investigated. The catalysts in question are Carbon-supported noble metals, such as platinum [22] and gold [23]. Pt is a well-known catalyst used in organic redox mechanisms, whereas Au is a much more novel catalyst. The carbon support provides high surface area [24], and high electrical conductance [25], enabling efficient use of expensive metallic catalytic nanoparticles. The detection of each individual isomer was possible by CV, and the selective identification of two or more isomers in the same solution was possible by DPV. The quantitative measurement was conducted by CA. A large concentration range of the analytes in acidic media was observed, ranging from close to saturation (3.9 M CC, 0.54 M HQ, 5 M RS) down to 1 µM for CC and HQ, and 100 nM for RS. Two different potentiostats, hereby referred to as Potentiostat 1 (Metrohm VIONIC) and Potentiostat 2 (PalmSens Emstat3 Blue) were used to verify the results and to check the repeatability of the measurements. The various factors contributing to the reaction mechanisms were noted and analysed, and SPE's were demonstrated as competent to detect benzenediol isomers selectively.

2. Results and discussion

2.1. Theoretical characterization

The structures of the three benzenediol isomers, CC, HQ, and RS are shown below in Fig. 2a. In order to understand the redox mechanisms of each isomer, the possibility of redox pairs [26] and polymerization [27] as seen in the equations below have to be considered.

$$C_6H_4(OH)_2 \leftrightarrow C_6H_4O_2 + 2H^+ + 2e^- \text{ (only for CC and HQ, reversible)} \quad (1)$$

$$n[C_6H_4(OH)_2] \rightarrow n\{C_6H_4O_2\} + n\,[2H^+ + 2e^-] \text{ (only for RS, irreversible)} \quad (2)$$

In the case of CC and HQ, redox pairs are possible [28], i.e., CC can be either or oxidized to 1,2-benzoquinone, and HQ to 1,4-benzoquinone (Eq. (1)). The reaction showing the oxidation of CC and HQ to their respective quinones can be seen in Fig. 2b. But RS does not have a corresponding stable redox quinone, as 1,3-benzoquinone is highly strained and non-planar. Thus, in the case of RS, the oxidation is a compounded polymerization [27] on the surface of the electrode. A consequence of the polymerization is the fouling of the working electrode due to the formation of a passivating film which leads to inactivation of the surface and subsequent loss of detection. [29] The mechanism due to which the oxidation occurs is also important. e.g., CC

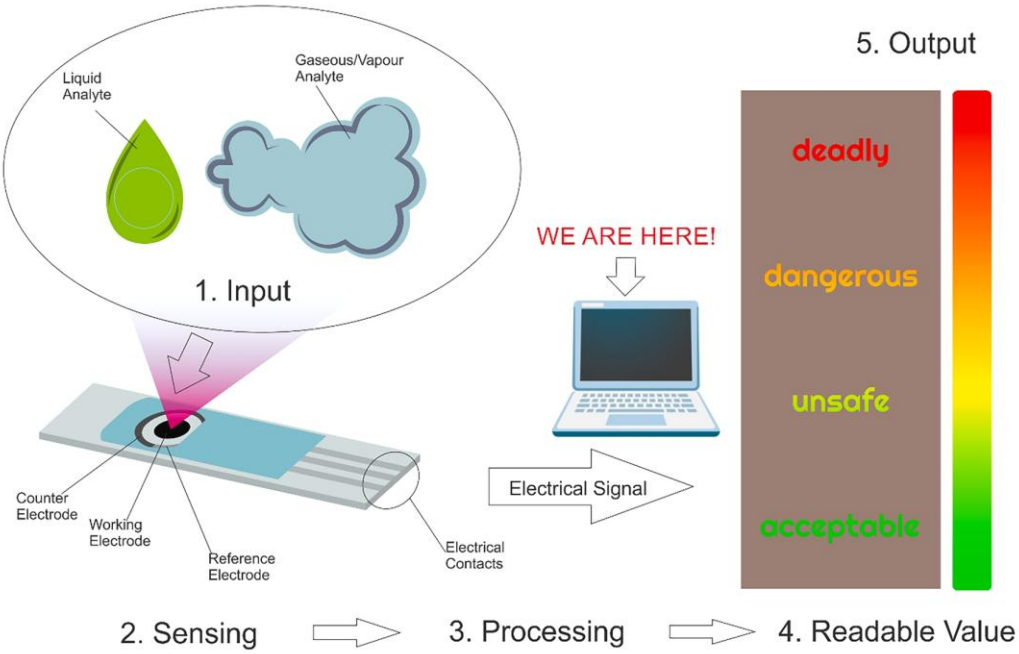


Fig. 1. Scheme of sensing volatile toxic organic compounds in air and water using modified screen-printed electrodes.

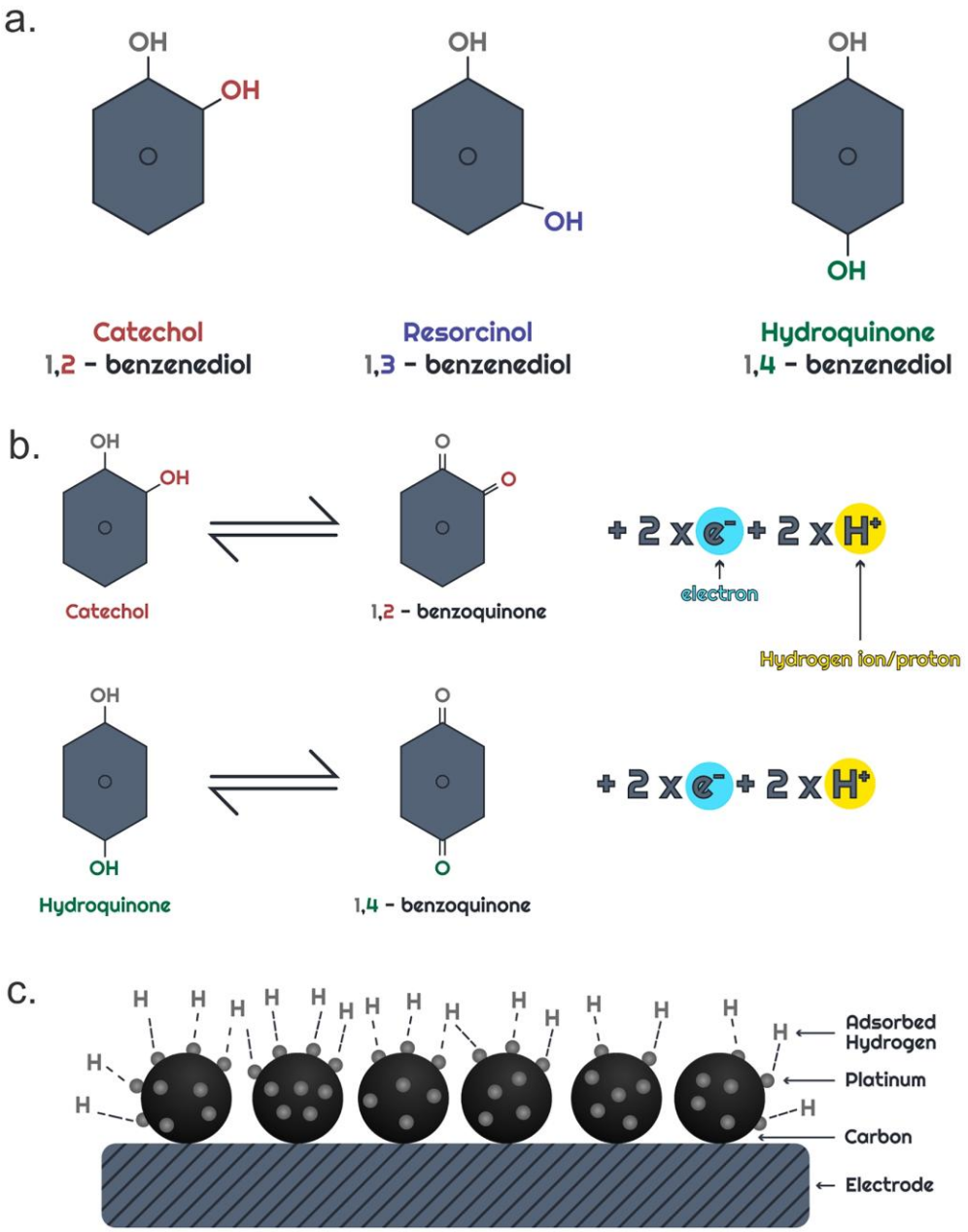


Fig. 2. a. Structures of catechol, resorcinol and hydroquinone b. Benzoquinone oxidation mechanisms of catechol and hydroquinone c. Overview of electrode surface modified with carbon-supported platinum catalyst.

and HQ are oxidized to their respective quinones, and in the process lose an electron and a proton (H^+). This electron transfer process relies on the conductivity of the material, i.e., the carbon support, and to an extent the metallic nanoparticles themselves. The high conductance of the working electrode surface due to the Vulcan XC-72R support should facilitate easier electron transfer, boosted further by the acidic media and therefore minimize any overpotentials. The metallic nanoparticles should act as sites for the electron transfer and catalysis. Pt nanoparticles adsorb hydrogen during the cathodic scan (negative current densities) and desorb hydrogen during the anodic scan (positive current densities), aiding the oxidation of organic molecules by weakening the hydrogen bonds and lowering the energy needed [30]. The catalysis mechanism of Au though is not as thoroughly understood as well as Pt's [31].

For the detection of benzenediols using Pt/C and Au/C, acidic media is chosen to enhance the conductance of the analyte and the activity of the metallic nanoparticles, and also to prevent the auto-oxidation of CC and HQ. While alkaline media facilitates better oxidation of organic compounds versus acidic media, it was observed that addition of CC and HQ to an alkaline solution almost instantly oxidizes them to their respective quinones, turning the clear solution brown for CC and yellowish-orange for HQ. This minimizes overpotentials and increases current densities, the nature of the analyte is no longer the same as the original after the addition of CC and or HQ to an alkaline solution, as the number of original analyte molecules is considerably altered even before

the start of the measurement. In contrast, the addition of an acid shifts the equilibrium of the oxidation in the opposite direction, resisting the auto oxidation of CC and or HQ until the application of a potential to the working electrode. Although this applied potential is higher in acidic media versus alkaline media, the end result is a much more accurate measurement of analyte molecules.

2.2. Surface characterization via SEM and TEM

In order to observe the surface morphology of C-based SPE working electrode and Pt/C modified working electrode the SEM was performed (Fig. 3). SEM images show non-modified C-based SPE electrode with C particles of sizes between 25 and 42 nm and Pt/C modified WE with C particles of sizes between 65 and 131 nm. TEM images show high magnification of the two different catalysts Pt/C and Au/C (Fig. 3), illustrating the variation in size between the two metallic nanoparticles. The size of Pt particles is between 2 and 3 nm and Au particles between 4 and 6 nm.

2.3. EDXS analysis of catalysts

To verify that the catalysts match the quoted specification of chemical composition by weight percentages, electron Energy Dispersive X-ray Spectroscopy (EDXS) was performed on the powders. The powders were applied to a double sided-conductive carbon tape, which was attached to a holder made of aluminium. Fig. 4 discusses the images and results obtained which shows the presence of the metallic nanoparticles over the carbon support. In order to minimize the errors due to specific points having a richer or lower presence of the metallic nanoparticles, 10 spectral points were chosen and the results averaged. Some deviation was observed due to the particles being considerably smaller than the carbon support particles, in addition to the carbon tape also contributing a larger portion of the backscatter due to the larger surface area. The curves shown in 4a and 4b show the sum of the spectra, wherein the software was autodetecting the presence of different elements. Figs. 4c and 4 d show the different points at which the spectra were measured. The autodetection picked up elements other than Pt, Au and C, most notably the presence of oxygen along with some stray signals causing the detection of S, Cl, Cu, and Al, but these elements were manually removed from the final analysis as there were no significant peaks observed and therefore concluded to be false positives.

Table 1 shows the quantitative measurement of the weight percentages of the two catalysts ignoring all the elements other than Pt, Au and C. The quoted weight percentage of 20 % metallic nanoparticles supported on carbon seemed to be roughly correct, accounting for variations detected at different measurement points. For Pt/C, the measurements showed an average of 23.03 % of metallic nanoparticles by weight, which is slightly higher than claimed, whereas for Au/C, the average was 14.8 %, considerably less than claimed. Considering the reasons for these variations, it could be due to the specific distribution of the particles over the given region of interest. Surface area could be another factor, given that Vulcan XC-72 and Vulcan XC-72R have high specific surface areas, contributing to a stronger backscatter signal compared to the metallic nanoparticles. One explanation for the higher than average presence of Pt could be due to the smaller particle sizes (between 2 and 3 nm), compared to Au (between 4 and 6 nm).

2.4. Detection of single Isomer

The detection of single isomer using Pt/C modified SPE's was done using CV. Figs. 5a, 5b and 5c show the cyclic voltammograms of CC, HQ and RS respectively at three different concentrations, 1 mM, 5 mM and 20 mM. For reference, a blank solution of 1 M HCl was used(black lines in all CV's). In the graphs, three distinct oxidation peaks for CC (e.g., +0.62 V vs ref at 20 mM shown in Fig. 5a), HQ (e.g., +0.52 V vs ref at 20 mM shown in Fig. 5b) and RS (e.g., +0.94 V vs ref at 20 mM shown in Fig. 5c) are seen. Also, distinct reduction peaks in the case of CC (e.g., +0.48 V vs ref at 20 mM shown in Fig. 5a) and HQ (e.g., +0.34 V vs ref at 20 mM shown in Fig. 5b) are observed, but not in the case of RS, which corroborates that the oxidation of CC and HQ is following the redox

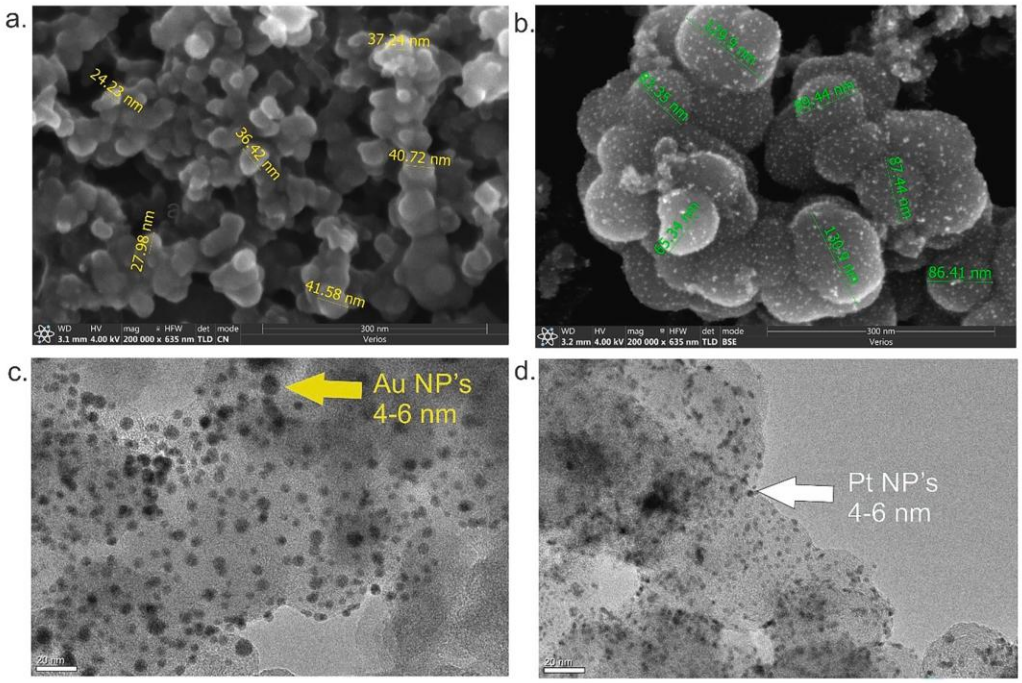


Fig. 3. Characterization of the catalytic materials and the SPE's a. SEM image of unmodified C-SPE, b. SEM image of C-SPE modified with Pt/C, c. Au nanoparticles (dark spots) on Vulcan XC-72, 20 % Au by mass d. Pt nanoparticles (dark spots) on Vulcan XC-72R, 20 % Pt by mass.

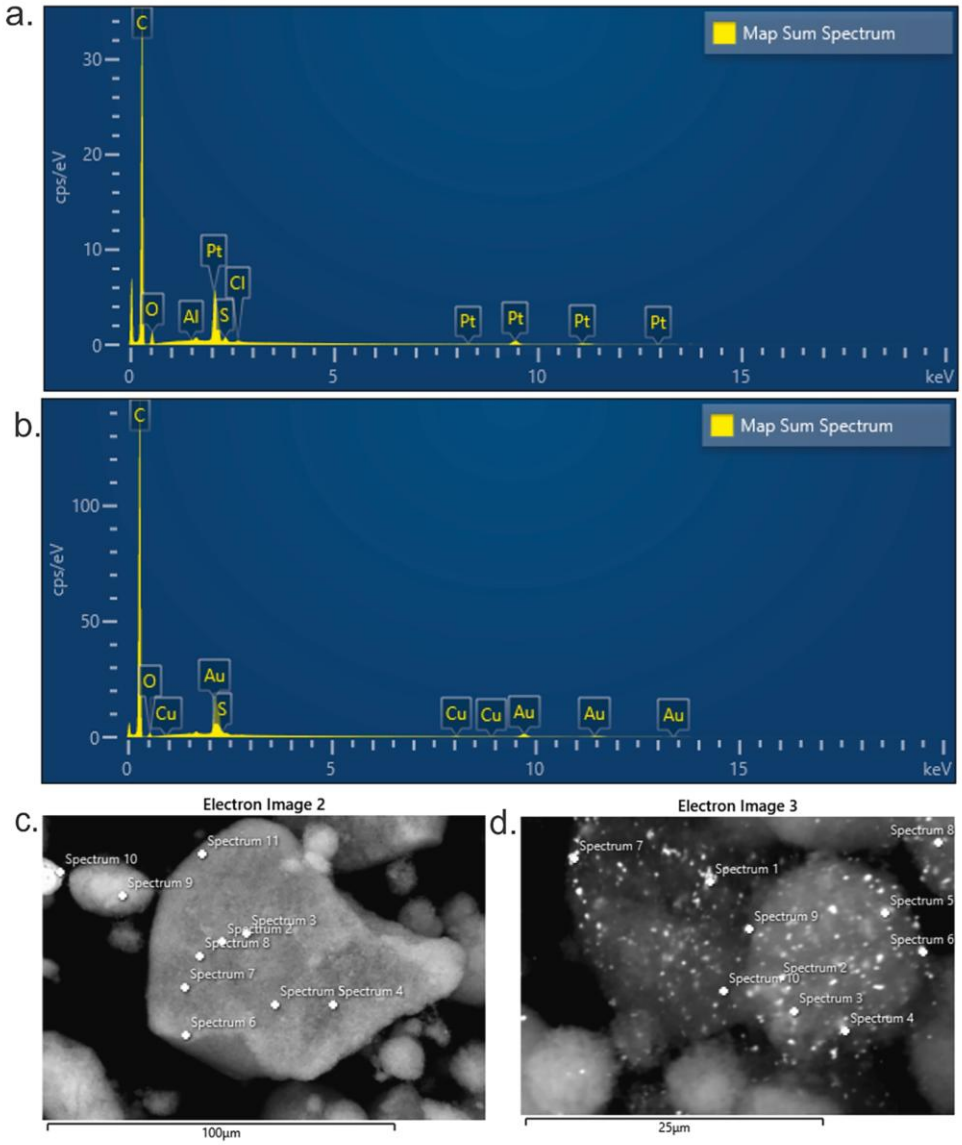


Fig. 4. a. sum spectrum of EDXS for Pt/C b. sum spectrum of EDXS for Au/C c. spectral points chosen for EDXS of Pt/C d. spectral points chosen for EDXS of Au/C.

Table 1
EDXS analysis of Pt/C and Au/C over 10 spectral points.

	Pt/C		Au/C	
Statistic	C	Pt	C	Au
Max	85.46	30.67	90.83	24.8
Min	69.33	14.54	75.2	9.17
Average	76.98	23.02	85.2	14.8
Standard Deviation	4.66	4.66	5.64	5.64

cycling from benzenediol to benzoquinone (Eq. (1)), whereas with RS it is a polymerizing one-way oxidation with no scope for reduction (Eq. (2)).

2.5. Detection of multiple isomers

In order to minimize the effect of charging and discharging of the electrolytic double layer, DPV is employed. Fig. 6a shows the differential pulse voltammogram using Pt/C modified SPE's of a solution containing CC, HQ and RS, each at 1 mM, and Figs. 6b, c and d show the voltammograms of varying concentrations of CC, HQ and RS, one at a time. Three distinct peaks, CC (e.g., +0.54 V vs Ag at 1 mM), HQ (e.g., +0.45 V vs Ag at 1 mM), and RS (e.g., +0.94 V vs ref at 1 mM) can be observed in Fig. 6a. Similar to the CV's, the potentials at which peak currents are observed also change with concentrations during DPV's, with lower concentrations producing peak currents at lower potentials due to the reduced charging and discharging. The increasing currents as a function of increasing concentrations demonstrate that the SPE's are successfully able to detect multiple isomers simultaneously.

2.6. Correlation between output current and concentration (Calibration curve)

The relationship between the output current and the concentration

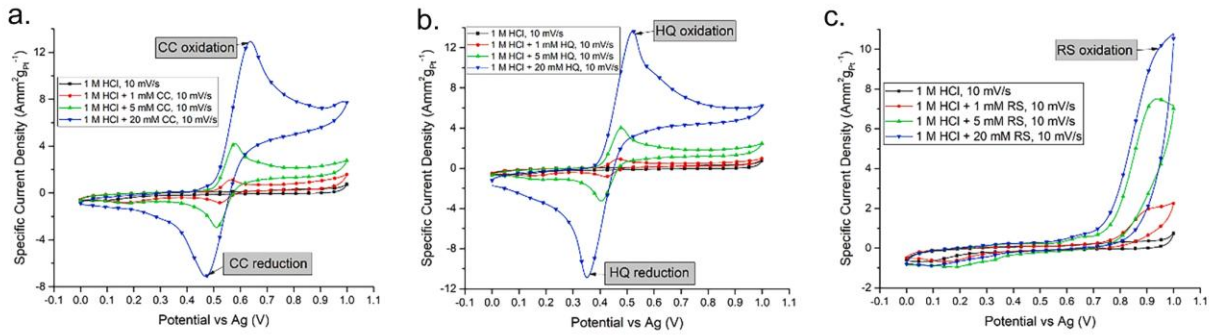


Fig. 5. CV's of benzenediols using Pt/C SPE's, cycle 2 of each measurement shown at scan rate 10 mVs^{-1} a. CV's of CC redox, b. CV's of HQ redox, c. CV's of RS oxidation.

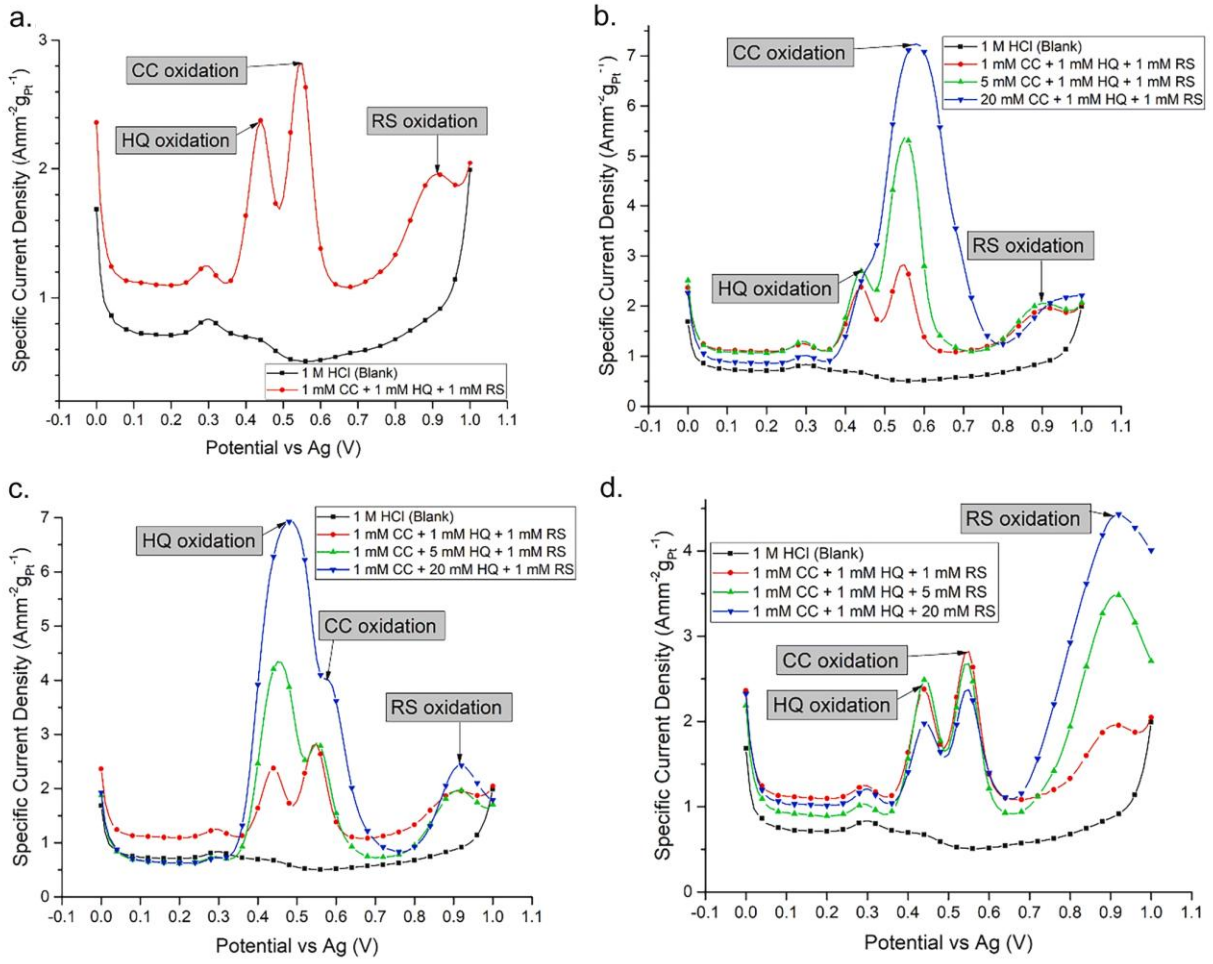


Fig. 6. DPV's of benzenediols using Pt/C SPE's a. DPV of solution containing 1 mM of all isomers, b. DPV of solution containing fixed concentration of HQ and RS but varying concentration of CC, c. DPV of solution containing fixed concentration of CC and RS but varying concentration of HQ, d. DPV of solution containing fixed concentration of HQ and CC but varying concentration of RS.

of the analyte should always be directly proportional, and ideally linear. However, this is rarely the case. For most devices, there exists a partial region of linear operation within a larger non-linear curve and electrochemical sensors are no exceptions. [32] To track the response of the sensor, different concentrations of all three analytes were checked and the output currents were plotted against concentration. The optimal way to observe these currents were to decrease the concentration until the lowest possible value, nearly indistinguishable from the baseline set by the blank solution was reached, or until the currents from two different concentrations are overlapping. The calibration curve was plotted using

values recorded from the CA's at different concentrations, for all analytes. CA was chosen as the method as it allows for two crucial advantages over voltammetric measurements, first one being that voltammetric measurements are unable to track changes in analyte concentration in real time since they rely on the measurement to reach the onset potential of the reaction until the current starts to rise, and the second one being the capacitive current being zero, since the potential is fixed. The equation for the capacitive current [33] is given by

$$i_C = C_{dl}\frac{dV}{dt} \tag{3}$$

Where, i_C = capacitive current (A), C_{dl} = double layer capacitance (F) and V = applied potential (V).

The potential is fixed for CA measurements, therefore $\frac{dV}{dt} = 0$ in Eq. (3) and consequently $i_C = 0$.

Figs. 7a, b and c show select CA curves as an illustration, where we plot current vs time for 60 s for different concentrations. At the start of the measurement, the currents spike momentarily, and slowly settle into a steady state, and at the end of 60 s, the final value is taken for the calibration curve.

The concentrations were stepped down in decades, starting from a saturated solution, until the concentration which would register a current that could be differentiated from a blank solution. For e.g., the following concentrations were recorded for CC (3.9 M, 1 M, 100 mM, 10 mM, 1 mM, 100 μM, 10 μM, 1 μM). Likewise, the range for HQ was 0.54 M to 1 μM, and for RS it was 5 M to 100 nM. The CA's were run at unique potentials for each analyte i.e., CC: +0.62 V; HQ: +0.52 V; RS: +0.94 V, all vs Ag reference. Three measurements were recorded for each concentration to account for variations. Figs. 8a, b and c show the calibration curve (current vs concentration), starting from μM range for HQ and CC, and nM for RS, rising up to molar range for all analytes.

Figs. 8d, e and f show the calibration curve over a smaller range (up to 1 mM) for all three analytes, to illustrate limiting the dynamic range of measurements to obtain pseudolinear behaviour of the system needed for simplification of analysis going forward. The curves in 8 a, b and c have to scaled logarithmically to accommodate such a large concentration range, and therefore make it difficult to assess a linear range of operation, and therefore the smaller ranges were measured where a curve could be fit with the form f(x) = ax+*b*, which is of the form of a straight line described by its slope and y-intercept.

Using the data from the linear range for all three analytes (100 μM-1 mM), the statistical limits of quantification (LoQ) and detection (LoD) can be obtained as shown in the following Table 2.

In order to calculate the LoD from the p-LoQ, which would make it a theoretical estimate once again we can divide the value by 3 assuming the 10σ to 3.3σ relation, we would end up with purely speculative "practical Limits of Detection (p-LoD)" of 0.33 μM for CC and HQ, and 33 nM for RS.

2.7. Au/C modified SPE's

As a way to compare the effectiveness of the Pt/C SPE's, similar measurements were attempted with Au/C SPE's. This way, if there are any effects that are either specific to the Pt nanoparticles or the C support, they can be isolated since the only differences arising should be due to the presence of Au nanoparticles.

Au has some critical differences versus Pt, the most obvious one being the tendency to oxidize at higher potentials as shown in Fig. 9a and b. 9 a shows the degradation of Au while running CV's in 1 M HCl, the peak current density decreased for every cycle due to the irreversible oxidation of Au to its oxide(s) (oxidation peak at > +0.8 V vs ref, reduction peak at +0.43 V vs ref) and thereby resulting in a loss of valuable active sites for catalysis. The peaks much more clearly seen in 9 b versus Pt, which in addition shows the peaks for the Hydrogen Evolution Reaction (HER) [34] and Oxygen Evolution Reaction (OER) [35] close to 0 V vs ref and 1 V vs ref respectively.

CV's were repeated using Au/C SPE's, and they were successfully able to qualitatively and quantitatively detect the presence of all benzenediol isomers as shown in Figs. 10a, b and c.

A few differences that are observed from the CV's is the presence of the Au oxidation peak in the blank 1 M HCl solution, and the changes in the delta between the oxidation and reduction peaks versus Pt/C SPE's. For CC, the oxidation peak at is +0.62 V vs ref at 20 mM, and the reduction peak at +0.43 V vs ref at 20 mM. So, while the oxidation peak is roughly the same as with Pt, the reduction peak is at a lower potential. In the case of HQ, the oxidation is at around +0.54 V vs ref at 20 mM, while the reduction peak is around +0.33 V vs ref at 20 mM. Once again, an increase is seen in the difference between the oxidation and peak potentials. RS shows a similar oxidation peak at +0.94 V vs ref but it is difficult to distinguish if this is due to oxidation of Au or RS. The same trend with the peaks moving towards higher potentials with increasing concentration during oxidation, and lower potentials with increasing concentration during reduction is seen.

DPV's were also repeated with Au/C SPE's and showed very similar results compared with Pt/C SPE's as seen in Figs. 11a, b, c and d. Distinct peaks are seen for each isomer at roughly the same potentials versus Pt/C, i.e., for CC, 0.55 V vs ref at 1 mM, for HQ, 0.44 V vs ref at 1 mM, and for RS, 0.92 V vs ref at 1 mM seen in Fig. 11a, as well as the increasing concentrations producing higher currents. The major difference is that the oxidation peak for Au cannot be ignored, which overlaps almost identically with the RS oxidation peak.

Due to the stability issues of Au with potentials over +0.8 V vs ref, CA's were not recorded for the Au/C modified SPE's

2.8. Interference with other electrochemically active compounds

To check the viability of the sensing element while in use in real samples, the possibility of interference with other electrochemically active compounds cannot be ignored. To check for interference, DPV

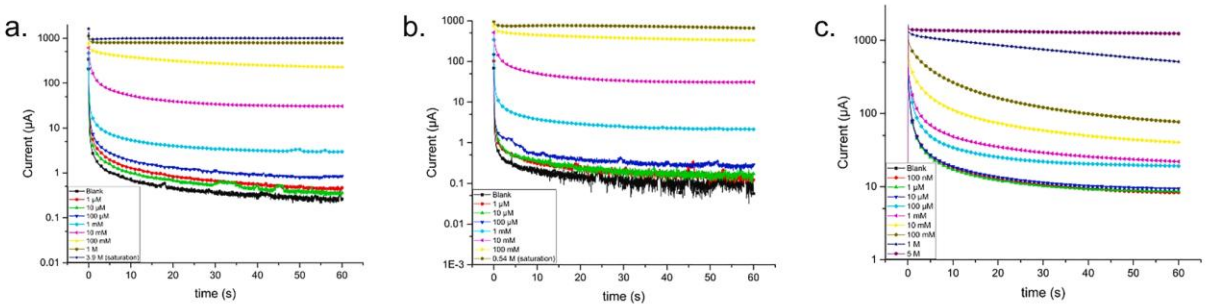


Fig. 7. CA's (single repetition shown for all concentrations) using Pt/C SPE's a. CA's of different CC concentrations (3.9 M to 1 μM), b. CA's of different HQ concentrations (0.54 M to 1 μM), c. CA's of different RS concentrations (5 M to 100 nM).

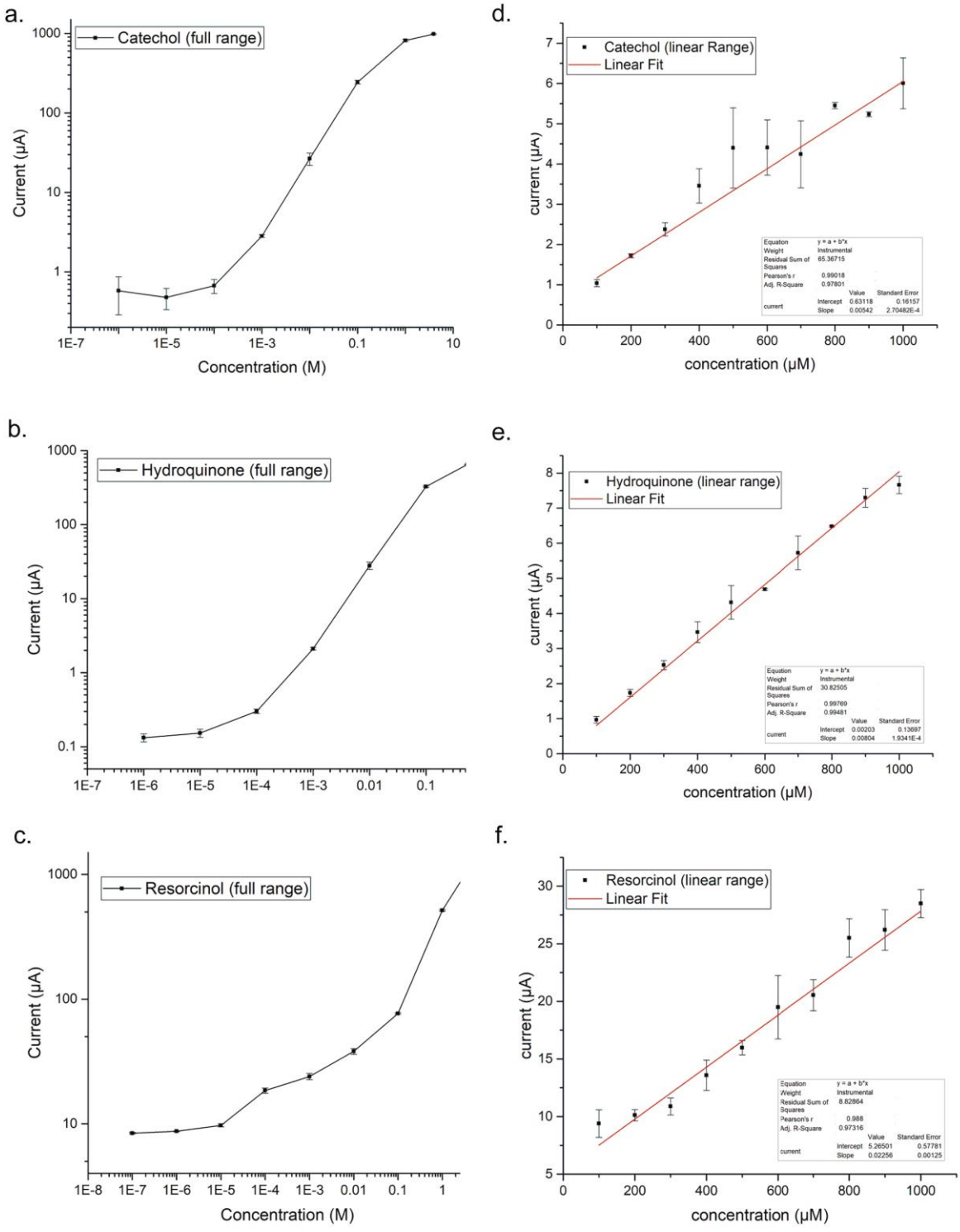


Fig. 8. CA's Calibration curves of benzenediols using Pt/C SPE's a. Calibration curve of CC full range with logarithmic scaling on both axes (3.9 M to 1 μM), b. Calibration curve of HQ full range with logarithmic scaling on both axes (0.54 M to 1 μM), c. Calibration curve of RS full range with logarithmic scaling on both axes (5 M to 100 nM), d. CC calibration curve linear region (0.1 mM to 1 mM), e. HQ calibration curve linear region (0.1 mM to 1 mM), f. RS calibration curve linear region (0.1 mM to 1 mM).

Table 2
Comparison of theoretical quantification and detection limits.

Analyte	Theoretical LoQ (10σ)	Theoretical LoD (3.3σ)
CC	26.4 μM	8.7 μM
HQ	41.7 μM	13.8 μM
RS	28.8 μM	9.5 μM

was performed with the following compounds using Pt/C modified SPE's as shown in Fig. 12. A baseline solution containing 1 mM CC + 1 mM HQ + 1 mM RS in 1 M HCl was used to establish positions where peak currents were recorded, and the following compounds: 10 mM ascorbic acid, 4 mM dihydrocaffeic acid, 0.5 mM acetaminophen, 1 mM benzisothiazolinone and 1 mM Bisphenol A were added to 1 M HCl individually and subjected to DPV under identical conditions as the baseline solution. The results are shown in Fig. 12 where ascorbic acid shows direct interference with HQ (+0.45 V vs Ag), dihydrocaffeic acid shows potential interference with both HQ and CC (+0.5 V vs Ag), acetaminophen showing interference due to one peak with both HQ and CC as well (+0.5 V vs Ag), with another peak (+0.75 V vs Ag) being clear of all the analytes. Both bisphenol A and benzisothiazolinone show possible interference with RS at (>+0.85 V vs Ag) but at these lower concentrations remain distinguishable.

2.9. Observations

The measurements obtained from the CV's and DPV's (both Pt/C and Au/C modified SPE's), and CA's (only Pt/C modified SPE's) confirm the assumptions made with the theoretical characterizations. In the case of the redox mechanisms of the CC and HQ, which were assumed to be reversible reactions, reflected in the presence of both oxidation and reduction peaks in the CV's. Whereas for RS since it was irreversible, this is observed due to the presence on only an oxidation peak with no reduction peak. For the issue of selectivity, each isomer has its own set of unique redox potentials, which can be exploited to detect a solution containing more than one isomer simultaneously using either CV, but preferably DPV to minimize the capacitive current component. Another effect of lowering the concentrations is that the DPV's produce less overlap, improving distinguishability between the three oxidation peaks, whereas higher concentrations tend to cause two peaks to blend, especially those of CC and HQ since they are separated by a smaller potential difference. Sensitivity is addressed through the CA's, where increases in the output current with increasing concentrations are seen. Although the calibration curves are not linear, the fact that the concentration varies over several degrees of magnitude of concentration makes it rather hard to evaluate a specific region of linear operation, which in this case would be quite small, but having such a large dynamic range is a possible trade-off for sacrificing linearity. The potentials selected for the CA's play a huge role in the final value of measured

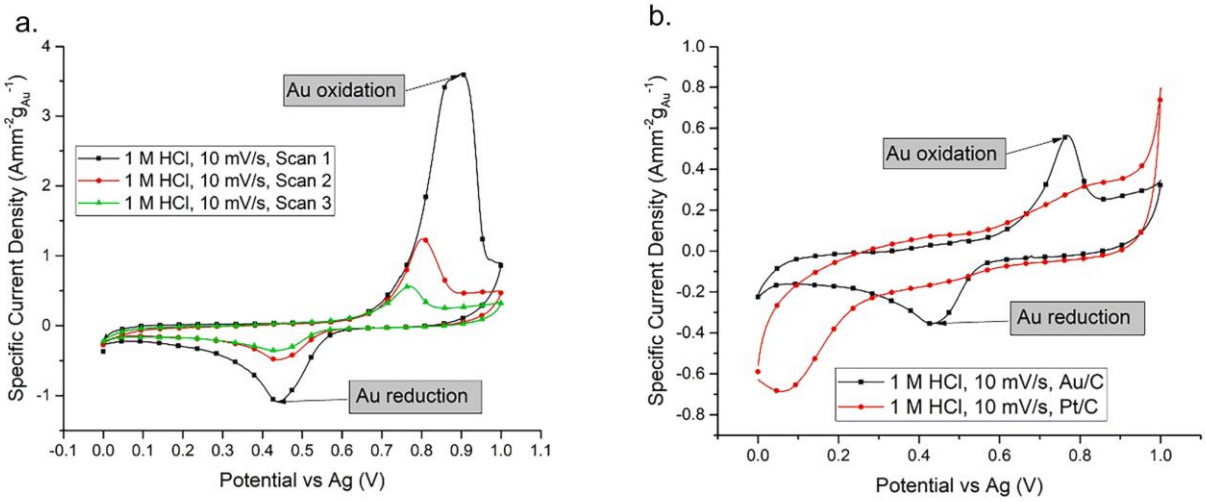


Fig. 9. Comparison of Au and Pt CV's in 1 M HCl at 10 mVs^{-1} a. Progressive degradation of Au due to oxidation during cycling b. Activity of Au vs Pt.

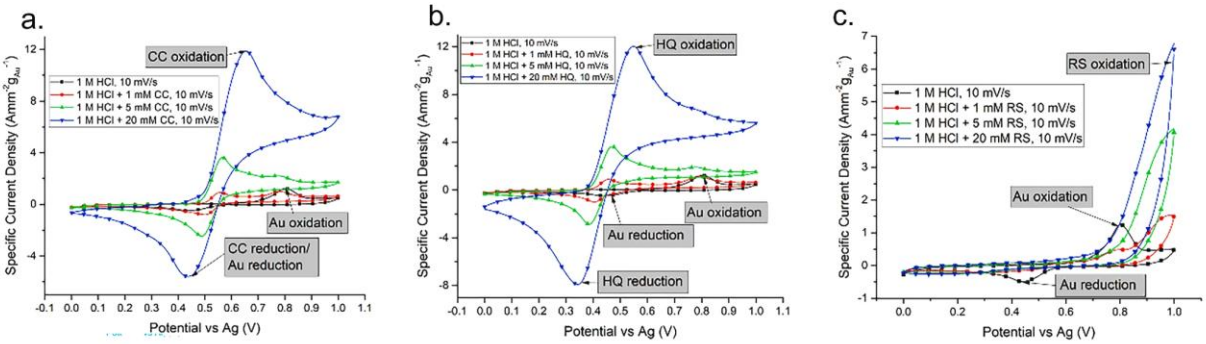


Fig. 10. CV's of benzenediols using Au/C SPE's, cycle 2 of each measurement shown at scan rate 10 mVs^{-1} a. CV's of CC redox, b. CV's of HQ redox, c. CV's of RS redox.

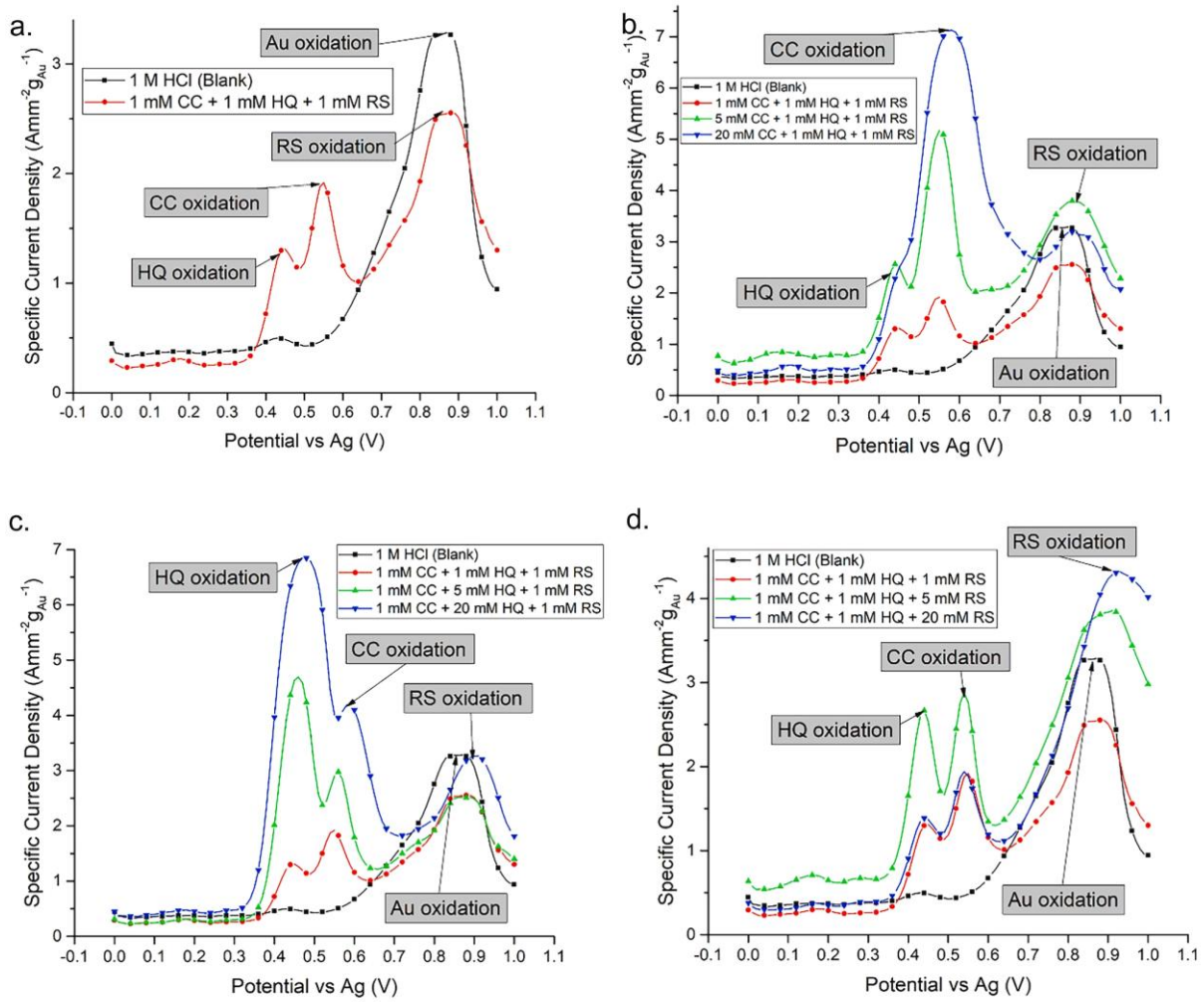


Fig. 11. DPV's of benzenediols using Au/C SPE's a. DPV of solution containing 1 mM of all isomers, b. DPV of solution containing fixed concentration of HQ and RS but varying concentration of CC, c. DPV of solution containing fixed concentration of CC and RS but varying concentration of HQ, d. DPV of solution containing fixed concentration of HQ and CC but varying concentration of RS.

currents, since the CV's indicate that the redox peaks are not the same for all the concentrations. As presented below in Table 3, Y Chen et al. [36] reported detection limits for the individual detection of HQ, CC and RS in the three-component system as 0.50, 0.85 and 0.67 μM using Pd-Au nanoflowers on graphene, respectively, while Ghanem M A et al. measured concentrations down to 0.05 mM for HQ, and 0.02 mM for CC using mesoporous Pt, while in the present work, using CA's we were able to measure concentrations down to 1 μM, 1 μM and 100 nM for the corresponding analytes. The potentiostat itself is capable of measuring lower currents, down to nanoamperes but the limit of quantification is realistically much higher due to external electromagnetic noise. Finally, coming to the catalysts being used, while both Pt and Au gave good results for the detection of all benzenediols, Pt was clearly the superior material in the end due to its higher stability in acidic media and lower overpotentials versus Au, which could not reliably detect RS analytes as the oxidation onset and peaks of Au and RS were almost identical.

3. Conclusion

Screen Printed Electrodes modified with carbon-supported platinum and gold catalysts were fabricated, with the aim of detecting the three benzenediols: catechol, resorcinol and hydroquinone. All the SPE's were fabricated to minimal tolerances to maintain consistency across all measurements. The SPE's were exposed to controlled quantities of the analytes by drop casting, and a series of electrochemical techniques such as cyclic voltammetry, differential pulse voltammetry and chronoamperometry were run. The CV's showed that the both the Pt/C and Au/C modified SPE's could detect the presence of all three benzenediols in acidic media, each producing an oxidation peak at a unique potential. The DPV's showed that all three isomers could be simultaneously detected using the modified SPE's selectively in acidic media, once again, each isomer having a distinct oxidation peak. The ranges of detection of the Pt/C-modified SPE's for all isomers were checked by CA's, which varied starting from saturation (molar) going down to the limit of detection (micromolar for CC and HQ, nanomolar for RS), accounting for background electromagnetic interference, TEM images showed that the commercial catalysts were to specification, with Pt particles being 2–3 nm on average, while the Au particles were 4–6 nm in comparison. The differences between the Pt/C and Au/C catalysts were also documented, with Pt being the superior choice, demonstrating good performance for the detection of all isomers, while Au showed good performance for the detection of CC and HQ, and encountering

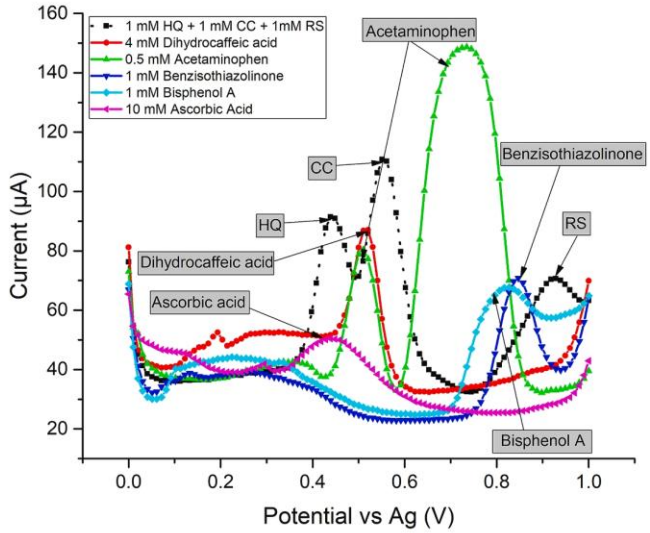


Fig. 12. Electrochemical interference in the detection of CC, HQ and RS due to the following electrochemically active compounds: ascorbic acid, dihydrocaffeic acid, acetaminophen, benzisothiazolinone and bisphenol A in 1 M HCl.

Table 3
Comparison of quantification and detection limits with literature.

Quantification Limits	CC	HQ	RS
Ghanem M A et al. [28]	0.02 mM	0.05 mM	–
Y Chen et al. [36]	2.5 μM (0.85 μM LoD)	1.6 μM (0.5 μM LoD)	2 μM (0.67 μM LoD)
This work*	*1 μM (0.33 μM p-LoD)*	*1 μM (0.33 μM p-LoD)*	*100 nM (33 nM p-LOD)*

problems with stability during RS detection. All measurements were repeated to ensure consistency and reproducibility, and to avoid or minimize the effects of random occurrences or disturbances. In summary, the successful detection of all the isomers while trying to meet the initial set criteria of selectivity, sensitivity, repeatability, large dynamic range, low detection limits was achieved. The overall system shows potential to be practically applied as a sensing platform for benzenediols.

4. Experimental section

Preparation of Catalyst Ink: Catalyst inks were created by adding 1 mg of 20 % by weight Platinum (2–3 nm particles) on Vulcan XC-72R support, or 20 % by weight Gold (4–6 nm particles) on Vulcan XC-72 (both catalysts purchased from FuelCellStore) to 0.995 ml of absolute ethanol. 5 μl of 5 % Nafion in ethanol solution (Sigma Aldrich) was added to the ink as a binder, and the ink was stirred with a 500 W ultrasonic probe at 25 % maximum amplitude for 2 min to obtain an evenly dispersed suspension. The ink was then used immediately for the creation of sensor elements to avoid the settling and agglomeration of particles.

Preparation of Sensor Element: Sensor elements were created using Metrohm DropSens DS150 SPE's (Working: C, Counter: Pt, Reference: Ag). The working electrode (WE) surface was cleaned with DI water, then ethanol and dried by placing on a hot surface maintained at 55 °C. 10 μl of catalyst ink (either Pt or Au) was carefully pipetted onto the working electrode while on the hot surface to expedite drying time. The ink was dropped giving adequate time to dry and making sure to avoid the counter and reference electrodes. The sensor elements were then stored in a dry, sealed container to avoid tarnishing of the silver contacts and reference electrode. 10 μl of the ink contains 10 μg of catalyst (1 mg/ml), of which 20 % is either Pt or Au, so in theory each sensor element has a metal loading of 2 μg. Given the working electrode has a diameter of 4 mm (surface area 12.56 mm^2), each sensor element should have about 159.23 ng of Pt or Au every mm^2 of the working electrode.

Preparation of Analyte: Various concentrations of the analytes were prepared by using a solution of known concentration of each, by dilution. All benzenediols (CC, HQ and RS) were purchased from Sigma Aldrich at analytical grade purity (> 99 %), and a stock solution (3.9 M CC, 0.54 M HQ, 5 M RS) of each was created by addition of 1 M HCl (created from 37 % HCl by dilution) and stirring in an ultrasonic bath, and lower concentrations were achieved by further dilution, pipetting calculated amounts of stock CC, HQ and RS solutions and addition of varying amounts of 1 M HCl to reach required values for all measurements. To ensure, consistency, 75 μl of analyte was dropped onto the surface of the SPE, adequate to cover all three electrodes for all measurements.

Instruments: CV's were measured using a Metrohm VIONIC (Potentiostat 1), on loan from Primalab d.o.o.; Parameters for CV: Scan Window: 0 V to 1 V, Scan Rates: 10 mVs^{-1}, 25 mVs^{-1}, 50 mVs^{-1}, 100 mVs^{-1}, Number of Scans: 3, Potential Step Size: approximately 1 mV (digital). All CA and DPV measurements were carried out using a PalmSens EmStat3 Blue (Potentiostat 2); Parameters for CA: $E_{CC} = +0.62$ V, $E_{HQ} = +0.52$ V, $E_{RS} = +0.94$ V, run time = 60 s, sampling time = 10 ms. Parameters for DPV: Scan Window: 0 V to 1 V, Potential Step Size: 10 mV, Pulse Magnitude: 30 mV, Pulse Duration: 50 ms, Scan Rate: 10 mVs^{-1}. All mentioned potentials are against a silver reference electrode. All electrochemical measurements were conducted in a climate-controlled laboratory setup at STP.

Characterization: Unmodified C-based WC of SPE and Pt/C modified WE of SPE were investigated using Scanning Electron Microscopy (SEM). Samples for SEM were embedded on sample holders using conductive carbon adhesive tape and observed in a field-emission gun scanning electron microscope (FEG-SEM Verios G4 HP, Thermo Fisher Scientific, USA). Preliminary examination of the samples showed that they were sufficiently electrically conductive for SEM analysis. The experimental conditions for imaging were set to an accelerating voltage of 4 kV, a beam current between 20 pA and 50 pA and a working distance of 3 mm. The electron micrographs were recorded using through-the-lens detector (TLD) for secondary electrons (SE) and backscattered electrons (BSE). To observe the Pt/C and Au/C NPs structure and size,

transmission electron microscopy (TEM) with energy-dispersive X-ray spectroscopy (EDS) was used (JEOL JEM-2100, Jeol Ltd., Tokyo, Japan). The samples for TEM observations were prepared by dispersing the nanoparticles after ultrasonic deagglomeration in water onto lacey carbon coated Cu grids. EDXS was performed separately using a Thermo Fisher Quanta 650 ESEM utilizing a Tungsten Filament, acceleration voltage 20 kV, observed beam current of 100 μA, at a working distance of 10 mm using CBS detector.

CRediT authorship contribution statement

Abhilash Krishnamurthy: Conceptualization, Data curation, Methodology, Validation, Writing – original draft, Writing – review & editing. **Zoran Samardžija:** Data curation, Formal analysis, Investigation, Resources, Validation, Visualization, Writing – original draft, Writing – review & editing. **Špela Trafela:** Validation, Writing – review & editing. **Anja Korent:** Validation, Writing – review & editing. **Sašo Šturm:** Funding acquisition, Project administration. **Kristina Žagar Soderžnik:** Conceptualization, Data curation, Formal analysis, Funding acquisition, Investigation, Methodology, Project administration, Resources, Supervision, Validation, Visualization, Writing – original draft, Writing – review & editing.

Declaration of competing interest

The authors declare that they have no known competing financial interests or personal relationships that could have appeared to influence the work reported in this paper.

Data availability

Data will be made available on request.

Acknowledgements

This research work was made possible due the Slovenian Research Agency (ARRS), grants P2–0084 (Program Nanostructured Materials), J2–1739 (High Performance Nanostructured Acrylamide Sensors), PR-09874 (Young Researcher Project). Special thanks to Primalab d.o.o. for the Metrohm VIONIC, and to Pika Štefančič for assistance with the graphics. Special thanks to Nikhil Bhootpur for assistance with the EDXS measurement.

References

[1] T. Harvey, K.R. Mahaffey, S. Velazquez, M. Dourson, Holistic risk assessment: an emerging process for environmental decisions, Regul. Toxicol. Pharm. 22 (2) (1995) 110–117.
[2] N. Singh, S.C. Davar, Noise pollution-sources, effects and control, J. Human Ecol. 16 (3) (2004) 181–187.
[3] F.D. Owa, Water pollution: sources, effects, control and management, Mediterr J. Soc. Sci. 4 (8) (2013) 65.
[4] Heinsohn, R.J., & Kabel, R.L. (1998). Sources and control of air pollution: engineering principles.
[5] J. Lelieveld, J.S. Evans, M. Fnais, D. Giannadaki, A. Pozzer, The contribution of outdoor air pollution sources to premature mortality on a global scale, Nature 525 (7569) (2015) 367–371.
[6] J. Zhang, K.R. Smith, Indoor air pollution: a global health concern, Br. Med. Bull. 68 (1) (2003) 209–225.
[7] S.K. Brown, M.R. Sim, M.J. Abramson, C.N. Gray, Concentrations of volatile organic compounds in indoor air–a review, Indoor Air 4 (2) (1994) 123–134.
[8] C.A. Redlich, J. Sparer, M.R. Cullen, Sick-building syndrome, Lancet North Am. Ed. 349 (9057) (1997) 1013–1016.
[9] N. Nematollahi, A. Doronila, P.J. Mornane, A. Duan, S.D. Kolev, A. Steinemann, Volatile chemical emissions from fragranced baby products, Air Quality, Atmos. Health 11 (7) (2018) 785–790.
[10] J. Angerer, G. Scherer, K.H. Schaller, J. Müller, The determination of benzene in human blood as an indicator of environmental exposure to volatile aromatic compounds, Fresenius J. Anal. Chem. 339 (10) (1991) 740–742.
[11] Hudson, Naomi L. "NIOSH skin notation (SK) profiles: catechol." (2019).
[12] E. Harel, A.M. Mayer, Y. Shain, Catechol oxidases, endogenous substrates and browning in developing apples, J. Sci. Food Agric. 17 (9) (1966) 389–392.
[13] Z.D. Draelos, Skin lightening preparations and the hydroquinone controversy, Dermatol. Ther. 20 (5) (2007) 308–313.
[14] J. Boer, G.B.E. Jemec, Resorcinol peels as a possible self-treatment of painful nodules in hidradenitis suppurativa, Clin. Exp. Dermatol. 35 (1) (2010) 36–40.
[15] F.I. Khan, A.K. Ghoshal, Removal of volatile organic compounds from polluted air, J. Loss Prev. Process Ind. 13 (6) (2000) 527–545.
[16] W. Lindinger, A. Jordan, Proton-transfer-reaction mass spectrometry (PTR–MS): on-line monitoring of volatile organic compounds at pptv levels, Chem. Soc. Rev. 27 (5) (1998) 347–375.
[17] G. Ycas, F.R. Giorgetta, K.C. Cossel, E.M. Waxman, E. Baumann, N.R. Newbury, I. Coddington, Mid-infrared dual-comb spectroscopy of volatile organic compounds across long open-air paths, Optica 6 (2) (2019) 165–168.
[18] G.G. Pandit, P.K. Srivastava, A.M. Rao, Monitoring of indoor volatile organic compounds and polycyclic aromatic hydrocarbons arising from kerosene cooking fuel, Sci. Total Environ. 279 (1–3) (2001) 159–165.
[19] B. Szulczyński, J. Gębicki, Currently commercially available chemical sensors employed for detection of volatile organic compounds in outdoor and indoor air, Environments 4 (1) (2017) 21.
[20] C. Elosua, I.R. Matias, C. Bariain, F.J. Arregui, Volatile organic compound optical fiber sensors: a review, Sensors 6 (11) (2006) 1440–1465.
[21] A. Hayat, J.L. Marty, Disposable screen printed electrochemical sensors: tools for environmental monitoring, Sensors 14 (6) (2014) 10432–10453.
[22] A. Schwartz, L.L. Holbrook, H. Wise, Catalytic oxidation studies with platinum and palladium, J. Catal. 21 (2) (1971) 199–207.
[23] A. Luengnaruemitchai, S. Osuwan, E. Gulari, Selective catalytic oxidation of CO in the presence of H2 over gold catalyst, Int. J. Hydrogen Energy 29 (4) (2004) 429–435.
[24] C.W.B. Bezerra, L. Zhang, H. Liu, K. Lee, A.L.B. Marques, E.P. Marques, et al., A review of heat-treatment effects on activity and stability of PEM fuel cell catalysts for oxygen reduction reaction, J. Power Sources 173 (2007) 891–908.
[25] S. Tang, G. Sun, J. Qi, S. Sun, J. Guo, Q. Xin, et al., Review of new carbon materials as catalyst supports in direct alcohol fuel cells, Chin. J. Catal. 31 (2010) 12–17.
[26] S.C. Chien, H.L. Chen, M.C. Wang, K. Seshaiah, Oxidative degradation and associated mineralization of catechol, hydroquinone and resorcinol catalyzed by birnessite, Chemosphere 74 (8) (2009) 1125–1133.
[27] K. Ngamchuea, B. Tharat, P. Hirunsit, S. Suthirakun, Electrochemical oxidation of resorcinol: mechanistic insights from experimental and computational studies, RSC Adv. 10 (47) (2020) 28454–28463.
[28] M.A. Ghanem, Electrocatalytic activity and simultaneous determination of catechol and hydroquinone at mesoporous platinum electrode, Electrochem. Commun. 9 (10) (2007) 2501–2506.
[29] V. Ball, M.L. Alfieri, K. Ziegler, Y. Arntz, M. d'Ischia, Structure-controlled electrodeposition and electrochemical behavior of films from isomeric diphenols at the solid-liquid interface, Surf. Interfaces 30 (2022) 101841.
[30] K. Yamamoto, D.M. Kolb, R. Kötz, G. Lehmpfuhl, Hydrogen adsorption and oxide formation on platinum single crystal electrodes, J. Electroanal. Chem. Interfacial Electrochem. 96 (2) (1979) 233–239.
[31] L.D. Burke, P.F. Nugent, The electrochemistry of gold: II the electrocatalytic behaviour of the metal in aqueous media, Gold Bull. 31 (2) (1998) 39–50.
[32] E. Desimoni, B. Brunetti, Presenting analytical performances of electrochemical sensors. Some suggestions, Electroanalysis 25 (7) (2013) 1645–1651.
[33] S. Westerlund, L. Ekstam, Capacitor theory, IEEE Trans. Dielectr. Electr. Insul. 1 (5) (1994) 826–839.
[34] S. Fang, X. Zhu, X. Liu, J. Gu, W. Liu, D. Wang, T. Yao, Uncovering near-free platinum single-atom dynamics during electrochemical hydrogen evolution reaction, Nature Comm. 11 (1) (2020) 1–8.
[35] J.O.M. Bockris, A.K.M. Shamshul Huq, The mechanism of the electrolytic evolution of oxygen on platinum, Proc. R. Soc. London. Series A. Math. Phys. Sci. 237 (1209) (1956) 277–296.
[36] Y. Chen, X. Liu, S. Zhang, L. Yang, M. Liu, Y. Zhang, S. Yao, Ultrasensitive and simultaneous detection of hydroquinone, catechol and resorcinol based on the electrochemical co-reduction prepared Au-Pd nanoflower/reduced graphene oxide nanocomposite, Electrochim. Acta 231 (2017) 677–685.

Abhilash Krishnamurthy is a young researcher enrolled as a PhD student since November 2019 at the Jožef Stefan International Postgraduate School, Ljubljana, Slovenia, and employed at the Department for Nanostructured Materials at The Jožef Stefan Institute, Ljubljana, Slovenia. He obtained his Masters at the Karlsruhe University ssof Applied Sciences at the Faculty of Electrical Engineering and Information Technology in the program Sensor Systems Technology in 2017. His focal areas are electrochemical systems, their theoretical and practical characterization, in particular electrochemical sensors.

Dr. Zoran Samardžija is a University graduate physicist, doctor of science (PhD) in the field of material science. Senior scientist and specialist adviser at the Department for nanostructured materials, Jožef Stefan Institute, Ljubljana, Slovenia. Research expertise in the field of materials characterization, electron probe microanalysis and advanced quantitative methods (EDS, WDS), scanning electron microscopy (SEM, FEGSEM), electron backscatter diffraction (EBSD), atomic force microscopy (AFM). Published 100 scientific articles.

Špela Trafela is a postdoctoral researcher at the Department for Nanostructured Materials at Jožef Stefan Institute. She obtained PhD degree in 2020 in the field of Nanoscience and Nanotechnologies at Jožef Stefan International Postgraduate School. Her main research

expertise is the chemical or electrochemical synthesis of nanostructured materials based on conductive polymers or metals. Currently, she is involved in the research and development of electrochemical sensors for the detection of toxic organic compounds and biosensors for the detection of viruses.

Dr. Anja Korent finished her PhD in 2022 at Jožef Stefan Postgraduate school, Slovenia, employed as an ARRS young researcher (program PR08337) at the Department for Nanostructured Materials at Jožef Stefan Institute. Her work included electrochemical detection of toxic organic compounds, electrochemically synthesized polyaniline, and its usage for sensing applications. Currently, she is working in the industry as an expert associate on dangerous substances, dangerous goods, and their transportation

Prof. Dr. Sašo Šturm (male), senior scientist, associate professor, head of the Department for Nanostructured Materials, the leader of the National Research Programme "Nanostructured Materials" (10FTE/year) and co-director of the International Associated Laboratory between CNRS (France) and JSI (Slovenia), is a world leader researcher in the field of advanced electron microscopy, combining material science processing and technology with the development and implementation of state-of-the-art scanning and transmission electron microscopy techniques for materials research, with core expertise focused on atomic resolution scanning transmission electron microscopy imaging, electron energy loss spectroscopy and modeling of buried interfaces in functional materials for sensor application, including in-situ electron microscopy combined with *in-situ* electrochemistry.

Kristina Žagar Soderžnik is a research fellow at the Department for Nanostructured Materials at Jožef Stefan Institute. She obtained PhD degree in 2011 in field of Nanoscience and Nanotechnologies of Jožef Stefan International Postgraduate School. In 2014 she was a postdoc at Vienna University of Technology in Austria and at Ernst Ruska-Centre (ER-C) for Microscopy and Spectroscopy with Electrons in Jülich, Germany. Her main research expertise are synthesis and characterisation of metal oxide nanomaterials processed via template-assisted electrophoretic deposition (EPD), electrochemical deposition (ED), electrochemical oxidation of nanoporous templates and hydrothermal synthesis. Currently, she is involved in research and development of electrochemical and resistivity sensors for detection of toxic organic compounds.

4.2 Analysis of Real-World Samples

This section provides a limited real-sample extension of the materials and electrochemical results presented in Section 4.1, demonstrating their applicability in chemically complex matrices.

To evaluate the applicability of the sensor beyond controlled laboratory conditions, selected real-world samples were tested for the presence of benzenediol isomers. While detection in standardised solutions with known concentrations is relatively straightforward, real consumer products present more complex chemical matrices that may interfere with signal clarity, analyte availability, or electrode performance. Three commercially available products containing benzenediol isomers were selected. Lookbrite cream, manufactured by Glenmark Pharmaceuticals Ltd., contains 2 % hydroquinone along with tretinoin (0.025 %) and mometasone furoate (0.1 %). Solu-Resorcinol hair lotion, produced by Pasteur Laboratories Pvt. Ltd., contains 4 % resorcinol and includes additional components such as mercuric chloride and cantharidin. For catechol, Mountain Herbal Tea (1001 Cvet, Nanoški Tip Čaja) was used as a natural sample, where CC is expected to form as a result of catechin degradation through pyrolysis. Although the exact concentration of CC or catechin is not listed on the product, literature confirms the presence of catechol in tea extracts (Lin, Sensitive and rapid determination of catechol in tea samples using mesoporous Al-doped silica modified electrode., 2009), which can be used to support its identification. Each sample was dispersed or dissolved in deionised water and acidified with 1 M HCl to ensure a stable electrochemical environment and to align redox peak potentials with those established in reference standards. The prepared samples were then analysed using differential pulse voltammetry. In all three cases, current responses consistent with the respective isomers were observed and matched reference signals with respect to the current peak positions, demonstrating the sensor's ability to function effectively within chemically diverse matrices.

The results are presented in Figure 4.2, confirming successful detection and distinguishing of CC, RS and HQ in commercially available formulations.

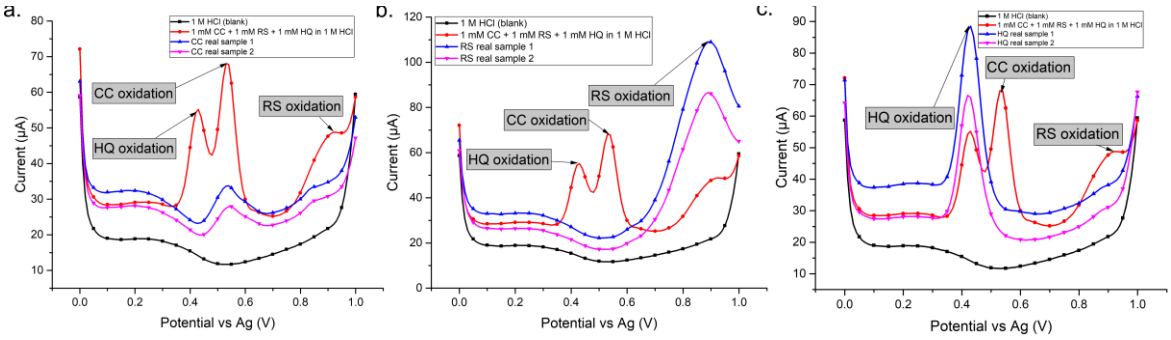


Figure 4.2: Voltammograms showing detection of benzenediol isomers in real samples: a. CC in tea, b. RS in anti-dandruff solution, c. HQ in acne cream.

Strong peak currents were observed for RS and HQ in Figures 4.1b and 4.1c, consistent with the high analyte concentrations present in prescription-only pharmaceutical products. In both cases, the peak currents exceeded those measured for 1 mM reference solutions of the respective isomers. In contrast, the herbal tea sample exhibited distinguishable peaks corresponding to two different concentrations of either catechol (CC) or catechin, which share identical redox characteristics. The sample was prepared by boiling a teabag in 1 M HCl for one hour at 100 °C to minimize water content and concentrate the catechol and the (catechin) precursor. However, the measured peak currents for the

CC-containing tea samples were noticeably lower than those recorded for a 1 mM CC reference in acid, indicating the presence of CC or catechin in the tea, albeit at a relatively low concentration. It is also critical to note that 100 °C is not sufficient to meaningfully pyrolyse catechin into catechol, more so within an aqueous solution. Voltammograms obtained from these samples therefore displayed clear, distinct responses for all three analytes in the expected potential ranges, confirming the sensor's ability to detect target compounds even in chemically complex formulations.

4.3 Sensor Characterisation via EIS

This section focuses on the electrode-level layer of the sensing workflow, where interfacial condition and drift determine the stability of the electrochemical response during repeated operation.

EIS was used in this study not merely as a post-characterisation tool, but as an embedded diagnostic method for monitoring sensor drift and degradation *in situ*. The approach involved periodic EIS measurements on both unmodified and Pt/C-modified DS150 SPEs, conducted before and after repeated CV cycling in various benzenediol-containing environments (CC, RS and HQ), as well as in a blank 1 M HCl solution.

EIS spectra were fitted using a modified Randles' circuit that included solution resistance (R_S), polarisation resistance (R_P), and a constant phase element (CPE) to model non-ideal capacitive behaviour. From these fits, the effective capacitance (C_{eff}) was derived. These parameters served as diagnostic indicators to track changes in electrochemical performance during extended operation. The simplified model excluded diffusion-related components to prioritise mechanistic interpretability.

Unmodified SPEs showed a progressive decrease in R_P and an increase in C_{eff} with increasing CV cycles, indicative of surface activation likely driven by electrochemical cleaning and improved electron transfer kinetics. In contrast, Pt/C-modified SPEs exhibited initial improvement (higher C_{eff}, lower R_P), followed by signs of degradation beyond five CV cycles. This trend suggests catalyst deterioration due to nanoparticle agglomeration, dissolution, or support oxidation, particularly under acidic conditions.

Quantitative analysis revealed that R_P in unmodified electrodes dropped by more than 80% after ten CV cycles, while C_{eff} more than tripled, indicating substantial performance enhancement. Pt/C-modified SPEs displayed a more complex pattern: R_P increased and C_{eff} peaked at five cycles before declining, supporting the hypothesis of transient enhancement followed by degradation.

These EIS-derived metrics were cross-validated by CV data, which showed matching trends in net charge transfer (Q_n), redox reversibility, and peak separation. Principal component analysis (PCA) of R_P, C_{eff}, and Q_n confirmed distinct diagnostic trajectories for each sensor type, with unmodified electrodes showing smooth progression and Pt/C-modified electrodes displaying scattered, non-monotonic behaviour.

The integration of EIS into the sensor workflow offers a powerful, non-destructive method for real-time performance monitoring. It enables early detection of degradation and distinguishes between resistive losses and capacitive changes. Unlike destructive techniques such as SEM, SERS or even electrochemical techniques, this impedance-based framework provides continuous diagnostics during operation and has strong potential for adaptation in embedded or IoT-enabled sensor systems. Figure 4.3 shows the graphical abstract from the associated publication, outlining the impedance-based diagnostic workflow used to monitor electrode stability and degradation. It illustrates how periodic EIS measurements and equivalent circuit modelling provide insight into sensor performance over time.

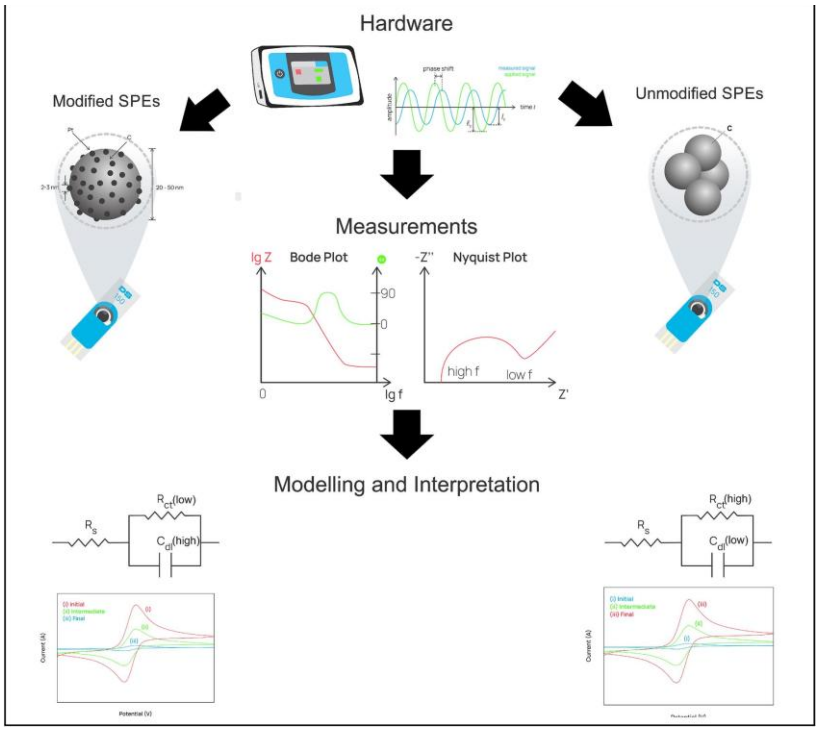


Figure 4.3: Graphical abstract of the EIS diagnostic workflow. Adapted from Krishnamurthy et al., Sensing and Bio-Sensing Research 50 (2025) 100871, shared under CC BY-NC-ND 4.0 licensing.

Full methodology and data are published in: Krishnamurthy et al., Sensing and Bio-Sensing Research, 50 (2025) 100871 https://doi.org/10.1016/j.sbsr.2025.100871. The print version is shared in the following pages under the CC BY-NC-ND 4.0 license agreement.

Sensing and Bio-Sensing Research 50 (2025) 100871

Contents lists available at ScienceDirect

Sensing and Bio-Sensing Research

journal homepage: www.elsevier.com/locate/sbsr

Multivariate diagnostics of electrochemical sensor drift by in situ impedance spectroscopy and voltammetry: A benzenediol-based framework

Abhilash Krishnamurthy [a,b,*], Kristina Žagar Soderžnik [a,b]

[a] Department for Nanostructured Materials, Jožef Stefan Institute, Jamova cesta 39, 1000 Ljubljana, Slovenia
[b] Jožef Stefan International Postgraduate School, Jamova cesta 39, 1000 Ljubljana, Slovenia

ARTICLE INFO

Keywords:
Electrochemical impedance spectroscopy (EIS)
Screen-printed electrode (SPE)
Benzenediols
Sensor diagnostics
Equivalent circuit modelling
Multivariate analysis

ABSTRACT

Performance drift in electrochemical sensors remains a challenge in long-term and/or corrosive applications. We present a generalisable, in situ diagnostic framework based on electrochemical impedance spectroscopy (EIS) and cyclic voltammetry (CV), using screen-printed electrodes (SPE) and benzenediols (catechol, resorcinol and hydroquinone) in acidic media as a model system. Two sensor types, unmodified and Pt/C-modified SPEs, were tested across repeated CV cycles, with polarisation resistance (R_P) and effective capacitance (C_{eff}) extracted from equivalent circuit models.

Unmodified SPEs showed progressive activation, while modified SPEs exhibited early improvement followed by degradation. To synthesise trends across R_P, C_{eff}, and net charge transfer (Q_n) obtained from CV data, principal component analysis (PCA) was applied. PCA revealed smooth, directional evolution for unmodified SPEs and disordered, non-monotonic drift in modified SPEs, reinforcing the EIS results.

This approach enables online, non-destructive tracking of electrochemical sensor health and offers a transferable framework for performance assurance, quality control, and lifecycle monitoring. It repositions EIS from static characterisation to an embedded, multivariate diagnostic tool.

1. Introduction

Growing public concern over "Sick Building Syndrome" [1] (SBS) has driven the rapid development of sensors for detecting volatile toxic organic compounds [2] (VTOC), which can accumulate to hazardous levels and cause both acute and chronic illnesses. The scientific community has addressed this need by developing sensors capable of detecting and quantifying VTOCs (e.g., benzene, formaldehyde [3]) with low detection limits and rapid, near real-time response [4]. Electrochemical sensing [5] is particularly well-suited to this task, offering selectivity, sensitivity, and speed [6] in both gas and liquid phases. It also offers a cost-effective alternative to optical [7] or calorimetric methods [8].

Electrochemical sensors are prone to performance drift when exposed to environmental stressors such as electrolyte [9] variation, analyte interaction, and corrosive media. These conditions alter reaction kinetics and compromise sensor integrity [10], especially during trace analyte detection [11] or extended operation under harsh conditions. Over time, such drift reduces the sensor's operational reliability and lifespan [12].

Conventional methods such as scanning electron microscopy (SEM) [13], energy-dispersive X-ray spectroscopy (EDXS) [14], X-ray photoelectron spectroscopy (XPS) [15], surface-enhanced Raman spectroscopy (SERS) [16], and X-ray diffraction (XRD) [17] offer valuable insights into material degradation. However, they are destructive, equipment-intensive, and require specialised training, making them impractical for routine diagnostics.

Electrochemical impedance spectroscopy (EIS) [18] offers a viable, non-destructive diagnostic alternative. It can sensitively track surface changes such as corrosion [19] or nucleation [20] without damaging the sensor. Because redox processes are directly linked to the electrochemically active surface area [21], EIS provides an effective means of evaluating sensor performance.

In this study, we diagnose performance drift in screen-printed electrodes (SPEs) by monitoring their electrical properties using periodic in situ EIS measurements. EIS spectra recorded at multiple time points were compared to track changes, and equivalent electrical circuits were fitted to assess the evolution of circuit elements. EIS is used here not as a post-modification tool but as an integrated diagnostic protocol embedded in the sensing workflow. This enables online health

* Corresponding author at: Department for Nanostructured Materials, Jožef Stefan Institute, Jamova cesta 39, 1000 Ljubljana, Slovenia.
E-mail address: abhilash.krishnamurthy@ijs.si (A. Krishnamurthy).

https://doi.org/10.1016/j.sbsr.2025.100871
Received 25 June 2025; Received in revised form 18 August 2025; Accepted 1 September 2025
Available online 2 September 2025
2214-1804/© 2025 The Authors. Published by Elsevier B.V. This is an open access article under the CC BY-NC-ND license (http://creativecommons.org/licenses/by-nc-nd/4.0/).

monitoring and offers a transferable framework adaptable across sensor types and analytes. Two sets of Metrohm DS150 electrodes were tested: one unmodified and one with the working electrode (WE) modified by drop-casting a 20 wt% Pt/C suspension [platinum nanoparticles (2–3 nm) on Vulcan XC-72R]. EIS spectra were recorded before and after cyclic voltammetry (CV) with three different benzenediol isomers [catechol (CC), resorcinol (RS) and hydroquinone (HQ)] in 1 M HCl. Building on our previous article in *Electrochimica Acta* (Krishnamurthy et al., 2024) [22], which demonstrated the viability of the modified SPE-based sensing platform and detailed the benzenediol redox mechanisms, we retain CC, RS, and HQ as model analytes due to their well-studied, reproducible electrochemistry. For the electrolyte, we employ 1 M HCl, also as discussed in the previous article, to suppress spontaneous oxidation and to decrease solution resistance, thereby providing a stable measurement matrix for the present analysis. The results confirm that EIS is an effective tool for assessing surface condition and sensor health [23]. While benzenediols served as model analytes, the framework is generalisable to other molecular classes. This work quantifies sensor performance evolution using impedance-derived metrics that are applicable across architectures. Fig. 1 illustrates the EIS-based characterisation process applied to both unmodified and Pt/C-modified SPEs.

2. Principles and modelling frameworks in electrochemical impedance spectroscopy

EIS is a powerful technique for probing the resistive and capacitive behaviour of electrochemical systems across a wide frequency range. In this study, we interpret EIS spectra using equivalent circuit models that represent key physical and electrochemical processes at the electrode–electrolyte interface.

Fig. 2 presents representative Nyquist, Bode, and complex capacitance plots with fitted curves from the equivalent circuit model. While Nyquist and Bode plots are traditionally used in control systems [24] to assess cut-off frequencies and system stability, our focus here is on circuit fitting and the evolution of electrical parameters. These plots therefore serve mainly as fitting tools rather than standalone diagnostic aids. Full datasets, theoretical background, and symbolic circuit diagrams (Supplementary Figs. S1–S4) are provided in the Supplementary Information.

2.1. Optimising equivalent circuits for mechanistic interpretation

Selecting an equivalent circuit [25] requires balancing completeness with interpretability. Over-modelling can yield near-perfect fits but risks introducing elements without clear electrochemical justification. Under-modelling, while sacrificing fit quality, ensures that each element corresponds to a physically meaningful process. In this work, we prioritised the latter approach to maintain mechanistic clarity. Diffusion-related components were excluded, as the SPE setup lacks controlled mass transport (e.g., flow systems or rotating electrodes). The simplified circuit thus emphasises clarity and interpretability over exhaustiveness.

3. Results and discussion

3.1. Extracting mechanistic insight from equivalent circuit analysis

EIS spectra were obtained to compare:

1. The performance of unmodified versus Pt/C-modified DS150 SPEs.
2. The evolution of unmodified SPE performance over baseline, post-five, and post-ten CV cycles.
3. The evolution of Pt/C-modified SPEs over the same cycling intervals.

EIS data were fitted using a modified Randles' circuit (Fig. 3), which

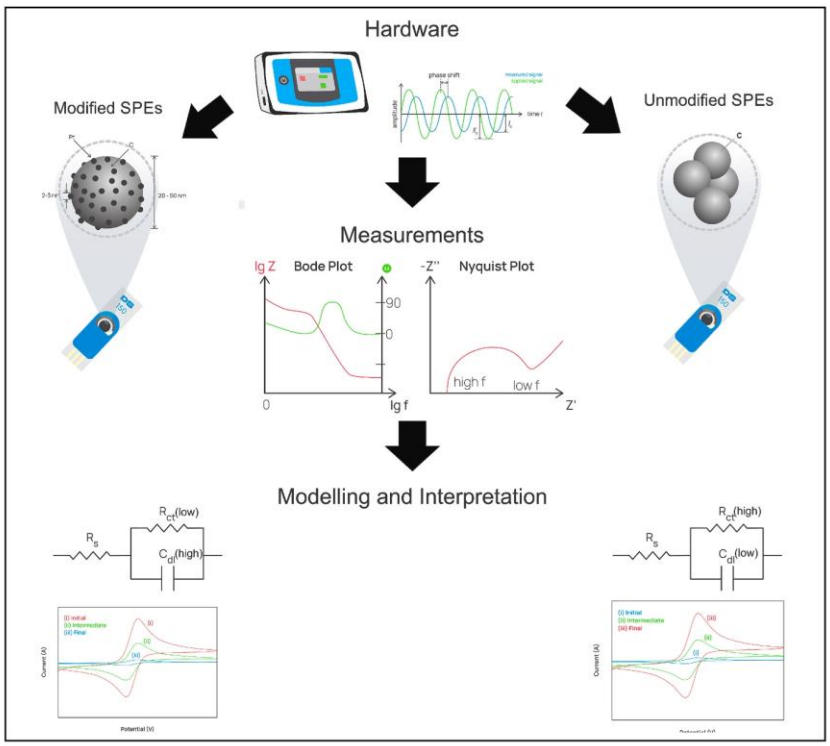


Fig. 1. (Graphical abstract): Schematic of the in situ EIS-based diagnostic workflow for SPEs. Impedance measurements yield R_P and C_{eff} as online, non-invasive indicators of sensor performance drift and degradation across unmodified and Pt/C-modified electrodes.

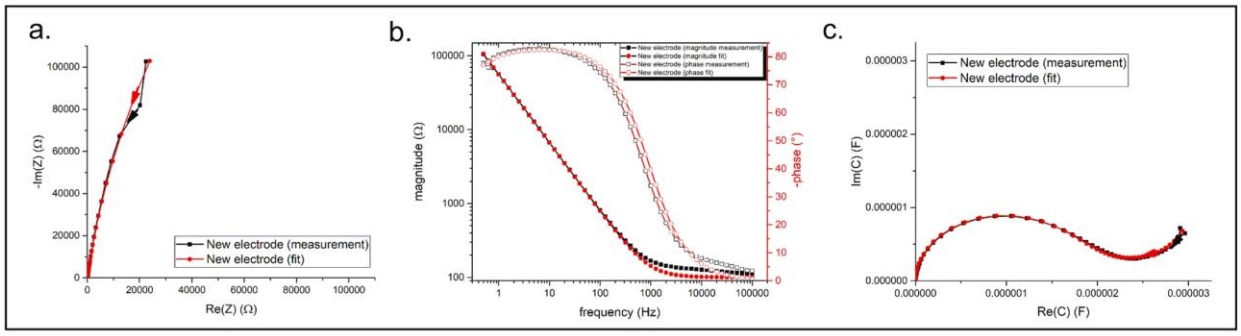


Fig. 2. EIS characterisation of an SPE in 1 M HCl, showing experimental data (black) and fitted model (red, $\chi^2 = 0.0020$). Plots include (a) Nyquist, (b) Bode, and (c) complex capacitance. Data were fitted using a Randles' circuit incorporating a constant phase element (CPE) to account for non-ideal double-layer behaviour. (For interpretation of the references to colour in this figure legend, the reader is referred to the web version of this article.)

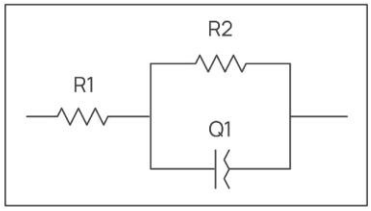


Fig. 3. Modified Randles' equivalent circuit used for EIS fitting. The model includes solution resistance (R1), polarisation resistance (R2), and a constant phase element (Q1) to account for non-ideal capacitive behaviour.

includes solution resistance (R_S), polarisation resistance (R_P), and a constant phase element (CPE) in place of an ideal capacitor to account for non-ideal capacitive [26] behaviour (see Supplementary Section 1.3.3). Mass transport effects were excluded, as they introduce additional elements (e.g., Warburg impedance [27]) that, while physically meaningful, complicate interpretation. By focusing on resistive and capacitive components, the model preserves mechanistic clarity. Each EIS dataset corresponds to a single SPE and reflects its individual condition.

We extracted values for solution resistance R_S (R1, Ω), polarisation resistance R_P (R2, Ω), and the CPE parameters T and ϕ, as defined in Supplementary Eqs. S12–S15. These parameters describe non-ideal double-layer capacitance. From these, we calculated the effective capacitance C_{eff} (F) [28], which we interpret as a diagnostic indicator of double-layer behaviour and surface integrity, using the following formula:

$$C_{eff} = T^{\frac{1}{\phi}}\left(\frac{1}{R_S} + \frac{1}{R_P}\right)^{\frac{(\phi-1)}{\phi}} \quad (1)$$

Supplementary Figs. S5–S13 show Nyquist, Bode, and complex capacitance plots for each condition, with one representative replicate displayed for clarity. Full fitted data from the EIS spectra are provided in Supplementary Tables S1–S9.

3.2. Translating electrical response into diagnostic indicators of sensor performance

3.2.1. Impedance-based comparison of unmodified and Pt/C-modified SPEs

Before evaluating the effects of sensor use on SPE performance, we first examined whether Pt/C modification [29] altered the electrodes' baseline electrochemical response. EIS measurements were performed on both unmodified and modified SPEs in 1 M HCl, as summarised in Table 1.

Table 1
Impedance parameters (R_P, C_{eff}) for unmodified and Pt/C-modified SPEs in 1 M HCl.

Parameter	R_P (kΩ)	C_{eff} (μF)
Unmodified SPE	900.00	1.75
Modified SPE	13.00	90.51

We assessed the impact of Pt/C modification using R_P and C_{eff} as key diagnostic indicators. Lower impedance values typically indicate enhanced electrochemical performance [30]. Following modification, R_P decreased while C_{eff} increased significantly. The rise in C_{eff} reduces capacitive reactance, consistent with their inverse relationship (see Eq. S8 in Supplementary Section 1.3.2). These shifts are substantial: R_P reduced by a factor of approximately seventy, and C_{eff} increased by nearly a factor of fifty. Because solution resistance (R_S) depends mainly on electrolyte concentration, which remained constant at 1 M HCl, it was not a primary comparison metric in this study.

3.2.2. Impedance-based performance tracking of unmodified SPEs during cyclic voltammetry

We evaluated the performance of unmodified SPEs under CV in four analyte solutions: 1 M HCl (blank), 1 mM CC, 1 mM RS and 1 mM HQ, all in 1 M HCl. For each analyte, EIS spectra were recorded at three stages: before cycling, after five cycles, and after ten cycles. These measurements were used to track changes in R_P and C_{eff}. Table 2 presents the corresponding circuit element values.

The unmodified SPEs exhibited a decrease in R_P and an increase in C_{eff} over successive cycles. This trend indicates surface activation and improved sensor response under corrosive conditions. It likely reflects electrochemical polishing [31], removing surface films and exposing more conductive substrate material [32]. These observations are consistent with previous reports of electrochemical carbon oxidation in acidic media [33].

3.2.3. Impedance-based performance tracking of Pt/C-modified SPEs during cyclic voltammetry

We conducted a parallel investigation using Pt/C-modified SPEs, following the same protocol applied to unmodified SPEs (Section 3.2.2). Table 3 summarises the circuit element values derived from EIS measurements in HCl, CC, RS, and HQ.

Similar to the unmodified SPEs, the Pt/C-modified counterparts showed consistent trends in R_P and C_{eff}. However, a key distinction emerged: in all four analytes, C_{eff} increased after five cycles but declined by the tenth. For R_P, a general increase was observed from baseline to ten cycles, except with resorcinol, where R_P decreased. These trends suggest that Pt/C-modified SPEs undergo transient improvement,

Table 2
Impedance evolution (R_P, C_{eff}) for unmodified SPEs at baseline, five and ten CV cycles in blank (1 M HCl), catechol, resorcinol, and hydroquinone.

Analyte	Blank		Catechol		Resorcinol		Hydroquinone	
Parameter	R_P (kΩ)	C_{eff} (μF)	R_P (kΩ)	C_{eff} (μF)	R_P (kΩ)	C_{eff} (μF)	R_P (kΩ)	C_{eff} (μF)
Baseline	900.00	1.80	2000.00	1.54	1700.00	2.28	1000.00	1.86
Post-five cycles	300.00	4.30	700.00	3.30	500.00	4.62	200.00	6.69
Post-ten cycles	180.00	5.70	300.00	4.10	350.00	5.11	100.00	11.65

Table 3
Impedance evolution (R_P, C_{eff}) for Pt/C-modified SPEs at baseline, five and ten CV cycles in blank (1 M HCl), catechol, resorcinol, and hydroquinone.

Analyte	Blank		Catechol		Resorcinol		Hydroquinone	
Parameter	R_P (kΩ)	C_{eff} (μF)	R_P (kΩ)	C_{eff} (μF)	R_P (kΩ)	C_{eff} (μF)	R_P (kΩ)	C_{eff} (μF)
Baseline	13.00	90.51	16.00	71.41	20.00	57.78	10.00	85.32
Post-five cycles	15.00	111.61	13.00	108.79	20.00	86.71	11.00	110.60
Post-ten cycles	18.00	77.44	18.00	95.10	17.00	77.40	15.00	82.13

followed by degradation, as reflected in the shifts in R_P and C_{eff}. The modified SPEs appear to maintain stable electrical characteristics for up to five cycles, after which degradation becomes evident. This likely results from Pt nanoparticle dissolution [34], carbon support oxidation, and agglomeration, all of which accelerate in acidic media [35] [36]. These effects reduce the electrochemically active surface area and alter the impedance profile over time [37]. Given the initial sharp decline in R_P and the rise in C_{eff} after modification, even modest catalyst loss could significantly impact performance, especially considering the low catalyst loading (~10 μg per SPE). These impedance-based findings were supported by complementary CV data, which revealed early signs of surface deterioration during operation.

Fig. 4 visually consolidates the impedance trends: unmodified electrodes improved progressively with CV cycling, while modified electrodes degrade post-five cycles. This divergence in log-scaled R_P and C_{eff} highlights EIS's strength in capturing early behavioural shifts, without relying on fixed performance thresholds. Logarithmic (base-10) scaling accommodates the wide dynamic range of R_P and C_{eff} across cycles.

Table 4 summarises parameter shifts and relative standard deviations (RSD) across cycling stages, providing comparative insight into performance trends. Unmodified SPEs showed large changes in R_P and C_{eff}, but with high variability. In contrast, Pt/C-modified electrodes exhibited smaller but more consistent changes: R_P generally increased, and C_{eff} peaked at five cycles before declining by ten. The lower RSDs in the modified electrodes indicate greater reproducibility. These results

Table 4
Summary of impedance parameter evolution over ten CV cycles for unmodified and Pt/C-modified SPEs.

Parameter	Metric	Unmodified SPE	Pt/C-modified SPE
R_P	Δ 0 → 5 cycles (%)	−65.50	12.10
	Δ 5 → 10 cycles (%)	2.60	20.10
	Δ 0 → 10 cycles (%)	−64.60	34.40
	Rate (%/cycle)	−6.460	3.44
	RSD (0–10 cycles) (%)	93.40	15.90
C_{eff}	Δ 0 → 5 cycles (%)	138.90	26.50
	Δ 5 → 10 cycles (%)	−4.60	−22.00
	Δ 0 → 10 cycles (%)	128.00	−1.30
	Rate (%/cycle)	12.80	−0.13
	RSD (0–10 cycles) (%)	51.20	19.00

Metrics include percentage changes, rate of drift, relative standard deviation (RSD), and coefficient of variation (CoV).

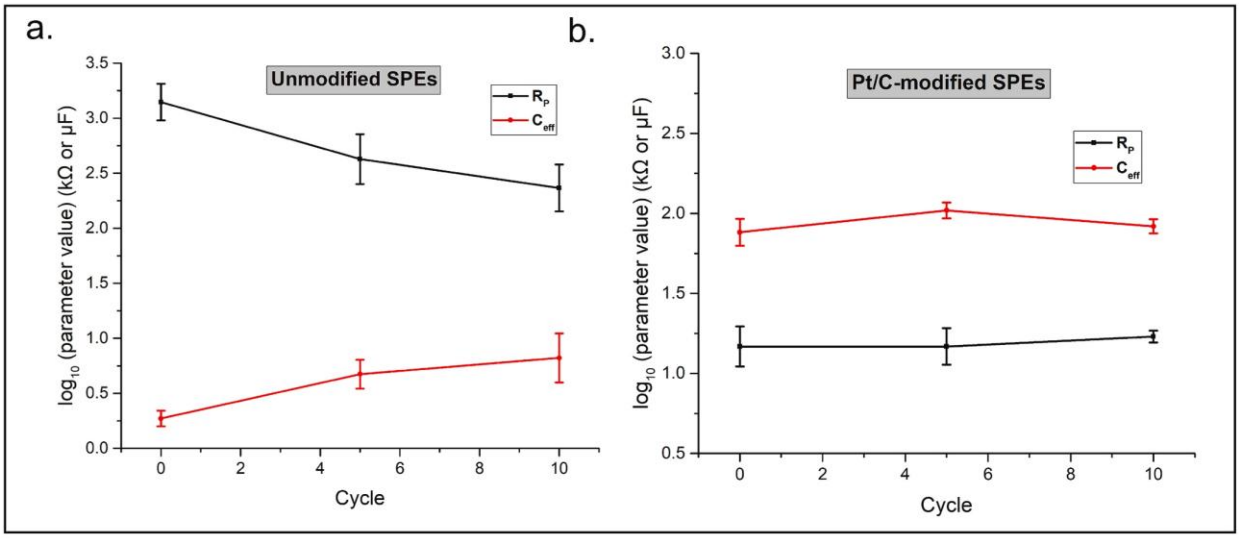


Fig. 4. Logarithmically-scaled evolution of polarisation resistance (R_P) and effective capacitance (C_{eff}) across baseline, five and ten CV cycles for (a) unmodified and (b) Pt/C-modified SPEs. Trends serve as diagnostic indicators of improvement in unmodified electrodes and degradation onset in modified specimens. Error bars show intra-analyte variability and confirm trend consistency.

suggest that surface modification not only improves consistency but also influences the trajectory of sensor drift, reinforcing the sensitivity of the proposed impedance-based diagnostic framework.

Trends in R_P and C_{eff} provide insight into sensor precision and stability, complementing traditional performance metrics such as limit of detection (LoD) and linearity. These impedance-derived indicators are particularly well-suited for long-term deployment and for ensuring metrological robustness.

3.3. Cross-validation of impedance metrics via cyclic voltammetry

We analysed CV data to corroborate the conclusions drawn from EIS. Since all measurements used a fixed CV window, differences in current magnitude or redox onset reflect variations in sensor responsiveness. Fig. 5 presents CV data in 1 M HCl from three representative experimental sets, based on the protocols outlined in Section 3.1.

Fig. 5a shows that Pt/C-modified SPEs produce higher current responses than unmodified electrodes, likely reflecting enhanced H^+ adsorption on the Pt [38] surface. This observation aligns with the impedance-based findings of lower R_P and higher C_{eff} following modification. Fig. 5b and c illustrate performance evolution over CV cycles: unmodified electrodes exhibit gradual improvement, whereas modified electrodes show an initial increase followed by a decline, consistent with the EIS trends. These patterns validate the circuit parameters derived from EIS.

Supplementary Figs. S14–S16 present the relevant CV plots for each experimental condition, with one representative replicate shown per condition for clarity and brevity.

CV data were used to extract key descriptors of electrochemical performance, including net charge transferred (Q_n), peak separation (ΔE_p), and their evolution over successive cycles. Q_n indicates the extent of redox activity, while ΔE_p reflects the reversibility and efficiency of electron transfer. These parameters help distinguish the two SPE types in terms of catalytic behaviour and stability. Pt/C-modified electrodes exhibited better kinetics, as shown by narrower ΔE_p and lower onset potentials, but also displayed signs of degradation over time, particularly with resorcinol, which is prone to fouling. In contrast, unmodified electrodes showed slower but more consistent redox behaviour, with either stable or slightly increasing charge transfer over repeated cycling. These results suggest that while the unmodified carbon surface is initially less active, it provides more stable diagnostic behaviour over time. By comparison, Pt/C modification enhances initial performance but reduces durability. Table 5 summarises these trends. Definitions and complete CV parameters are provided in Supplementary Section 1.5 and Tables S10–S17.

Tables 4 and 5 provide complementary evidence from EIS and CV, respectively. Together, they confirm both qualitative and quantitative shifts in performance, reinforcing the diagnostic potential of the proposed methodology. Notably, EIS detects subtle changes in sensor behaviour before degradation becomes apparent in CV data. These trends reflect the progressive, cycle-dependent evolution of the electrode surface.

Table 5
Summary of cyclic voltammetry parameters for unmodified and Pt/C-modified SPEs, showing net charge transfer (Q_n), peak separation (ΔE_p), and their evolution across cycles.

SPE Type	Analyte	Q_n Range (μC)	ΔE_p (mV)	Q_n Trend	Interpretation
Unmodified	HCl	7.9–25.3	–	↑	Minimal activity; non-faradaic blank system
	HQ	233–261	180 → 150	↑ (+28 μC)	Progressive activation and stable redox reversibility
	CC	239–243	200 → 210	Stable	Consistent performance, minor improvement
	RS	97.9 → 3.8	–	↓ (−94 μC)	Rapid degradation due to polymerisation
Pt/C-modified	HCl	115–167	–	↓ (−51 μC)	Some signal drift; potential surface evolution
	HQ	236–264	60	↑ (+28 μC)	Sustained catalytic activity; gradual drift in Q_{pn}
	CC	261–344	60 → 70	↑ (+83 μC)	Strong catalytic response with stable reversibility
	RS	147 → 101	–	↓ (−46 μC)	Partial degradation; initial performance then decline

3.4. Principal component analysis of electrochemical drift

To complement the impedance and voltammetric analyses, we applied principal component analysis (PCA) to visualise the evolution of sensor behaviour across CV cycles. PCA was performed on three descriptors: R_P, C_{eff}, and Q_n. Separate analyses were conducted for unmodified and Pt/C-modified SPEs, capturing the distinct diagnostic trajectories of each platform. Fig. 6 shows the two PCA biplots for unmodified and Pt/C-modified SPEs.

For unmodified SPEs, the first two principal components (PC1 and PC2) accounted for 92.1 % of total variance (PC1 = 56.8 %, PC2 = 35.3 %). The PCA scores plot revealed smooth, directional shifts with increasing cycles, especially in HCl and HQ, consistent with progressive surface activation. Feature loadings indicated that PC1 was dominated

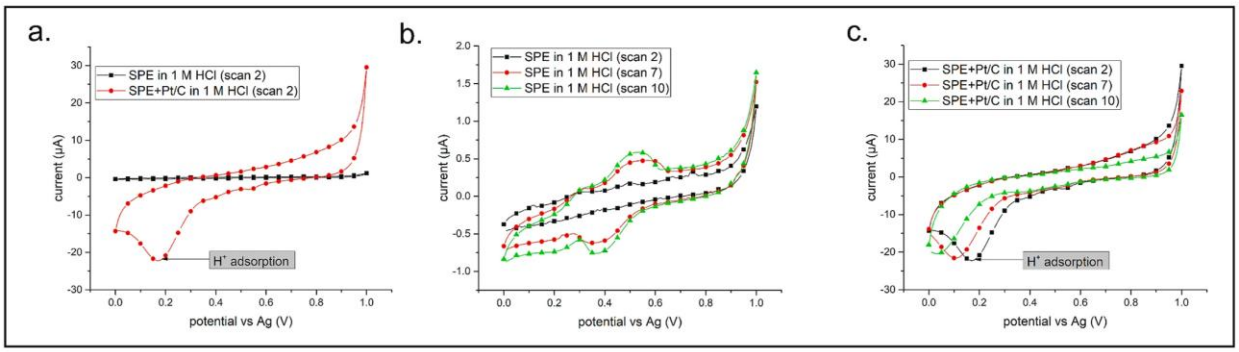


Fig. 5. CV data for SPEs in 1 M HCl across 0–1 V vs quasi Ag reference at 10 mV s^{-1}. (a) Pt/C-modified electrodes exhibit higher current response compared to unmodified SPEs. (b) Unmodified electrodes show progressive performance shifts with cycling. (c) Modified electrodes demonstrate initial improvement, followed by decline after extended cycling.

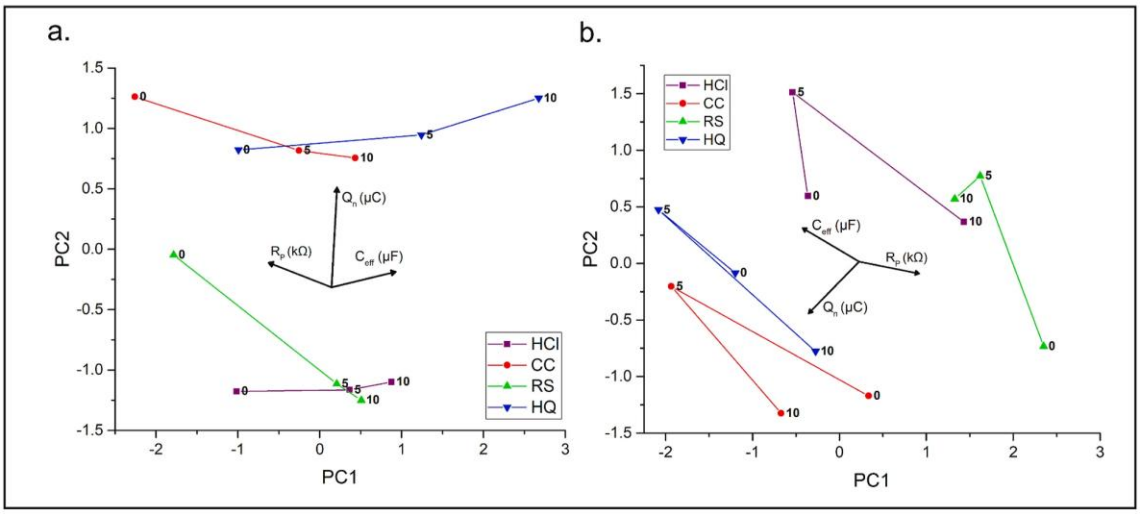


Fig. 6. PCA of SPE performance across CV cycles based on R_P, C_{eff}, and Q_n. (a) Unmodified SPEs show clear, cycle-dependent progression. (b) Pt/C-modified SPEs exhibit scattered behaviour consistent with degradation.

by inverse trends in R_P and Q_n, while PC2 captured secondary contributions from C_{eff}. This supports the interpretation that sensor improvement over time results from simultaneous resistive and capacitive enhancement.

In contrast, Pt/C-modified SPEs exhibited more scattered behaviour. The first two components explained 88.4 % of variance (PC1 = 54.6 %, PC2 = 33.8 %), but progression between cycles was less structured. The PCA biplot showed that C_{eff} and Q_n still influenced PC1 most strongly, but the vector directions were less aligned, reflecting the non-monotonic degradation observed experimentally. In particular, electrodes modified with Pt/C exhibited increasing R_P but decreasing C_{eff} after five to ten cycles, which disrupted the directional trend visible in unmodified electrodes.

Together, the PCA results reinforce the notion that unmodified carbon SPEs undergo consistent electrochemical activation, whereas Pt/C-modified SPEs have a limited peak performance window due to catalyst degradation. The dimensionality reduction confirms that R_P, C_{eff}, and Q_n are sufficient to track sensor health in reduced space, offering a potential framework for automated or embedded diagnostics.

3.5. Synthesis of impedance and voltammetric trends

To consolidate the trends observed across all experimental conditions, Table 6 summarises the evolution of R_P and C_{eff} for both unmodified and Pt/C-modified SPEs across each analyte after five and ten CV cycles. The table highlights directional changes, allowing straightforward comparison of performance evolution during cycling.

Table 6
Summary of qualitative R_P and C_{eff} trends for unmodified and Pt/C-modified SPEs across all analytes post-five and ten CV cycles.

SPE Type	Analyte	Post five cycles	Post ten cycles	Observation from CV
Unmodified	HCl	$R_P \downarrow, C_{eff} \uparrow$	$R_P \downarrow, C_{eff} \uparrow$	*Consistent improvement in diagnostic indicators*
	HQ			
	CC			
	RS			
Pt/C-modified	HCl	$R_P \uparrow, C_{eff} \uparrow$	$R_P \uparrow, C_{eff} \downarrow$	*Emerging signs of degradation*
	HQ			
	CC	$R_P \downarrow, C_{eff} \uparrow$		
	RS	$R_P -, C_{eff} \uparrow$	$R_P \downarrow, C_{eff} \downarrow$	

Arrows indicate parameter changes; qualitative observations describe performance evolution.

Trends observed in both EIS and CV data suggest that acidic corrosion, rather than analyte-specific redox reactions, is the primary driver of changes in electrode surface state and impedance parameters. While CV captures broader behavioural changes, EIS offers higher-resolution, quantitative insight and allows direct comparison to baseline conditions. This underscores the value of using EIS alongside complementary techniques for comprehensive sensor evaluation.

4. Applications and prospects

A key advantage of this method is its ability to assess SPE health and performance in situ, without removing the sensor from operation. Unlike SEM, SERS, XPS, or XRD, which require disassembly and interrupt sensing, this approach enables continuous, non-invasive diagnostics. This work redefines the role of EIS in sensing applications. In traditional sensor studies, EIS is used only as a static characterisation tool, limited to Nyquist plots recorded before and after modification. By contrast, our method integrates EIS directly into the sensing workflow, enabling online diagnostic tracking. Monitoring R_P and C_{eff} over time allows the framework to identify degradation and distinguish between charge transfer loss and capacitive drift. This shifts EIS from a passive characterisation method to an active performance assurance tool. Potential applications include quality control during sensor fabrication, predictive maintenance in environmental or biomedical systems, and embedded diagnostics in portable devices. Although this diagnostic strategy appears scalable, the trends reported here are specific to DS150 SPEs and may not directly generalise to other platforms. Extending the framework to additional systems is a key focus of ongoing work. This positions EIS not just as an analytical method but as a foundation for intelligent sensor design and lifecycle management.

5. Scope and limitations

Due to the complexity of the dataset, which includes Nyquist, Bode, and complex capacitance plots at three stages (baseline, post-five cycles, and post-ten cycles) across four analytes in triplicate, we present only representative spectra for clarity. Trends within each analyte were reproducible across replicates, as illustrated by the error bars in Fig. 4. These margins reflect intra-condition variability and demonstrate

consistent directional changes, though they do not imply statistical significance. Directional trends in R_P and C_{eff} were observed across all four analytes: three redox-active and one non-faradaic, the former serving as functional replicates. This approach enabled internal validation while preserving the variability characteristic of commercial SPEs. Batch-to-batch variability among SPEs limited the comparability of baseline impedance values, as reflected in the high RSDs for unmodified electrodes shown in Table 4. For modified electrodes, additional variability arose from the manual drop-casting process, which, despite careful technique, introduced inconsistencies in catalyst deposition. These factors contributed to fluctuations in fitted parameters and complicated direct comparison across samples. Each SPE effectively served as an individual case study, with fabrication variation, surface morphology, and catalyst distribution driving unique electrochemical responses. As such, the absolute values of the fitted parameters are less critical than their evolution within a given sample across cycles. Reproducibility was established through protocol repetition across multiple analytes, all of which exhibited consistent directional trends. This approach prioritises mechanistic interpretation and trend validation over inter-sample averaging.

As discussed in Section 3.2, while EIS effectively characterises and investigates the electrical behaviour of SPEs, the underlying phenomena responsible for the observed changes in parameter values remain to be confirmed. SEM provides the most direct means of validating these findings, allowing examination before and after CV cycling. However, since SEM sample preparation is destructive, it precludes further electrochemical testing on the same SPE. SERS, with its high surface sensitivity similar to EIS, could potentially validate the impedance data under a robust test protocol. Nonetheless, SERS also typically requires destructive sample preparation, precluding comparative before-and-after measurements on the same SPE. Another potential solution involves employing an electrochemical quartz crystal microbalance (EQCM) [39] to monitor changes in resonant frequency during CV cycling. However, this approach necessitates the development of a suitable method to integrate the SPE with the EQCM electrode. Alternatively, we could assess material erosion [40] by depositing a proxy layer on the EQCM electrode and extrapolating the results to the SPE, while carefully considering the subtle differences between the two systems.

6. Conclusion

In situ electrochemical impedance spectroscopy (EIS) was used to characterise screen-printed electrodes (SPE) by modelling them as networks of discrete circuit elements. We diagnosed performance drift in both unmodified and Pt/C-modified SPEs using periodic EIS measurements taken before and after sensing. The impedance spectra were fitted using a Randles' circuit, with a constant phase element (CPE) replacing the ideal capacitor to account for non-ideal double-layer behaviour. From these fits, we extracted polarisation resistance (R_P) and effective capacitance (C_{eff}) as diagnostic indicators. Modification reduced R_P and increased C_{eff}, confirming enhanced baseline performance with Pt/C deposition. Both electrode types were evaluated using cyclic voltammetry (CV) with four analytes: 1 M HCl (blank), 1 mM catechol, 1 mM resorcinol, and 1 mM hydroquinone in 1 M HCl. EIS spectra were recorded at three points: before cycling, after five cycles, and after ten cycles. Unmodified SPEs showed progressive improvements in impedance characteristics, indicating increased electrochemical activity over time. In contrast, modified SPEs displayed initial improvement followed by degradation, suggesting loss of catalytic integrity. These trends, supported by CV results, confirm the reliability of R_P and C_{eff} as indicators of surface condition and sensor drift. Although demonstrated with benzenediols, this diagnostic approach is generalisable to other molecular systems and sensing platforms. The proposed framework offers a modular strategy for tracking sensor performance and positions EIS as a foundational tool for intelligent lifecycle management of electrochemical systems.

7. Materials and methods

7.1. Catalyst preparation

Catalyst ink was prepared by dispersing 20 wt% Pt/C [platinum nanoparticles (2–3 nm) on Vulcan XC-72R (20–50 nm), sourced from FuelCellStore] in 0.995 ml of absolute ethanol. A 5 µl aliquot of 5 % Nafion solution (in ethanol, Sigma Aldrich) was added as a binder. The mixture was ultrasonicated using a 500 W probe at 25 % amplitude for 2 min to ensure uniform dispersion. The ink was used immediately to minimise particle settling and agglomeration.

7.2. Sensor element fabrication

Sensor elements were prepared using Metrohm DropSens DS150 SPEs with a carbon working electrode (WE), platinum counter electrode (CE), and silver reference electrode (RE). The WE was cleaned with deionised water and ethanol, then dried on a 55 °C hot plate. A 10 µl aliquot of catalyst ink was pipetted onto the WE while still on the hot plate to accelerate drying. Care was taken to avoid spill-over onto the CE and RE. The sensors were stored in a sealed, dry container to prevent tarnishing of the RE and silver contacts. Each 10 µl ink dose contained 10 µg of catalyst (1 mg/ml), with 20 % Pt, resulting in a metal loading of 2 µg per sensor and an estimated Pt loading of approximately 160 ng mm^{-2} for a 4 mm WE diameter.

7.3. Analyte solution preparation

Analyte solutions of various concentrations were prepared by diluting stock solutions of each benzenediol. Catechol (CC), resorcinol (RS) and hydroquinone (HQ), all of analytical grade purity (>99 %) and purchased from Sigma Aldrich, were used. Stock solutions of each benzenediol (50 mM) were created by dissolving the analyte in 1 M HCl (prepared by dilution of 37 % HCl) with stirring, aided by ultrasonication. Working solutions were prepared by diluting the stock with 1 M HCl to reach target concentration. For each measurement, 75 µl of analyte solution was dispensed onto the SPE surface to ensure full coverage of all three electrodes.

7.4. Framework summary

This protocol integrates EIS into the sensing workflow to track sensor performance over time. The steps are as follows:

7.4.1. Baseline measurement

Record EIS on a freshly prepared sensor to extract initial R_P and C_{eff} values.

7.4.2. Electrochemical cycling - Phase I

Perform x cycles of CV, followed by stabilisation.

7.4.3. Midpoint assessment

Measure EIS again and compare results to the baseline to observe early trends.

7.4.4. Cycling - Phase II

Apply another x CV cycles (total $2x$) and allow the system to stabilise.

7.4.5. Post-cycling measurement

Conduct a third EIS measurement and evaluate parameter evolution across 0, x, and $2x$ cycles.

7.4.6. Data interpretation

Compute % change and RSD for R_P and C_{eff}. Track directional trends to differentiate charge transfer shifts and capacitive changes.

7.4.7. Extension (Optional)

Repeat as needed for extended diagnostics. In this study, $x = 5$ cycles was used to capture early- and mid-stage sensor behaviour.

7.5. Electrochemical measurement protocols and data fitting

CV was performed using a PalmSens4 potentiostat with the following parameters: E_{begin} = 0 V, $E_{vertex1}$ = 1 V, $E_{vertex2}$ = 0 V vs quasi Ag reference; Scan rate: 10 mV s^{-1}; Number of scans: 10; Potential step size: approximately 1 mV. EIS was also performed using the PalmSens4 potentiostat under the following conditions: Equilibration time: 0 s; Scan Type: Default; DC potential (E_{dc}): 0 V; AC amplitude (E_{ac}): 10 mV (rms); Frequency type: Scan; Number of frequencies: 54 (10 per decade); Maximum frequency: 100 kHz; Minimum frequency: 0.5 Hz; Minimum sampling time: 0.5 s; Maximum equilibration time: 10 s.

Equivalent circuit fitting used non-linear least squares regression. For the representative dataset shown in Fig. 2, the model yielded a reduced χ^2 value of 0.0020, indicating excellent agreement between experimental data and the fitted response. Similar fit quality was observed across all datasets used for performance tracking.

Funding

This research was supported by the Slovenian Research Agency (ARIS) under grants P2–0084, J2–1739, J2–3051, and PR-09874.

Ethical approval

Not applicable.

CRediT authorship contribution statement

Abhilash Krishnamurthy: Writing – review & editing, Writing – original draft, Visualization, Validation, Methodology, Investigation, Formal analysis, Data curation, Conceptualization. **Kristina Žagar Soderžnik:** Writing – review & editing, Validation, Supervision, Resources, Project administration, Methodology, Investigation, Funding acquisition.

Declaration of competing interest

The authors declare no competing interests.

Acknowledgements

The authors gratefully acknowledge the Slovenian Research Agency (ARIS) for their financial contribution to this work provided through grants: P2–0084 (Programme Nanostructured Materials), J2–1739 (High Performance Nanostructured Acrylamide Sensors), J2-3051 (SensePMC), and PR-09874 (Young Researcher Project). The authors also thank Pika Štefančič for her assistance with the graphical artwork.

Appendix B. Supplementary data

While we generated a comprehensive collection of EIS plots, we provide it as supplementary material to ensure the main article remains concise. The supplement also includes a detailed theoretical overview of electrochemical impedance spectroscopy (EIS), including explanations of key electrical circuit elements such as resistors, capacitors, and constant phase elements (CPEs), along with symbolic representations and derivations. Supplementary data to this article can be found online at [https://doi.org/10.1016/j.sbsr.2025.100871].

Data availability

All data supporting the findings of this study are available within the article and its Supplementary Information. Additional datasets can be provided by the corresponding author upon reasonable request.

References

[1] C.A. Redlich, J. Sparer, M.R. Cullen, Sick-building syndrome, Lancet 349 (9057) (1997) 1013–1016.
[2] S.K. Brown, M.R. Sim, M.J. Abramson, C.N. Gray, Concentrations of volatile organic compounds in indoor air–a review, Indoor Air 4 (2) (1994) 123–134.
[3] Š. Trafela, A. Krishnamurthy, K.Ž. Soderžnik, U. Kavčič, I. Karlovits, B. Klopčič, K. Žužek, IoT electrochemical sensor with integrated Ni (OH) 2–Ni nanowires for detecting formaldehyde in tap water, Sensors 23 (10) (2023) 4676.
[4] R. Mall, Real-Time Systems: Theory and Practice, Pearson Education India, 2009.
[5] A. Hayat, J.L. Marty, Disposable screen printed electrochemical sensors: tools for environmental monitoring, Sensors 14 (6) (2014) 10432–10453.
[6] M.J. Tierney, H.O.L. Kim, Electrochemical gas sensor with extremely fast response times, Anal. Chem. 65 (23) (1993) 3435–3440.
[7] C. Elosua, I.R. Matias, C. Bariain, F.J. Arregui, Volatile organic compound optical fiber sensors: a review, Sensors 6 (11) (2006) 1440–1465.
[8] B. Szulczyński, J. Gębicki, Currently commercially available chemical sensors employed for detection of volatile organic compounds in outdoor and indoor air, Environments 4 (1) (2017) 21.
[9] N. Govindarajan, A. Xu, K. Chan, How pH affects electrochemical processes, Science 375 (6579) (2022) 379–380.
[10] E.E. Stansbury, R.A. Buchanan, Fundamentals of electrochemical corrosion, ASM Int. (2000).
[11] E.S. Cross, L.R. Williams, D.K. Lewis, G.R. Magoon, T.B. Onasch, M.L. Kaminsky, J. T. Jayne, Use of electrochemical sensors for measurement of air pollution: correcting interference response and validating measurements, Atmos. Meas. Tech. 10 (9) (2017) 3575–3588.
[12] E. Demir, K.K. Kırboga, M. Işık, An overview of stability and lifetime of electrochemical biosensors, Novel Nanostruct. Mater. Electrochem. Bio-sens. Appl. (2024) 129–158.
[13] W. Zhou, R. Apkarian, Z.L. Wang, D. Joy, Fundamentals of scanning electron microscopy (SEM), Scann. Microsc. Nanotechnol. (2007) 1–40.
[14] D. Shindo, T. Oikawa, D. Shindo, T. Oikawa, Energy dispersive x-ray spectroscopy, Anal. Electron Microsc. Mater. Sci. (2002) 81–102.
[15] J. Chastain, R.C. King Jr., Handbook of X-ray photoelectron spectroscopy, Perkin-Elmer Corp. 40 (221) (1992) 25.
[16] P.L. Stiles, J.A. Dieringer, N.C. Shah, R.P. Van Duyne, Surface-enhanced Raman spectroscopy, Annu. Rev. Anal. Chem. 1 (2008) 601–626.
[17] J. Epp, X-ray diffraction (XRD) techniques for materials characterization, in: Materials Characterization Using Nondestructive Evaluation (NDE) Methods, Woodhead Publishing, 2016, pp. 81–124.
[18] B.Y. Chang, S.M. Park, Electrochemical Impedance Spectroscopy, Annu. Rev. Anal. Chem. 3 (1) (2010) 207–229.
[19] D.V. Ribeiro, J.C.C. Abrantes, Application of electrochemical impedance spectroscopy (EIS) to monitor the corrosion of reinforced concrete: a new approach, Constr. Build. Mater. 111 (2016) 98–104.
[20] C.X. Wang, M. Wang, X. Zhou, Nucleation and growth of apatite on chemically treated titanium alloy: an electrochemical impedance spectroscopy study, Biomaterials 24 (18) (2003) 3069–3077.
[21] A. García-Miranda Ferrari, C.W. Foster, P.J. Kelly, D.A. Brownson, C.E. Banks, Determination of the electrochemical area of screen-printed electrochemical sensing platforms, Biosensors 8 (2) (2018) 53.
[22] A. Krishnamurthy, Z. Samardžija, Š. Trafela, A. Korent, S. Šturm, K.Ž. Soderžnik, Electrochemical detection of benzenediols using carbon-supported catalysts, Electrochim. Acta 493 (2024) 144389.
[23] F. Arduini, F. Di Nardo, A. Amine, L. Micheli, G. Palleschi, D. Moscone, Carbon black-modified screen-printed electrodes as electroanalytical tools, Electroanalysis 24 (4) (2012) 743–751.
[24] G.F. Franklin, J.D. Powell, A. Emami-Naeini, Feedback Control of Dynamic Systems vol. 10, Pearson, Upper Saddle River, NJ, 2010.
[25] A.J. Bard, L.R. Faulkner, H.S. White, Electrochemical Methods: Fundamentals and Applications, John Wiley & Sons, 2022.
[26] B.B. Damaskin, O.A. Petrii, Historical development of theories of the electrochemical double layer, J. Solid State Electrochem. 15 (2011) 1317–1334.
[27] J. Huang, Diffusion impedance of electroactive materials, electrolytic solutions and porous electrodes: Warburg impedance and beyond, Electrochim. Acta 281 (2018) 170–188.
[28] B. Hirschorn, M.E. Orazem, B. Tribollet, V. Vivier, I. Frateur, M. Musiani, Determination of effective capacitance and film thickness from constant-phase-element parameters, Electrochim. Acta 55 (21) (2010) 6218–6227.
[29] G. Paimard, E. Ghasali, M. Baeza, Screen-printed electrodes: fabrication, modification, and biosensing applications, Chemosensors 11 (2) (2023) 113.
[30] N.O. Laschuk, E.B. Easton, O.V. Zenkina, Reducing the resistance for the use of electrochemical impedance spectroscopy analysis in materials chemistry, RSC Adv. 11 (45) (2021) 27925–27936.
[31] G. Yang, B. Wang, K. Tawfiq, H. Wei, S. Zhou, G. Chen, Electropolishing of surfaces: theory and applications, Surf. Eng. 33 (2) (2017) 149–166.

[32] F. Nazneen, P. Galvin, D.W. Arrigan, M. Thompson, P. Benvenuto, G. Herzog, Electropolishing of medical-grade stainless steel in preparation for surface nano-texturing, J. Solid State Electrochem. 16 (2012) 1389–1397.
[33] Z. Siroma, M. Tanaka, K. Yasuda, K. Tanimoto, M. Inaba, A. Tasaka, Electrochemical corrosion of carbon materials in an aqueous acid solution, Electrochemistry 75 (2) (2007) 258–260.
[34] S. Mitsushima, Y. Koizumi, S. Uzuka, K.I. Ota, Dissolution of platinum in acidic media, Electrochim. Acta 54 (2) (2008) 455–460.
[35] N. Linse, L. Gubler, G.G. Scherer, A. Wokaun, The effect of platinum on carbon corrosion behavior in polymer electrolyte fuel cells, Electrochim. Acta 56 (22) (2011) 7541–7549.
[36] H. Tang, Z. Qi, M. Ramani, J.F. Elter, PEM fuel cell cathode carbon corrosion due to the formation of air/fuel boundary at the anode, J. Power Sources 158 (2) (2006) 1306–1312.
[37] M. Lee, M. Uchida, D.A. Tryk, H. Uchida, M. Watanabe, The effectiveness of platinum/carbon electrocatalysts: dependence on catalyst layer thickness and Pt alloy catalytic effects, Electrochim. Acta 56 (13) (2011) 4783–4790.
[38] F.G. Will, Hydrogen adsorption on platinum single crystal electrodes: I. Isotherms and heats of adsorption, J. Electrochem. Soc. 112 (4) (1965) 451.
[39] A.R. Hillman, The EQCM: electrogravimetry with a light touch, J. Solid State Electrochem. 15 (2011) 1647–1660.
[40] O. Schneider, An EQCM study of the corrosion of synthetic aluminium alloys, ECS Trans. 16 (52) (2009) 13.

4.4 Frequency-Domain Characterisation via Fourier Analysis

This section addresses the signal layer of the sensing workflow, examining how waveform structure and spectral content shape the electrochemical information that is extracted from the electrode interface.

This study introduces a frequency-domain approach to voltammetric signal analysis using Fourier decomposition, offering new insight into faradaic and non-faradaic processes during benzenediol detection. While traditional electrochemical techniques such as CV, LSV, DPV, and SWV are interpreted in the time domain, this work demonstrates how their signal structure can be decomposed into harmonic spectra to enhance redox resolution and optimise sensing parameters.

Using ACV across frequencies from 3 to 2000 Hz, it was observed that faradaic peaks from CC, HQ, and RS become increasingly masked by capacitive currents at higher frequencies. A peak-to-RMS current ratio was calculated to quantify this effect, showing an inverse logarithmic relationship between frequency and signal clarity. These findings highlight the trade-off between capacitive suppression and faradaic enhancement, guiding the selection of optimal excitation frequencies for analyte detection.

Fourier analysis was then applied to canonical voltammetric waveforms. CV signals exhibited dominant odd harmonics with rapidly decaying amplitudes, while LSV introduced both even and odd harmonics. DPV, modelled as a superposition of LSV and a modulated pulse train, displayed sinc-shaped spectral nulls based on duty cycle. SWV waveforms showed high harmonic distortion, with square-wave contributions producing rich high-frequency content, exacerbating capacitive interference. Spectral metrics such as centroid, bandwidth, flatness, and low-frequency power were computed for each technique, providing a quantitative basis for waveform tuning.

These findings were synthesised into a practical framework recommending optimal parameter settings for each voltammetric method. For instance, slower scan rates in CV and LSV reduce capacitive noise, while lower pulse and square wave frequencies in DPV and SWV improve redox peak visibility. The framework allows researchers to design voltammetric protocols based on spectral behaviour rather than empirical tuning.

This study repositions voltammetric waveforms as structured spectral inputs with measurable frequency characteristics. By aligning experimental parameters with harmonic behaviour, this frequency-domain perspective supports more informed electrochemical sensing strategies.

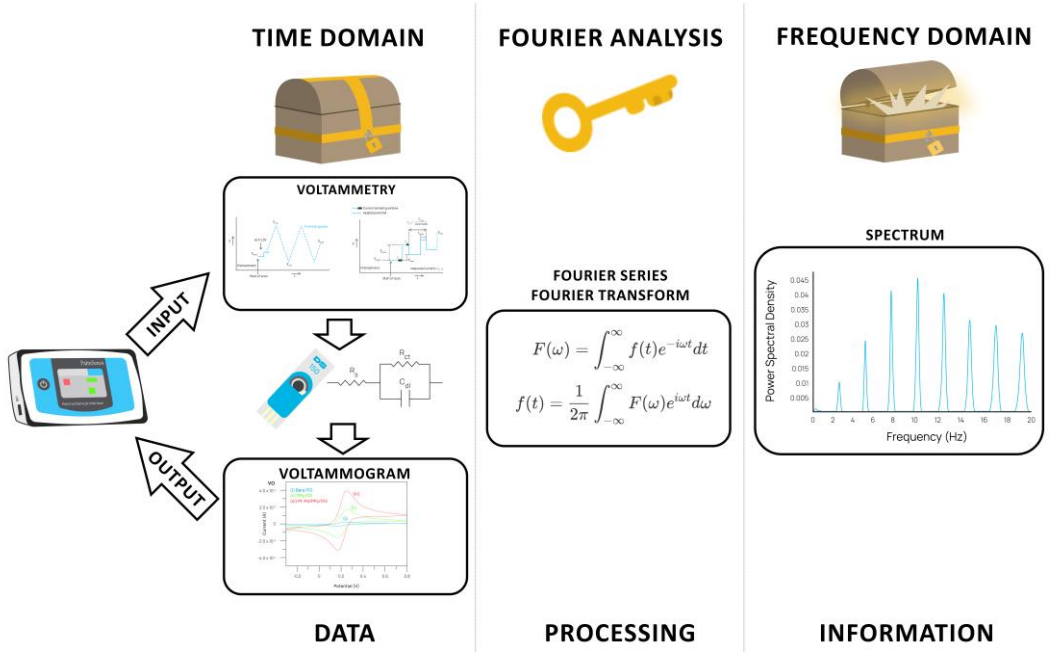


Figure 4.4: Graphical abstract of the frequency-domain analysis workflow. Adapted from Krishnamurthy et al., Measurement 259 volume B (2026) 119706, shared under CC BY-NC-ND 4.0 licensing.

Full methodology and data are published in: Krishnamurthy et al., *Measurement*, 259 Volume B (2026), 119706, https://doi.org/10.1016/j.measurement.2025.119706. The print version is shared in the following pages under the CC BY-NC-ND 4.0 license agreement.

Measurement 259 (2026) 119706

Contents lists available at ScienceDirect

Measurement

journal homepage: www.elsevier.com/locate/measurement

Frequency-domain analysis of voltammetric signals: a framework to augment electrochemical sensing explored through benzenediol detection

Abhilash Krishnamurthy [a,b,*], Kristina Žagar Soderžnik [a,b]

[a] Department for Nanostructured Materials, Jožef Stefan Institute, Jamova Cesta 39, 1000 Ljubljana, Slovenia
[b] Jožef Stefan International Postgraduate School, Jamova Cesta 39, 1000 Ljubljana, Slovenia

ARTICLE INFO

Keywords:
Frequency domain
Spectral decomposition
Fourier analysis
Voltammetry
Electrochemical sensors
Benzenediols

ABSTRACT

Electrochemical signals are traditionally interpreted in the time domain, where overlapping faradaic and non-faradaic currents, noise, and drift obscure frequency-dependent behaviour. This study introduces a frequency-domain framework that complements time-domain analysis by decomposing voltammetric signals into their harmonic components through Fourier methods.

AC voltammetry provides experimental evidence of how increasing excitation frequency progressively suppresses faradaic clarity, while a modified Randles equivalent circuit model explains this response through the interplay of charge-transfer, diffusion, and double-layer charging processes. Fourier series analysis of canonical voltammetric techniques, including linear sweep, cyclic, differential pulse, and square wave voltammetry, shows that waveform geometry uniquely defines harmonic structure. Fast Fourier transform analysis of practical data reveals artefacts introduced by finite sampling, binning, and spectral leakage. These effects highlight the need for conceptual awareness when interpreting experimental spectra. Quantitative spectral descriptors such as the centroid, bandwidth, flatness, and low-frequency power fraction link waveform design directly to faradaic visibility and measurement clarity.

Frequency-domain analysis therefore establishes that electrochemical measurement is inherently frequency-structured. By combining experimental data, equivalent circuit modelling and spectral metrics within a single framework, this approach provides a general route to optimise waveform parameters, reduce capacitive interference, and improve interpretability across electrochemical techniques. Viewed more broadly, this perspective reframes the process of the measurement itself, showing that time-domain signals are projections of an underlying spectral reality.

1. Introduction

Electrochemical measurements translate interfacial redox processes into electrical signals. Conventional voltammetric techniques [1] such as chronoamperometry, linear sweep (LSV), cyclic (CV) [2], differential pulse (DPV) [3], and square wave voltammetry (SWV) [4] are interpreted in the time domain [5], where currents are plotted as functions of time or potential. Although straightforward and intuitive, this representation conceals how electrochemical systems respond to excitation frequency. Faradaic and non-faradaic [6] currents overlap in time, while external variables such as drift and noise further obscure their independent contributions [7].

To visualise this hidden dimension, the present study applies AC voltammetry (ACV) [8] to examine the frequency response [9] of an electrochemical sensor based on 20 wt% Pt/C-modified Metrohm DS150 screen-printed electrodes. The electrode platform, previously optimised for benzenediol detection [hydroquinone (HQ), catechol (CC), and resorcinol (RS)], provides a reproducible and well-characterised system in which faradaic and capacitive processes can be observed simultaneously. By superimposing a small sinusoidal perturbation onto a linear potential sweep, ACV reveals how increasing excitation frequency progressively boosts capacitive currents and diminishes faradaic clarity. These experimental observations form the empirical foundation of the frequency-domain framework developed in this work.

The observed trends are rationalised using a modified Randles equivalent circuit, which serves as the mathematical scaffold for interpreting frequency-dependent electrochemical behaviour. The circuit partitions the system into discrete elements representing charge

* Corresponding author at: Department for Nanostructured Materials, Jožef Stefan Institute, Jamova Cesta 39, 1000 Ljubljana, Slovenia.
E-mail address: abhilash.krishnamurthy@ijs.si (A. Krishnamurthy).

https://doi.org/10.1016/j.measurement.2025.119706
Received 17 June 2025; Received in revised form 21 October 2025; Accepted 10 November 2025
Available online 12 November 2025
0263-2241/© 2025 The Author(s). Published by Elsevier Ltd. This is an open access article under the CC BY-NC-ND license (http://creativecommons.org/licenses/by-nc-nd/4.0/).

transfer, diffusion, and double-layer charging, linked through the solution resistance. This abstraction layer explains the competing influences of faradaic and capacitive processes independent of specific analytes and their unique redox mechanisms, and predicts the same frequency-dependent trends evident in the ACV data.

Building on these results, the framework is extended through Fourier [10] and spectral [11] analysis of canonical voltammetric waveforms. Fourier decomposition demonstrates that each technique (LSV, CV, DPV, and SWV) has a distinct harmonic [12] signature dictated by its waveform geometry. Comparing their spectra unifies these methods within a single analytical language, showing how waveform design and parameter selection govern frequency content and consequently the quality of electrochemical signals.

This approach differs fundamentally from electrochemical impedance spectroscopy (EIS) [13], which probes steady-state systems under small perturbations. Here, frequency-dependent behaviour is analysed under dynamic scanning conditions, representative of real voltammetric operation. The emphasis is therefore metrological rather than analytical: the study characterises the structure of electrochemical signals rather than the selectivity, sensitivity, or detection limits for the analytes, which have been reported previously for the same benzenediol system [14].

This study follows a reverse-signal logic: integrating experimental ACV data, mathematical interpretation via the Randles circuit, and spectral generalisation through Fourier analysis to reveal that electrochemical measurement is inherently frequency-structured. The resulting framework provides a practical route to tune waveform parameters, minimise capacitive noise, and improve interpretability across multiple voltammetric techniques. The analysis mirrors this logic in practice, tracing the signal path in reverse: from the measured output (ACV spectra), through the system response (Randles circuit), to the input design (waveform spectra). Fig. 1 (Graphical Abstract) schematically presents a general overview of Fourier analysis.

2. Foundations of Fourier analysis in electrochemical signal decomposition

The Supplementary Information provides a brief theoretical exposition of the Fourier series and Fourier transforms. This section outlines the mathematical framework with Eqs. S1 through S10 offering a step-by-step description of the essentials. These formulae elucidate the decomposition of periodic and aperiodic functions into their constituent frequency components, thereby offering insight into the analytical methods used.

The Supplementary Information also examines the harmonic decomposition of several commonly used waveforms, including the square wave, triangular wave, sawtooth wave, and pulse train. This analysis explores the harmonic content characteristic of each waveform illustrating how specific frequency components shape their unique time-domain profiles. Additionally, the rate at which harmonic amplitudes decay with increasing frequency index is discussed, providing insight into the spectral richness or smoothness of each waveform type.

Fig. 2 illustrates the process of spectral resolution via Fourier analysis. Any periodic waveform in the time domain is the sum of sinusoidal components, each characterised by a distinct frequency and amplitude. By extracting and plotting these amplitudes against their respective frequencies, we obtain the spectrum of the original signal. One can visualise this transformation geometrically in three dimensions, with time on the x-axis, amplitude on the y-axis, and frequency on the z-axis. Projecting this representation onto the time–amplitude (xy) plane retrieves the original waveform, while projection onto the frequency-amplitude (yz) plane reveals its spectral composition.

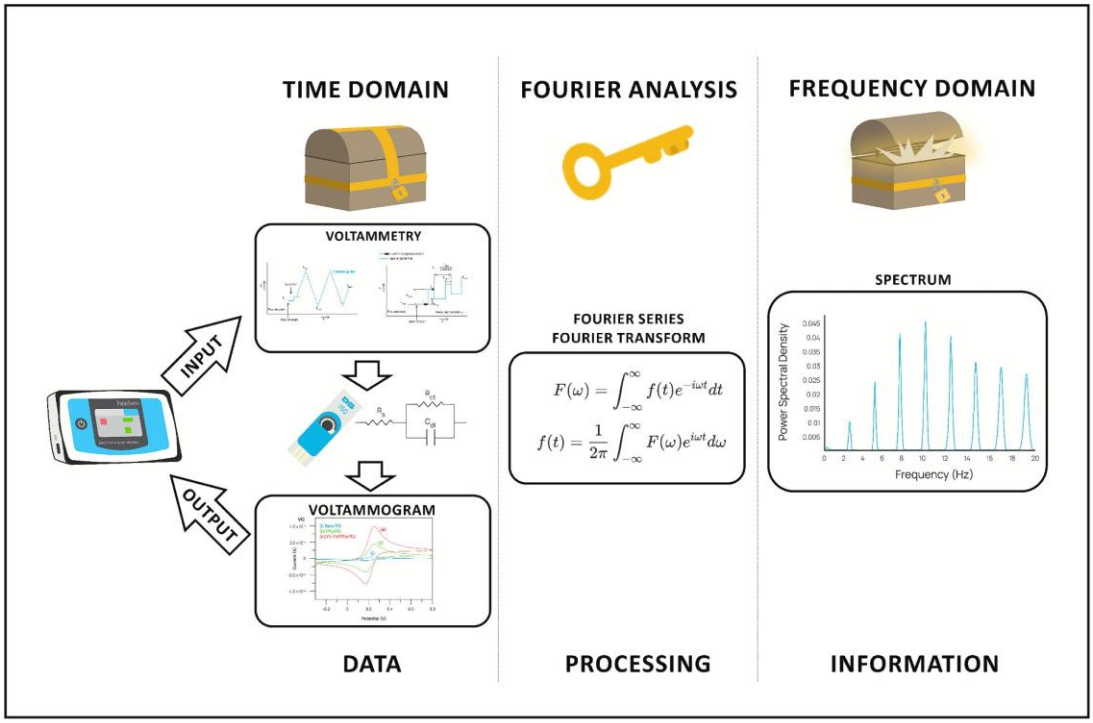


Fig. 1. (Graphical Abstract): Fourier analysis illustrated as the transformation of electrochemical time-domain signals into frequency-domain spectra. Faradaic and capacitive components are separated through signal processing to enhance measurement clarity.

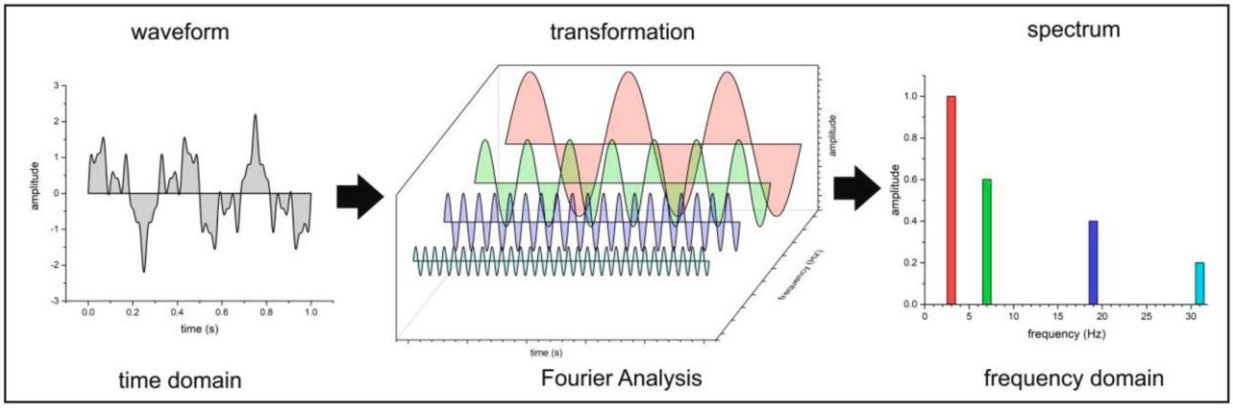


Fig. 2. Fourier analysis illustrated as decomposition of a time-domain waveform into its frequency-domain spectrum. Sinusoidal components combine to reconstruct the original signal.

3. Results and discussion

3.1. Response layer (output): AC voltammetry as a probe of frequency-resolved faradaic and non-faradaic processes

To ground the framework experimentally, ACV probes electrochemical behaviour by superimposing a small sinusoidal perturbation onto a linear potential sweep, enabling frequency-resolved observation of the system response. Unlike EIS, which requires small perturbations and steady-state conditions, ACV provides spectral insight during dynamic voltammetric scans. While wavelet-based methods can capture non-stationary features, the Fourier-based framework adopted here offers a simpler and broadly applicable route for analysing global frequency-dependent behaviour using standard voltammetric protocols under the assumption of linear time invariance (LTI).

3.1.1. Waveform structure and experimental parameters in AC voltammetry

Fig. 3 shows the ACV potential waveform, composed of the sum of a DC component (a linear sweep) and a sinusoidal AC component.

The small AC amplitude enables simultaneous analysis of faradaic and non-faradaic responses. The frequency (f) of the superimposed sine wave critically influences the relative contributions of the two responses. Maintaining a sufficiently slow scan rate allows the sinusoidal perturbation to dominate the system response, thereby reducing the influence of the underlying sweep and providing quasi-stationary conditions consistent with piecewise-LTI behaviour.

3.1.2. Benzenediol detection under variable frequency: suppression of capacitive currents to unmask faradaic signals

To investigate the frequency response of the electrochemical system during benzenediol detection, we performed ACV with a scan rate of 10 mV s^{-1}, an AC amplitude of 10 mV (RMS), a potential step of 10 mV, and voltage limits between 0 V to 1 V versus quasi-reference Ag electrode. We examined the effect of varying the AC frequency from 3 Hz to 2000 Hz using this setup, and the results are shown in Fig. 4.

At lower frequencies, distinct oxidation peaks [15,16] are observed. As frequency increases, the overall current rises. Notably, the background current (predominantly capacitive) increases proportionally with applied frequency.

As a result, the faradaic oxidation peaks of the benzenediols become progressively less prominent and are overwhelmed at higher frequencies by the capacitive current. To further examine this degradation, the Fast Fourier transform (FFT) [17] was applied to the ACV output data. The resulting spectra, shown in Fig. 5a, display sharp, well-localised peaks at the imposed excitation frequencies with no additional harmonic

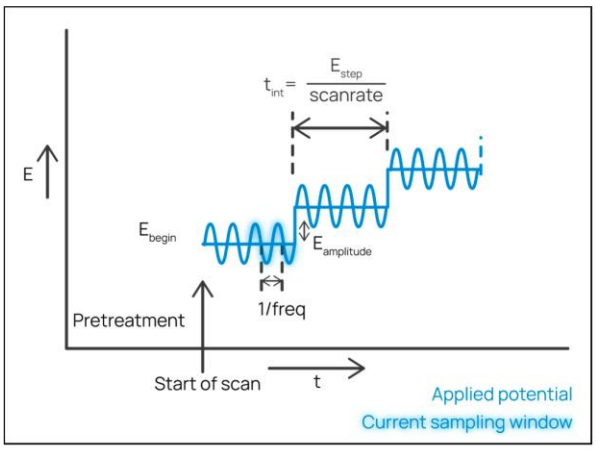


Fig. 3. AC voltammetry (ACV) waveform composed of a linear DC sweep and superimposed sinusoidal perturbation.

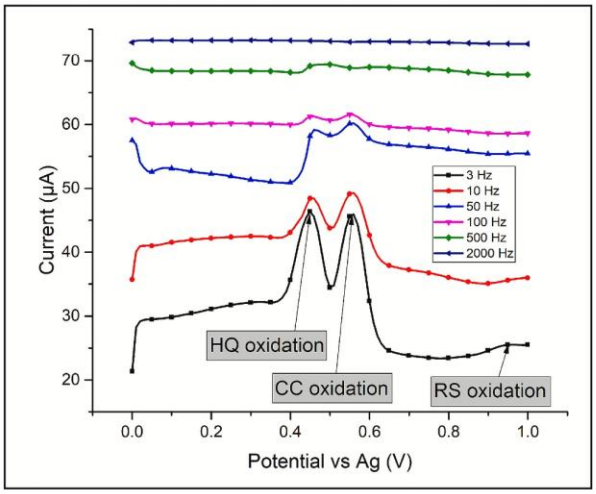


Fig. 4. AC voltammograms of benzenediols (1 mM catechol, 1 mM resorcinol and 1 mM hydroquinone in 1 M HCl) from 3 Hz to 2000 Hz; increasing frequency boosts capacitive current and progressively masks faradaic peaks.

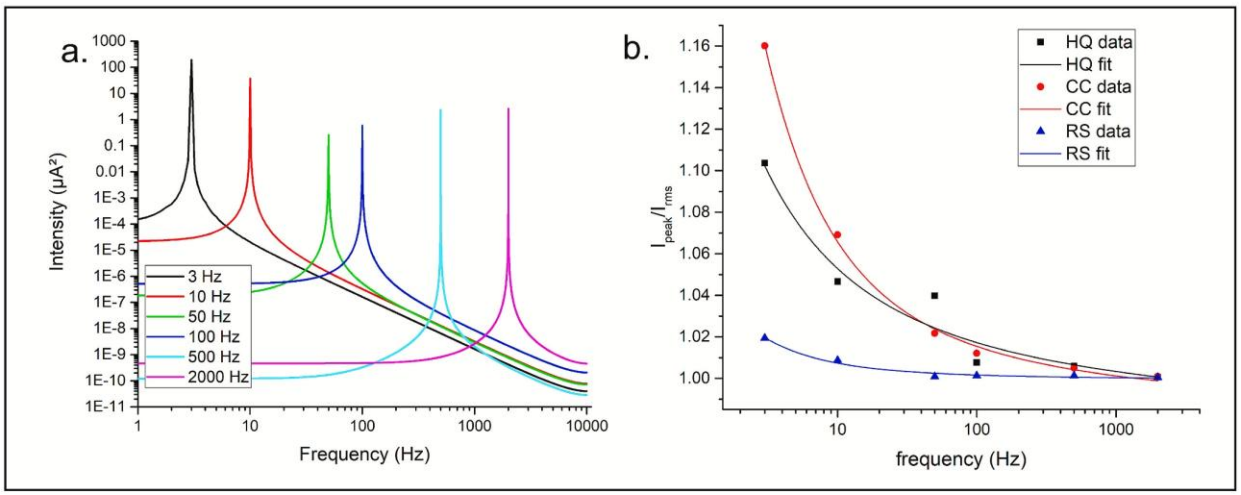


Fig. 5. (a) Fast Fourier transform spectra of ACV outputs, showing recovery of excitation frequencies and the absence of spurious harmonics, confirming linear time-invariant behaviour. (b) Peak-to-RMS current ratios decline with frequency, reflecting reduced faradaic clarity. Inverse logarithmic fits are included to guide the eye.

components. The FFT thus faithfully recovers in the output stage the exact frequencies introduced at the input, providing strong evidence of LTI system behaviour. In parallel, the peak-to-RMS current ratio (detailed in Eq. S15 in Supplementary Section 3.5.5) was calculated for each analyte across the frequency range of 3 Hz to 2000 Hz. This ratio quantifies signal prominence relative to background and, as shown in Fig. 5b, decreases systematically with frequency, reflecting the progressive loss of faradaic clarity due to capacitive effects. Together, the FFT spectra and the peak-to-RMS analysis reveal a consistent correlation between excitation frequency and signal degradation, confirming the utility of the frequency-domain framework for diagnosing the onset of capacitive masking.

These results highlight the challenge of detecting faradaic processes at high frequencies due to dominant capacitive currents. Selecting an appropriate frequency is therefore critical to balance analyte sensitivity and minimise interference from capacitive currents, allowing for a clearer observation of the redox processes of interest. Although both faradaic and capacitive processes are frequency-dependent, their relative dominance shifts with frequency, allowing selective enhancement or suppression of signal components through tuning. These frequency-dependent, qualitative trends indicate that the electrochemical cell itself imposes a structured response, largely independent of analyte identity, and thus provide the experimental foundation for the framework developed in the following sections.

3.2. *Transfer function (system): modelling frequency-dependent capacitive and faradaic current components*

Building on the ACV output-stage observations, the next section examines the electrochemical system through an equivalent circuit model that translates these empirical frequency trends into a formal description of interfacial behaviour.

To understand how frequency affects electrochemical currents, we model the system using a modified Randles circuit, shown in Fig. 6. In this equivalence, the charge transfer resistance (R_{ct}) represents electron transport across the electrode–electrolyte interface, encapsulating the kinetics of redox reactions. The Warburg element [18] (Z_w) accounts for semi-infinite linear diffusion of species to and from the electrode, reflecting mass-transport limitations. The double-layer capacitance [19] (C_{dl}) describes the charging and discharging of the interfacial electrolyte layer, i.e. non-faradaic contributions. The solution resistance (R_s) represents the ionic conduction through the electrolyte. Taken together,

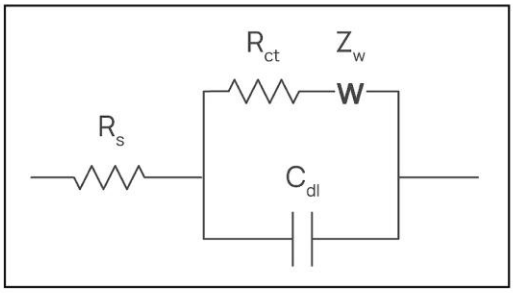


Fig. 6. Modified Randles equivalent circuit used to model the electrochemical cell comprising a solution resistance (R_s), a charge transfer resistance (R_{ct}) to model electron transfer in series with a Warburg element (Z_W) to model mass transport, and a double-layer capacitance (C_{dl}), representing electrolytic charging and discharging.

these circuit elements form a simplified analogue that captures the essential processes of electron transfer, mass transport, and double-layer charging. The Randles circuit is used here as a mechanistic abstraction layer: it consolidates the frequency response into discrete components agnostic of analyte-specific mechanisms, and enabling a general interpretation of frequency effects across electrochemical systems. By deconvolving charge transfer, double-layer charging and diffusion into standalone frequency-dependent components, the Randles circuit formalises the empirical observations from AC voltammetry and establishes the mathematical scaffold for spectral analysis.

The electrical double layer is formed at the interface between the electrode and the electrolyte solution, emulating a capacitor that stores charge. Double-layer charging and discharging contributes to the non-faradaic (capacitive) current (I_C) through the C_{dl} branch in Fig. 6. The non-faradaic current from double-layer [20] charging increases proportionally with the frequency of the applied AC signal, as shown in Eq. (1).

$$\boldsymbol{I_C(\omega) = \omega C_{dl} V_C(\omega)} \tag{1}$$

where I_C (A) is the non-faradaic or capacitive current, V_C (V) is the voltage across the double layer, C_{dl} (F) is the double-layer capacitance and $\boldsymbol{\omega = 2\pi f}$ (rad s^{-1}) is the angular frequency [f (Hz) is the linear frequency].

Simplifying Eq. (1),

$$|I_C(\omega)| \propto \omega \tag{1.1}$$

$$\angle I_C(\omega) \rightarrow 90^\circ \text{ or } \frac{\pi}{2} \tag{1.2}$$

The faradaic current (I_F) through the path containing R_{ct} and Z_W in Fig. 6 arises from electron transfer between the electrode and chemical species leading to redox reactions. The rate of these reactions is influenced by both the electrode potential and the kinetics of the electron transfer. Reaction kinetics [21] and the diffusion [22] of reactants to the electrode primarily govern the faradaic current, which also depends on the frequency. However, its frequency dependence is different from that of the capacitive current as shown in Eq. (2).

$$I_F(\omega) = \frac{V_F(\omega)}{R_{ct} + Z_W(\omega)} \tag{2}$$

where, I_F (A) is the faradaic current, V_F (V) is the voltage across the series combination of the charge transfer resistance R_{ct} (Ω) and the Warburg impedance Z_W (Ω).

R_{ct} represents the opposition to electron transport between the electrode and the redox species and is frequency-invariant.

Z_W represents the diffusion limitation, i.e., the resistance to mass transport of the redox species to/from the electrode and is defined in Eqs. (2.1) and (2.2).

$$|Z_W| = \frac{\sigma}{\sqrt{\omega}} \tag{2.1}$$

$$\angle Z_W = -45^\circ \text{ or } -\frac{\pi}{4} \tag{2.2}$$

where σ ($\Omega\ s^{-0.5}$) is the Warburg coefficient.

When $\omega \rightarrow 0$, $Z_W \gg R_{ct}$,

$$I_F = \frac{V_F\sqrt{\omega}}{\sigma} \tag{2.3}$$

Simplifying Eq. (2.3),

$$|I_F| \propto \sqrt{\omega} \tag{2.4}$$

$$\angle I_F \rightarrow 45^\circ \text{ or } \frac{\pi}{4} \tag{2.5}$$

When $\omega \rightarrow \infty$, $Z_W \ll R_{ct}$,

$$|I_F| = \frac{V_F}{R_{ct}} \tag{2.6}$$

$$\angle I_F \rightarrow 0^\circ \tag{2.7}$$

Fig. 7 visually consolidates the above equations on how redox and capacitive current magnitudes vary with frequency. In physical terms, these relations describe how diffusion-controlled faradaic currents dominate at low frequencies, while capacitive charging increasingly governs the response at higher frequencies, leading to the crossover frequency highlighted at the intersection of the two current curves.

Eqs. (1.1) through (2.7) and Fig. 7 show that:

1. The non-faradaic current increases proportionally with frequency. At regimes where this current is dominant the phase should be tending to 90° or $\frac{\pi}{2}$. In electrochemical terms, this reflects the charging and discharging of the double layer, which behaves as a capacitor. Within physical limits, the capacitive charging and discharging current is therefore a linear function of the excitation frequency.
2. Faradaic current increases with the square root of frequency at low ω, before becoming essentially frequency-invariant at higher values. Electrochemically, this means that at low frequencies, the dominant limitation is mass transport (diffusion of analyte to the electrode) which should be visible in the phase tending towards 45° or $\frac{\pi}{4}$. As frequency rises, diffusion constraints are progressively overcome until charge transfer becomes the bottleneck, beyond which further increases in frequency no longer influence the system which should reflect in the phase tending to 0°.

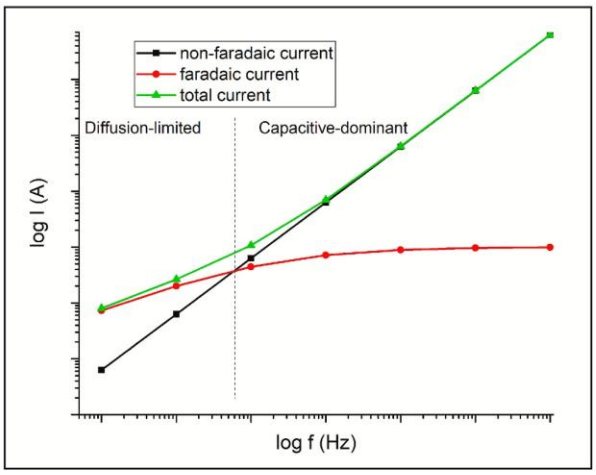


Fig. 7. Log–log illustration comparing faradaic and capacitive current magnitudes as functions of frequency, based on the equivalent circuit model. Highlights the crossover point where capacitive current begins to dominate and guides optimal frequency selection.

This presents a trade-off: at low frequencies, faradaic signals are diffusion-limited, whereas at high frequencies, capacitive currents dominate and mask the faradaic response.

Together, these relationships confirm that both the amplitude and the phase of the electrochemical system evolve predictably with excitation frequency. The Randles circuit therefore provides a reliable mathematical description of frequency-structured electrochemical behaviour, linking current magnitude and phase to the dominant transport and interfacial processes, and setting the stage for analysis of how excitation waveforms themselves encode this frequency structure.

3.3. Excitation characterisation (input): spectral analysis of canonical voltammetric waveforms

Having established the system's frequency response, the discussion now moves upstream to the input stage, where electrochemical techniques operate by applying time-varying potential waveforms that each carry their own frequency signature defined by shape, period and symmetry. Together, these techniques can be viewed as a single methodological family derived from LSV, with CV adding a reversed scan that returns to the initial potential and cycles between the vertices, DPV superimposing a train of rapid potential pulses onto a slow baseline LSV, and SWV modulating the LSV with a square-wave signal, each producing a distinctive harmonic distribution.

The measured output current is a function of both the input waveform and the electrochemical system's frequency response. Consequently, its spectrum reflects both the temporal evolution of the driving signal and the system's underlying transfer characteristics. Fourier analysis provides a practical means to obtain the spectra of these input signals, revealing how waveform design accentuates or attenuates specific frequency regions.

The relative amplitude and distribution of spectral components determine how strongly different electrochemical processes are stimulated. Recognising this intrinsic frequency structure clarifies the characteristic strengths of each voltammetric approach: some favour

mechanistic simplicity, whereas others gain sensitivity through deliberate modulation and sampling. Viewed in the frequency domain, these diverse techniques converge into a unified description where differing time-domain parameters coalesce into directly comparable information.

Figs. 8–11 summarise some examples of canonical voltammetric waveforms and their corresponding spectra obtained using Fourier series (FS) decomposition, illustrating how waveform geometry determines harmonic content and spectral distribution.

3.3.1. Linear sweep voltammetry: harmonic complexity in sawtooth potential sweeps

For a LSV with the following parameters: $E_{begin} = 0$ V, $E_{end} = 1$ V, and scan rate = 10 mV s^{-1}, Fig. 8 shows the waveform and the spectrum.

In LSV, the potential increases linearly between fixed vertices at a constant rate. The corresponding spectrum reveals both odd and even harmonics (f_0, $2f_0$, $3f_0$, …) of the 10 mHz fundamental frequency along with a strong DC component at 0 Hz, reflecting the waveform's amplitude asymmetry.

3.3.2. Cyclic voltammetry: odd harmonic dominance in triangular waveforms

For a CV with the following parameters: $E_{begin} = 0$ V, $E_{vertex1} = 1$ V, $E_{vertex2} = 0$ V, and scan rate = 10 mV s^{-1}, Fig. 9 shows the waveform and the spectrum.

In CV, the potential sweeps linearly between two limits and then reverses to form a triangular profile. The corresponding spectrum contains only odd harmonics (f_0, $3f_0$, $5f_0$, …) of the 5 mHz fundamental and exhibits a faster decay of higher-order harmonics than LSV. A DC component arises from amplitude asymmetry in the waveform.

3.3.3. Differential pulse voltammetry: harmonic complexity and sinc-shaped spectra from pulse trains

For a DPV with the following parameters: $E_{begin} = 0$ V, $E_{end} = 1$ V, scan rate = 10 mV s^{-1}, pulse amplitude = 30 mV, pulse duration = 50 ms, voltage step = 10 mV, and pulse interval = 1 s, Fig. 10 shows the waveform and the spectra.

In DPV, a linear potential sweep is combined with a high-frequency pulse train, producing two distinct spectral components: a low-frequency sawtooth and a high-frequency sinc-shaped ($\frac{\sin\pi t}{\pi t}$) envelope. The 5 % duty cycle used in this illustration introduces nulls at every twentieth harmonic (f_0, $20f_0$, $40f_0$, …), consistent with the reciprocal relation between duty cycle and harmonic spacing.

3.3.4. Square wave voltammetry: high harmonic distortion from square wave superposition on a linear sweep

For a SWV with the following parameters: $E_{begin} = 0$ V, $E_{end} = 1$ V, scan rate = 10 mV s^{-1}, square-wave amplitude = 30 mV, square-wave period = 0.1 s (fundamental frequency = 10 Hz), and voltage step = 10 mV, Fig. 11 shows the waveform and the spectra.

In SWV, a linear potential ramp is superimposed with a square-wave modulation, generating two spectral components: a low-frequency ramp and a high-frequency square-wave contribution. The latter displays harmonic peaks at odd integer multiples (f_0, $3f_0$, $5f_0$, …) consistent with the 50 % duty cycle that suppresses even harmonics. SWV therefore provides a useful mathematical contrast to the DPV example in this study, where a 5 % duty cycle produced nulls at every twentieth harmonic. The square wave's slower harmonic decay yields stronger higher-order contributions, while the waveform's amplitude symmetry eliminates the DC component.

3.3.5. Fast Fourier transform spectra of canonical voltammetric waveforms

The FS spectra presented earlier describe idealised, infinitely periodic waveforms. To complement these, the FFT was applied to the same canonical waveforms described in Sections 3.3.1 to 3.3.4. These quasi-simulations illustrate how the signals would appear if the waveforms were fed directly into a spectral analyser.

The simulated spectra in Fig. 12 highlight the practical challenges that arise when moving from mathematical decomposition to empirical analysis. The quality of the spectra depends critically on parameters defined by the user, such as the sampling frequency and the bin resolution. While oversampling can in principle improve fidelity, it also generates redundant data and brings optimisation into the conversation. Improper binning can introduce artefacts. For example, in CV, the FFT spectrum exhibits weak even harmonics, which are absent from the FS spectrum and result from finite sampling and binning artefacts. For DPV, the FFT spectrum combines both contributions observed earlier: the low-frequency sweep component and the high-frequency pulse train. These appear as one spectrum with the sinc-shaped envelope of the high frequency pulses being dominant, illustrating how composite waveforms yield complex spectral distributions. In SWV, the FFT correctly shows the absence of even harmonics, but lobes appear around the odd harmonics due to binning artefacts, unlike the sharp lines observed in the Fourier series decomposition.

Together, these examples illustrate the phenomenon of spectral leakage [23], which arises because the FFT operates on finite, discrete

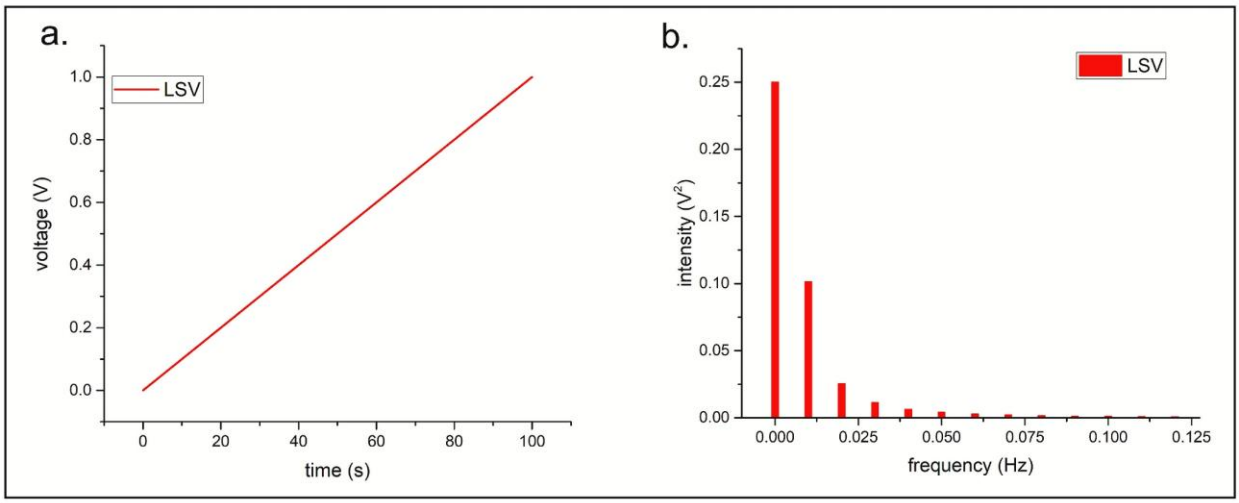


Fig. 8. Linear Sweep Voltammetry (LSV): (a) time-domain sawtooth waveform; (b) Fourier series spectrum showing both odd and even harmonics of the 10 mHz fundamental, with a strong DC component.

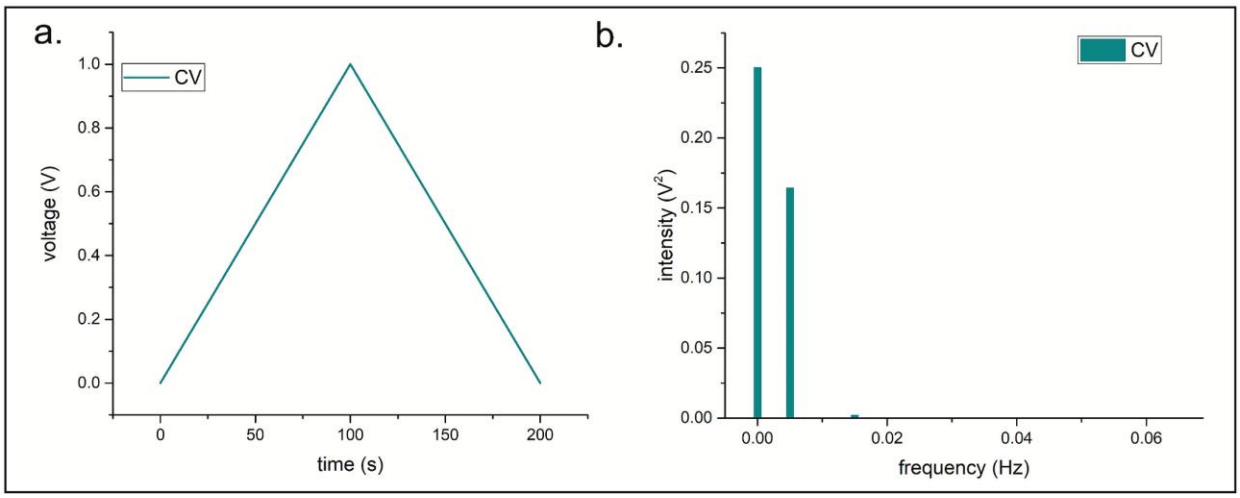


Fig. 9. Cyclic Voltammetry (CV): (a) triangular waveform; (b) Fourier series spectrum containing only odd harmonics (5 mHz fundamental), with rapid harmonic decay, and a DC component caused by amplitude asymmetry.

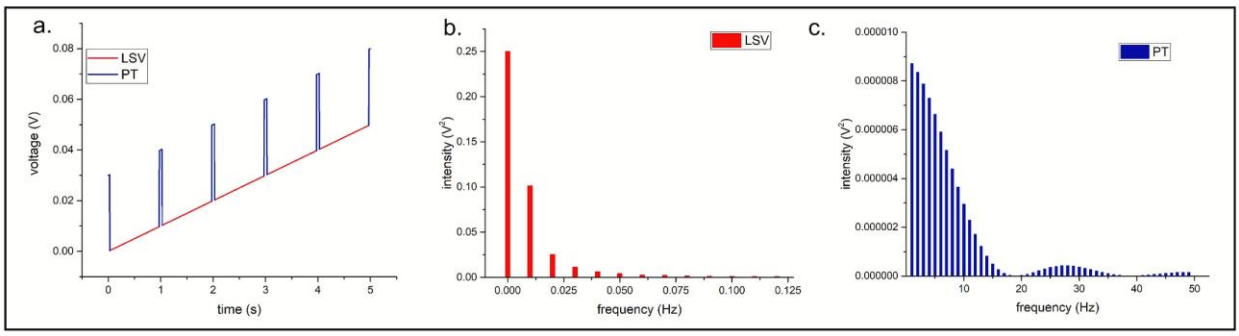


Fig. 10. Differential Pulse Voltammetry (DPV): (a) composite sawtooth plus pulse-train waveform (first 5 s shown); (b) low-frequency sawtooth Fourier series spectrum; (c) sinc-modulated pulse Fourier series spectrum with nulls at every 20th harmonic (5 % duty cycle).

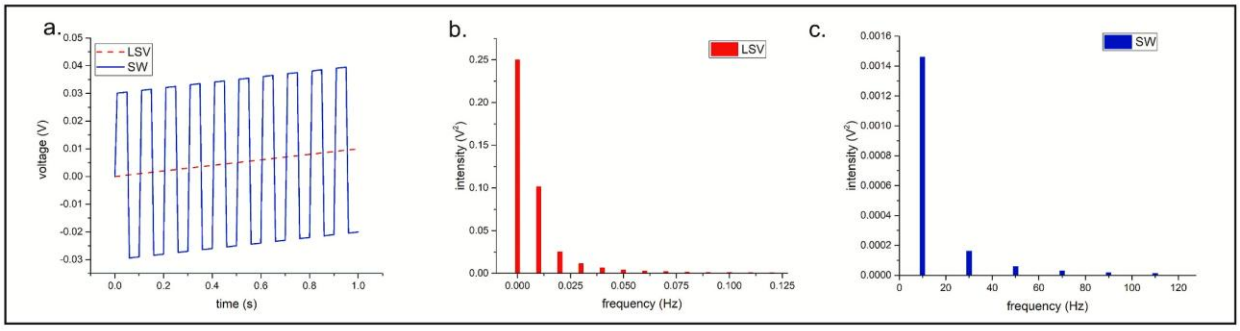


Fig. 11. Square Wave Voltammetry (SWV): (a) sawtooth plus square wave (first 1 s shown); (b) low-frequency sawtooth Fourier series spectrum; (c) square-wave Fourier series spectrum with odd harmonics only and slower decay.

signals rather than infinitely periodic, continuous ones. Unlike FS analysis, which assumes perfect periodicity and yields clean harmonic structure, the FFT outputs are susceptible to leakage, artefacts, and noise. Recognising these differences highlights that the discrete, finite nature of real signals broadens and redistributes spectral energy, yet the underlying harmonic relationships revealed by Fourier-series analysis remain embedded within experimental spectra. Without the knowledge of these effects, practitioners may misinterpret the FFT outputs. By placing the ideal mathematical FS results alongside the quasi-simulated FFT spectra, this framework informs readers what features to expect and what artefacts to avoid when applying spectral analysis in practice. Fourier decomposition shows that canonical voltammetric waveforms are inherently frequency-coded, while FFT artefacts can even collapse distinct techniques into deceptively similar spectra. Quantitative

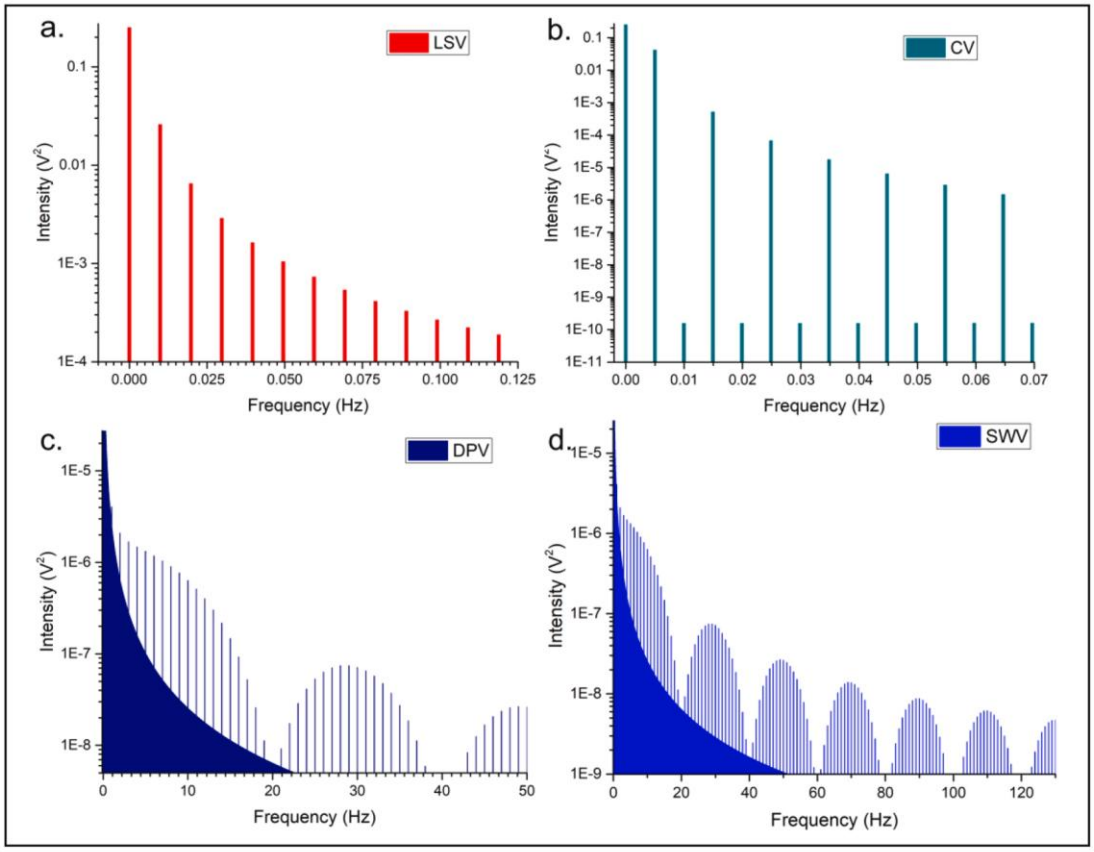


Fig. 12. Fast Fourier transform spectra of canonical voltammetric waveforms: (a) linear sweep voltammetry, (b) cyclic voltammetry, (c) differential pulse voltammetry, (d) square wave voltammetry. Quasi-simulations highlight artefacts from finite-sampling, binning effects, and spectral leakage that are absent from the Fourier series decompositions.

spectral descriptors are therefore essential for reliable discrimination and design.

3.4. From waveform tuning to electrochemical measurement design: a unified frequency-structured framework

ACV observations on capacitive and faradaic frequency dependence offer a framework for optimising voltammetric parameters to enhance faradaic signals and reduce capacitive interference. As discussed in Section 3.3, although techniques such as LSV, CV, DPV, and SWV operate in the time domain, their waveforms contain a spectrum of frequency components that stimulate faradaic and non-faradaic processes differently.

Across all voltammetric modes, frequency tuning governs the balance between diffusion-limited and capacitive-dominated regimes. In LSV and CV, slower scan rates reduce capacitive background and sharpen redox peaks, whereas excessively low rates lead to diffusion limitation. In DPV and SWV, longer pulse widths, intervals, or longer periods for square waves similarly suppress capacitive interference but must be optimised to maintain adequate diffusion. Overall, parameter selection represents a simple trade-off: too high a frequency amplifies capacitive currents, too low a frequency restricts mass transport.

This frequency-dependent behaviour links waveform design directly to measurement clarity and defines practical boundaries for each technique. For example, as seen from the SWV spectra in Section 3.3.4, choosing 10 Hz as the fundamental frequency seems reasonable. However, ACV results show a significant difference between 3 Hz and 10 Hz. At 10 Hz, RS oxidation is completely masked by the capacitive current, while at 3 Hz it remains faintly visible. The peaks for HQ and CC, while still visible at 10 Hz, are much better defined at 3 Hz. The square wave in SWV introduces the fundamental frequency along with a cascade of odd harmonics (30 Hz, 50 Hz, 70 Hz, …), increasing total frequency content and further exacerbating capacitive interference. At frequencies above 100 Hz, the peaks become only faintly discernible, blending into the error margins and rendering them nearly indistinguishable from the background. These results also show that an ACV frequency of 3 Hz sufficiently overcomes diffusion limitations, revealing distinct oxidation peaks over the capacitive background.

This frequency dependence also explains why different voltammetric techniques display varying sensitivities to the same electrochemical system. For instance, chronoamperometry effectively drives the excitation frequency towards zero, thereby suppressing capacitive currents almost entirely. DPV and SWV, on the other hand, introduce higher-frequency components and thus more capacitive current than cyclic voltammetry. Yet this apparent drawback is exploited at the output stage: potentiostats sample the current signal at the end of each pulse (as shown in the Supplement in Fig. S2), when the capacitive transient has decayed, allowing the residual faradaic current to be captured with sharper clarity. In this way, DPV can outperform CV in apparent sensitivity, even though its underlying frequency content is less favourable.

To extend the qualitative comparison of Fourier series and FFT spectra, we quantified waveform frequency characteristics using a set of spectral descriptors. These metrics were computed for LSV, CV, DPV, and SWV to characterise how signal energy is distributed across

frequencies. Table 1 summarises four key spectral parameters: spectral centroid, bandwidth, flatness, and low-frequency power fraction (below 30 Hz) comparing the theoretical FS and practical FFT data. Detailed formulations are provided in Supplementary Eqs. S11 to S14.

LSV and CV show extremely low centroids and bandwidths, while DPV and SWV show relatively low centroids, and their bandwidths are significantly wider due to the high-frequency components. The waveforms show generally flat spectra, and all demonstrate that most of their power lies below 30 Hz, chosen as a conservative soft limit since the ACV results show distinguishable peaks up to 50 Hz. Differences between the theoretical (FS) and practical (FFT) values reflect spectral leakage and finite sampling, as discussed in Section 3.3.5. The spectral metrics also highlight the pitfalls of applying the FFT without sufficient rigour. The practical spectra of both DPV and SWV yield identical values across all metrics, effectively implying that the two waveforms are the same. The FS results, however, show that their spectral structures differ markedly, demonstrating that uncritical use of the FFT can obscure essential distinctions between voltammetric techniques.

Collectively, these findings position spectral interpretation as a core tool for selecting parameters, designing sensors, and understanding mechanisms. Insights from ACV, which clearly showed how capacitive currents can mask faradaic signals above certain frequencies, directly inform the selection of time-domain parameters. By understanding that lower frequency components limit diffusion and higher frequency components tend to amplify capacitive effects, researchers can strategically select parameters in LSV, CV, DPV, and SWV to enhance the faradaic response. Careful time-domain parameter selection is essential for achieving adequate sensitivity in frequency-dependent electrochemical sensing. Taken together, the empirical ACV results, circuit model and waveform spectra converge on the same message: electrochemical measurement is inherently frequency-structured, and this approach offers a practical route to tune experiments for faradaic clarity.

To support practical application, Table 2 summarises the key frequency-domain features of common voltammetric waveforms and offers guidance on parameter choices to enhance faradaic signal detection by aligning waveform design with spectral behaviour.

Table 1
Spectral metrics of canonical voltammetric waveforms. Values describe how signal energy is distributed across frequencies and highlight their suitability for resolving frequency-specific redox and capacitive behaviours.

Waveform		Centroid (mHz)	Bandwidth (mHz)	Flatness	Low-frequency power fraction: Power below 30 Hz (%)
LSV	**Theoretical**	9.36	22.93	0	100
	Practical	4.42	24.13	0	100
CV	**Theoretical**	2.07	2.77	0	100
	Practical	0.75	1.95	0	100
DPV	**Theoretical**	10.64	142.4	0	100
	Practical	10.29	578.81	0	100
SWV	**Theoretical**	89.06	2137.61	0	99.92
	Practical	10.29	578.81	0	100

Table 2
Summary of waveform types, spectral characteristics, and tuning strategies for improving faradaic signal clarity.

Technique	Waveform model	Spectral insight and optimisation	Tuning guidance
LSV	Sawtooth wave	High low-frequency power; moderate scan rate balances redox clarity and time resolution	Lower scan rate to reduce capacitive background
CV	Triangle wave	Narrowband, odd harmonics; low centroid and flatness support mechanistic interpretation	Lower scan rate to enhance peak definition
DPV	Sawtooth + pulse train	Broad spectrum with clustered harmonics; optimise pulse interval to preserve peak shape	Use longer pulse width and interval for better resolution
SWV	Sawtooth + square wave	High centroid and flatness; reducing frequency improves faradaic visibility	Lower modulation frequency to minimise background interference
ACV	Sawtooth + sine wave	Spectral response depends on excitation; use peak-to-RMS to select optimal frequency	Adjust excitation frequency to isolate faradaic signal

4. Limitations of Fourier analysis in electrochemistry

The framework presented here is metrological rather than analytical in scope, addressing the structure and interpretation of electrochemical signals generally, independent of the underlying system and its corresponding specificities.

4.1. Noise

Electrochemical signals often contain noise from multiple sources that Fourier analysis cannot fully eliminate [24]. While it can help identify certain noise frequencies, when noise overlaps with the signal of interest, it can distort the spectra and hinder accurate interpretation of electrochemical processes [25].

4.2. Non-ideal conditions and non-linearities

Fourier analysis assumes linear systems but electrochemical systems can exhibit non-linear behaviour under non-ideal conditions [26]. Non-linearities introduce spurious harmonics that complicate analysis [27]. Uncompensated resistance [28] and frequency-dependent capacitive behaviour (capacitive dispersion) [29] contribute to these non-linearities.

4.3. Complexity of electrode kinetics

Intricate multi-step mechanisms [30] in electrochemical reactions often produce complex frequency responses. While Fourier analysis provides valuable information, researchers often need complementary techniques and modelling to decompose these complex responses and fully understand the underlying kinetics.

4.4. Hardware considerations

The present analysis treats the electrochemical cell as a continuous-time system, an assumption justified because electrochemical time constants are far longer than the sampling intervals of modern potentiostats. Although a fully discrete treatment using Z-transforms and difference equations could, in principle, be applied, it lies beyond the scope of this work. A comparison of analogue and digital signal modes using the same potentiostat has been discussed elsewhere [31], where quantisation and staircase inputs were shown to influence double-layer charging. Under typical experimental conditions, treating the system as continuous remains accurate and widely applicable. Fig. 13 illustrates the practical distinction between analogue and digital CV waveforms, where the exaggerated staircase shape of digital signals reflects quantised sampling.

4.5. Time resolution and stationarity

Fourier analysis assumes stationary signals and involves a trade-off between frequency and time resolution. Electrochemical systems are

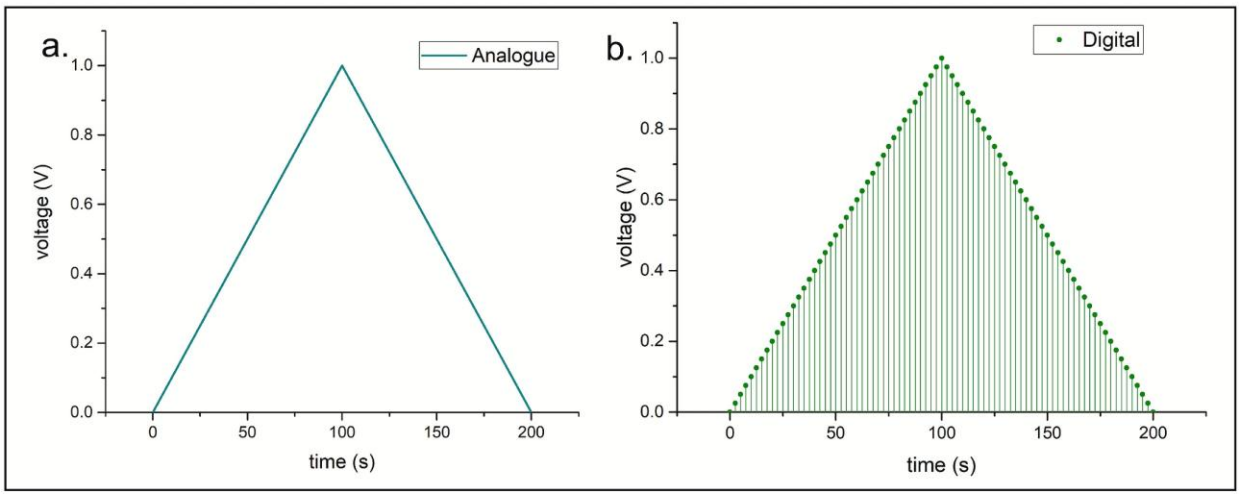


Fig. 13. CV waveforms in (a) analogue and (b) digital modes. Analogue mode produces a continuous triangular ramp, digital mode yields a quantised staircase approximation.

generally stochastic and can be non-stationary, and researchers must use specialised approaches [32] when applying Fourier analysis to systems with time-varying signals. While Fourier analysis provides valuable frequency-domain insights for stationary or quasi-stationary electrochemical signals, future studies could apply wavelet transforms [33] to systems with significant non-stationarity, using localised time–frequency analysis to gain additional insights.

5. Broader applications and future work

Fourier and frequency-domain approaches extend well beyond sensing [34] and can inform studies of corrosion [35], batteries [36], fuel cells [37], and electrocatalysis, where frequency-dependent transport and charge transfer also govern performance. Comparable behaviour has been observed in aniline electropolymerisation, where lower scan rates produced porous, high-capacitance films while higher rates yielded compact, resistive deposits [38]. Such examples highlight a common principle: excessive high-frequency content prioritises non-faradaic processes, whereas low-frequency components tend to enhance functional efficiency. Extending the present framework to these broader contexts could therefore support more rational design of electrochemical systems and materials.

6. Conclusion

This study demonstrates that electrochemical measurement is inherently frequency-structured. The behaviour of the electrochemical interface cannot be fully understood in the time domain alone, and frequency-domain analysis provides the complementary view required to separate and quantify the intertwined faradaic and capacitive processes.

AC voltammetry (ACV) established the experimental foundation for this framework. By varying the excitation frequency, ACV revealed that capacitive currents increase proportionally with frequency while faradaic currents become progressively masked. This behaviour was reproducible across three benzenediols with distinct redox chemistries, confirming that the phenomenon originates from the measurement system rather than the analytes.

A modified Randles equivalent circuit provided the mathematical basis for interpreting this response. Through its frequency-dependent elements, which represent charge transfer, diffusion and double-layer capacitance, the model explains how the relative magnitudes of faradaic and capacitive currents evolve with frequency. It defines the balance between diffusion-limited and capacitance-dominated regimes and clarifies the transition between them.

Fourier and spectral analysis of canonical voltammetric waveforms extended these insights into a general framework. The harmonic structure of linear sweep, cyclic, differential pulse and square wave voltammetry links waveform geometry directly to frequency content and therefore to the visibility of faradaic signals. Quantitative spectral descriptors such as the centroid, bandwidth, flatness and low-frequency power fraction provide practical metrics for comparing and optimising waveform parameters.

Together, these three components form a coherent and logical methodology for interpreting and designing electrochemical measurements. The framework guides the optimal selection of time-domain parameters to reduce capacitive interference, enhance faradaic visibility and improve measurement interpretability.

Although demonstrated here using benzenediol detection on Pt/C-modified screen-printed electrodes, the principles are broadly applicable to any system governed by convolved diffusion, charge-transfer and capacitive processes. Extending frequency-domain analysis to areas such as corrosion, electrocatalysis and energy storage can enable better insights into electrochemical system behaviours.

In summary, frequency-domain analysis provides a unified and robust approach to link electrochemical experimental design with interfacial dynamics. The study traces this relationship in reverse, from output spectra obtained by ACV, through system behaviour modelled by the modified Randles circuit, to input spectra defined by waveform geometry. This reverse progression mirrors the logic of signal analysis, connecting measurement, theory, and design within a single framework. By combining ACV results, equivalent circuit modelling and Fourier analysis, this work establishes a foundation for potential electrochemical methods that treat frequency not as a peripheral or specialist variable but as an intrinsic coordinate of electrochemical behaviour. Ultimately, this perspective reframes electrochemical measurement as a spectral science, where time-domain measurements are understood as projections of frequency-structured interfacial dynamics.

7. Experimental section: catalyst, sensor, analyte, and measurement setup

7.1. Catalyst preparation

The catalyst ink was prepared by dispersing 20 wt% Pt/C [platinum nanoparticles (2–3 nm) on Vulcan XC-72R (20–50 nm) support] sourced from FuelCellStore, in 0.995 ml of absolute ethanol. To this suspension, 5 µl of a 5 % Nafion solution in absolute ethanol (Sigma Aldrich) was added as a binder. The suspension was then ultrasonicated using a 500 W probe at 25 % amplitude for 2 min to ensure uniform dispersion. The ink was used immediately to prevent particle settling and agglomeration.

7.2. Sensor element fabrication

Sensor elements were fabricated using Metrohm DropSens DS150 screen-printed electrodes (SPE) with carbon working electrode (WE), platinum counter electrode (CE), and silver reference electrode (RE). The WE surface was cleaned with deionised water and ethanol, then dried on a hot plate maintained at 55 °C. 10 µl of catalyst ink was pipetted onto the WE on the hot plate to speed drying. Care was taken to isolate the CE and RE from deposition spill-over. The fabricated sensor elements were then stored in a dry, sealed container to prevent tarnishing of the silver contacts and RE. Each 10 µl aliquot of ink contained 10 µg of catalyst (1 mg/ml), of which 20 % was Pt, resulting in a theoretical metal loading of 2 µg per sensor element. Given the WE diameter of 4 mm, this corresponds to a Pt loading of approximately 160 ng mm^{-2} on the WE surface.

7.3. Analyte solution preparation

Analyte solutions of various concentrations were prepared by diluting stock solutions of each benzenediol. Catechol (CC), resorcinol (RS) and hydroquinone (HQ), all of analytical grade purity (>99 %) and purchased from Sigma Aldrich, were used. Stock solutions of each benzenediol (50 mM) were created by dissolving the analyte in 1 M HCl (prepared by diluting 37 % HCl) with stirring, aided by an ultrasonic bath. Working solutions were prepared by diluting the stock with 1 M HCl to reach target concentrations. For each measurement, 75 µl of the analyte solution was carefully dispensed onto the SPE surface, ensuring complete coverage of all three electrodes.

7.4. Instruments and electrochemical measurements

AC voltammetry (ACV) measurements were performed using a PalmSens4 potentiostat with the following parameters: scan rate: 10 mV s^{-1}; E_{ac}: 10 mV (root-mean-square value, RMS); E_{step}: 10 mV; E_{begin} = 0 V, E_{end} = 1 V (all vs quasi-reference Ag); frequency range: 3 Hz to 2000 Hz.

CRediT authorship contribution statement

Abhilash Krishnamurthy: Writing – review & editing, Writing – original draft, Visualization, Validation, Software, Methodology, Investigation, Formal analysis, Data curation, Conceptualization. **Kristina Žagar Soderžnik:** Validation, Supervision, Resources, Project administration, Methodology, Investigation, Funding acquisition.

Declaration of competing interest

The authors declare that they have no known competing financial interests or personal relationships that could have appeared to influence the work reported in this paper.

Acknowledgements

The authors gratefully acknowledge the Slovenian Research and Innovation Agency (ARIS) for their financial contribution to this work provided through grants: P2–0084 (Programme Nanostructured Materials), J2–1739 (High Performance Nanostructured Acrylamide Sensors), J2-3051 (SensePMC), and PR-09874 (Young Researcher Project). The authors also thank Pika Štefančič for her assistance with the graphical artwork.

Appendix A. Supplementary data

Supplementary data to this article can be found online at https://doi.org/10.1016/j.measurement.2025.119706.

Data availability

Data will be made available on request.

References

[1] A.J. Bard, L.R. Faulkner, H.S. White, Electrochemical methods: fundamentals and applications, John Wiley & Sons, 2022.
[2] V.D. Parker, Linear sweep and cyclic voltammetry, in: Comprehensive Chemical Kinetics, Elsevier, 1986, pp. 145–202.
[3] A.P. Brown, F.C. Anson, Cyclic and differential pulse voltammetric behavior of reactants confined to the electrode surface, Anal. Chem. 49 (11) (1977) 1589–1595.
[4] L. Ramaley, M.S. Krause, Theory of square wave voltammetry, Anal. Chem. 41 (11) (1969) 1362–1365.
[5] R.W. Newcomb, Analysis in the time domain, in: Circuit Analysis and Feedback Amplifier Theory, CRC Press, 2018, p. 9.
[6] P.M. Biesheuvel, S. Porada, J.E. Dykstra, The difference between Faradaic and non-Faradaic electrode processes, (2018), arXiv preprint arXiv:1809.02930.
[7] P.S. Singh, S.G. Lemay, Stochastic processes in electrochemistry, Anal. Chem. 88 (10) (2016) 5017–5027.
[8] S.O. Engblom, J.C. Myland, K.B. Oldham, Must ac voltammetry employ small signals? J. Electroanal. Chem. 480 (1–2) (2000) 120–132.
[9] T. Kadyk, Y. Sun, J. Kaur, A. Kulikovsky, M. Eikerling, Frequency response diagnostics of electrochemical energy devices, Curr. Opin. Electrochem. 42 (2023) 101378.
[10] A. Vretblad, A. Vretblad, Fourier analysis and its applications, Springer, New York, 2003.
[11] R.J. Marks, Handbook of Fourier analysis & its applications, Oxford University Press, 2009.
[12] Y. Katznelson, An introduction to harmonic analysis, Cambridge University Press, 2004.
[13] B.Y. Chang, S.M. Park, Electrochemical impedance spectroscopy, Annu. Rev. Anal. Chem. 3 (1) (2010) 207–229.
[14] A. Krishnamurthy, Z. Samardžija, Š. Trafela, A. Korent, S. Šturm, K.Ž. Soderžnik, Electrochemical detection of benzenediols using carbon-supported catalysts, Electrochimica Acta 493 (2024) 144389.
[15] M.A. Ghanem, Electrocatalytic activity and simultaneous determination of catechol and hydroquinone at mesoporous platinum electrode, Electrochem. Commun. 9 (10) (2007) 2501–2506.
[16] K. Ngamchuea, B. Tharat, P. Hirunsit, S. Suthirakun, Electrochemical oxidation of resorcinol: mechanistic insights from experimental and computational studies, RSC Adv. 10 (47) (2020) 28454–28463.
[17] W.T. Cochran, J.W. Cooley, D.L. Favin, H.D. Helms, R.A. Kaenel, W.W. Lang, P. D. Welch, What is the fast Fourier transform? Proc. IEEE 55 (10) (1967) 1664–1674.
[18] S.R. Taylor, E. Gileadi, Physical interpretation of the Warburg impedance, Corrosion 51 (9) (1995) 664–671.
[19] S. Westerlund, L. Ekstam, Capacitor theory, IEEE Trans. Dielectr. Electr. Insul. 1 (5) (1994) 826–839.
[20] B.B. Damaskin, O.A. Petrii, Historical development of theories of the electrochemical double layer, J. Solid State Electrochem. 15 (2011) 1317–1334.
[21] K.J. Vetter, Electrochemical kinetics: theoretical aspects, Elsevier, 2013.
[22] H. Züchner, N. Boes, Electrochemical methods for diffusion measurements, Berichte Der Bunsengesellschaft Für Physikalische Chemie 76 (8) (1972) 783–790.
[23] A. Breitenbach, Against spectral leakage, Measurement 25 (2) (1999) 135–142.
[24] A. Aballe, M. Bethencourt, F.J. Botana, M. Marcos, Wavelet transform-based analysis for electrochemical noise, Electrochem. Commun. 1 (7) (1999) 266–270.
[25] R.A. Cottis, Interpretation of electrochemical noise data, Corrosion 57 (3) (2001) 265–285.
[26] M.T. Koper, Non-linear phenomena in electrochemical systems, J. Chem. Soc. Faraday Trans. 94 (10) (1998) 1369–1378.
[27] K. Krischer, Nonlinear dynamics in electrochemical systems, Adv. Electrochem. Sci. Eng. 8 (2002) 89–208.

[28] K.B. Oldham, The effect of uncompensated resistance on the potential-step method of investigating electrochemical kinetics, J. Electroanalyt. Chem., 11(3) (1966), 171–187.
[29] T. Pajkossy, Impedance of rough capacitive electrodes, J. Electroanal. Chem. 364 (1–2) (1994) 111–125.
[30] M.C. Lefebvre, Establishing the link between multistep electrochemical reaction mechanisms and experimental Tafel slopes, in: Modern Aspects of Electrochemistry, Springer, US, Boston, MA, 2002, pp. 249–300.
[31] A. Krishnamurthy, K. Žagar Soderžnik, Influence of Potentiostat Hardware on Electrochemical Measurements, Sensors 24 (15) (2024) 4907.
[32] D. Griffin, J. Lim, Signal estimation from modified short-time Fourier transform, IEEE Trans. Acoust. Speech Signal Process. 32 (2) (1984) 236–243.
[33] P.M. Bentley, J.T.E. McDonnell, Wavelet transforms: an introduction, Electr. Commun. Eng. J. 6 (4) (1994) 175–186.
[34] D.W. Kimmel, G. LeBlanc, M.E. Meschievitz, D.E. Cliffel, Electrochemical sensors and biosensors, Anal. Chem. 84 (2) (2012) 685–707.
[35] R.H. Brown, R.B. Mears, The electrochemistry of corrosion, Trans. Electrochem. Soc. 74 (1) (1938) 495.
[36] K. Schmidt-Rohr, How batteries store and release energy: explaining basic electrochemistry, J. Chem. Educ. 95 (10) (2018) 1801–1810.
[37] S. Srinivasan, Fuel cells: from fundamentals to applications, Springer Science & Business Media, 2006.
[38] A. Kellenberger, D. Ambros, N. Plesu, Scan rate dependent morphology of polyaniline films electrochemically deposited on nickel, Int. J. Electrochem. Sci. 9 (12) (2014) 6821–6833.

4.5 Hardware Influence on Electrochemical Response (Analogue vs Digital)

This section evaluates the hardware layer of the sensing workflow, focusing on how potentiostat design, specifically analogue versus digital voltage scan modes, affects electrochemical measurements. Using the Metrohm VIONIC potentiostat, which supports both true linear analogue and staircase digital scan options, CV was performed to study the redox behaviour of HQ on Pt/C-modified SPEs.

Experiments conducted at scan rates between 10 and 100 mV s^{-1} revealed subtle but consistent differences between the two scan modes. Digital scans showed higher peak currents compared to analogue scans, particularly at higher scan rates. These elevated currents were attributed to capacitive charging effects, as the staircase signal induces discrete potential jumps that act as rapid perturbations to the system. These transitions can provoke transient, non-faradaic responses that distort the faradaic signal.

In contrast, the analogue scan mode produced smoother voltammograms with more organic capacitive behaviour. This behaviour was confirmed through simulations of a Randles-type equivalent circuit using MATLAB, which compared system responses under ramp (analogue) and step (digital) excitations. The results demonstrated that analogue signals yield more accurate representations of redox processes by avoiding abrupt current spikes induced by step transitions.

Although modern digital potentiostats can approximate analogue behaviour with increased resolution, the results show that true analogue scanning still provides cleaner and more interpretable signals. This distinction becomes especially important when working with systems that involve subtle redox features or are sensitive to capacitive distortion. Figure 4.4 contrasts analogue and digital waveform characteristics, illustrating how continuous and quantised signal representations coexist within modern potentiostat architectures.

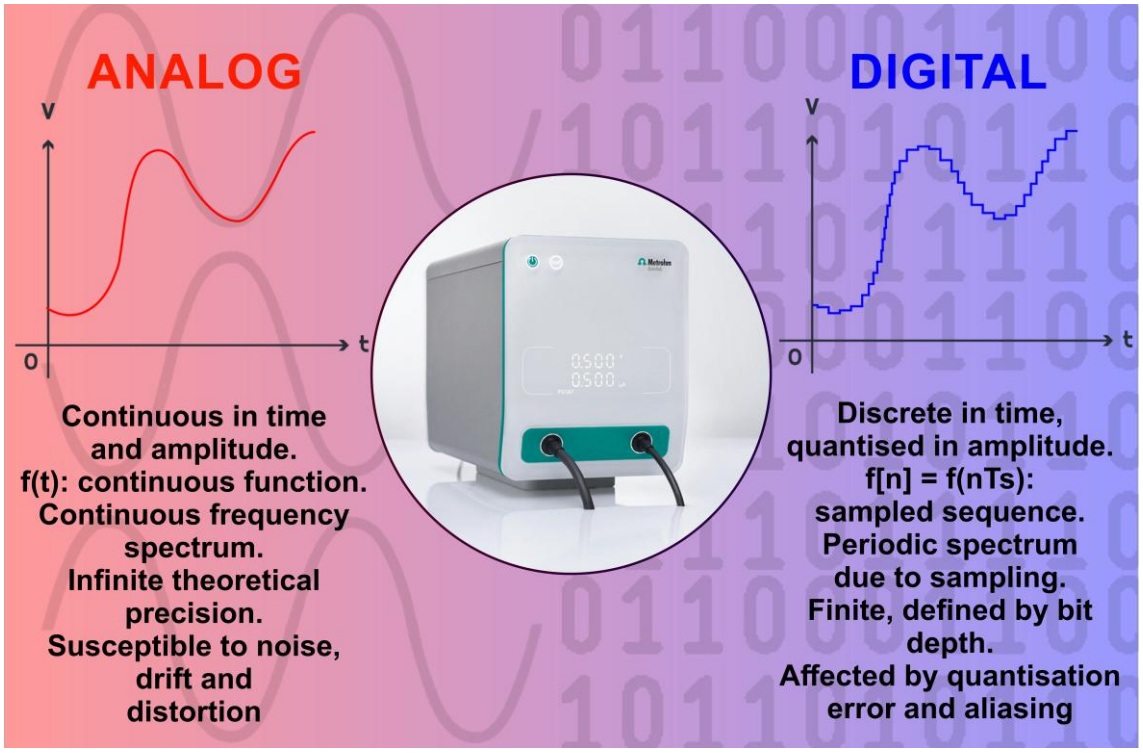


Figure 4.5: Comparison of analogue and digital waveforms, illustrating signal representation in potentiostat systems. Concept adapted from Krishnamurthy et al., Sensors 24 (2024) 4907 (https://doi.org/10.3390/s24154907).

Full experimental and simulation details can be found in the original publication: Krishnamurthy, A.; Žagar Soderžnik, K. Influence of Potentiostat Hardware on Electrochemical Measurements. Sensors 2024, 24(15), 4907. https://doi.org/10.3390/s24154907. The print version is shared in the following pages under the CC BY 4.0 license agreement.

sensors

MDPI

Article

Influence of Potentiostat Hardware on Electrochemical Measurements

Abhilash Krishnamurthy [1,2,*] and Kristina Žagar Soderžnik [1,2]

[1] Department for Nanostructured Materials, Jožef Stefan Institute, Jamova 39, 1000 Ljubljana, Slovenia; kristina.zagar@ijs.si
[2] Jožef Stefan International Postgraduate School, Jamova 39, 1000 Ljubljana, Slovenia
* Correspondence: abhilash.krishnamurthy@ijs.si

Abstract: We describe two operating modes for the same potentiostat, where the redox processes of hydroquinone in a hydrochloric acid medium are contrasted for cyclic voltammetry (CV) as functions of a digital/staircase scan and an analogue/linear scan. Although superficially there is not much to separate the two modes of operation as an end user, differences can be seen in the voltammograms while switching between the digital and analogue modes. The effects of quantization clearly have some impact on the measurements, with the outputs between the two modes being a function of the equivalent-circuit model of the electrochemical system under investigation. Increasing scan rates when using both modes produces higher peak redox currents, with the differences between the analogue and digital modes of operation being consistent as a function of the scan rate. Differences between the CV loops between the analogue and digital modes show key differences at certain points along the scans, which can be attributed to the nature of the electrolyte affecting the charging and discharging processes and consequently changing the peak currents of the redox processes. The faradaic processes were shown to be independent of the scan rates. Simulations of the equivalent-circuit behaviour show differences in the responses to different input signals, i.e., the step and ramp responses of the system. Both the voltage and current steps and ramp responses showed the time-domain behaviour of distinct elements of the equivalent electrochemical circuit model as an approximation of the applied digital and analogue CV input signals. Ultimately, it was concluded that similar parameters between the two modes of operation available with the potentiostat would lead to different output voltammograms and, despite advances in technology, digital systems can never fully emulate a true analogue system for electrochemical applications. These observations showcase the value of having hardware capable of true analogue characteristics over digital systems.

Keywords: electrochemical sensing; potentiostat; hardware; analogue; digital; cyclic voltammetry

check for updates

Citation: Krishnamurthy, A.; Žagar Soderžnik, K. Influence of Potentiostat Hardware on Electrochemical Measurements. *Sensors* **2024**, *24*, 4907. https://doi.org/10.3390/s24154907

Academic Editor: Alisa Rudnitskaya

Received: 31 May 2024
Revised: 17 July 2024
Accepted: 25 July 2024
Published: 29 July 2024

Copyright: © 2024 by the authors. Licensee MDPI, Basel, Switzerland. This article is an open access article distributed under the terms and conditions of the Creative Commons Attribution (CC BY) license (https://creativecommons.org/licenses/by/4.0/).

1. Introduction

Utilizing the available hardware to its maximum benefit also extends to phenomena that can sometimes go unnoticed to most end users. While modern devices with their well-optimized, cutting-edge "digital" hardware [1] and software advances can obtain the desired results for most measurements, they are still only approximating the behaviour of a true "analogue" device [2]. In order to fully understand the differences between digital and analogue devices, a deeper look is necessary into how the data signals [3] are transmitted in computation. Analogue systems are continuous in nature, while digital signals are discrete. In particular, the digital signals used in computing are predominantly encoded as binaries made up of 0s and 1s. The modern digital computing [4] revolution has rendered older analogue computing systems [5] almost obsolete, as digital devices possess two major advantages over their analogue counterparts. Firstly, digital systems allow the use of memory devices based on semiconductors [6], which can store the information more reliably compared to analogue memory devices such as magnetic tapes [7]. The second advantage is that digital signals and systems are inherently more immune to noise [8] when compared to analogue ones since the signals are encoded as binary [9]. However,

Sensors **2024**, *24*, 4907

this encoding also brings with it some drawbacks, such as a time lag since most of the signals originating in nature are analogue and would need to be encoded into a digital signal to be read by a digital computer. This encoded signal is a mere approximation of reality. Since the data must be made to fit into discrete chunks, quantization errors can lead to compounding, especially with numbers that have extremely large or small magnitudes. This is especially noticeable in, for example, sensors, which generally operate on analogue inputs. These data lose their integrity during the encoding and decoding processes [10]. Figure 1 shows the difference between an analogue and a digital signal, albeit exaggerated as these differences are usually only visible upon close inspection with special hardware. This is because modern devices now have the ability to produce nearly analogue signals using digital hardware.

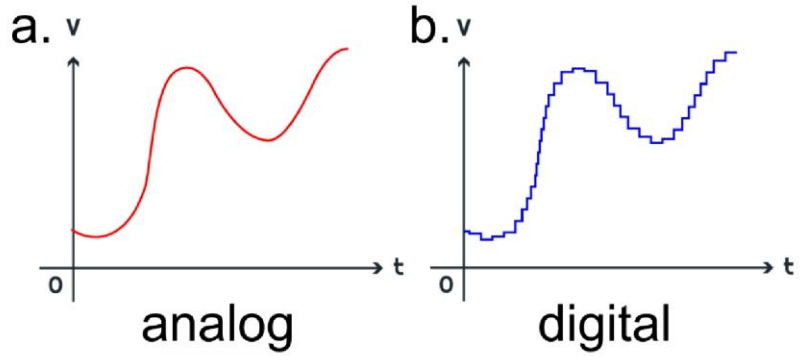


Figure 1. Exaggerated waveforms showcasing the infinitesimal differences between (**a**) an analogue signal and (**b**) a digital signal.

The use of analogue [11] hardware in an electrochemical [12] potentiostat [13] offers an optimistic change towards a better understanding of the processes that occur when subjecting electrochemical systems to traditional measurement techniques [14]. Focusing on one method, cyclic voltammetry (CV) [15], the Metrohm VIONIC potentiostat [16] offers the user the choice of performing CVs as either digital (staircase) (Figure 1b) or analogue (linear) (Figure 1a). The CV is generally accomplished by starting the measurement at a given potential, increasing or decreasing the potential to another value over a given period at a predetermined rate of change in the potential called the "scan rate" and then returning to the initial potential, hence, cyclic. The rate of change in the potential plays a large role in electrochemical systems as the electrolyte is inevitably subjected to the charging and discharging processes of the double layer [17]. The double layer is modelled as an imperfect capacitor and represents the non-faradaic processes, whereas the redox processes are represented by a resistor and correspond to the faradaic processes. Most electrochemical systems also consist of an uncompensated resistance in series, usually the resistance of the electrolytic solution; these three components are shown in Figure 2, the simplest electrical model of an electrochemical system known as a Randles' circuit [18].

In order to understand the charging and discharging behaviour of a capacitor, let us take a look at the circuit in Figure 3, where a resistor and a capacitor are connected in series to a power source and the output voltage is the voltage across the capacitor.

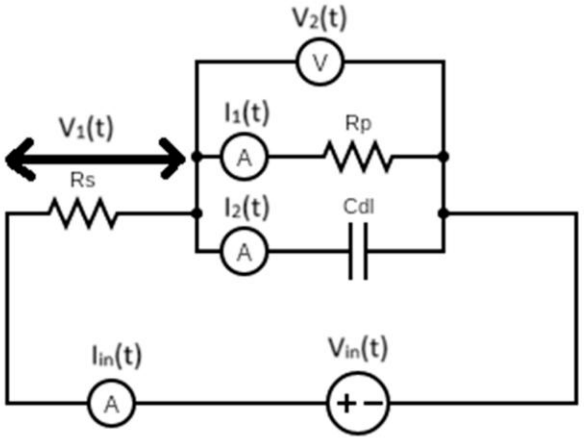


Figure 2. Randles' circuit. Where, $V_{in}(t)$ = input voltage, $I_{in}(t)$ = input current, $V_1(t)$ = output voltage across the solution resistance R_S, $V_2(t)$ = output voltage across the polarization resistance R_p and double-layer capacitance C_{dl}, $I_1(t)$ = output current through the polarization resistance R_p, $I_2(t)$ = output current through the double-layer capacitance C_{dl}.

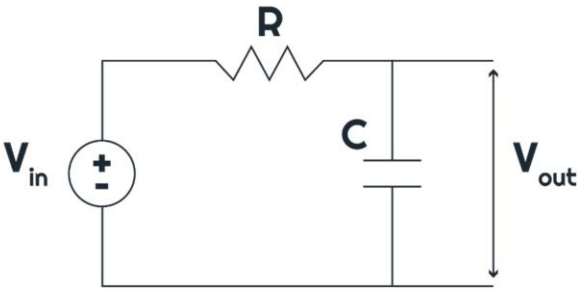


Figure 3. Series RC circuit.

The electrical circuit forms a first-order system [19] since the capacitor is the only energy-storage device. Solving the first-order differential equation gives the general solutions in Equations (1) and (2).

For charging,

$$V_O = V_i\left(1 - e^{\frac{-t}{RC}}\right) \quad (1)$$

For discharging,

$$V_O = V_i\left(e^{\frac{-t}{RC}}\right) \quad (2)$$

Here, V_O is the output voltage (across the capacitor), V_i is the input voltage, R is the resistance, and C is the capacitance. The factor "RC" is defined as the time constant of the circuit, denoted by τ. When $t = \tau$, we obtain $V_O = 0.632\ V_i$ for charging and $V_O = 0.368\ V_i$ for discharging. Hence, the definition of the time constant is the time required for the output voltage to rise to 63.2% of the input voltage during charging or fall to 36.8% of the input voltage during discharging. As long as the R and C values are fixed, the time constant is also fixed. If $t = 5\tau$, $V_O = 0.993\ V_i \approx V_i$ for charging and $V_O = 0.006\ V_i \approx 0$ for discharging. Thus, it takes about five time-constant durations for the output to reach nearly the same value as the input. Figure 4 shows the charging and discharging curves of the circuit in Figure 3, indicating the time constant for both scenarios.

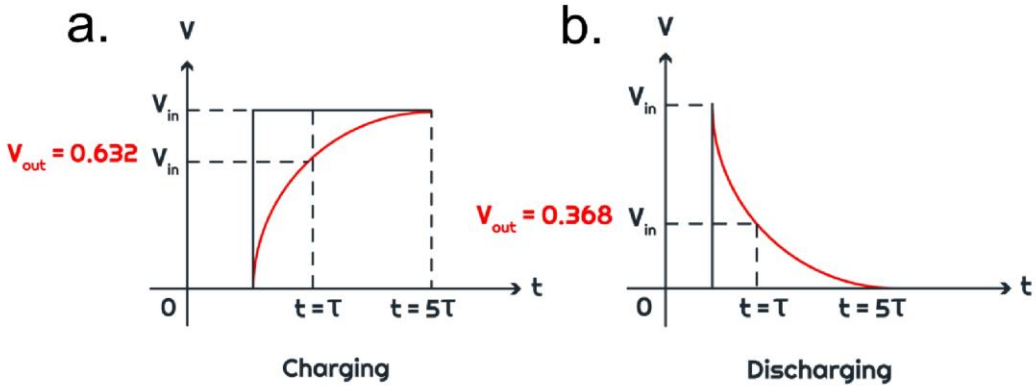


Figure 4. (**a**) Charging curve of series RC circuit. (**b**) Discharging curve of series RC circuit.

Looking at Figure 1 again, which shows that analogue signals are smooth and continuous while digital signals are discrete with abrupt jumps, each abrupt jump can be considered as a voltage step, either up or down, as shown in Figure 4a,b. Given that the Randles' circuit shown in Figure 3 has a capacitor, the electrochemical system will be subjected to charging and discharging with every quantization jump of a digital signal and thereby experience a comparative "lag" in contrast to the smooth analogue curve. For the end user, this is to be verified with experimental data comparing the analogue and digital CVs.

The state-of-the-art electrochemical potentiostats on the market are still predominantly digital-hardware-based systems, subject to all the aforementioned pros and cons inherent to digital electronic systems. Electrochemical potentiostats with analogue-hardware-based systems have existed in a niche space where the accuracy of the measurements has priority over the device complexity and cost [20], usually as an application-specific add-on [21]. However, now with devices such as the Metrohm VIONIC including the analogue hardware as an option for end users, the prospects of having general-purpose analogue computers as a readily available measurement tool in electrochemical labs adds considerable value when studying electrochemical systems much more thoroughly.

2. Experimental Section

Materials: A 5 mM hydroquinone solution in 1 M HCl was prepared using analytical grade hydroquinone (>99%) and 37% HCl purchased from Sigma Aldrich, mixed with Milli-Q deionized water. Sensor elements were prepared using Metrohm DRP150 electrodes (working electrode: carbon; counter electrode: platinum; reference: silver) modified with solution of 20% platinum on carbon black (Vulcan XC-72R) catalyst purchased from Fuel Cell Store, 1 W Bronze Ln, Bryan, TX 77807, USA with Pt particle sizes of 2–3 nm. An ink of the aforementioned 20% Pt on carbon was prepared by dispersing 1 mg of the catalyst in a solution containing 0.995 mL of absolute ethanol and 5 µL of 5% Nafion solution in ethanol as the binder. Then, 10 µL of the catalyst ink was drop cast only on the working electrode after cleaning the surface with DI water and ethanol and dried on a hot plate at 60 °C. The sensor elements were then allowed to cool and dry overnight in a cool, dark environment before being used for measurements.

Instruments: CVs were measured using a Metrohm VIONIC, on loan from Primalab d.o.o., Pod Bregom 27, 3313 Breg pri Polzeli, manufactured by Metrohm AG, Ionenstrasse, 9100 Herisau, Switzerland Parameters for CV: scan window: 0 V to 1 V; scan rates: 10 mVs^{-1}, 25 mVs^{-1}, 50 mVs^{-1}, 100 mVs^{-1}; number of scans: 3; potential step size: approximately 1 mV (digital). All mentioned potentials were against a silver reference electrode. All electrochemical measurements were conducted in a climate-controlled laboratory setup at STP.

Sensors **2024**, *24*, 4907

Simulations were performed with MATLAB R2017b using the control systems toolbox to obtain the step and ramp responses.

3. Results and Discussion

3.1. Effect of Scan Rate

The scan rate plays an important role in the value of the measured current in all the potentiodynamic electrochemical measurements. The simplest definition of the scan rate is the rate of change in the potential with respect to time. The instantaneous current flowing through a capacitor [22] is given by Equation (3).

$$i_C = C_{dl} \frac{dV}{dt} \tag{3}$$

where i_C = capacitive current (A), C_{dl} = double-layer capacitance (F), and V = applied potential (V).

The capacitive current is directly proportional to $\frac{dV}{dt}$, which is the rate of change in voltage with respect to time, i.e., the scan rate. Faster scan rates should yield higher overall measured currents, simply due to the larger contribution of the capacitive current compared to the faradaic current. This is evident in Figure 5, comparing analogue and digital CVs at different scan rates.

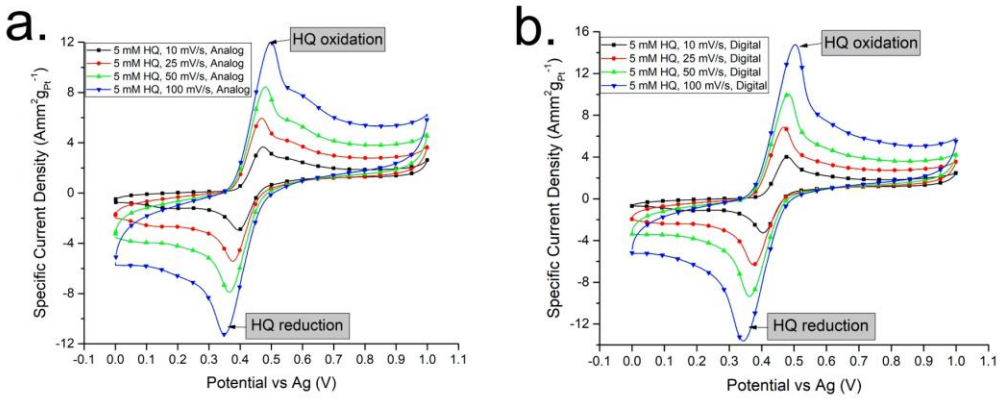


Figure 5. (**a**) Analogue CVs of hydroquinone redox at different scan rates. (**b**) Digital CVs of hydroquinone redox at different scan rates.

In both the analogue and digital CVs, we can see that increasing the scan rates produces a higher overall measured output current as we go from 10 mVs^{-1} to 25 mVs^{-1}, 50 mVs^{-1}, and 100 mVs^{-1} despite having the same concentration of hydroquinone (5 mM) [23]. This agrees with the theory that the increase in current is due to the increase in the capacitive current only, with no contribution from the faradaic current of the redox of hydroquinone.

3.2. Comparing Analogue and Digital Measurements

Although Figure 5a,b seem to suggest that the analogue and digital CVs are identical, there are some differences visible upon closer inspection of the curves. The main difference is that the currents produced with the digital CVs seem to be higher compared to the currents produced with the analogue CVs, comparing the Y-axes of both graphs. In order to take a deeper look, comparing each analogue CV to the digital CV measured at the same scan rate should provide a better perspective, as show in Figure 6.

Looking at each scan rate individually and comparing the analogue and digital measurements, subtle differences can be observed. While the overall profile of both CVs appears almost identical, in every measurement the digital measurement produces a higher peak current for both the oxidation of hydroquinone to 1,4-benzoquinone and during the reduction in 1,4-benzoquinone back to hydroquinone. There is also a subtle bump in the

analogue curve where it momentarily produces a higher current compared to the digital CV between 0.5 and 0.6 V vs. Ag reference. Both these differences can be attributed to the nature of the CVs themselves: as the analogue CV is smooth, it produces a more natural output-current curve. The digital CV has a quantization limit, and being abrupt is probably subjecting the electrolytic solution of hydroquinone in hydrochloric acid to experience a "lag", which would appear due to minor charging and discharging of the solution in an attempt to follow the sharp changes in the digital signal. This would explain why the higher peak currents are observed during both oxidation and reduction, as the electrolyte is not undergoing as much of the charging and discharging with the analogue signal due to the smoother and more gradual rise and fall in the potential over time.

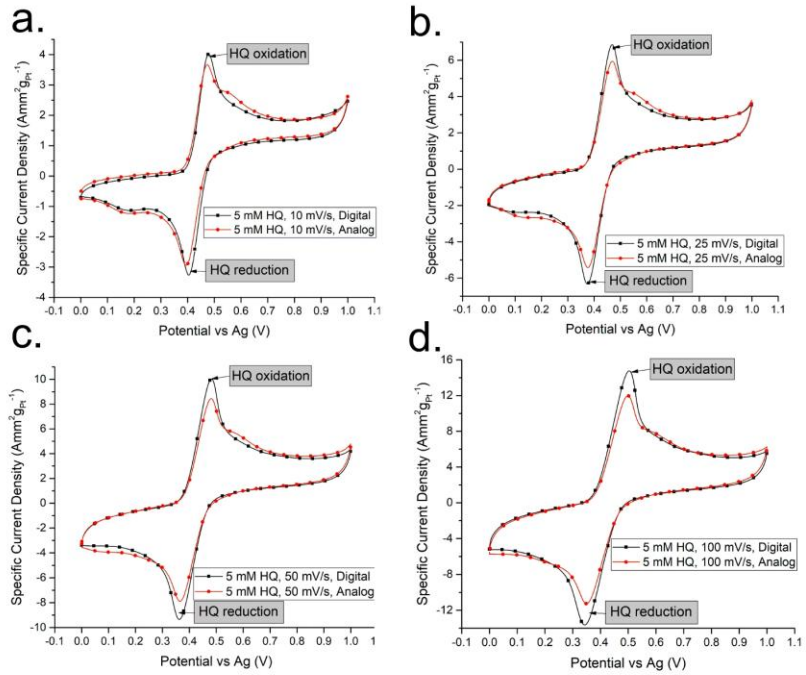


Figure 6. Analogue vs. digital CVs of hydroquinone redox at different scan rates: (**a**) 10 mVs^{-1}, (**b**) 25 mVs^{-1}, (**c**) 50 mVs^{-1}, (**d**) 100 mVs^{-1}.

While on the surface it is easy to associate all the noticeable changes to the switching of the operational modes on the potentiostat, the internal electronics and the employed algorithms within the device also play a key role in how the data obtained are processed. Quantization errors caused by the conversion of the data between analogue and digital form, which is necessary for the data to be processed by the computer, can also be a factor, and the total harmonic distortion of the analogue-to-digital converter (ADC) determines the integrity of the signal after conversion, which is a function of the resolution of the ADC. However, this information is not readily available to the end users and, for all intents and purposes, the potentiostat is a black box for the end user.

3.3. Simulation of Equivalent-Circuit Behaviour Using MATLAB

Assuming the electrochemical system to be ideal, the behaviour can be simulated by analysing the Randles' circuit shown in Figure 2. The primary elements of interest are the polarization resistance, the path through which the current produces useful work, and the double-layer capacitance, which is responsible for the observed charging–discharging effects. By determining the transfer functions for the element of interest, the voltages across

and the currents through all the circuit elements can be expressed as a function of the input parameter.

3.4. Step Response and Ramp Response

The step response and the ramp response of any system are defined as the system's behaviour when subjected to the unit-step function and the unit-ramp function, which are shown in Figure 7 [24].

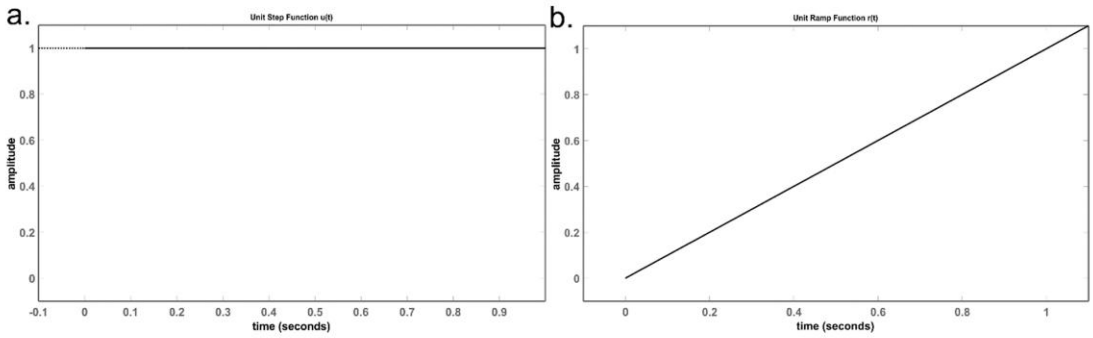


Figure 7. (**a**) Unit-step function. (**b**) Unit-ramp function.

The unit-step function, also known as the Heaviside step function, is defined as follows in Equation (4).

$$H(t) \text{ or } u(t) = \begin{cases} 1, & t \geq 0 \\ 0, & t < 0 \end{cases} \tag{4}$$

The unit -ramp function is defined as follows in Equation (5).

$$r(t) = \begin{cases} t, & t \geq 0 \\ 0, & t < 0 \end{cases} \tag{5}$$

Both the above functions are continuous. The digital counterparts of the unit-step and unit-ramp functions are $u(n)$ and $r(n)$, where n represents discrete sampling instants instead of a continuous time scale on the time axis, and, in the case of the ramp function, the values increment in fixed, discrete steps along the amplitude axis. The analogue waveform is a true-ramp function, whereas the digital waveform is approximated to be a ramp function by adding a series of digital-step functions, which can be mathematically described as in the following Equation (6).

$$r(n) = \lim_{\substack{\Delta t \to 0 \\ \Delta a \to 0}} k_a \Delta a \sum_{i=0}^{\infty} a_i u(n - k_t \Delta t n_i) \tag{6}$$

where k_a = amplitude scaling factor, Δa = limit of amplitude resolution, a_i = amplitude index, k_t = time scaling factor, Δt = limit of time resolution, n_i = time index, and $u(n)$ = digital unit-step function.

By looking at how the equivalent circuit responds to the voltage and current steps and ramp functions, we can gain an understanding of why there are differences between the analogue and digital inputs.

For ease of analysis, consider three different electrochemical systems with the following parameters. For system 1, series resistance R_{S1} = 100 Ω, polarization resistance R_{P1} = 25 Ω, and double-layer capacitance C_{dl1} = 1 µF. System 2 retains the same values for the series and polarization resistances: R_{S2} = 100 Ω and R_{P2} = 25 Ω but has a higher double-layer capacitance C_{dl2} = 10 µF. System 3 also retains the same values for the series and polarization resistances: R_{S3} = 100 Ω and R_{P3}= 25 Ω but has a lower double-layer capacitance C_{dl3} = 0.1 µF. By calculating the transfer function for the voltage across the

double-layer capacitance/polarization resistance and obtaining the time-constant $R_S C_{dl}$, increasing or decreasing C while having the same value of R has a corresponding effect on the time constant. So, system 2, having a value of C 10× larger than system 1, should have a time constant 10× larger, making it slower to respond, while system 3, having a value of C 10× smaller than system 1, should have a time constant 10× smaller in theory.

3.4.1. Voltage Step and Ramp Response

Since the polarization resistance and double-layer capacitance are in parallel, the voltages across them are the same and, therefore, the voltage-step and ramp responses are identical for both. Figure 8 shows the voltage-step response across the two elements.

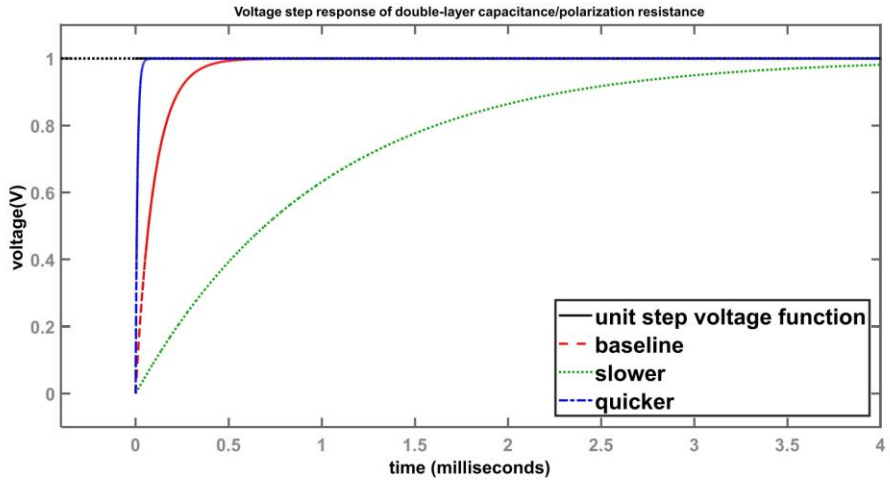


Figure 8. Voltage-step response of double-layer capacitance/polarization resistance.

The black curve shows the unit-step function, while the red curve shows the voltage-step response for system 1. System 2, having a larger time constant (green), takes a longer time to reach the final value of 1 V compared to system 1, while system 3, having a smaller time constant, reaches the final value significantly faster than system 1, as expected.

Figure 9 shows the voltage-ramp response across the two elements.

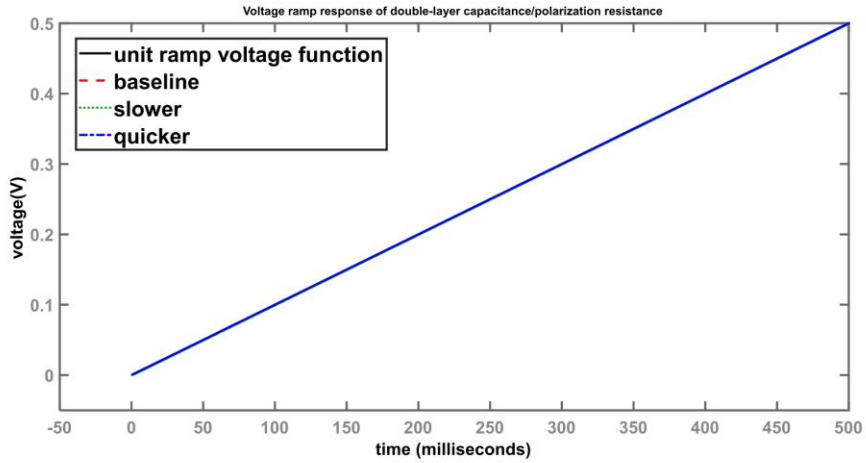


Figure 9. Voltage-ramp response of double-layer capacitance/polarization resistance (longer time scale).

While in the case of the step response, differences can be seen with respect to the different behaviour of the systems, for the ramp response, the curves lie on top of each

other over a time scale of 0.5 s. However, when viewed on a shorter time scale, the differences start to become apparent, as shown in Figure 10.

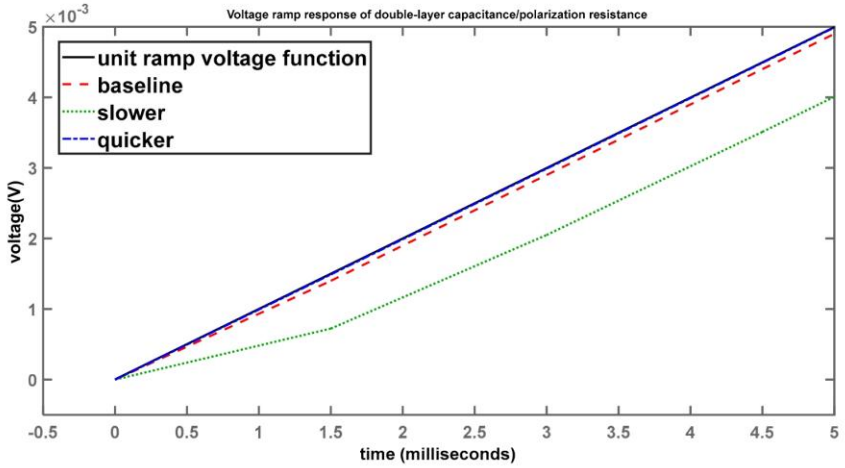


Figure 10. Voltage-ramp response of double-layer capacitance/polarization resistance (shorter time scale).

Here we see, once again, the baseline (red) system is slightly lagging the input-ramp function (black). System 2 (green), with the larger time constant, is considerably slower than the baseline, while system 3 (blue), with the smaller time constant, is much quicker to follow the input voltage. However, once the time scale becomes large enough, these differences become less apparent and the curves overlap, making it appear as if there are no discernible differences between them.

3.4.2. Current-Step Responses

Simulations were also performed using the control systems toolbox in MATLAB to obtain the current-step responses through R_p and C_{dl}, as shown in Figures 11 and 12.

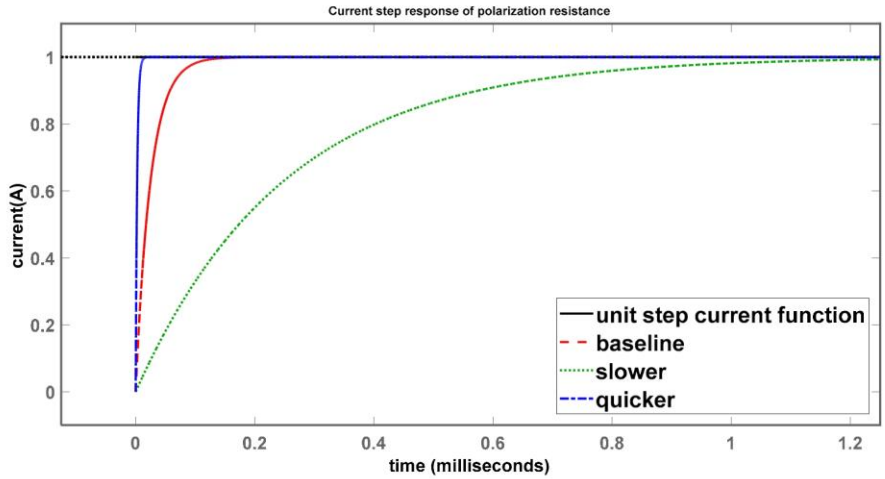


Figure 11. Current-step response of polarization resistance.

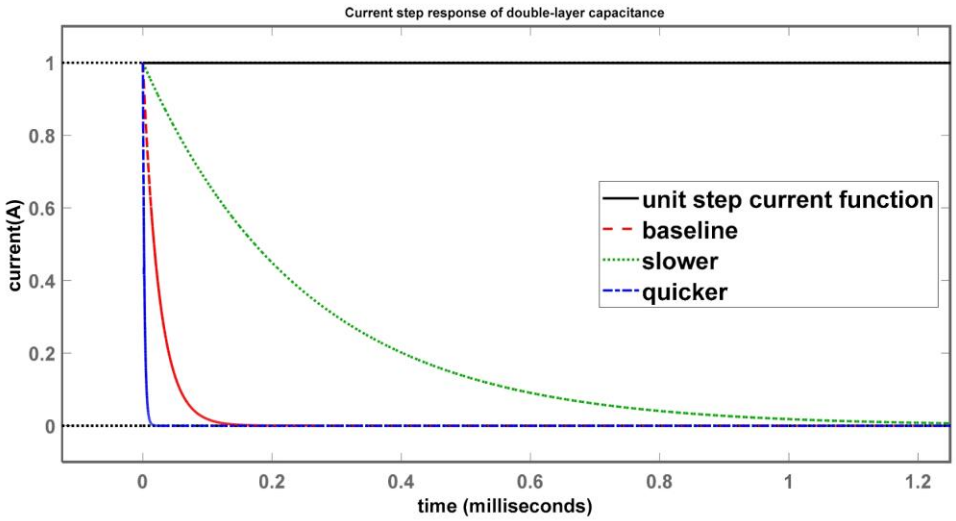


Figure 12. Current-step response of double-layer capacitance.

The black curve shows the unit-step current function, while the red curve shows the step response of system 1 (baseline). System 2, which has a time constant 10× larger than system 1, shows a slower step response (green), as expected, taking considerably longer to reach the final value of 1 A, while system 3, having a time constant 10× smaller (blue) than system 1, reached the steady-state value much more quickly than system 1, which is once again in agreement with the expectations.

The current-step response through the double-layer capacitance shown in Figure 12 follows the same trend as the polarization resistance. The black curve shows the current rising to 1 A at 0 s and, in contrast to the current-step response of the polarization resistance, the currents through C_{dl} start at 1 and settle at 0 A. The baseline (red) is set by system 1, while system 2 (green), having a time constant 10× larger in magnitude, is considerably slower to reach the final value of 0 A, and system 3 (blue), with the smaller time constant, settles to 0 A much more quickly than system 1, in agreement with the assumptions.

The explanation for the current-step responses through R_p and C_{dl} makes sense, as the currents through R_p and C_{dl} add to the total current flowing through the network. So, as the current through one element increases, the current through the other should decrease as their sum cannot exceed the source current. The current rises through R_p because the voltage across is also rising. For C_{dl}, it is slightly more complicated; because the voltage across the terminals is increasing with time, the capacitor charges and slowly starts to apply a voltage opposing the source, steadily decreasing the current through it, and, when fully charged, completely blocks the current.

3.4.3. Current-Ramp Responses

The current-ramp responses through R_p and C_{dl} were also obtained with MATLAB simulations, using the control systems toolbox. The current-ramp response through the polarization resistance R_p is shown in Figure 13.

Considering a longer time scale (0.5 s), all three systems (red, green, and blue curves) generally follow the input current-ramp function (black curve) as it rises linearly with time, indistinguishable from each other. However, when viewing a much shorter time scale, as shown in Figure 14, the differences become much more apparent.

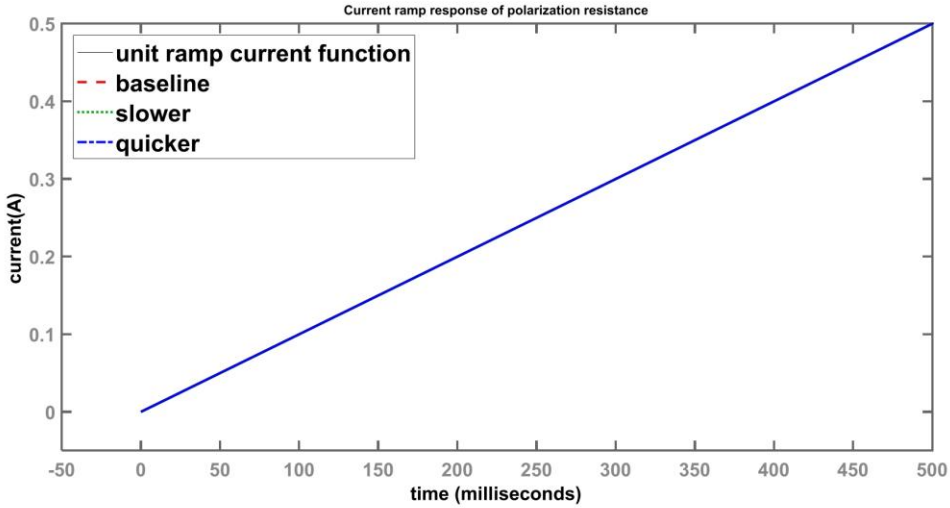


Figure 13. Current-ramp response of polarization resistance (longer time scale).

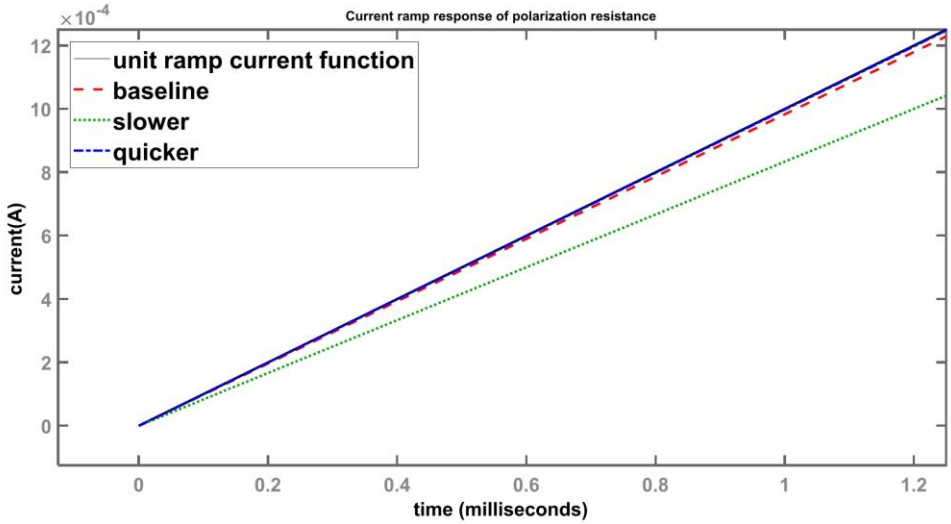


Figure 14. Current-ramp response of polarization resistance (shorter time scale).

Once again, the baseline (red) system 1 is trying to follow the input-current ramp (black) as closely as possible, but a minor divergence can be seen. System 2 (green), with the larger time constant, shows a much larger deviation compared to the baseline, while system 3 (blue), with the smaller time constant, is noticeably quicker when following the input. These results logically follow the same pattern as the step responses, which confirms the theoretical assumptions with respect to the time constants of each individual system. However, once the timeframe becomes large enough, these minor deviations become insignificant and it appears as if the output follows the input without any lag, as shown in Figure 13.

The current-ramp response through C_{dl} is shown in Figure 15.

Looking at the final settling values of all the systems, they appear to be suppressed to 0 A, while the unit-ramp current function increases linearly with time; this makes sense as the capacitor will not be receiving any current, as the polarization resistance is essentially

taking all the input current through its branch, as shown in Figure 13. Taking a closer look by zooming in on the time and current axes, Figure 16 shows some minor differences.

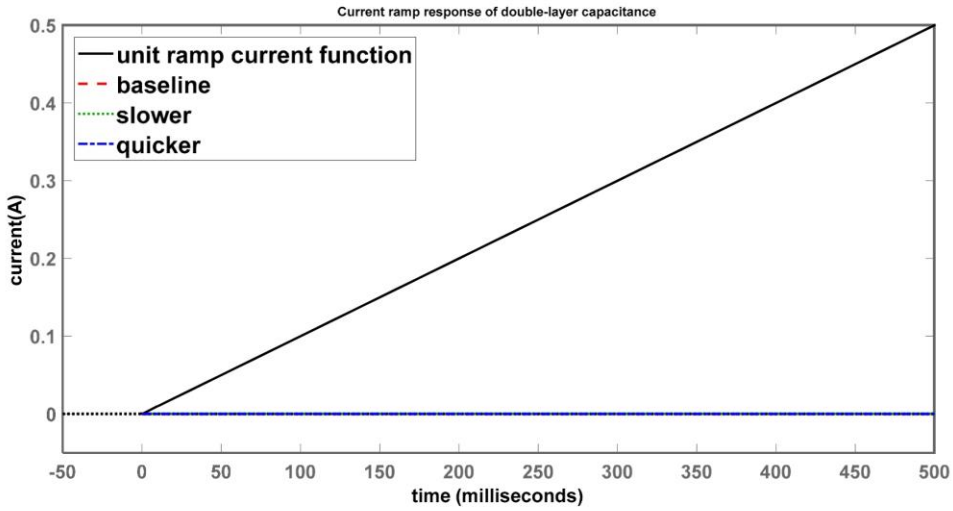


Figure 15. Current-ramp response of double-layer capacitance (longer time scale).

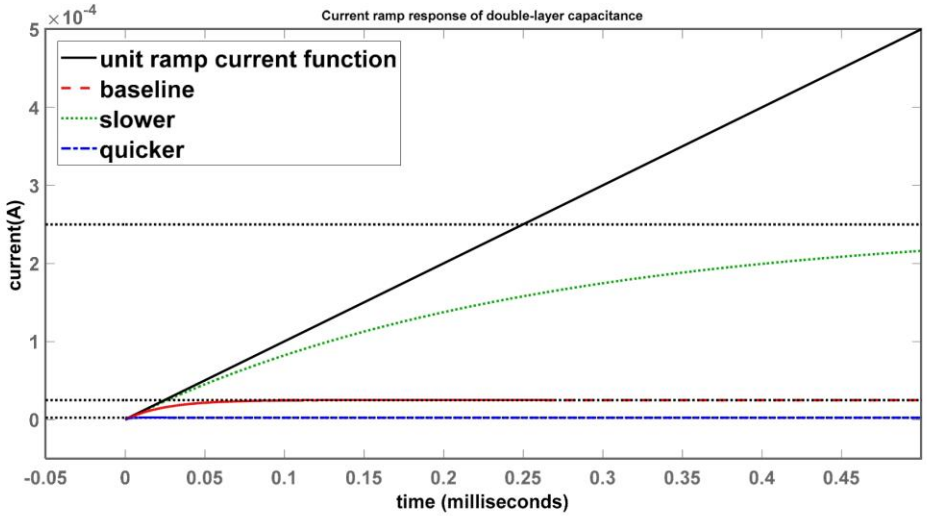


Figure 16. Current-ramp response of double-layer capacitance (shorter time scale).

In this instance, minor variations to the behaviour of the systems can be observed, as once again system 1 (red) sets the baseline, which shows a minor increase in current before settling to a stable value of around 25 µA. At the same time, system 2 (green), with the larger time constant, reacts much more slowly as it rises to settle at almost 250 µA and is not suppressed as quickly as system 1. System 3 (blue), with the smaller time constant, is almost at 0 A, reacting very quickly and suppressing the current much sooner than the baseline, which once again agrees with the theoretical assumptions as before.

The simulations show the effects that the values of the individual elements have on the overall system, with the time constant being functions of various elements, usually in combination with each other. It is important to stress that these results are only applicable if the system under consideration is assumed to be ideal, since, in practice, it is nearly impossible to emulate electrical circuits without factoring in non-ideal behaviours in multiple

aspects. These simulations provide a perspective into how the elements behave under the application of the two different types of input signals. While the analogue signal is a smooth ramp, the digital signal has several abrupt steps that force the sensor to behave differently, resulting in an output curve that, on the surface, appears to be identical but, when zoomed in, shows minor differences. The values of the circuit parameters also influence the step and ramp responses, as seen with the different coloured curves representing the responses of the different systems.

4. Conclusions

Analogue and digital modes of operation on the Metrohm VIONIC were used to test the sensor capabilities of a screen-printed electrode, with the working electrode modified with platinum on a carbon catalyst. The sensor element was used to detect hydroquinone in a hydrochloric acid medium, in the form of redox peaks while running CVs. Both analogue and digital CVs showed the peaks in identical positions, confirming the successful operation of the sensor element. The effect of the scan rate on the redox of hydroquinone was checked. It showed that the total measured currents were directly proportional to the scan rate in the case of both the analogue and digital CVs. While comparing individual analogue and digital scan rates, subtle differences were noticed between the two, with the analogue CVs producing smaller total currents compared to the digital CVs and some changes in the shape of the analogue curves when compared side by side with the digital ones. This proved that the type of potentiostat hardware does play a role in the results obtained in electrochemical measurements. Simulations confirmed the assumptions made about the nature of the input signals being responsible for the difference observed in the measured voltammograms. Step and ramp responses of the assumed ideal electrochemical systems showed that the individual elements of the electrochemical equivalent circuit determine how the applied signals, be it voltage or current, appear across the individual elements and how they are affected by the digital and analogue inputs. The results conclude that the use of analogue hardware vs. digital hardware causes some differences that are noticeable to the end user, though their effect on the underlying electrochemical processes may not be very significant.

Author Contributions: Conceptualization, A.K. and K.Ž.S.; Methodology, A.K. and K.Ž.S.; Validation, A.K. and K.Ž.S.; Formal analysis, A.K.; Investigation, A.K. and K.Ž.S.; Resources, K.Ž.S.; Data curation, A.K.; Writing—original draft, A.K.; Writing—review & editing, A.K. and K.Ž.S.; Visualization, A.K. and K.Ž.S.; Supervision, K.Ž.S.; Project administration, K.Ž.S.; Funding acquisition, K.Ž.S. All authors have read and agreed to the published version of the manuscript.

Funding: This research was funded by the Slovenian Research Agency (ARRS), grants P2-0084 (Program Nanostructured Materials), J2-1739 (High Performance Nanostructured Acrylamide Sensors), and PR-09874 (Young Researcher Project).

Data Availability Statement: Data will be made available by the authors on request.

Acknowledgments: Special thanks to Primalab d.o.o. for the Metrohm VIONIC, Pika Štefančič for assistance with the graphics, and Paul McGuiness for proofreading the final version of the manuscript.

Conflicts of Interest: The authors declare no conflicts of interest.

References

1. Dally, W.J.; Poulton, J.W. *Digital Systems Engineering*; Cambridge University Press: Cambridge, UK, 1998.
2. Yarlagadda, R.R. *Analog and Digital Signals and Systems*; Springer: Berlin/Heidelberg, Germany, 2010; Volume 1, pp. 1–569.
3. Oppenheim, A.V.; Verghese, G.C. Signals, systems & inference. *IEEE Control Syst. Mag.* **2017**, *37*, 97–98.
4. Atanasoff, J.V. Advent of electronic digital computing. *Ann. Hist. Comput.* **1984**, *6*, 229–282. [CrossRef]
5. Ulmann, B. *Analog Computing*; Oldenbourg Wissenschaftsverlag Verlag: Munich, Germany, 2013.
6. Hwang, C.S. Prospective of semiconductor memory devices: From memory system to materials. *Adv. Electron. Mater.* **2015**, *1*, 1400056. [CrossRef]
7. Dee, R.H. Magnetic tape for data storage: An enduring technology. *Proc. IEEE* **2008**, *96*, 1775–1785. [CrossRef]

8. Kang, S.; Jin, B.; Yoo, M.; Son, H.; Kim, K.; Wi, J.; Ko, H. Low-Noise and Process Variation-Tolerant Readout Circuit for Electrochemical Sensors. *IEEE Sens. J.* **2024**, *24*, 19274–19285. [CrossRef]
9. Vaseghi, S.V. *Advanced Digital Signal Processing and Noise Reduction*; John Wiley & Sons: Hoboken, NJ, USA, 2008.
10. Rosenfeld, J.B. *Information Processing: Encoding and Decoding*; Indiana University: Bloomington, Indiana, USA, 1967.
11. Kissinger, P.T. Introduction to analog instrumentation. In *Laboratory Techniques in Electroanalytical Chemistry, Revised and Expanded*; CRC Press: Boca Raton, FL, USA, 2018; pp. 165–194.
12. Smutok, O.; Katz, E. Electroanalytical instrumentation—How it all started: History of electrochemical instrumentation. *J. Solid State Electrochem.* **2024**, *28*, 683–710. [CrossRef]
13. EC08, Autolab Application Note. Basic overview of the working principle of a potentiostat/galvanostat (PGSTAT)–Electrochemical cell setup. *Metrohm Autolab BV*. 2011; pp. 1–3. Available online: https://www.metrohm.com/en/applications/application-notes/autolab-applikationen-anautolab/an-ec-008.html (accessed on 30 May 2024).
14. Colburn, A.W.; Levey, K.J.; O'Hare, D.; Macpherson, J.V. Lifting the lid on the potentiostat: A beginner's guide to understanding electrochemical circuitry and practical operation. *Phys. Chem. Chem. Phys.* **2021**, *23*, 8100–8117. [CrossRef] [PubMed]
15. Kissinger, P.T.; Heineman, W.R. Cyclic voltammetry. *J. Chem. Educ.* **1983**, *60*, 702. [CrossRef]
16. Snizhko, D.; Zholudov, Y.; Kukoba, A.; Xu, G. Potentiostat design keys for analytical applications. *J. Electroanal. Chem.* **2023**, *936*, 117380. [CrossRef]
17. Damaskin, B.B.; Petrii, O.A. Historical development of theories of the electrochemical double layer. *J. Solid State Electrochem.* **2011**, *15*, 1317–1334. [CrossRef]
18. Alavi, S.M.M.; Mahdi, A.; Payne, S.J.; Howey, D.A. Identifiability of generalized randles circuit models. *IEEE Trans. Control. Syst. Technol.* **2016**, *25*, 2112–2120. [CrossRef]
19. Horowitz, P.; Hill, W.; Robinson, I. *The Art of Electronics*; Cambridge University Press: Cambridge, UK, 1989; Volume 2, p. 658.
20. von Zuben, T.W.; Salles Jr, A.G.; Bonacin, J.A. Low-cost open-source potentiostats: A comprehensive review of DIY solutions and fundamental concepts of electronics and its integration with electrochemistry. *Electrochim. Acta* **2024**, *498*, 144619. [CrossRef]
21. Ashoori, E.; Goderis, D.; Inohara, A.; Mason, A.J. Wide Voltage Swing Potentiostat with Dynamic Analog Ground to Expand Electrochemical Potential Windows in Integrated Microsystems. *Sensors* **2024**, *24*, 2902. [CrossRef] [PubMed]
22. Westerlund, S.; Ekstam, L. Capacitor theory. *IEEE Trans. Dielectr. Electr. Insul.* **1994**, *1*, 826–839. [CrossRef]
23. Krishnamurthy, A.; Samardžija, Z.; Trafela, Š.; Korent, A.; Šturm, S.; Soderžnik K, Ž. Electrochemical Detection of Benzenediols using Carbon-Supported Catalysts. *Electrochim. Acta* **2024**, *493*, 144389. [CrossRef]
24. Franklin, G.F.; Powell, J.D.; Workman, M.L. *Digital Control of Dynamic Systems*; Addison-Wesley: Reading, MA, USA, 1998; Volume 3.

Disclaimer/Publisher's Note: The statements, opinions and data contained in all publications are solely those of the individual author(s) and contributor(s) and not of MDPI and/or the editor(s). MDPI and/or the editor(s) disclaim responsibility for any injury to people or property resulting from any ideas, methods, instructions or products referred to in the content.

4.6 Case Study: IoT Sensor for Formaldehyde Detection

This section presents a system-level integration of the preceding layers, placing materials, electrode behaviour, signal structure, and hardware implementation in the context of portable, real-world sensing deployment.

This case study presents a field-deployable electrochemical sensor platform for the rapid detection of formaldehyde (HCHO) in alkaline media, developed as a collaboration between multiple researchers. The core sensing element was fabricated using $Ni(OH)_2$-Ni nanowires deposited onto paper-based SPEs, a process led by Špela Trafela and co-authors. Figure 4.6 presents the graphical abstract from the related publication, summarising the IoT-enabled formaldehyde sensing platform. It illustrates the integration of $Ni(OH)_2$–Ni nanowire-modified paper-based electrodes with custom-built potentiostat hardware for remote electrochemical detection.

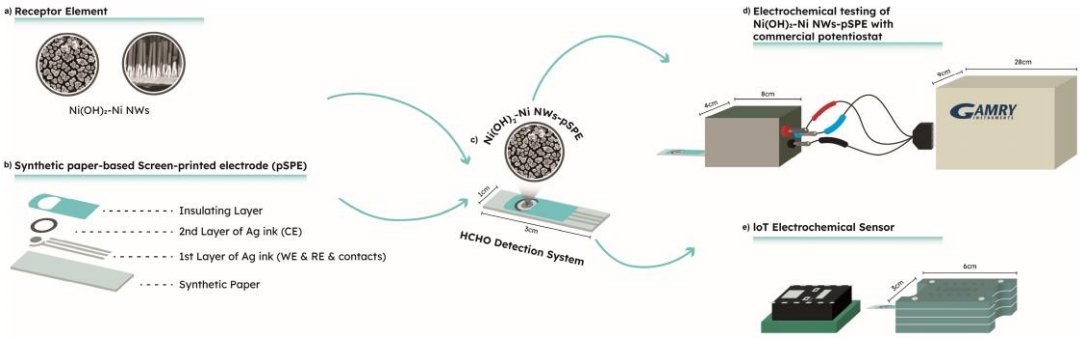


Figure 4.6: Graphical abstract of the IoT formaldehyde sensing platform. Adapted from Trafela et al., Sensors 23 (2023) 4676, shared under CC BY 4.0 licensing.

The present author's contributions focused on the integration, configuration, and validation of the custom-built potentiostat system used to drive the sensor platform. Working with a Photon IoT development board programmed in C/C++, specific adjustments were made to the firmware to define and fine-tune the chronoamperometric (CA) bias potentials. Since HCHO oxidation occurs above +0.6 V vs Ag, different setpoints were tested within the code to determine the optimal detection window. These changes were essential for correlating applied voltage with current response sensitivity.

Verification tasks involved checking that programmed voltages were correctly translated into actual output, using both internal debugging and comparison with a second prototype unit. In one case, a mismatch between expected and observed voltages was resolved by cross-referencing measurements between two devices, highlighting a discrepancy in hardware quality. These corrections ensured consistent signal delivery across units.

Serial communication was implemented using a microUSB link to a host PC, with data streamed live into a text interface via PuTTY. Delimiters were configured to format output into structured logs that could be easily imported into Excel for analysis. Additionally, Wi-Fi connectivity was set up through the Photon board's native wireless interface, allowing for remote access, monitoring, and potential cloud-based deployment in future iterations.

Beta testing was performed using both breadboard and PCB-based versions of the device. The breadboard prototype featured a hardware-adjustable potentiometer to set voltage levels manually, while the final PCB variant relied entirely on digital code for voltage control. The author was responsible for ensuring that both platforms produced consistent and reproducible responses to HCHO exposure. Performance was benchmarked

against commercial potentiostats including the Gamry Ref 600, PalmSens4, and EmStat3 Blue to validate output quality and measurement reliability.

Although these contributions were primarily focused on the integration and operational verification of the sensor system, they were essential in translating a functional lab-built circuit into a robust, deployable prototype. This work reinforces the importance of system-level debugging, firmware adaptability, and signal integrity testing in enabling practical, IoT-compatible chemical sensing platforms.

The full dataset and material characterisation are available in the original article [Sensors 2023, 23, 4676; https://doi.org/10.3390/s23104676]. The print version is shared in the following pages under the CC BY 4.0 license agreement.

sensors

MDPI

Article

IoT Electrochemical Sensor with Integrated $Ni(OH)_2$–Ni Nanowires for Detecting Formaldehyde in Tap Water

Špela Trafela [1,*], Abhilash Krishnamurthy [1,2], Kristina Žagar Soderžnik [1,2], Urška Kavčič [3], Igor Karlovits [3], Beno Klopčič [1], Sašo Šturm [1,2] and Kristina Žužek [1,2]

[1] Department for Nanostructured Materials, Jožef Stefan Institute, Jamova c. 39, 1000 Ljubljana, Slovenia; abhilash.krishnamurthy@ijs.si (A.K.)
[2] Jožef Stefan International Postgraduate School, Jamova c. 39, 1000 Ljubljana, Slovenia
[3] Pulp and Paper Institute, Bogišićeva 8, 1000 Ljubljana, Slovenia
* Correspondence: spela.trafela@ijs.si

Abstract: Simple, low-cost methods for sensing volatile organic compounds that leave no trace and do not have a detrimental effect on the environment are able to protect communities from the impacts of contaminants in water supplies. This paper reports the development of a portable, autonomous, Internet of Things (IoT) electrochemical sensor for detecting formaldehyde in tap water. The sensor is assembled from electronics, i.e., a custom-designed sensor platform and developed HCHO detection system based on $Ni(OH)_2$–Ni nanowires (NWs) and synthetic-paper-based, screen-printed electrodes (pSPEs). The sensor platform, consisting of the IoT technology, a Wi-Fi communication system, and a miniaturized potentiostat can be easily connected to the $Ni(OH)_2$–Ni NWs and pSPEs via a three-terminal electrode. The custom-made sensor, which has a detection capability of 0.8 μM/24 ppb, was tested for an amperometric determination of the HCHO in deionized (DI) and tap-water-based alkaline electrolytes. This promising concept of an electrochemical IoT sensor that is easy to operate, rapid, and affordable (it is considerably cheaper than any lab-grade potentiostat) could lead to the straightforward detection of HCHO in tap water.

Keywords: formaldehyde; electrochemical sensor; nickel

check for updates

Citation: Trafela, Š.; Krishnamurthy, A.; Soderžnik, K.Ž.; Kavčič, U.; Karlovits, I.; Klopčič, B.; Šturm, S.; Žužek, K. IoT Electrochemical Sensor with Integrated $Ni(OH)_2$–Ni Nanowires for Detecting Formaldehyde in Tap Water. *Sensors* **2023**, 23, 4676. https://doi.org/10.3390/s23104676

Academic Editor: Sergi Garcia-Segura

Received: 16 March 2023
Revised: 6 April 2023
Accepted: 9 May 2023
Published: 11 May 2023

Copyright: © 2023 by the authors. Licensee MDPI, Basel, Switzerland. This article is an open access article distributed under the terms and conditions of the Creative Commons Attribution (CC BY) license (https://creativecommons.org/licenses/by/4.0/).

1. Introduction

Formaldehyde (HCHO) is a serious pollutant. It is classified as toxic, allergenic, and carcinogenic for humans, with a maximum permissible level of 0.1 ppm for homes and 1 ppm for workplaces [1,2]. It can be found in many everyday products, including disinfectants, cosmetics, textiles, and paint [1–4]. It can also be found in water, usually in a rapidly hydrated form (i.e., methylene glycol), and therefore it can easily enter drinking water as a by-product of disinfectants or as a leachate from plumbing fixtures.

Several electrochemical sensors have been developed to detect HCHO in the gas phase [2,5–11]. However, a cost-effective, miniaturized, and portable electrochemical sensor (lab-on-a-chip) to monitor aqueous solutions of HCHO ($HCHO_{aq}$) is not available. In general, $HCHO_{aq}$ is detected with expensive, bulky laboratory equipment, e.g., impractical electrochemical cells with a three-electrode system (working, counter, and reference electrodes) and large potentiostats with all the electronics required to control the cell and run the experiments. Although this equipment can measure $HCHO_{aq}$ at the low-ppb level [2], its practical application for domestic use is prevented by cost, complexity, and a lack of portability [5]. These limitations can be overcome to provide portable, real-time monitoring by assembling miniaturized electronics, a three-terminal electrode connector, and Wi-Fi communication support [3,5,12,13] to provide an inexpensive, disposable, and portable detection system.

Furthermore, the practical advantage of electrochemical $HCHO_{aq}$ detection could have future implications for low-cost, mass-produced devices using a three-electrode system

based on screen-printed electrodes (SPEs) [14,15]. They are seen as ideal for developing portable, inexpensive sensors because of their simplicity, the flexibility of their surface modification, and their ease of disposability compared to traditional electrode materials [3]. Usually, commercially available SPEs, which are mainly printed on ceramics, are used for sensor-based detection systems. However, screen-printing technology offers the possibility to print conductive inks on lighter, ecological materials such as synthetic paper [16,17]. The paper substrates are mainly produced from chemical or mechanical pulp using a different ratio of fibers (e.g., hardwood and softwood) with additional components (e.g., fillers, retention aids, binders) that enhance the structural and surface properties of the paper [16]. Synthetic paper-based SPEs (pSPE) can also be modified with nanostructured materials to improve their electroanalytical characteristics for the detection of many harmful chemical species, including $HCHO_{aq}$ [18,19].

In recent years, various types of nanostructured materials based on noble metals (Au [20,21], Pt [22], Ag [23], etc.) have been reported as promising for highly sensitive electrochemical HCHOaq detection. However, the cost and limited supply of noble-metals-based nanostructures is a major barrier to the development of disposable sensor platforms for $HCHO_{aq}$ detection [24–27]. Among the noble-metals-based materials [24,25,28–31], Ni [32–34], within the highly active redox couple of $Ni(OH)_2/NiOOH$, has excellent physical and chemical properties for $HCHO_{aq}$ detection by virtue of its electro-analytical properties, e.g., low cost, rapid response, high sensitivity, and detection limits at ppb levels [27,35,36].

In this study, a portable, autonomous, IoT electrochemical sensor was developed to determine the HCHO in tap water. The sensor was constructed on a custom-designed sensor platform with IoT technology and a three-terminal electrode connector to plug in the SPE-based system for monitoring $HCHO_{aq}$. The sensor platform consists of several electronic components, including a commercially available Photon WiFi Development Board, a miniaturized, static electrochemical cell (SEC), combined with a potentiostat, a USB port, and the SPE connector. The $HCHO_{aq}$ was detected using an already-developed system based on $Ni(OH)_2$–Ni nanowires (NWs) [36,37] and pSPEs. The proof-of-principle HCHO analysis was performed with a lab-grade potentiostat, showing high sensitivity, rapid response (1 s), and a low-level detection capability (24 ppb). Later, the $Ni(OH)_2$–Ni NWs pSPEs was connected to an assembled sensor platform to test it as a lab-on-a-chip for monitoring $HCHO_{aq}$. The measurements showed comparable values with a commercial potentiostat and the developed portable, autonomous, IoT electrochemical sensor. Furthermore, the developed sensor was also able to detect HCHO in tap water.

2. Materials and Methods

2.1. Chemicals and Materials

Anodized aluminum oxide (AAO) templates were purchased from Whatman Anodics Filter Membranes, Merck, Ljubljana Slovenia, the gold electrolyte, Ecolyt SG100, was purchased from Gramm, Heimerle + Meule GmbH, Pforzeim, Germany, and double-sided Cu-foil tape was purchased from 3M^{TM}, Saint Paul, MN, USA. Formaldehyde ($HCHO_{aq}$, 37% *w*/*v*) was purchased from Carlo Erba, Cornaredo, Italy. Nickel sulfate hexahydrate ($NiSO_4 \cdot 6H_2O$, 98+%) was purchased from Acros Organics, Geel, Belgium. Boric acid (H_3BO_3), sulfuric acid (H_2SO_4, 99.9%), sodium hydroxide pellets (NaOH), and potassium hydroxide pellets (KOH) were purchased from Sigma-Aldrich, St. Louis, MO, USA.

2.2. Preparation of the HCHO Detection System Based on $Ni(OH)_2$–Ni NWs pSPEs

The $Ni(OH)_2$–Ni NW-based receptor elements (Figure 1) were prepared electrochemically. The experiments were performed in a Teflon electrolytic cell, on a Gamry Reference 600 potentiostat at room temperature. A standard three-electrode system was used; the reference electrode (RE) was a conventional Ag/AgCl/3.5 M KCl (HANA Instruments; HI5311), and a hollow-circular platinum mesh was used as the counter electrode (CE). To prepare the $Ni(OH)_2$–Ni NW-based receptor elements for $HCHO_{aq}$ detection, two-step

electrochemical synthesis routes were employed. The first step covers the amperometric deposition of free-standing Ni NWs. The Ni NWs were electrodeposited by applying a constant potential of −1.0 V for 1200 s into commercially available anodized aluminum oxide (AAO) membranes (Whatman Anopore, pore diameter ~200 nm) using 0.2 M $NiSO_4 \cdot 6H_2O$ and 0.1 M H_3BO_3 aqueous solution. The pH of the prepared solution was adjusted to 2.0 by adding H_2SO_4 [38]. After the deposition, the AAO membrane was removed in 10 M NaOH solution in order to obtain a one-dimensional material, i.e., free-standing Ni NWs. Detailed information about the electrochemical deposition of Ni NWs can be found in our recent publication, i.e., Trafela et al. [36]. Furthermore, the as-prepared Ni NWs were electrochemically modified (i.e., potential cycling at a scan rate of 200 mV/s) in the 0.1 M KOH electrolyte. The second step, i.e., KOH modification, was chosen as it enables an effective transformation of the Ni NWs surface to highly active $Ni(OH)_2$ for $HCHO_{aq}$ detection [37]. For more detailed information about the KOH modification process, please refer to our publications [36,37]. The resulting homogeneous $Ni(OH)_2$–Ni NWs, with an average length of 2 µm, diameter of 200 nm, and $Ni(OH)_2$ surface layer thickness of 8–10 nm, were characterized by FEG-SEM, TEM, FT-IR, and XRD [36,37], and further used as a receptor element for sensor manufacturing.

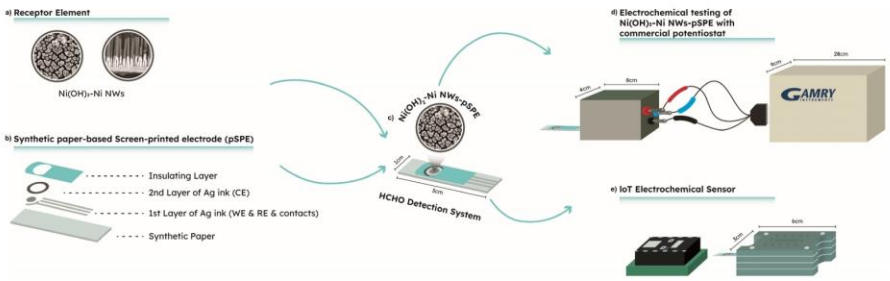


Figure 1. Schematic of the IoT electrochemical sensor's fabrication process: (**a**) FEG-SEM images of the $Ni(OH)_2$–Ni NW-based receptor element: left—top view and right—side view (the original FEG-SEM images are available in our recent publication, i.e., Trafela et al. [36]). (**b**) The synthetic-paper-based screen-printed electrodes (pSPEs) with individual (ink) layers, and (**c**) the fabricated $HCHO_{aq}$ detection system with its dimensions. Design and dimensions of (**d**) laboratory equipment (Gamry) and (**e**) IoT fabricated electrochemical sensor for HCHO testing.

The screen-printed electrodes (Figure 1) were fabricated using conductive ink printed on synthetic paper (Monotex L, 254 g/m^2), i.e., pSPE, using a GTO EVO 570 machine (GTO, Emilia Romagna, Italy). The pSPE was designed to fit the commercial potentiostat measuring system [16]. The printing process was performed in three layers with two different printing inks, i.e., Ag ink (CRSN 2442, SunTronic Silver 280; SunChemical, Parsippany-Troy Hills, NJ, USA) and dielectric ink (CFSN6057 SunTronic Dielectric 681; SunChemical, Parsippany-Troy Hills, NJ, USA). Two layers of the conductive Ag ink were screen-printed (mesh count of 77–55 L cm^{-1}) on the paper to form the electrodes. Firstly, the quasi-RE (q-RE) and the working electrode (WE) were printed and cured at 110 °C for 30 s, and, secondly, the CE was printed and cured at 90 °C for 30 s. Finally, the layer of dielectric ink was screen-printed (mesh count of 90–48 L cm^{-1}) and cured at 90 °C for 30 s. After printing, the pSPEs were additionally cured at 110 °C for 150 s [16,39].

The integration of the $Ni(OH)_2$–Ni NW-based receptor element onto the pSPEs (Figure 1): the as-prepared receptor elements, i.e., $Ni(OH)_2$–Ni NWs, were attached to the WE (φ = 4 mm) of the pSPE using double-sided Cu-foil adhesive tape. The resulting electrode, i.e., the $HCHO_{aq}$ detection system (Figure 1), was then used for the electrochemical detection of HCHO.

2.3. Electrochemical Measurements Using Commercially Available Laboratory Equipment

The electrochemical testing of the HCHO detection system (i.e., $Ni(OH)_2$–Ni NWs pSPEs) was carried out via cyclic voltammetry (CV) and chronoamperometry (CA) using commercially available laboratory equipment (Figure 1). The $Ni(OH)_2$–Ni NWs pSPEs were placed in a boxed DropSens connector, connected to a Gamry Reference 600 potentiostat. The sample sensing areas (i.e., $Ni(OH)_2$–Ni NWs) were wetted with the 1 mL working solution containing known concentrations of HCHO (from 0 to 1×10^{-2} M) and 0.1 M NaOH (pH = 13.7). All the measurements were made at room temperature. The cyclic voltammograms were recorded from 0.3 V to 1.0 V vs. q-RE at a scan rate of 100 mV/s. The CA measurements were executed at constant potentials of 0.7 V vs. q-RE for 3–5 s.

2.4. Sensor Manufacture

The IoT electrochemical sensor for HCHO detection in alkaline media consists of two main components (i and ii, Figure 1): (i) the $Ni(OH)_2$–Ni NWs pSPEs-based detection system (the preparation of the system is described in Section 2.2) placed in a connector of (ii) a sensor platform. The sensor platform was constructed on an electronic breadboard kit and consisted of a miniaturized potentiostat, a Photon WiFi Development Board (Particle lnc., San Francisco, CA, USA), and a USB port. The detection system and potentiostat together represent a static electrochemical cell (SEC) which gives 2.5 W of single-supply power as the CA measurements were performed when a constant voltage was maintained. During the measurement time, the only electrochemical method available was chronoamperometry, so the potential was set (independent variable) and the current was measured. The voltage range was set using a digital-to-analog converter (DAC) from 0 V to 1.5 V. Furthermore, the SEC was adapted to be suitable for connection to the Photon WiFi Development Board, and the IoT. The device has a powerful industrial microcomputer and a set of peripherals that provide versatility: an ARM M4 processor (120 MHz), a flash memory for storing software, a RAM for storing various data, and a Wi-Fi system (802.11 b/g/n). Furthermore, the IoT is connected to the PC via a USB, from where it receives 2.5 W of power (USB 2.0 enables a theoretical maximum of 500 mA @ 5 V output), and sends data to the terminal. To protect the electronics from mechanical and water/chemical damage, the potentiostat and Photon WiFi Development Board were enclosed in a water-resistant case. The protective case still makes it possible to plug in a USB port and a three-terminal electrode connector for the pSPEs (10 mm × 30 mm). The sensor itself is small in size (60 mm × 30 mm), providing low-power, long-range wireless data transfer. Additionally, it is not an expensive production process as it is fabricated with low-cost parts.

The electrochemical testing of the sensor connected with the $Ni(OH)_2$–Ni NWs pSPEs detection system via a three-terminal electrode plug (Figure 1) was performed using CA. The measurements were carried out under a constant potential of 0.7 V vs. Ag q-RE. The working solutions of 1-μM HCHO and 0.1 M NaOH were prepared using distilled (DI) and tap water. Once the $Ni(OH)_2$–Ni NWs receptor element was wetted with the electrolyte, the IoT-based sensor platform started the measurements, i.e., sets the counter of i to 1 and shows the voltage of 0.7 V and the output currents (μA). Since the IoT sensor is connected to the PC via a USB port, the continuously written data accessible via the TCP-IP server are sent to the terminal/cloud.

3. Results and Discussion

3.1. The Strategy of HCHO Electrochemical Detection with the $Ni(OH)_2$–Ni-NWs pSPE-Based Detection System

The $Ni(OH)_2$–Ni NWs pSPE-based detection system was installed in the three-terminal electrode plug of the box (DropSens, Oviedo, Spain) connected to a lab-grade potentiostat. The system was tested for HCHO detection by monitoring its oxidation ability in alkaline media. Figure 2 shows the representative cyclic voltammograms of the $Ni(OH)_2$–Ni NWs pSPEs, investigated in 0–0.01 M HCHO alkaline electrolyte (0.1 M NaOH) at a scan rate of 100 mV/s. In the absence of HCHO (Figure 2, black-dot), one couple of well-defined

redox peaks was observed at 0.65 V (A) in the anodic region and 0.5 V (B) in the cathodic region. The anodic peak current is attributed (I ≈ 1 mA) to the oxidation reaction of $Ni(OH)_2 + OH^- \rightarrow NiOOH + e^-$ (A). Once the NiOOH is formed, it oxidizes HCHO. However, the substance that is involved in electrochemical reactions is not HCHO, as the studies are performed in an alkaline electrolyte. After the addition of HCHO to the 0.1 M NaOH electrolyte, the formaldehyde exists in the hydrated form of methylene glycol, i.e., $CH_2(OH)O^-$ [40], and is therefore oxidized at the surface of the NWs through the chemical reaction: NiOOH (formed at A) + $CH_2(OH)O^- \rightarrow Ni(OH)_2$ (i.e., newly formed) + $CH_2(O)O^-$ [36,37,41–44]. From Figures 2 and 3, it is clear that the anodic peak current (A) increases with increasing HCHO concentration from 1 µM to 50 mM, indicating the additional oxidation of the newly formed $Ni(OH)_2$ to NiOOH [36,37]. Furthermore, an examination of CVs shows that the anodic peak potential (A) shifts to a more positive potential with increasing HCHO concentration. This is attributed to the IR drop arising from the high current values at the high HCHO concentrations [36,45]. In the cathodic region, the cathodic peak current (B) was observed at the potential +0.5 V, attributed to the reversible transformation, i.e., the reduction of NiOOH + $H_2O + e^- \rightarrow Ni(OH)_2 + OH^-$ (B). Thus, these reduction (A) and oxidation peaks (B) correspond to the reversible reaction: $Ni(OH)_2 + OH^- \leftrightarrow NiOOH + e^-$.

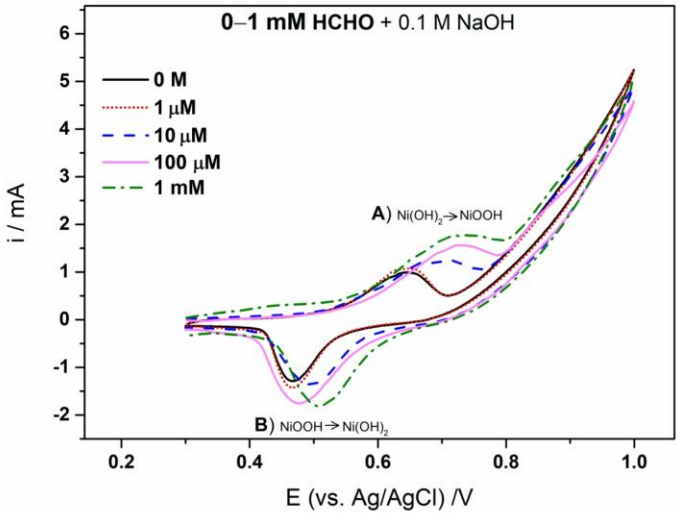


Figure 2. CVs of the $Ni(OH)_2$–Ni NWs pSPEs obtained at different HCHO concentrations (from 0 to 1 mM) in 0.1 M NaOH solution, observed at a scan rate of 100 mV/s.

The maximum, still sensitive, HCHO concentration was found to be ≤10 mM. Above this optimal HCHO concentration, additional anodic (Figure 3C,E) and cathodic (Figure 3D) peaks were observed. The anodic peak current (C) at E ≈ 0.5 V (orange) or E ≈ 0.6 V (grey) indicates a measurable side effect, an additional reaction occurring at Ag q-RE of the pSPE [46]. The Ag q-RE can interfere with the electrochemical measurements and cause non-negligible artifacts, which are attributed to the redox reactions of Ag in HCHO alkaline media [46–49]. The additional anodic peaks (C, Figure 3) are related to the electro-oxidation of Ag to $[Ag(OH)2]^-$ and finally to Ag oxides (Ag_2O/AgO). The results indicate that the HCHO is indeed oxidized by the Ag species, and the one with a higher valence (Ag_2O/AgO) oxidizes the formaldehyde (to final product, probably CO_2) and is followed by the generation of low-valence Ag [41]. From Figure 3, it is clear that the reactivity of the HCHO with Ag increases with its concentration. Hence, the additional cathodic peaks (D, Figure 3) at E ≤ 0.3 V (grey curve; not visible in this potential range for orange curve) can be attributed to the reversible processes involved in the reduction of Ag_2O/AgO to Ag. The typical behavior for Ag q-RE in alkaline media and a broader discussion of the

oxidation–reduction results are mentioned elsewhere [46–49]. Furthermore, a tail of the signal current was observed at E ≈ 0.93 V (E, Figure 3). This tail could be attributed to the bubble burst (e.g., oxygen that is formed during the oxygen-evolution reaction at a high anodic potential, or CO_2 which can be formed during the reaction between HCHO and Ag q-RE). This means that the $Ni(OH)_2$–Ni NWs pSPE begins to saturate and the formed bubble hinders the HCHO oxidation [45]. Based on these findings, the target concentration range for amperometric HCHO detection was selected to be from 1 µM to 10 mM. The determination of HCHO in alkaline media using the $Ni(OH)_2$–Ni NWs pSPEs-based detection system was then investigated using both laboratory equipment and the developed IoT electrochemical sensor.

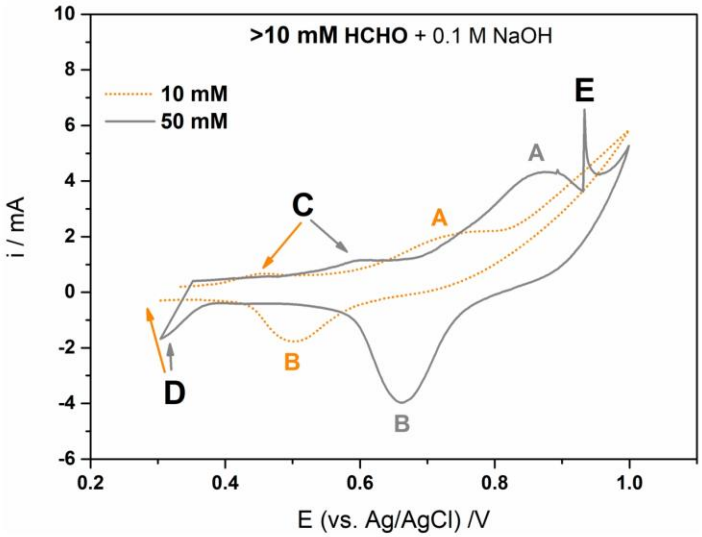


Figure 3. CVs of the $Ni(OH)_2$–Ni NWs pSPEs obtained at different HCHO concentrations: 10 (orange) and 50 (grey) mM in a 0.1 M NaOH solution, observed at a scan rate of 100 mV/s.

3.2. HCHO Electrochemical Detection Using Laboratory Equipment

The amperometric $HCHO_{aq}$ detection in alkaline media was first tested using the $Ni(OH)_2$–Ni NWs pSPEs detection system connected to the laboratory potentiostat via a three-terminal electrode plug on the DropSens box (Figure 1). Figure 4a shows typical current–time plots observed for 0–10 mM HCHO in 0.1 M NaOH at an operating potential of 0.7 V. As seen from Figure 4a, a sharp rise in the current was observed in the first second, which was followed by an exponential drop until the steady state was reached. Each peak in the first second represents an increase in current due to the oxidation reaction of $Ni(OH)_2$ (reactions 1 and 3), which demonstrates the rapid response and the high sensitivity of the $Ni(OH)_2$–Ni NWs pSPEs. The calibration (Figure 4b) was made by plotting the amperometric response of the lab potentiostat versus the $HCHO_{aq}$ concentrations (0.8 µM–10 mM). Two linear relations were obtained, i.e., from 0.8 to 500 µM (red line) and 0.5–10 mM (blue line). The experiments for each concentration were carried out in triplicate. Considering the limit of quantification (LOQ) for the $Ni(OH)_2$–Ni NWs-based receptor element, its value was found to be 0.8 µM/24 ppb (Figure 4a, light green). In comparison with some previous works where Ni-based electrodes were used for the detection of HCHO in 0.1 M NaOH, it seems clear that $Ni(OH)_2$–Ni NWs pSPE can act as a comparable electrode/catalyst in HCHO oxidation (Table 1).

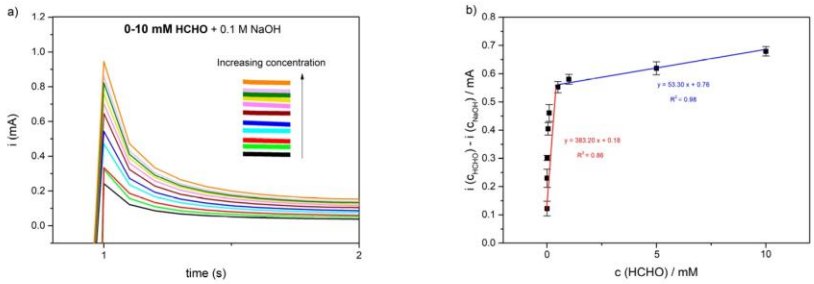


Figure 4. (**a**) CA responses of the $Ni(OH)_2$–Ni NWs pSPEs observed with lab-grade potentiostat and HCHO concentrations: 0.0—(black), 0.8—(light green), 1—(red), 5—(cyan), 10—(blue), 50—(brown), 100—(pink), 50—(yellow) µM, 1—(green), 5—(purple), and 1—(orange) mM in 0.1 M NaOH, observed at an applied potential of 0.7 V; (**b**) calibration plot of HCHO detection. Black square dots are oxidation peak values for HCHO concentrations, obtained in the first second of CA measurement (Figure 4a). Error bars are the standard deviation from the mean of three replicates.

Table 1. Comparison of the $Ni(OH)_2$–Ni NWs pSPE for HCHO oxidation with some of the previously reported Ni-based electrodes.

Ni-Based Electrodes	Electrolyte	Operating Potential [V]	LOQ [mM]	Saturation Limit of HCHO [mM]	Ref.
$Ni(OH)_2$/POT (TX-100)/MCNTPE	0.1 M NaOH	0.7	4.9	48	[33]
Ni/P-nanozeolite-modified electrode	0.1 M NaOH	0.58	5.8	>11.5	[27]
Ni/P(NMA)MCPE	0.1 M NaOH	0.74	8	70	[34]
Ni-CHIT/CPE	0.1 M NaOH	0.56	3	90	[32]
$Ni(OH)_2$–Ni NWs pSPE	0.1 M NaOH	0.7	0.8	50	Our work

Furthermore, the reusability of the $Ni(OH)_2$–Ni NWs pSPEs was investigated with the CA responses in the 1 mM HCHO + 0.1 M NaOH solution three times. The results showed that the output current values are very close, with a relative standard deviation (RSD) of 0.37%. Another significant feature of the $Ni(OH)_2$–Ni NWs pSPEs in a practical application is their reproducibility. We studied the CA responses of ten different $Ni(OH)_2$–Ni NWs pSPEs to the addition of 1 mM HCHO to a 0.1 M NaOH solution. The ten $Ni(OH)_2$–Ni NWs pSPEs were very reproducible, since the RSD of their output current responses was 0.63% [43]. Furthermore, considering the stability of the electrochemical responses of $Ni(OH)_2$–Ni NW-based receptor elements, there is no requirement to repeat the conditioning step while the measurement potential is applied. High selectivity is also another important property of the proposed material. The $Ni(OH)_2$–Ni NWs pSPE was tested for four potential interferences, including ethanol, 1-propanol, acetaldehyde, and hydrogen peroxide. It was shown that these related compounds do not contribute to the HCHO response in alkaline electrolytes [43].

3.3. HCHO Electrochemical Detection Assisted by an IoT Electrochemical Sensor (Lab-on-a-Chip)

The detection of amperometric $HCHO_{aq}$ in alkaline media was also tested using a portable IoT electrochemical sensor (Figure 1). Figure 5a represents the individual parts of the fabricated IoT electrochemical sensor consisting of the integrated $Ni(OH)_2$–Ni NWs pSPEs, the miniaturized potentiostat (i.e., the static electrochemical cell, SEC), the IoT-enabled platform (i.e., commercially available Photon WiFi Development Board), and a USB port. A sensor enables all the necessary operations, including the digitization of signals, voltage regulation between the q-RE and the WE of the SPEs, recording data at the required time, instantly displaying the data on the PC terminal, rapid communication via LED (both wired and wireless), and TCP-IP access to various settings.

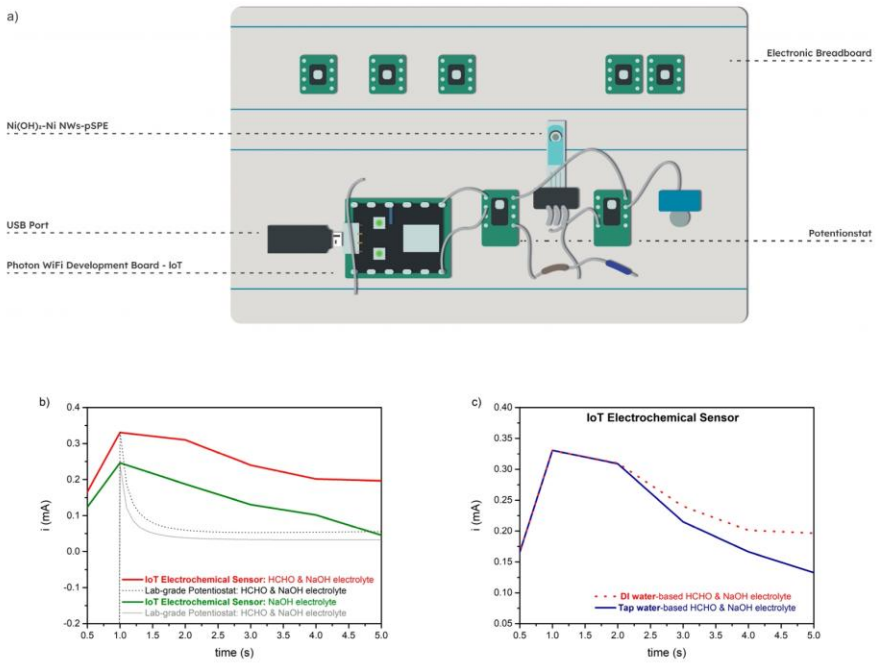


Figure 5. (**a**) Schematic of the IoT electrochemical sensor's individual parts with an integrated $Ni(OH)_2$–Ni NWs pSPEs-based detection system; (**b**) amperometric responses of custom-made IoT electrochemical sensor to injection of 0.1 M NaOH electrolyte (green) and 1 µM HCHO + 0.1 M NaOH electrolyte (red). Amperometric responses of lab-grade potentiostat observed in 0.1 M NaOH electrolyte (grey) and 1 µM HCHO + 0.1 M NaOH electrolyte (black); (**c**) amperometric responses of custom-made IoT electrochemical sensor to the injection of 1 µM HCHO + 0.1 M NaOH prepared in DI—(red) and tap-water-based (blue) electrolytes. All the curves were recorded at an applied potential of 0.7 V.

Figure 5b depicts the amperometric response of the custom-designed IoT sensor to the dripping of 0.1 M NaOH electrolyte (green) or 1 µM HCHO + 0.1 KOHM NaOH electrolyte (red) onto the WE of the SPE (i.e., $Ni(OH)_2$–Ni NWs). The amperometric measurements were performed at a constant applied potential of 0.7 V vs. Ag q-RE. In the absence of HCHO (green), the output current reaches the maximum values in the first second, indicating a rapid oxidation reaction of $Ni(OH)_2$ to NiOOH (reaction 1), followed by a current-output drop due to the analyte diffusion restriction. When a 1 µM concentration of HCHO was added to the 0.1 M NaOH electrolyte (red), the maximum current output (0.34 mA) was also observed in the first second, meaning that the HCHO oxidation started directly after the formation of the first NiOOH species (reaction 3). Hence, the response time required for the sensor platform to reach its maximum current was 1 s. This indicates that the sensitivity of the proposed sensor for $HCHO_{aq}$ detection depends on the efficiency of the current output at the start of the measurement. Furthermore, to determine the accuracy of the amperometric measurements observed with the custom-designed sensor, the current–time plots were compared with the amperometric measurements observed using the laboratory potentiostat (Figure 5b, black and grey). The current outputs in the first second are comparable for the commercial potentiostat and the developed sensor, indicating that the fabricated sensor platform does not affect the sensitivity of the $HCHO_{aq}$ detection. However, after that point, the curves differ as the settling time of the lab-grade potentiostat is shorter than that of the fabricated IoT electrochemical sensor. Hence, the obtained data demonstrate that the developed IoT electrochemical sensor would suit

applications for rapid (1 s) and low-cost (i.e., considerably cheaper than any lab-grade potentiostat) monitoring of HCHO in water.

4. Conclusions

In summary, we have constructed a portable, autonomous, IoT electrochemical sensor that detects $HCHO_{aq}$ in distilled or tap water. The sensor comprises assembled electronics consisting of a Photon "Internet of Things (IoT)" development kit, a USB port for charging, and a miniaturized potentiostat, all enclosed in a small, protective case (size 58 mm × 33 mm). The external part of the sensor can connect to the HCHO detection system via a three-terminal electrode connector. The HCHO detection system based on custom-made $Ni(OH)_2$–Ni NWs pSPEs allowed us to rapidly (1 s) detect $HCHO_{aq}$ in alkaline media. The detection system can detect concentrations of HCHO at 0.8 μM/24 ppb, a linear response over two wide ranges of HCHO concentrations (0.8×10^{-6}–5×10^{-4} M and 5×10^{-4}–1×10^{-2} M). It also assembles the basic requirements for real-time applications, including low cost, simplicity, selectivity, and sensitivity, together with reusability and reproducibility. Thus, this study demonstrated that the developed IoT electrochemical sensor, which also allows for the easy replacement of an external detection system, can be used as an effective, portable, inexpensive device for testing HCHO and other organic/inorganic pollutants in real-life conditions.

Author Contributions: Š.T.: investigation, visualization, formal analysis, data curation, and writing—original draft, A.K.: formal analysis, data curation, and writing—review and editing. K.Ž.S.: writing—review and editing. U.K. and I.K.: investigation, writing—review and editing. B.K.: investigation, visualization, analysis, and data curation. S.Š.: funding acquisition, writing—review and editing. K.Ž.: supervision, conceptualization, funding acquisition, and writing—review and editing. All authors have read and agreed to the published version of the manuscript.

Funding: This research received no external funding.

Institutional Review Board Statement: Not applicable.

Informed Consent Statement: Not applicable.

Data Availability Statement: Availability Statements are available in section "MDPI Research Data Policies" at https://www.mdpi.com/ethics (accessed on 15 March 2023).

Acknowledgments: This study was supported by the Slovenian Research Agency through the P2-0084 research program and the J2-8182 and PR-06805 projects, of which this investigation forms a part.

Conflicts of Interest: The authors declare that they have no known competing financial interest or personal relationships that could have appeared to influence the work reported in this paper.

References

1. Chou, C.-H.; Chang, J.-L.; Zen, J.-M. Effective analysis of gaseous formaldehyde based on a platinum-deposited screen-printed edge band ultramicroelectrode coated with Nafion as solid polymer electrolyte. *Sens. Actuators B Chem.* **2010**, *147*, 669–675. [CrossRef]
2. Zhang, S.; Zhao, L.; Huang, B.; Li, X. Enhanced sensing performance of Au-decorated TiO_2 nanospheres with hollow structure for formaldehyde detection at room temperature. *Sens. Actuators B Chem.* **2022**, *358*, 131465. [CrossRef]
3. del Torno-de Román, L.; Alonso-Lomillo, M.A.; Domínguez-Renedo, O.; Merino-Sánchez, C.; Merino-Amayuelas, M.P.; Arcos-Martínez, M.J. Fabrication and characterization of disposable sensors and biosensors for detection of formaldehyde. *Talanta* **2011**, *86*, 324–328. [CrossRef] [PubMed]
4. Herschkovitz, Y.; Eshkenazi, I.; Campbell, C.; Rishpon, J. An electrochemical biosensor for formaldehyde. *J. Electroanal. Chem.* **2000**, *491*, 182–187. [CrossRef]
5. Yao, D.; Wang, Y.; Li, H. Silver clusters based sensor for Low content formaldehyde detection in colorimetric and fluorometric dual Mode. *Sens. Actuators B Chem.* **2020**, *305*, 127451. [CrossRef]
6. Zhang, N.; Lu, Y.; Fan, Y.; Zhou, J.; Li, X.; Adimi, S.; Liu, C.; Ruan, S. Metal–organic framework-derived $ZnO/ZnCo_2O_4$ microspheres modified by catalytic PdO nanoparticles for sub-ppm-level formaldehyde detection. *Sens. Actuators B Chem.* **2020**, *315*, 128118. [CrossRef]

7. Bian, Y.; Nie, L.; Wang, A.; Zhang, L.; Yue, R.; Han, N.; Chen, Y. Facile synthesis of stoichiometric InOCl mesoporous material for high performance formaldehyde gas sensors. *Sens. Actuators B Chem.* **2020**, *319*, 128078. [CrossRef]
8. Sun, Y.; Yang, H.; Zhao, Z.; Suematsu, K.; Li, P.; Yu, Z.; Zhang, W.; Hu, J. Fabrication of ZnO quantum dots@ SnO_2 hollow nanospheres hybrid hierarchical structures for effectively detecting formaldehyde. *Sens. Actuators B Chem.* **2020**, *318*, 128222. [CrossRef]
9. Feng, X.; Wei, Q.; Li, S.; Wei, X.; Yang, X.; Song, Z.; Geng, B.; Li, Z.; Zhang, J.; Yan, M. Organic-inorganic photoelectrochemical sensor based on aza-cope rearrangement reaction for formaldehyde. *Sens. Actuators B Chem.* **2021**, *330*, 129342. [CrossRef]
10. Ma, Z.; Yang, K.; Xiao, C.; Jia, L. C-Doped $LaFeO_3$ Porous Nanostructures for Highly Selective Detection of Formaldehyde. *Sens. Actuators B Chem.* **2021**, *347*, 130550. [CrossRef]
11. Kang, Z.; Zhang, D.; Li, T.; Liu, X.; Song, X. Polydopamine-modified SnO_2 nanofiber composite coated QCM gas sensor for high-performance formaldehyde sensing. *Sens. Actuators B Chem.* **2021**, *345*, 130299. [CrossRef]
12. Ling, W.; Zhu, D.; Pu, Y.; Li, H. The ppb-level formaldehyde detection with UV excitation for yolk-shell MOF-derived ZnO at room temperature. *Sens. Actuators B Chem.* **2022**, *355*, 131294. [CrossRef]
13. Chouler, J.; Cruz-Izquierdo, Á.; Rengaraj, S.; Scott, J.L.; Di Lorenzo, M. A screen-printed paper microbial fuel cell biosensor for detection of toxic compounds in water. *Biosens. Bioelectron.* **2018**, *102*, 49–56. [CrossRef] [PubMed]
14. Singh, R.; Hong, S.; Jang, J. Label-free detection of influenza viruses using a reduced graphene oxide-based electrochemical immunosensor integrated with a microfluidic platform. *Sci. Rep.* **2017**, *7*, 42771. [CrossRef] [PubMed]
15. Tancharoen, C.; Sukjee, W.; Thepparit, C.; Jaimipuk, T.; Auewarakul, P.; Thitithanyanont, A.; Sangma, C. Electrochemical biosensor based on surface imprinting for zika virus detection in serum. *ACS Sens.* **2018**, *4*, 69–75. [CrossRef] [PubMed]
16. Kavčič, U.; Karlovits, I. The influence of process parameters of screen-printed invasive plant paper electrodes on cyclic voltammetry. *Nord. Pulp Pap. Res. J.* **2020**, *35*, 299–307. [CrossRef]
17. Morrin, A.; Killard, A.J.; Smyth, M.R. Electrochemical characterization of commercial and home-made screen-printed carbon electrodes. *Anal. Lett.* **2003**, *36*, 2021–2039. [CrossRef]
18. Arduini, F.; Forchielli, M.; Amine, A.; Neagu, D.; Cacciotti, I.; Nanni, F.; Moscone, D.; Palleschi, G. Screen-printed biosensor modified with carbon black nanoparticles for the determination of paraoxon based on the inhibition of butyrylcholinesterase. *Microchim. Acta* **2015**, *182*, 643–651. [CrossRef]
19. Arduini, F.; Di Nardo, F.; Amine, A.; Micheli, L.; Palleschi, G.; Moscone, D. Carbon black-modified screen-printed electrodes as electroanalytical tools. *Electroanalysis* **2012**, *24*, 743–751. [CrossRef]
20. He, P.; Wang, X.; Liu, Y.; Liu, X.; Yi, L. Comparison of electrocatalytic activity of carbon-supported Au–M (M = Fe, Co, Ni, Cu and Zn) bimetallic nanoparticles for direct borohydride fuel cells. *Int. J. Hydrogen Energy* **2012**, *37*, 11984–11993. [CrossRef]
21. Yeo, B.S.; Bell, A.T. In Situ Raman study of nickel oxide and gold-supported nickel oxide catalysts for the electrochemical evolution of oxygen. *J. Phys. Chem. C* **2012**, *116*, 8394–8400. [CrossRef]
22. Min, Y.; Chen, Y.; Zhao, Y.; Chen, C. Simple approach to synthesis Pt/NiO flower microspheres and their electrocatalytic properties. *Mater. Lett.* **2008**, *62*, 4503–4505. [CrossRef]
23. Miao, Y.; Wu, J.; Zhou, S.; Yang, Z.; Ouyang, R. Synergistic effect of bimetallic Ag and Ni alloys on each other's electrocatalysis to glucose oxidation. *J. Electrochem. Soc.* **2013**, *160*, B47–B53. [CrossRef]
24. Zhang, Y.; Zhang, M.; Cai, Z.; Chen, M.; Cheng, F. A novel electrochemical sensor for formaldehyde based on palladium nanowire arrays electrode in alkaline media. *Electrochim. Acta* **2012**, *68*, 172–177. [CrossRef]
25. Baez-Gaxiola, M.; Fernández-Sánchez, C.; Mendoza, E. Gold cluster based electrocatalytic sensors for the detection of formaldehyde. *Anal. Methods* **2015**, *7*, 538–542. [CrossRef]
26. Farjami, E.; Rottmayer, M.A.; Deiner, L.J. Evidence for oxygen reduction reaction activity of a Ni $(OH)_2$/graphene oxide catalyst. *J. Mater. Chem. A* **2013**, *1*, 15501–15508. [CrossRef]
27. Azizi, S.N.; Ghasemi, S.; Amiripour, F. Nickel/P nanozeolite modified electrode: A new sensor for the detection of formaldehyde. *Sens. Actuators B Chem.* **2016**, *227*, 1–10. [CrossRef]
28. De Lima, R.; Massafera, M.; Batista, E.; Iwasita, T. Catalysis of formaldehyde oxidation by electrodeposits of PtRu. *J. Electroanal. Chem.* **2007**, *603*, 142–148. [CrossRef]
29. Olivi, P.; Bulhoes, L.; Léger, J.-M.; Hahn, F.; Beden, B.; Lamy, C. The electrooxidation of formaldehyde on Pt (100) and Pt (110) electrodes in perchloric acid solutions. *Electrochim. Acta* **1996**, *41*, 927–932. [CrossRef]
30. Zhou, Z.-L.; Kang, T.-F.; Zhang, Y.; Cheng, S.-Y. Electrochemical sensor for formaldehyde based on Pt–Pd nanoparticles and a Nafion-modified glassy carbon electrode. *Microchim. Acta* **2009**, *164*, 133–138. [CrossRef]
31. Safavi, A.; Maleki, N.; Farjami, F.; Farjami, E. Electrocatalytic oxidation of formaldehyde on palladium nanoparticles electrodeposited on carbon ionic liquid composite electrode. *J. Electroanal. Chem.* **2009**, *626*, 75–79. [CrossRef]
32. Hassaninejad-Darzi, S.K. A novel, effective and low cost catalyst for formaldehyde electrooxidation based on nickel ions dispersed onto chitosan-modified carbon paste electrode for fuel cell. *J. Electroceram.* **2014**, *33*, 252–263. [CrossRef]
33. Raoof, J.-B.; Ojani, R.; Abdi, S.; Hosseini, S.R. Highly improved electrooxidation of formaldehyde on nickel/poly(o-toluidine)/Triton X-100 film modified carbon nanotube paste electrode. *Int. J. Hydrogen Energy* **2012**, *37*, 2137–2146. [CrossRef]
34. Raoof, J.-B.; Omrani, A.; Ojani, R.; Monfared, F. Poly (N-methylaniline)/nickel modified carbon paste electrode as an efficient and cheep electrode for electrocatalytic oxidation of formaldehyde in alkaline medium. *J. Electroanal. Chem.* **2009**, *633*, 153–158. [CrossRef]

35. Trafela, Š.; Šturm, S.; Rožman, K.Ž. Surface modification for the enhanced electrocatalytic HCHO oxidation performance of Ni-thin-film-based catalysts. *Appl. Surf. Sci.* **2020**, *537*, 147822. [CrossRef]
36. Trafela, Š.; Zavašnik, J.; Šturm, S.; Rožman, K.Ž. Formation of a $Ni(OH)_2$/NiOOH active redox couple on nickel nanowires for formaldehyde detection in alkaline media. *Electrochim. Acta* **2019**, *309*, 346–353. [CrossRef]
37. Trafela, Š.; Zavašnik, J.; Šturm, S.; Rožman, K.Ž. Controllable voltammetric formation of a structurally disordered NiOOH/Ni $(OH)_2$ redox pair on Ni-nanowire electrodes for enhanced electrocatalytic formaldehyde oxidation. *Electrochim. Acta* **2020**, *362*, 137180. [CrossRef]
38. Rahman, I.; Razeeb, K.; Kamruzzaman, M.; Serantoni, M. Characterisation of electrodeposited nickel nanowires using NCA template. *J. Mater. Process. Technol.* **2004**, *153*, 811–815. [CrossRef]
39. Karlovits, I.; Kavčič, U.; Trafela, Š.; Rožman, K.Ž. Comparison of Cyclic Voltammetry Measurements of Paper-Based Screen Printed Electrodes via Proprietary and Open Source Potentiostats. *BioResources* **2021**, *16*, 3916–3933. [CrossRef]
40. Hassaninejad-Darzi, S.K.; Rahimnejad, M.; Shajie, F.; Kootenaei, A.H.S. Electrocatalytic Oxidation of Formaldehyde onto Carbon Paste Electrode Modified with Hydrogen Titanate Nanotubes, Including Nickel Hydroxide. *Iran. J. Sci. Technol. Trans. A Sci.* **2018**, *42*, 1259–1268. [CrossRef]
41. Ojani, R.; Raoof, J.B.; Zavvarmahalleh, S.R.H. Preparation of Ni/poly(1,5-diaminonaphthalene)-modified carbon paste electrode; application in electrocatalytic oxidation of formaldehyde for fuel cells. *J. Solid State Electrochem.* **2009**, *13*, 1605–1611. [CrossRef]
42. Miao, Y.; Ouyang, L.; Zhou, S.; Xu, L.; Yang, Z.; Xiao, M.; Ouyang, R. Electrocatalysis and electroanalysis of nickel, its oxides, hydroxides and oxyhydroxides toward small molecules. *Biosens. Bioelectron.* **2014**, *53*, 428–439. [CrossRef] [PubMed]
43. Trafela, Š. *Development of Nanostructured Redox Couple $Ni(OH)_2$/NiOOH-Ni Based Receptor Elements for Detection of Formaldehyde in Alkaline Media*; Jožef Stefan International Postgraduate School: Ljubljana, Slovenia, 2020.
44. Trafela, Š.; Rožman, K.Ž. Modified Nickel Nanowires for Electro-Catalytic Oxidation of Formaldehyde in Alkaline Solutions. *Multidiscip. Digit. Publ. Inst. Proc.* **2019**, *15*, 43. [CrossRef]
45. Rahim, M.A.; Hameed, R.A.; Khalil, M. Nickel as a catalyst for the electro-oxidation of methanol in alkaline medium. *J. Power Sources* **2004**, *134*, 160–169. [CrossRef]
46. Perera, R.T.; Rosenstein, J.K. Quasi-reference electrodes in confined electrochemical cells can result in in situ production of metallic nanoparticles. *Sci. Rep.* **2018**, *8*, 1965. [CrossRef] [PubMed]
47. Yakushenko, A.; Mayer, D.; Buitenhuis, J.; Offenhäusser, A.; Wolfrum, B. Electrochemical artifacts originating from nanoparticle contamination by Ag/AgCl quasi-reference electrodes. *Lab Chip* **2014**, *14*, 602–607. [CrossRef]
48. Kong, L.-B.; Wang, R.-T.; Wang, X.-W.; Yang, Z.-S.; Luo, Y.-C.; Kang, L. Electrooxidation of Formaldehyde on Silver/Ordered Mesoporous Carbon Composite Electrode in Alkaline Solutions. *Int. J. Appl. Phys. Math.* **2011**, *1*, 5. [CrossRef]
49. Geng, J.; Bi, Y.; Lu, G. Morphology-dependent activity of silver nanostructures towards the electro-oxidation of formaldehyde. *Electrochem. Commun.* **2009**, *11*, 1255–1258. [CrossRef]

Disclaimer/Publisher's Note: The statements, opinions and data contained in all publications are solely those of the individual author(s) and contributor(s) and not of MDPI and/or the editor(s). MDPI and/or the editor(s) disclaim responsibility for any injury to people or property resulting from any ideas, methods, instructions or products referred to in the content.

4.7 Future Work

Building on the findings and limitations of this study, several key directions are proposed to advance the platform from a laboratory proof-of-concept toward a scalable, field-ready electrochemical sensing solution.

A primary goal is the expansion to gas-phase sensing, enabling the detection of volatile organic compounds in air. This will require sensor interface adaptations such as gas-permeable membranes or controlled diffusion layers to allow stable electrochemical performance outside of liquid environments.

The platform also stands to benefit from real-time, multi-analyte detection, using sensor array configurations where multiple modified electrodes operate in parallel. This approach would enable simultaneous monitoring of chemically related compounds and support applications in complex environmental or industrial settings. Integration with signal deconvolution or machine learning algorithms would further enhance resolution and specificity.

Automated parameter optimisation represents another promising direction. Embedding feedback-controlled logic into the potentiostat would allow the system to dynamically adjust bias voltages, scan rates, or waveform profiles based on signal feedback, maximising sensitivity and efficiency under varying conditions.

From a deployment perspective, the fabrication process can be streamlined by shifting electrode modification to the point of manufacture. Pre-functionalised electrodes would reduce user error, improve reproducibility, and eliminate the need for laboratory-based catalyst deposition prior to each use.

Equally important is the pursuit of sustainable and cost-effective materials. While platinum-group metals (PGMs) offer excellent catalytic performance, their high cost and environmental impact make them less viable for large-scale or disposable sensors. Future work should investigate alternatives such as carbon nanotubes (CNTs), graphene, and Vulcan XC-72R, which combine high surface area and electrical conductivity with significantly lower material cost and environmental burden. Incorporating such materials into biodegradable substrates like paper-based SPEs would further support green chemistry principles and reduce waste in high-throughput applications.

Lastly, long-term field trials will be essential to validate system performance under real-world conditions. This includes testing in wastewater facilities, industrial sites, and outdoor environments, where variables such as temperature, pH, humidity, and matrix complexity can affect stability and accuracy. Durability, fouling resistance, and calibration drift over extended use must be evaluated to ensure the platform's reliability in unsupervised or remote deployments.

Future studies could also explore emerging frequency-domain and time–frequency methods such as the STFT, Gabor, and wavelet transforms, as well as digital electrochemistry frameworks based on the Z-transform, to provide deeper insight into transient behaviour and to improve the modelling of discrete-time measurement systems.

By addressing these areas, future iterations of the system can evolve into an adaptable, scalable, and environmentally conscious tool for next-generation chemical sensing applications.

Chapter 5

Conclusions

Electrochemical sensing is often presented as a direct analytical readout of chemical processes occurring at an electrode surface. In practice, however, the information extracted from an electrochemical experiment is mediated by a layered measurement system comprising the excitation waveform, the instrumentation used to generate and acquire signals, and the evolving physicochemical state of the electrode–electrolyte interface. Each of these elements introduces constraints that shape observed sensitivity, selectivity, and stability, yet they are rarely examined in combination. This dissertation therefore investigates electrochemical sensing as an integrated measurement system, examining how experimental design choices across waveform, hardware, and interface collectively govern sensor performance.

This work explored the development of an electrochemical sensing system tailored for the detection of volatile toxic organic compounds, with an emphasis on benzenediol isomers. By combining modified SPEs with embedded signal processing, IoT connectivity, and advanced waveform analysis, the study aimed to bridge the gap between laboratory-grade performance and field-ready chemical sensing platforms.

Taken together, the results demonstrate that electrochemical sensing performance emerges from the coupling of materials, signal structure, instrumentation, and system-level deployment considerations. Viewed as a coupled system, improvements at one layer, such as catalytic enhancement of the electrode surface, only translate into practical gains when supported by appropriate waveform design and faithful hardware implementation. Frequency-domain analysis revealed how signal structure governs the balance between faradaic information and capacitive artefacts, while impedance-based diagnostics exposed stability and degradation as limiting factors beyond initial sensitivity. Hardware comparisons further showed that measurement fidelity is not solely determined by chemistry, but also by how electrochemical signals are generated and evaluated. When integrated into portable and IoT-enabled platforms, these layers collectively define whether laboratory-scale performance can be sustained under real-world conditions. This systems-level perspective provides a unifying framework for designing robust, interpretable, and deployable electrochemical sensors.

Beyond the technical objectives, one of the implicit goals of this work was to bring together traditionally distinct disciplines: analytical chemistry, electrochemistry, materials science, and electrical engineering into a unified, application-driven approach to sensor development. While these fields occasionally intersect in sensor design, they often operate with different priorities, vocabularies, and methodological frameworks. This project demonstrated that meaningful integration of these disciplines not only enhances the robustness of sensor systems but also enables novel functionality and deployment strategies that would not be possible within the bounds of any single domain.

5.1 Summary of Findings

The core objective of this work was to develop a deployable electrochemical sensor platform capable of detecting volatile toxic organic compounds (VTOC), with a focus on the redox-active benzenediols: catechol (CC), hydroquinone (HQ), and resorcinol (RS). To achieve this, the project followed a modular and scalable strategy that combined key elements fields, while related in scope, often pursue independent methodologies and design priorities. Their integration in this project proved essential for developing a system that was both scientifically rigorous and practically deployable.

At the materials level, screen-printed electrodes (SPEs) were modified with carbon-supported platinum and gold nanoparticles to enhance electrocatalytic response. Using techniques such as cyclic voltammetry (CV) and differential pulse voltammetry (DPV), CC and HQ exhibited well-defined, reversible redox peaks, while RS produced irreversible oxidation profiles, consistent with surface-bound polymerisation. Chronoamperometric measurements enabled quantification, with detection limits reaching 0.33 µM for CC and HQ, and 33 nM for RS. The fabrication method, relying on simple drop-casting and commercial fuel-cell grade catalysts, offered a reproducible and cost-effective route for producing deployable sensor elements.

The system's practical utility was validated using commercial formulations containing benzenediols. These real-world matrices introduced additional chemical complexity, including surfactants, solvents, and stabilisers. Despite these factors, the sensors were able to detect target analytes with good selectivity, indicating a promising level of robustness and reliability under field-relevant conditions.

Electrochemical impedance spectroscopy (EIS) was used not only for endpoint characterisation but also as a tool for tracking sensor stability and surface degradation during operation. By fitting impedance spectra to simplified equivalent circuits, values for polarisation resistance and effective capacitance were extracted and monitored over time. Unmodified SPEs demonstrated performance improvements due to electrochemical activation, while Pt-modified electrodes showed a more complex degradation profile after initial enhancement. These observations were supported by trends in CV behaviour, validating EIS as a real-time diagnostic tool within the sensor workflow.

A second layer of analysis involved examining voltammetric signal content in the frequency domain using Fourier transforms. Spectral decomposition of cyclic voltammetry, linear sweep voltammetry, differential pulse voltammetry, and square wave voltammetry wave functions revealed how waveform shape directly influences the harmonics of the aforementioned electrochemical techniques. These insights enabled the quantification of harmonic contributions and provided a framework for waveform selection and optimisation of their parameters based on frequency-dependent behaviour. This signal processing perspective is uncommon in classical electrochemical analysis but draws heavily from communication engineering, further demonstrating the interdisciplinary scope of the work.

The impact of hardware design was also explored by comparing digital staircase and true analogue voltage scans. Analogue scans produced smoother current responses and more consistent peak shapes, while digital scans obscured minor details due to abrupt potential steps. These differences, though subtle, had measurable effects on signal interpretation and highlighted the importance of matching hardware capability with the resolution required for quantitative analysis.

Lastly, a custom IoT-enabled potentiostat was integrated into a formaldehyde sensor platform as a case study. Although the sensing material and electrode fabrication were led by collaborators, the present author contributed to the functional deployment of the device. Tasks included adapting firmware to control applied potentials, configuring and

setting up RS232 serial communication for data logging, integrating Wi-Fi functionality, and conducting quasi-alpha and -beta testing to validate system behaviour against commercial instruments. These steps ensured the sensor system transitioned from bench prototype to fully operational device.

Taken together, the results presented in this dissertation demonstrate that electrochemical sensing performance is often constrained not solely by materials or chemistry, but by the measurement system itself, including excitation design, instrumentation, and the evolving electrode–electrolyte interface. By treating electrochemical sensing as an interdependent measurement system rather than a transparent analytical window, this work provides a framework for interpreting sensor performance, limitations, and transferability under real-world conditions. In summary, this work demonstrates that integrating concepts from traditionally distinct fields can result in a sensing platform that is analytically sound, reliable, and practically deployable. Each component, from surface chemistry and waveform optimisation to hardware tuning and field integration, contributed to a complete system that performs beyond the sum of its parts.

5.2 Limitations and Recommendations

While the sensing system presented in this work demonstrated strong analytical performance and versatility, several limitations remain that should be addressed in future development cycles.

First, the system is currently limited to liquid-phase detection, with all electrochemical measurements performed in aqueous media. This restricts its application scope, particularly for VTOCs that are primarily encountered in air, such as formaldehyde, and benzene. Expanding the platform to include gas-phase detection capabilities, potentially through integration with gas-permeable membranes or pre-concentration layers, would significantly increase its practical relevance in environmental and industrial settings.

Second, the electrode substrates used throughout this project are alumina-based screen-printed electrodes (SPEs), which offer mechanical and chemical robustness, along with reliable electrical performance but are neither biodegradable and are recyclable to a limited extent. Since many of these electrodes are used in a single-use format, the cumulative environmental footprint is non-trivial. Future work could explore the use of renewable and biodegradable substrates, such as paper-based or cellulose-derived SPEs, which have begun to emerge as sustainable alternatives in the field.

Another challenge lies in the inherent response time of electrochemical systems. Techniques such as chronoamperometry and voltammetry require measurable interaction times for charge transfer and diffusion processes to stabilise, which limits their suitability for rapid or instantaneous sensing. While data smoothing and predictive algorithms may improve perceived responsiveness, hard real-time detection remains a technical challenge for electrochemical platforms, particularly in dynamic or safety-critical environments.

Additionally, the quality control of commercially sourced SPEs was found to be variable. Certain batches exhibited inconsistencies in baseline currents, mainly due to working electrode material and surface quality, which can undermine reproducibility. These issues are difficult to detect without full pre-screening of each sensor. For broader deployment, either tighter manufacturing quality standards or in-house fabrication with post-production characterisation may be necessary to ensure batch-to-batch reliability.

Finally, although the integration of EIS and frequency-domain analysis improved data interpretability, these methods also introduced computational overhead and required post-processing expertise. For future field-oriented versions of the platform, automated

signal analysis pipelines or embedded onboard processing would be beneficial to translate these diagnostic insights into accessible outputs for non-specialist users.

The present analysis is limited to stationary signal treatment, whereas most electrochemical processes are inherently non-stationary and would benefit from time–frequency domain approaches for a more complete characterisation.

Overall, while the current system provides a solid foundation, these limitations highlight several areas for refinement in terms of sustainability, versatility, responsiveness, and reliability. Addressing them will be key to transforming the platform from a proof-of-concept into a truly field-ready sensing tool.

References

Alaba, F. A. (2017). Internet of Things security: A survey. *Journal of Network and Computer Applications, 88*, 10-28.

Angerer, J. S. (1991). The determination of benzene in human blood as an indicator of environmental exposure to volatile aromatic compounds. *Fresenius' journal of analytical chemistry, 339(10)*, 740-742.

Auer, E. F. (1998). Carbons as supports for industrial precious metal catalysts. *Applied Catalysis A: General, 173(2)*, 259-271.

Bakker, E. &.-D. (2002). Electrochemical sensors. *Analytical chemistry, 74(12)*, 2781-2800.

Bard, A. J. (2022). Electrochemical methods: fundamentals and applications. John Wiley & Sons.

Božiček, B. L. (2024). Unveiling the potential of (CoFeNiMnCr)3O4 high-entropy oxide synthesized from CoFeNiMnCr high-entropy alloy for efficient oxygen-evolution reaction. *Journal of Materials Science, 59(21)*, 9189-9207.

Brown, S. K. (1994). Concentrations of volatile organic compounds in indoor air–a review. *Indoor air, 4(2)*, 123-134.

Chang, B. Y. (2010). Electrochemical impedance spectroscopy. *Annual Review of Analytical Chemistry, 3(1)* , 207-229.

Chen, Y. L. (2017). Ultrasensitive and simultaneous detection of hydroquinone, catechol and resorcinol based on the electrochemical co-reduction prepared Au-Pd nanoflower/reduced graphene oxide nanocomposite. *Electrochimica Acta, 231*, 677-685.

Cochran, W. T. (1967). What is the fast Fourier transform? *Proceedings of the IEEE, 55(10)*, 1664-1674.

Colburn, A. W. (2021). Lifting the lid on the potentiostat: a beginner's guide to understanding electrochemical circuitry and practical operation. *Physical Chemistry Chemical Physics, 23(14)*, 8100-8117.

Control, C. f. (1990). *NIOSH pocket guide to chemical hazards (No. 90-117).* United States: National Institute for Occupational Safety and Health.

Desimoni, E. &. (2013). Presenting analytical performances of electrochemical sensors. Some suggestions. *Electroanalysis, 25(7)*, 1645-1651.

Dücso, C. Á. (2003). Explosion-proof monitoring of hydrocarbons by mechanically stabilised, integrable calorimetric microsensors. *Sensors and Actuators B: Chemical, 95(1-3)*, 189-194.

Elosua, C. M. (2006). Volatile organic compound optical fiber sensors: A review. *Sensors, 6(11)*, 1440-1465.

Fiedler, U. &. (1973). Selectrode—the universal ion-selective electrode: Part VII. A valinomycin-based potassium electrode with nonporous polymer membrane and solid-state inner reference system. *Analytica chimica acta, 67(1)*, 179-193.

Freiser, H. (2012). *Ion-selective electrodes in analytical chemistry.* Springer Science & Business Media.

Gattia, D. M. (2009). Study of different nanostructured carbon supports for fuel cell catalysts. *Journal of Power Sources, 194(1)*, 243-251.

Ghanem, M. A. (2007). Electrocatalytic activity and simultaneous determination of catechol and hydroquinone at mesoporous platinum electrode. *Electrochemistry communications, 9(10)*, 2501-2506.

Grafakos, L. (2008). *Classical fourier analysis (Vol. 2).* New York: Springer.

Griffin, D. &. (1984)). Signal estimation from modified short-time Fourier transform. *IEEE Transactions on acoustics, speech, and signal processing, 32(2)*, 236-243.

Hahn, S. (2006). *Resorcinol (No. 71).* World Health Organization.

Harvey, T. M. (1995). Holistic risk assessment: an emerging process for environmental decisions. *Regulatory Toxicology and Pharmacology, 22(2)*, 110-117.

Harwood, J. E. (1969). The use of an ion-selective electrode for routine fluoride analyses on water samples. *Water Research, 3(4)*, 273-280.

Hayat, A. &. (2014). Disposable screen printed electrochemical sensors: Tools for environmental monitoring. *Sensors, 14(6)*, 10432-10453.

Heller, A. &. (2008). Electrochemical glucose sensors and their applications in diabetes management. *Chemical reviews, 108(7)*, 2482-2505.

Hintz, K. &. (n.d.). Microcontrollers: architecture, implementation, and programming. 1992: McGraw-Hill, Inc.

Hübschmann, H.-J. (2025). Handbook of GC-MS: fundamentals and applications. John Wiley & Sons.

Hudson, N. L. (2019). NIOSH skin notation (SK) profiles: catechol.

Hughes, A. E. (2021). Platinum group metals: A review of resources, production and usage with a focus on catalysts. *Resources, 10(9)*, 93.

Inzelt, G. (2014). Chronoamperometry, Chronocoulometry, and Chronopotentiometry. In Encyclopedia of Applied Electrochemistry (pp. 207-214). New York, NY: Springer.

Kissinger, P. T. (1983). Cyclic voltammetry. *Journal of chemical education, 60(9)*, 702.

Kung, H. H. (1989). Transition metal oxides: surface chemistry and catalysis (Vol. 45). Elsevier.

Lewis, F. (2004). Wireless sensor networks. Smart environments: technologies, protocols, and applications, 11-46.

Lin, H. G. (2009). Sensitive and rapid determination of catechol in tea samples using mesoporous Al-doped silica modified electrode. *Food Chemistry, 113(2)*, 701-704.

Lovrić, M. &. (1982). Theory of differential normal pulse voltammetry. *Electrochimica Acta, 27(7)*, 963-968.

Macdonald, D. D. (1998). Characterizing electrochemical systems in the frequency domain. *Electrochimica Acta, 43(1-2)*, 87-107.

Mall, R. (2009). *Real-time systems: theory and practice.* Pearson Education India.

Mallat, S. (1999). A wavelet tour of signal processing. Academic Press.

Mooring, C. I. (1977). AC Voltammetry at large amplitudes: A simplified theoretical approach. *Journal of Electroanalytical Chemistry and Interfacial Electrochemistry, 78(2)*, 219-227.

Nematollahi, N. D. (2018). Volatile chemical emissions from fragranced baby products. *Air Quality, Atmosphere & Health, 11(7)*, 785-790.

Ngamchuea, K. T. (2020). Electrochemical oxidation of resorcinol: mechanistic insights from experimental and computational studies. *RSC advances, 10(47)*, 28454-28463.

Oppenheim, A. V. (1997). *Signals & systems.* Pearson Education.

Patel, B. A. (2020). Amperometry and potential step techniques. *Electrochemistry for Bioanalysis, 1*, 9-26.

Redlich, C. A. (1997). Sick-building syndrome. *The Lancet, 349(9057)*, 1013-1016.

Roberge, J. K. (1975). Operational amplifiers: theory and practice (Vol. 197). New York: Wiley.

Scozzari, A. (2008). Electrochemical sensing methods: a brief review. *Algal Toxins: Nature, Occurrence, Effect and Detection*, 335-351.

Spiegel, M. R. (1965). *Laplace transforms.* New York: McGraw-Hill.

Spiegel, M. R. (1965). *Laplace transforms (p. 249).* New York: McGraw-Hill.

Sundararajan, D. (2001). The discrete Fourier transform: theory, algorithms and applications. World Scientific.

Swartz, M. E. (2005). UPLC™: an introduction and review. *Journal of Liquid Chromatography & Related Technologies, 28*, 7-8.

Szulczyński, B. &. (2017). Currently commercially available chemical sensors employed for detection of volatile organic compounds in outdoor and indoor air. *Environments, 4(1)*, 21.

Tietze, U. S. (2015). Electronic circuits: handbook for design and application. Springer.

Trafela, Š. Z. (2019). Formation of a Ni (OH) 2/NiOOH active redox couple on nickel nanowires for formaldehyde detection in alkaline media. *Electrochimica Acta, 309*, 346-353.

Vretblad, A. (2003). Laplace and Z transforms. In Fourier Analysis and Its Applications . New York, NY: Springer New York.

Yao, J. (1993). Complete Gabor transformation for signal representation. *IEEE Transactions on image processing, 2(2)*, 152-159.

Yu, X. &. (2007). Recent advances in activity and durability enhancement of Pt/C catalytic cathode in PEMFC: Part II: Degradation mechanism and durability enhancement of carbon supported platinum catalyst. *Journal of power sources, 172(1)*, 145-154.

Zhang, J. &. (2003). Indoor air pollution: a global health concern. *British medical bulletin, 68(1)*, 209-225.

Bibliography

Publications Related to the Thesis

Journal Articles

Trafela, Š., Krishnamurthy, A., Soderžnik, K. Ž., Kavčič, U., Karlovits, I., Klopčič, B., ... & Žužek, K. (2023). IoT Electrochemical Sensor with Integrated Ni (OH) 2–Ni Nanowires for Detecting Formaldehyde in Tap Water. *Sensors, 23*(10), 4676.

Krishnamurthy, A., Samardžija, Z., Trafela, Š., Korent, A., Šturm, S., & Soderžnik, K. Ž. (2024). Electrochemical detection of benzenediols using carbon-supported catalysts. *Electrochimica Acta, 493*, 144389.

Krishnamurthy, A., & Žagar Soderžnik, K. (2024). Influence of Potentiostat Hardware on Electrochemical Measurements. *Sensors, 24*(15), 4907.

Krishnamurthy, A., & Soderžnik, K. Ž. (2025). Multivariate diagnostics of electrochemical sensor drift by in situ impedance spectroscopy and voltammetry: A benzenediol-based framework. *Sensing and Bio-Sensing Research, 50,* 100871.

Krishnamurthy, A., & Soderžnik, K. Ž. (2025). Frequency-domain analysis of voltammetric signals: a framework to augment electrochemical sensing explored through benzenediol detection. *Measurement,* 119706.

Biography

The author of this thesis, Abhilash Krishnamurthy, was born on 20 March 1991 in Bengaluru, India. He completed a Bachelor of Engineering in Electronics and Communication Engineering at Sri Jayachamarajendra College of Engineering, Mysore, in 2013, graduating with First Class with Distinction. In 2017, he obtained a Master of Science in Sensor Systems Technology from Karlsruhe University of Applied Sciences, Germany. The master's research, carried out at the Fraunhofer Institute for Chemical Technology in Karlsruhe, examined the influence of carbon dioxide on anion-exchange membrane direct methanol fuel cells.

In 2019, the author began doctoral studies at the Jožef Stefan International Postgraduate School, Ljubljana, under the supervision of Asst. Prof. Dr. Kristina Žagar Soderžnik at the Jožef Stefan Institute, Department for Nanostructured Materials (K7). The doctoral research, entitled "Comprehensive Approach to Electrochemical Sensing of Volatile Toxic Organic Compounds," focused on the design, fabrication, and evaluation of portable electrochemical sensor platforms integrating advanced high-performance materials, high-fidelity measurement principles, signal-processing and IoT-based instrumentation.

During the doctoral period, the author participated in several research projects funded by the Slovenian Research and Innovation Agency (ARIS, formerly ARRS). The results of this work were published in Electrochimica Acta, Sensors, and Sensing and Bio-Sensing Research and Measurement.

Prior to undertaking doctoral studies, the author worked as an Associate Software Engineer at Robert Bosch Engineering and Business Solutions, Bengaluru (2013–2014), contributing to software integration and testing for automotive engine-management systems.

The author's research interests centre on the application of electrical engineering principles, particularly frequency-domain and signal-processing methods, to enhance the fidelity, interpretability, and analytical depth of electrochemical systems and measurements.